Determination of the convective heat transfer coefficients from the surfaces of buildings within urban street canyons

Smith, James

Award date:
2010

Awarding institution:
University of Bath

Determination of the convective heat transfer coefficients from the surfaces of buildings within urban street canyons

James Oliver Smith

A thesis submitted for the degree of Doctor of Philosophy

University of Bath

Department of Mechanical Engineering

March 2010

Abstract

In the summer of 2007, the number of people living in the world's urban areas exceeded that of those living in the countryside. Such urbanisation tends to modify the climates of towns and cities as a result of a number of factors which together form the 'urban heat island' effect. In order to better design buildings and urban areas to cope with these effects, it is first necessary to understand the heat transfer mechanisms which are taking place. The aim of the current research has therefore been to provide convective heat transfer data appropriate for low-rise urban environments by investigating the effects of wind speed, direction and street geometry.

The research has employed the naphthalene sublimation technique which has been extended in several fundamental areas including development of a novel approach to measure the rate of sublimation from wind tunnel models. This technique has permitted measurements to be made over an array of discrete locations, revealing the variation across building surfaces. The uncertainty in the convective heat transfer coefficients obtained was calculated to be approximately ±6%. Tests were conducted in the BRE wind tunnel with an atmospheric boundary layer simulation appropriate to inner city areas. Cube models were arranged so as to form long rows of flat-roofed buildings referred to as 'street canyons'.

A series of correlations have been derived from the experimental results from which the rate of convection occurring from each building surface may be obtained with respect to wind speed. The greatest rates of convective heat transfer have been shown to occur at the top of the windward wall and leading edge of the roof, the lowest rates from the leeward wall of a building. Convection was found to be reduced in narrow street canyons. In wider street canyons, the convective coefficients on the exposed windward and roof surfaces of buildings were higher, but the values on the leeward wall are lessened due to the distancing of the downstream windward vortex. The effect of wind direction was found to be relatively small and therefore it is proposed that the convective heat transfer relationships presented may be applied irrespective of wind direction.

Acknowledgments

This research project was conducted at the Building Research Establishment (BRE) in a joint collaboration with the Department of Mechanical Engineering at the University of Bath. I would sincerely like to thank Dr John Burdett and the BRE Trust for their funding and support of this project.

My thanks go to all of the staff at BRE who have provided me with help, support and encouragement during the course of this research, especially to Dr Paul Blackmore, Gordon Breeze, Dave Richardson and Dr Philippa Westbury.

Also, thanks to my internal examiner at the University of Bath, Dr Stuart MacGregor and my external examiner from the University of Sheffield, Professor Steve Sharples.

Table of Contents

Chapter 1 Introduction 1
1.1 Background 1
1.2 Overview of this thesis 4
1.3 Summary of the gaps in current knowledge 5
1.4 Aims of current research 7

Chapter 2 Urban heat islands 8
2.1 Introduction 8
2.2 The causes of urban heat islands 12
2.3 Determining the presence of an urban heat island 14
2.4 Ameliorating urban heat islands 16
2.4.1 Modification of the urban geometry 16
2.4.2 Increasing the surface albedo 17
2.4.3 Increasing urban vegetation 21
2.4.4 Installation of green roofs and façades 22
2.4.5 Increasing urban wind speeds 24
2.4.6 Reducing anthropogenic heat fluxes 27
2.5 The consequences of an urban heat island 29
2.6 Summary and conclusions 32

Chapter 3 Review of convective heat transfer 33
3.1 Overview of theory 33
3.2 Research to date 35
3.3 Design guidance 61
3.4 Use in computational modelling 65
3.5 Summary and conclusions 67

Chapter 4 The naphthalene sublimation technique 71
4.1 Introduction to the technique 71
4.2 About naphthalene 73
4.3 Overview of experimental methodology 75
4.4 The heat / mass transfer analogy 76
4.4.1 Heat transfer 77
4.4.2 Mass transfer 79
4.4.3 Comparison of heat and mass transfer 81

Chapter 5 Preliminary trials of the naphthalene technique 82
5.1 Experimental methodology 82
5.1.1 Measurement of the naphthalene coating thickness 82
5.1.2 The wind tunnel model 86
5.1.3 Naphthalene coating technique 87
5.2 Preliminary experiments 88
5.3 Improvements to the methodology 96
5.4 Summary of experimental methodology 100

Chapter 6 Development of a wind tunnel simulation 104
6.1 The BRE boundary layer wind tunnel 104
6.2 Vertical mean velocity profile 106
6.3 The development of the boundary layer 111

6.4 The effect of wind tunnel velocity 113
6.5 Reynolds numbers 115
6.6 Turbulence Intensity 117
6.7 Turbulence integral length 119
6.8 Conclusions 124

Chapter 7 Air flow in urban street canyons 125
7.1 Methodology 126
7.2 Processing of data 129
7.3 Tests to determine the repeatability of results 131
7.4 Arrangement of models 132
7.4.1 The effect of canyon length 135
7.4.2 The effect of the number of surrounding canyons 136
7.4.3 Summary of the selected model arrangements 138
7.5 Experimental results 140
7.5.1 Flow perpendicular to the street canyon 140
7.5.2 Flow parallel to the street canyon 144
7.5.3 Flow from intermediate angles 145
7.6 Conclusions 145

Chapter 8 Naphthalene sublimation measurements 146
8.1 Calculation of convective heat transfer coefficients 146
8.2 Selection of experimental variables 151
8.3 Sensitivity analysis 158
8.4 Assessment of measurement accuracy 161
8.5 Assessment of measurement uncertainties 164

Chapter 9 The effect of wind speed upon convective transfer 165
9.1 Introduction 165
9.2 Free convection results 168
9.3 Forced convection results 171
9.4 Derivation of equations with respect to the free-stream velocity 175
9.5 The effect of reference wind speed height 188
9.6 Derivation of equations with respect to met. standard wind speeds 192
9.7 Comparison with standard correlations 197
9.8 Comparison with full-scale measurements 199
9.9 Summary and conclusions 208

Chapter 10 The effect of canyon width upon convective transfer 211
10.1 Introduction 211
10.2 Experimental results 212
10.3 Comparison of results for varying height-to-width ratios 215
10.4 Quantifying the effects of changing canyon widths 218
10.5 Conclusions 221

Chapter 11 The effect of wind direction upon convective transfer 223
11.1 Introduction 223
11.2 Experimental results 225
11.3 Comparison of results for varying wind angles 227
11.4 Conclusions 230

Chapter 12 Identifying regions of peak convective transfer 231
12.1 Introduction 231
12.2 Results and discussion 232
12.3 Conclusions 234

Chapter 13 The effect of surface roughness 235
13.1 Introduction 235
13.2 Results and discussion 236
13.3 Conclusions 238

Chapter 14 Conclusions 239
14.1 The naphthalene sublimation technique 239
14.2 Convective heat transfer from building surfaces 241
14.3 Application of results 244
14.4 Example calculation 245
14.5 Suggestions for further work 246

Chapter 15 References 248

ANNEXES 260

Annex A Naphthalene sublimation methodology 261

Annex B Power spectral density plots for the BRE wind tunnel 266

Annex C Calculations 270
Annex C1 - Calculation of the turbulence scale factor (S) 270
Annex C2 - Calculation of convective heat transfer coefficient (CHTC) 271
Annex C3 - Calculation of the density of humid air 273
Annex C4 - Calculation of the Reynolds number 275

Annex D Assessment of experimental uncertainty 276
Annex D1 – Background to the 'GUM' approach 276
Annex D2 - Overview of methodology 277
Annex D3 – Calculation of uncertainty in the CHTC values 283
Annex D4 - Calculation of combined standard and expanded uncertainties . 299

Annex E Convective heat transfer coefficient spreadsheet 300

Annex F Naphthalene sublimation result sheets 303

Annex G Naphthalene sublimation results 309

Annex H Apparatus 310

Annex I Publications and conference papers by the author 311

Table of Figures

All images were made by the author of this thesis, except where a source is stated below:

Figure 1.1: The Earth by night viewed from space
(source: NASA Visible Earth, 2000) 1
Figure 1.2: Predicted change in average summer daily air temperatures in 2080
(source: DEFRA, 2003) 2
Figure 2.1: Urban and rural mean annual temperatures for 1807-1818
(source: redrawn from data by Howard, 1833) 8
Figure 2.2: Air temperature distribution across London
(source: Watkins, 2002) 9
Figure 2.3: A photograph and infra-red image of the Shinjuku area of Tokyo
(source: Voogt, 2006) 14
Figure 2.4: The formation of an air temperature heat island over a typical city
(Sailor, 2002) 15
Figure 2.5: The reduction in surface temperature on a typical cool roof
(source: Hydro-Stop Incorporated, 2006) 18
Figure 2.6: The composition of sunlight (source: Levinson, 2004) 19
Figure 2.7: A range of 'cool roof' tiles in traditional colours
(source: American Rooftile Coatings, 2006) 20
Figure 2.8: The view across London from Primrose Hill
(source: WIKIPEDIA, 2003b) 21
Figure 2.9: Examples of green roofs in the Faroe Islands and Manhattan
(source: WIKIPEDIA, 2003a) 22
Figure 2.10: Examples of 'green walls' at the BRE Innovation Park, Watford 23
Figure 2.11: An infrared image of buildings with varying levels of insulation
(source: WIKIPEDIA, 2003c) 27
Figure 2.12: Cooling energy saving from cool roof installation in four US cities
(source: State of California Energy Commission, 2005) 30
Figure 3.1: Experimental results presented by Schwarz
(source: Schwarz, 1972) 42
Figure 3.2: Comparison of the 'WIND-CHTC' code with full-scale data
(source: Gandrille *et al.*, 1988) 52
Figure 3.3: Convective coefficients on the upwind cube
(source: Meinders and Hanjalic, 2002) 57
Figure 3.4: The convection coefficients for different building materials
(drawn from Equation 3.53 and Table 3.7) 66
Figure 3.5: Comparison of expressions for convection from a windward surface 69
Figure 4.1: The structure of naphthalene $C_{10}H_8$ (source: WIKIPEDIA, 2002) 73
Figure 4.2: Naphthalene crystal formation on the lid of a storage container 74
Figure 5.1: Sub-sections of a monopitched roof considered for wind loading
(source: BSI, 2005a) 83
Figure 5.2: Elcometer 456 coating thickness gauge and probe options
(source: Elcometer Limited, 2009) 85
Figure 5.3: The array of measurement locations over each cube's surface 89
Figure 5.4: The preliminary naphthalene coating setup 90
Figure 5.5: Reduction in average naphthalene thickness with time 91
Figure 5.6: Preliminary convective heat transfer coefficients for building surfaces

.....92
Figure 5.7: CHTC contour plots at wind speeds of 5 and 10 m/s.....94
Figure 5.8: Revised hollow wind tunnel model design showing hose connections 96
Figure 5.9: Plan view of hollow model showing inner walls and water flow path.97
Figure 5.10: Coated model showing red measurement point markers.....98
Figure 5.11: The wind tunnel models prior to and after coating with naphthalene 100
Figure 5.12: Preparations for dip coating the models in a fume cupboard.....100
Figure 5.13: Hot-water bath, pump and underside of the model.....101
Figure 5.14: Detail of the water bath, pump and hose connections to the model 101
Figure 5.15: The coated model in the wind tunnel and during measurements..102
Figure 5.16: Simplified naphthalene sublimation methodology flowchart.....103
Figure 6.1: A $^{1}/_{17}^{th}$ scale model of the BRE boundary layer wind tunnel 104
Figure 6.2: The upwind fetch of the BRE boundary layer wind tunnel 105
Figure 6.3: Dantec 55P11 CTA probe and 55H20 probe holder (source: Dantec Dynamics Limited, 2006).....106
Figure 6.4: The horizontal velocity profile in BRE wind tunnel.....107
Figure 6.5: Log-law fit to wind tunnel velocity profile 108
Figure 6.6: The velocity profile plotted against a logarithmic axis.....109
Figure 6.7: Velocity scaling factors with respect to the reference velocity 110
Figure 6.8: Plan view diagram showing profile measurement locations.....111
Figure 6.9: Development of the boundary layer along the wind tunnel test 112
Figure 6.10: Wind tunnel velocity profiles at various speed settings.....113
Figure 6.11: Velocity profiles expressed as ratios of velocity at 900 mm.....114
Figure 6.12: Turbulence intensity in the BRE wind tunnel 118
Figure 6.13: Power spectral density at z = 100 mm plotted on log-log axis 119
Figure 6.14: Turbulence power spectrum at a height of 100 mm.....120
Figure 6.15: Along-wind integral length.....122
Figure 6.16: Turbulence scale factor.....122
Figure 7.1: Pressure tapped cube model 126
Figure 7.2: A diagram showing tap locations and numbering on the cube model 127
Figure 7.3: The underside of the pressure tapped model in the wind tunnel.....128
Figure 7.4: Arrangement of pressure tapped model within street canyons 128
Figure 7.5: Tap row numbering system on pressure tapped cube.....130
Figure 7.6: Repeatability of results for perpendicular flow.....131
Figure 7.7: Repeatability of results for parallel flow.....131
Figure 7.8: Isolated flow regime at a height-to-width ratio of 0.33 133
Figure 7.9: The skimming flow regime at a height-to-width ratio of 1.0.....133
Figure 7.10: Wake interference flow regime at a height-to-width ratio of 0.5 133
Figure 7.11: Canyon height-to-width ratios and flow regimes.....134
Figure 7.12: Arrangement of models to determine the effect of canyon length.135
Figure 7.13: The effect of canyon length on surface pressures at 0 degrees ...136
Figure 7.14: The arrangement of models in the wind tunnel.....137
Figure 7.15: The effect of the number of upwind and downstream canyons.....137
Figure 7.16: Models at H/W ratios of 2.0, 1.0, 0.5 and 0.25 respectively.....139
Figure 7.17: Models arranged at 45 and 90 degrees (H/W = 0.5).....139
Figure 7.18: Pressure coefficient plots for perpendicular flow 140
Figure 7.19: Smoke visualisation of flow recirculating in the windward vortex..141
Figure 7.20: Smoke visualisation showing the separation on the roof 142
Figure 7.21: Typical pressure distributions over building surfaces (source: Cook, 1985).....142
Figure 7.22: Time-series photograph for flow visualisation around a cube model

.....143
Figure 7.23: Pressure coefficient plots for parallel flow 144
Figure 7.24: Pressure coefficient plots for intermediate angle flow.....145
Figure 8.1: Comparison of building layouts with the same plan area density....152
Figure 8.2: Typical street canyon geometries and notation 153
Figure 8.3: Some common roof types (source: BobVila.com, 2001).....154
Figure 8.4: Typical experimental results for H/W = 0.50 showing ±6% error bars 163
Figure 8.5: Typical experimental results for H/W = 0.25 showing ±6% error bars 163
Figure 9.1: The wake interference flow regime at height-to-width ratio of 0.5...165
Figure 9.2: Free convection coefficients derived from zero wind speed test.....168
Figure 9.3: The measured CHTC's across the two-dimensional model 171
Figure 9.4: Variation of CHTC by row with wind speed 173
Figure 9.5: Average convection coefficient data across all surfaces.....177
Figure 9.6: Average convection coefficient data across the windward surface.177
Figure 9.7: Average convection coefficient data across the roof surface.....178
Figure 9.8: Average convection coefficient data across the leeward surface....178
Figure 9.9: Average convection coefficient data at the exposed edge.....179
Figure 9.10: Comparison of equation types at low wind speeds.....181
Figure 9.11: Comparison of equation types at high wind speeds 182
Figure 9.12: Offset power-law best-fit curve for all surfaces.....183
Figure 9.13: Offset power-law best-fit curve for the windward surface 184
Figure 9.14: Offset power-law best-fit curve for the roof surface 184
Figure 9.15: Offset power-law best-fit curve for the leeward surface.....185
Figure 9.16: Offset power-law best-fit curve for the exposed edge.....185
Figure 9.17: Summary plot of offset power-law correlation curves 187
Figure 9.18: Offset power-law curves for wind speeds at alternative heights ...189
Figure 9.19: Average for all surfaces 193
Figure 9.20: Average across the windward surface.....193
Figure 9.21: Average across the roof surface 194
Figure 9.22: Average across leeward surface 194
Figure 9.23: Average for exposed edge area 195
Figure 9.24: Summary plot of offset power-law correlation curves 196
Figure 9.25: Comparison of results with the equation of BS EN 6946 197
Figure 9.26: Comparison of results with Nicol's expression.....200
Figure 9.27: Comparison of results (10 m winds) with Schwarz's expressions.201
Figure 9.28: Comparison of free-stream results with Schwarz's expressions...201
Figure 9.29: Comparison of results with Loveday and Taki's expressions.....202
Figure 9.30: Comparison of results with Sharples' windward expressions 204
Figure 9.31: Comparison of results with Sharples' leeward expressions.....204
Figure 9.32: Comparison of results with Sturrock's expressions 205
Figure 9.33: Comparison of results with the expression of Shao *et al.* 207
Figure 9.34: Comparison with the expression of Shao *et al.* for V < 5 m/s 207
Figure 10.1: Measured CHTC's for a height-to-width ratio of 1.00.....213
Figure 10.2: Measured CHTC's for a height-to-width ratio of 0.50.....213
Figure 10.3: Measured CHTC's for a height-to-width ratio of 0.25.....214
Figure 10.4: Variation of the height-to-width ratio at 45% tunnel speed.....215
Figure 10.5: Variation of the height-to-width ratio at 30% tunnel speed.....216
Figure 10.6: Variation of the height-to-width ratio at 15% tunnel speed.....217
Figure 11.1: The model street canyons arranged diagonal to the flow 224
Figure 11.2: The model street canyons arranged parallel to the flow 224
Figure 11.3: Experimental results for perpendicular (0 degrees) flow angle 225
Figure 11.4: Experimental results for intermediate (45 degree) flow angle.....226
Figure 11.5: Experimental results for parallel (90 degree) flow angle.....226

Figure 11.6: Comparison of CHTC for different wind directions..... 227
Figure 12.1: Photographs showing the typical patterns of naphthalene erosion232
Figure 12.2: Erosion of naphthalene with parallel flow 233
Figure 13.1: Comparison with surface roughness relationships 236
Figure 13.2: Comparison of the forced component of convection..... 237

Nomenclature

The following nomenclature has been employed in this thesis:

Variables:

A	Area of surface
C	Specific heat capacity
C_p	Pressure coefficient, or specific heat capacity
d	Zero plane displacement
D	Mass diffusivity coefficient, or depth of building
H	Height of building
h_c	Heat transfer coefficient
h_m	Mass transfer coefficient
k	Thermal diffusivity
K	Thermal conductivity
l	Length
L	Length scale
m	Mass
n	Frequency
P	Pressure
Q	Thermal energy
R	Gas constant
S	Building spacing
t	Time
T	Coating thickness
u_*	Friction velocity
v	Kinematic viscosity
V	Velocity
W	Width of street canyon
z	Height in the boundary layer
z_0	Roughness length
θ	Temperature, or roof pitch angle
μ	Viscosity
ρ	Density
κ	Von Kármán constant

Subscripts:

a	Air
f	Free-stream winds
hum	Humid air
H	At building height
m	Met. standard winds
n	Naphthalene
ref	Denotes reference value
v	Vapour
w	Water
x_u	Along-wind direction
∞	Free-stream flow

Superscripts:

~	Molar quantity

Dimensionless Parameters:

Gr	Grashof number
Nu	Nusselt number
Pr	Prandtl number
Re	Reynolds number
Sc	Schmidt number
Sh	Sherwood number

Conversion factors:

Heat transfer coefficients:
1 $Btu/ft^2h = 5.6786\ W/m^2K$
1 $W/m^2K = 0.1761\ Btu/ft^2h$

and:
1 $kcal/m^2hK = 1.163\ W/m^2K$
1 $W/m^2K = 0.860\ kcal/m^2hK$

Determination of the convective heat transfer coefficients from the surfaces of buildings within urban street canyons.

This doctoral research project has been undertaken as a joint project between the Building Research Establishment (BRE) and the University of Bath. The work was carried out under BRE project number ZBF066. The project was funded by the BRE Trust, formerly the Foundation for the Built Environment (FBE).

Chapter 1 Introduction

1.1 Background

Sometime during the summer of 2007, the human race reached a significant milestone in its evolution; for the first time ever, the number of people living in urban areas exceeded that of those living in rural areas (UN DESA 2006b). The so-called 'Urban Millennium' had arrived.

At the beginning of the 20th Century, only 13% of the world's inhabitants lived in towns and cities. This number had more than doubled by 1950 and by 2005 it was almost half of the entire population. The UN estimates that all regions of the world will have urban-living majorities by 2030, and that two-thirds of the world's total population will live in cities within the next 50 years. The last century has also seen the growth of 'mega-cities', each with more than 10 million inhabitants. In 1950 there were only two such mega-cities (New York and Tokyo), but this figure had risen to a total of 20 by 2005 with their inhabitants accounting for more than 9% of the world's total urban population (UN DESA, 2006a).

At home, over 89% of UK residents currently live in urban areas; a figure set to rise to over 92% in the next 25 years. The 7.6 million residents of London, the UK's largest urban sprawl, account for nearly 13% of the country's total population. The latest research shows that urban areas now cover 3% of the Earth's total land surface (The Earth Institute, 2005) - a figure double that of previous estimates.

Figure 1.1: The Earth by night viewed from space
(source: NASA Visible Earth, 2000)

The net result of this influx of people into the cities from the countryside is that our urban landscapes are changing. With inner-city land at a premium, buildings are becoming increasingly more dense and higher-rise. Open 'green' areas are fast disappearing as cities swell, pushing out into the suburbs and beyond. Once isolated towns now coalesce into indistinguishable districts of vast agglomerations. It is therefore not surprising that our urban climate is also changing. Towns and cities are typically warmer than the surrounding countryside as a result of the shelter from wind and retention of heat provided by our buildings. This 'urban heat island' phenomenon has now been documented in countless cities around the world as varied as London and Reykjavík, or Milan and Singapore.

In some colder countries this warming effect may be very welcome, at least for the time being. Heating loads are reduced, gardens bloom much earlier and the need for the gritting of roads in winter is minimised. However, in other parts of the world urban heat islands can be a serious risk to health, arising on top of already sweltering summer heat waves. Energy consumption for air-conditioning spirals, pumping out yet more heat onto the streets and so further exasperating the problem. Mortality rates soar, especially among the very young and elderly, and the general quality of city life deteriorates.

Furthermore, the Earth's climate is also changing. The recent *Stern Review* (Stern, 2006) showed that the scientific evidence for global warming was now "overwhelming" and its consequences "disastrous". If current trends continue, the average global temperatures are set to rise by at least 2 to 3 °C within the next 50 years, possibly by several degrees more. Heat waves like that experienced in Europe during the summer of 2003 in which an estimated 35,000 people died may become increasingly common.

Some researchers argue that global warming may already have had a significant effect on the climate in the UK. Last year (2008) was the sixth warmest since records began in 1850, exceeded only by 1998, 2002, 2003, 2004 and 2005; all years within the last decade. By the middle of the century, annual temperatures in the south-east of England could, on average, be more than 2 °C warmer than they are today. The maps shown in Figure 1.2 show the change in average summer daily temperatures predicted by the UK Meteorological Office's climate change model for both low and high greenhouse gas emissions scenarios (DEFRA, 2003). It can be seen that the south of England will be particularly affected with an average temperature rise of up to 6 °C. Summers will become hotter, longer and drier. Winter rainfall will become more frequent and much heavier and snowfall will become rare. The combined effect of global warming and urban heat islands could therefore be disastrous for our towns and cities.

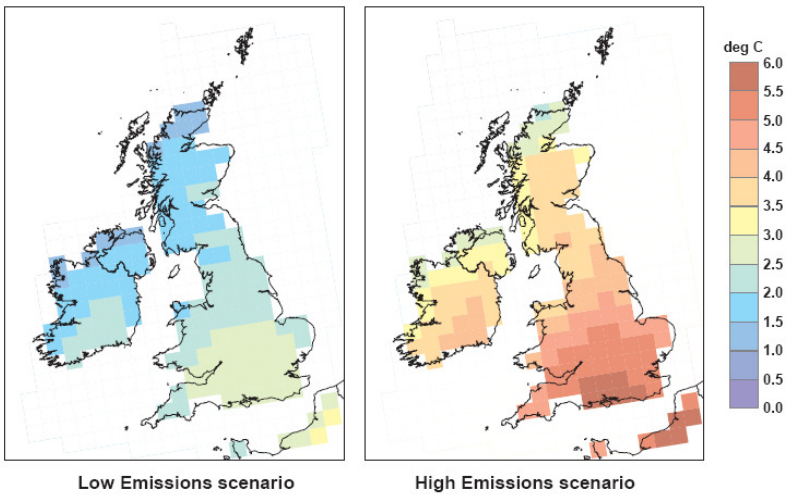

Figure 1.2: Predicted change in average summer daily air temperatures in 2080 (source: DEFRA, 2003)

Another significant factor affecting our urban way of life is the cost of domestic energy. In the UK, this has seen sharp rises in recent years. The overall price paid for fuel and light increased by a massive 26% in the 12 months up to December 2006 (DTI, 2007). In this same period, electricity prices rose by an average 24% and gas by nearly 38%. Of the total energy consumed in the UK during 2001, 30% of this was used by the domestic sector (DTI, 2002). Of this, 62% was used for space heating and a further 20% for water heating. A phenomenal 40% of the total energy consumed in the UK during 2000 was used solely for space heating.

By the year 2000, nearly 90% of British homes had central heating installed and average internal temperatures had risen from 13 °C three decades earlier to 18 °C (DTI, 2002). This rise in energy consumption was partly offset by improvements in energy efficiency. In 1987, only 3% of the houses that could potentially do so had full insulation fitted. This had seen a dramatic rise to 14% by 2001, but still leaving huge scope for future improvement. The number of homes with the majority of their windows double-glazed had tripled to over 47% by 2001. So whilst we are undoubtedly using much more energy in our homes than we were several decades ago, the rising costs are now at least beginning to make us think about using it more efficiently. Hence both consumer demand and recent government legislation is driving forward improvements in the design and construction of new buildings to minimise their heating (and often at the same time their cooling) requirements.

The recent energy price rises, together with a growing consumer desire to be more environmentally friendly, are helping to bring renewable energy technologies into the mainstream market. Although the actual whole-life benefits of some of these systems are still to be proven, the ‘feel good factor’ of generating your own ‘free’ power has certainly gripped the marketplace. Incorporating such renewable technologies into the urban fabric brings its own challenges; wind speeds are typically lower in towns and cities than in open areas and so the exact siting of domestic wind turbines is critical (Phillips *et al.*, 2007). Similarly, whilst solar photovoltaic panels need full sunlight to generate maximum output, they also benefit from a cooling breeze to reduce operating temperature and hence maximise conversion efficiency. These are all issues which consumers, manufacturers and researchers are only just beginning to come to terms with.

These are all just some of the many factors which currently affect our urban environments. As such, they collectively form the backdrop to the current research into the rate of convective heat transfer from building surfaces.

1.2 Overview of this thesis

This thesis continues in **Chapter 2** with an examination of the phenomena of urban heat islands, the factors that contribute to their formation and a look at some of the ways that they could potentially be ameliorated. In **Chapter 3**, a review of convective heat transfer is provided with particular emphasis on that which occurs from the surfaces of buildings.

Chapter 4 investigates the naphthalene sublimation experimental methodology and a description of the author's preliminary trials of this technique is given in **Chapter 5**. The development of the 1/100th scale atmospheric boundary layer simulation in the BRE wind tunnel necessary to maximise the size of the model buildings is detailed in **Chapter 6**. **Chapter 7** describes the air flow in urban street canyons and also various experiments conducted with pressure-tapped models and smoke visualisation which helped to determine the appropriate experimental conditions for the main naphthalene sublimation tests detailed in **Chapter 8**.

The results from these naphthalene sublimation experiments are presented and analysed in the subsequent chapters. **Chapter 9** examines the effect of wind speed upon the rates of convective heat transfer across building surfaces and **Chapter 10** looks at the effect of street canyon width. **Chapter 11** then considers the effects of wind direction whilst **Chapter 12** contains details of additional tests conducted after the primary naphthalene sublimation measurements were made in order to investigate the areas of peak convective heat transfer from buildings. The likely effects of surface roughness are discussed in **Chapter 13**.

The main results and achievements of the current research are then summarised in the conclusions in **Chapter 14**, followed by the references in **Chapter 15**.

The thesis then concludes with the **Annexes** which include example calculations, an assessment of experimental uncertainty, the naphthalene sublimation summary results and processing sheets, and copies of conference papers presented by the author relating to the current work. The full raw data files from the naphthalene sublimation experiments are provided in various electronic formats on the enclosed CD-ROM disc.

1.3 Summary of the gaps in current knowledge

Reviews of the current literature in the fields of urban heat islands and convective heat transfer from buildings are documented in the following chapters of this thesis. Based upon these reviews, a number of gaps in the current state-of-the-art have been identified as follows:

- Improved building and city-scale thermal simulations are required to allow modelling of the effects of climate change and urban heat islands. These are also required to assess the effectiveness of the possible amelioration measures which could be used to improve the climate of our towns and cities.
- Appropriate convective heat transfer correlations are required for the external surfaces of buildings for inclusion in such thermal models.
- An array of expressions for the rate of convective heat transfer has been previously determined from a variety of theoretical and experimental studies. The range of convection coefficients which may be obtained for a given scenario from these equations is vast and there is little evidence to suggest which result is the most appropriate.
- Existing full-scale results have generally been measured on high-rise structures. The majority of buildings in urban areas are low-rise, residential dwellings arranged in arrays of buildings of similar heights. Limited data is currently available for such scenarios.
- Convective heat transfer data has been presented by previous workers for both windward and leeward vertical surfaces, but there is less information regarding the horizontal or inclined surfaces of buildings (i.e. the roof surfaces).
- The effect that the wind direction has upon the rate of convective heat exchange is not clear. The existing literature is often conflicting with some results suggesting that wind direction is virtually insignificant, and other suggesting that it is highly critical.
- Few data are currently available from which the role of the urban form (e.g. building spacing and street widths) with respect to convective transfer can be determined.
- The existing convective coefficient relationships have either been presented with respect to local wind speeds adjacent to the test surface, or else to a location which was anticipated to be representative of the free-stream velocity. This variation in the wind speed measurement location has been shown to be the biggest source of disagreement between expressions presented by different researchers. Equations presented with respect to surface wind speeds are of limited use to engineers, designers or programmers since such data is rarely available.

- Only limited equations currently exist which permit the rate of convective transfer to be established based upon a true meteorological wind speed. Those that have been derived are likely to only be appropriate to the test building since the variation in the building geometry and surroundings is likely to have significant effect.
- The effects of atmospheric turbulence and velocity profiles across urban areas have not fully been considered in any of the model-scale investigations. Such effects are inherently simulated in full-scale work, but lack of documentation of the surrounding buildings, topography and wind conditions means that these are unquantified.
- Wind tunnel measurements have typically generated only surface averaged convection data and full-scale tests have only been conducted at a limited number of discrete locations on each test building. The variations of the convective heat transfer coefficients across the surfaces of buildings are therefore not yet fully documented.

1.4 Aims of current research

After considering the previously presented gaps in the current knowledge of convective heat transfer from urban areas, the following research aims were proposed for the current work:

- To establish the appropriateness of current convective heat transfer coefficient equations for the application to the external surfaces of buildings.
- To take account of realistic atmospheric conditions in the boundary layer above urban areas, including the mean velocity profile and levels of turbulence.
- To consider generic, but representative building geometries that will permit the convective heat transfer results obtained to be applied to the widest range of scenarios.
- To conduct experimental investigations in order to determine the effect of wind speed upon the rate of convection from typical building surfaces. Such convective heat transfer coefficients should be related to 'free stream' wind velocities above the city so that wind speed records from local meteorological stations may be employed.
- To determine the effect that the incident wind direction has upon the rate of convective transfer from the surfaces of buildings.
- To determine the effect that various typical building spacings (street canyon widths) will have upon the rate of convective transfer.
- To determine the variation of the convective heat transfer coefficient across the various surfaces of a building, and to ascertain the distribution of coefficients across each surface.
- To present the results in a manner that permits incorporation into future urban climate and building thermal models. This requires a dimensional form of equation (i.e. convective heat transfer coefficients rather than non-dimensional Nusselt number correlations).
- To ensure that radiation effects are completely removed from the derived relationships, isolating only the convective component of heat transfer from buildings.

Chapter 2 Urban heat islands

2.1 Introduction

It has been noted for many years that urban environments have a tendency to modify the local climate. The phenomenon was first documented by the amateur meteorologist Luke Howard (1772-1864), now best remembered for his work categorising and naming the types of clouds. Howard was concerned that his own air temperature measurements recorded from 1807 to 1818 at various rural locations around the City of London varied from measurements made at the Royal Society in the city centre. He presented these findings as part of his work 'The Climate of London' which was first published in 1818, and then later updated with fourteen years of additional observations (Howard, 1833). In this second edition, Howard writes:

> *"… the temperature of the city is not to be considered as that of the climate; it partakes too much of artificial warmth, induced by its structure, by a crowded population, and the consumption of great quantities of fuel in fires…"*

Howard realised that these urban - rural temperature variations were predominantly a nocturnal effect with the countryside cooling to a greater extent overnight. Daytime peak temperatures were found to be similar, but the diurnal temperature range was found to be over 2 °C greater in the countryside than in the city. A plot of Howard's mean annual temperature data for the period 1807 to 1818 is shown in Figure 2.1; the difference between London and the surrounding countryside is clearly evident. Mean monthly temperature differences were found to vary throughout the year, being greatest in wintertime and peaking at around 1.2 °C in November. Howard also presented his conclusions regarding the causes of urban heat islands, all of which remain valid.

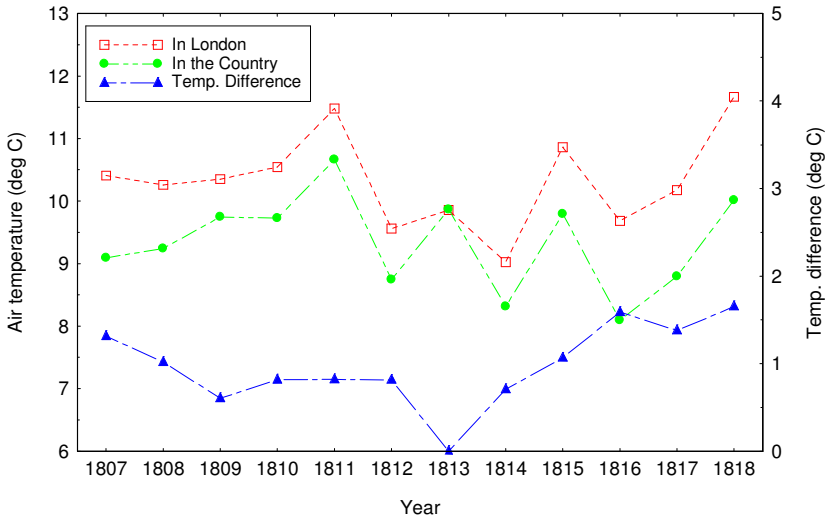

Figure 2.1: Urban and rural mean annual temperatures for 1807-1818 (source: redrawn from data by Howard, 1833)

The difference between urban and rural temperatures first described by Howard is what we now refer to as the 'Urban Heat Island' effect since it typically results in an 'island' of raised temperatures surrounded by a 'sea' of cooler countryside. The Glossary of Weather and Climate (Geer, 1996) defines an urban heat island (UHI) as:

> *"An area of higher temperature in an urban setting compared to the temperatures of the suburban and rural surroundings. It appears as an island in the pattern of isotherms on a surface map."*

The most comprehensive examination of London's urban heat island resulted from doctoral research by Professor Tony Chandler (1928-2008). His book 'The Climate of London' (Chandler, 1965) is still regarded as the definitive account of the capital's climate. Chandler combined temperature and humidity readings made during transects across the city in a mobile recording station, with weather recordings made by more than 60 schools and individuals. He found that the peak of London's heat island occurred north-east of central London around Hackney and Islington as a result of the prevailing south-westerly winds. These results continue to be discussed widely and have been confirmed by a number of subsequent researchers.

More recent research (Watkins, 2002) concluded that the London's current air temperature peak is located close to the British Museum. The heat island was confirmed to be a predominantly nocturnal effect with the dense urban form retaining solar and anthropogenic heat well into the night. Figure 2.2 shows a temperature contour plot produced during Watkin's research from data recorded just before midnight on the 7th August 1999. A 2 to 3 °C heat island can clearly be seen in the centre of the plot, which corresponds to an area surrounding Oxford Street and the Britsh Museum in Central London. Generally, the greatest heat island intensities occur two to three hours after sunset (Grimmond, 2007).

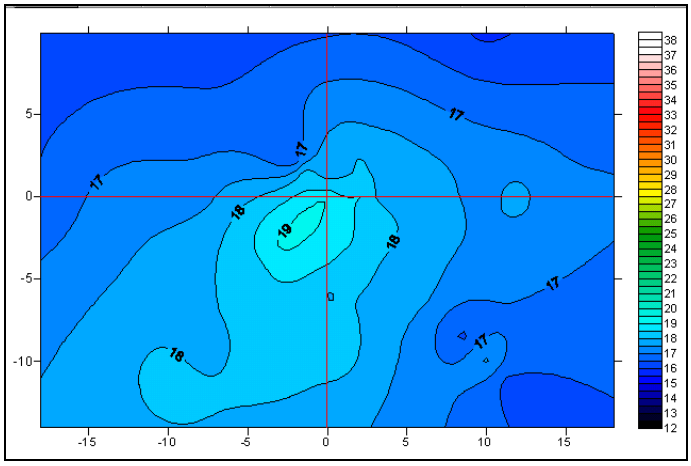

Figure 2.2: Air temperature distribution across London
(source: Watkins, 2002)

Currently, two EPSRC funded research projects are investigating ways to predict and mitigate the effects of climate change for UK cities. The 'SCORCHIO'[(a)] project led by the University of Manchester is aiming to develop tools for analysis of adaptation options in urban areas, with a particular emphasis on heat and human comfort (Smith and Lindley, 2008). The objective of the 'LUCID'[(b)] project led by University College London is to devise methods for calculating local temperatures and air quality in the urban environment in order to then be able to investiagte energy usage and the health consequences of a changing climate (UCL, 2007). The fact that two such research projects are currently in progress in the UK demonstrates how seriously the impacts of urban heat islands and more general climate change are being taken.

Urban heat island effects are however not unique to the United Kingdom. Similar phenomena have also been recorded in many other towms and cities around the world. A selection of some of the research that has been conducted to date documenting these effects is summarised in Table 2.1 on the following page, although it should be noted that this list is by no means exhaustive. The purpose of this table is to illustrate the wide diversity in geographical locations, sizes and climates of the range of urban areas which have been shown to experience urban heat island effects.

(a) 'Sustainable Cities: Options for Responding to Climate cHange Impacts and Outcomes'
(b) 'The Development of a Local Urban Climate Model and its Application to the Intelligent Design of Cities'

Table 2.1: Examples of worldwide towns and cities where urban heat islands have been observed.

City (Country)	**Source**	**Comments**
Reykjavik (Iceland)	(Steinecke, 1999)	Weak UHI (typically 1 - 2 °C) which converts to a 'cold island' (mostly -1.5 °C) by day in mid-summer.
Lódź (Poland)	(Klysik and Fortuniak, 1999)	UHI intensity in the city may reach more than 10 °C in special cases.
Tokyo (Japan)	(Saitoh *et al.*, 1996)	Field observations recorded a nocturnal UHI intensity of 8.1 °C one night in wintertime.
Melbourne (Australia)	(Morris and Simmonds, 2000)	Maximum UHI intensity 6 °C. Early morning advection events of warm continent air result in an 'urban cool island' of up to minus 3 °C.
Singapore (Singapore)	(Priyadarsini *et al.*, 2008)	UHI intensities up to 4 °C. Façade albedos are a significant factor in determining canyon air temperature.
Montreal, Vancouver (Canada)	(Oke and Maxwell, 1974)	UHI grows rapidly after sunset with a maximum occurring 3 to 5 hours after sunset throughout the year.
Szeged (Hungary)	(Unger, 1996)	A medium-sized town. Extreme UHI events related to anticyclonic weather and calm winds.
Norwich, Newcastle, Cardiff (UK)	(Hughes, 2006)	Weak UHI's averaging 0.5 °C, 0.9 °C and 1.0 °C respectively were identified. Rural to urban temperature gradients greatest in summertime.
Rome (Italy)	(Bonacquisti *et al.*, 2006)	UHI is a nocturnal phenomenon present in winter (about 2 °C) and summer (about 5 °C).
Tel-Aviv (Israel)	(Saaroni *et al.*, 2000)	Surface temperature differences up to 10 °C and air temperature differences 3-5 °C.
San Juan (Puerto Rico)	(Velazquez-Lozada *et al.*, 2006)	UHI intensity increasing at a rate of 0.06 °C per year for the last 40 years. Predicted to be as high as 8 °C by 2050.
Aveiro (Portugal)	(Pinho and Orgaz, 2000)	A small coastal city. The maximum UHI intensity was found to be 7.5 °C at night.
Seoul (Korea)	(Kim and Baik, 2004)	Average annual daily maximum UHI intensity was found to be 3.3 °C.
Hong Kong (Hong Kong)	(Giridharan *et al.*, 2005)	Case studies of three residential developments. The maximum nocturnal UHI's was of the order of 1.3 °C.

2.2 The causes of urban heat islands

A number of factors have been identified as contributing to the development or prolongation of heat islands in urban areas. Each of these has been shown to be significant in particular conditions, but there exists no 'golden rule' which can be generically applied in all situations. In *Boundary Layer Climates* (Oke, 1987), the author summarises the six primary causations as:

(i) **Increased absorption of solar radiation**
An urban environment has a greater total surface area than that of open countryside due to the additional wall area of buildings. Hence there is a larger area over which solar radiation may be absorbed into the urban fabric. This is compounded by the geometries of typical buildings which tend to encourage multiple reflections between surfaces, and in doing so ensure that a higher proportion of received solar radiation is ultimately absorbed.

(ii) **Increased amounts of sensible heat storage**
Building materials tend to have both a higher thermal admittance and greater heat capacity than rural materials such as soil and vegetation. Greater quantities of sensible heat are therefore stored within the urban fabric which keeps developed areas warmer for longer after sunset. This is a significant factor in the formation of nocturnal heat islands.

(iii) **Direct anthropogenic heat influxes**
Buildings are continuously 'leaking' heat into their surroundings as a result of inefficient insulation, vents from air-conditioning systems and the various other appliances essential to modern living. The heat flux from vehicles adds to the problem, with congestion and gridlock further compounding matters. This anthropogenic heat often flows into our built environment at pedestrian level, thereby directly affecting people's perception of the local climate.

(iv) **Decreased levels of evapotranspiration**
Reduced amounts of vegetation and large expanses of non-porous surfaces (such as concrete and tarmac) result in a much lower availability of surface water compared to in the open countryside. Streets are usually well-drained ensuring that any precipitate which falls is rapidly directed underground. The result is that evaporation and transpiration processes are limited, and thereby not able to cool built-up areas to the same extent that they do in rural settings where there is a greater availability of surface moisture.

(v) **Decreased long-wave radiation loss to the sky**
Solar radiation absorbed by building surfaces is re-emitted as long-wave radiation. However as building height and density increases, the sky-view factors from urban surfaces decrease. The result is that long-wave radiation is more likely to be re-absorbed by adjacent building surfaces than it is to be emitted back out into the atmosphere. Consequently the net heat input into the urban fabric is increased and so temperatures rise.

(vi) **Decreased turbulent heat transport from the urban canyon**
Deep and narrow street canyons are a feature of many townscapes around the world. Whilst this may provide welcome solar shading in hot climates, air movement is reduced within the canyon as it becomes decoupled from the winds passing above. The amount of turbulent 'flushing' of the canyon is therefore restricted and so warm polluted air is able to stagnate at street level.

Each of these factors contributes to a greater or lesser extent to the formation of the majority of urban heat islands. The exact relative significance of each will depend upon the particular urban form, the local climate and on recent weather conditions. Their importance to a particular urban area may also vary from day to day and from one heat island occurrence to the next. However it would appear that the increased levels of solar absorption and the higher thermal capacities of building materials are the prime factors in the majority of cases. Anthropogenic heat flux will vary throughout the year (depending upon the mechanical heating and cooling loads of the buildings) and may be as significant as incoming solar radiation on dark winter days (Oke, 1987).

Other factors may help to prolong existing heat islands by impairing the cooling potential of the town or city. The lower sky-view factor typical of an urban canyon will reduce the amounts of long-wave radiation which is re-emitted back into the atmosphere (Oke, 1988). The shelter effect provided by buildings means that wind speeds are generally lower in street canyons (Cook, 1985) and therefore warm air is less likely to be swept away. These lesser wind speeds also impair the convective cooling of surfaces which were heated by the sun during the day. The combined effect of these factors can ensure that cities are able to maintain a raised temperature level well into the night, long after surrounding rural areas have cooled back down (Watkins *et al.*, 2002).

Another important consideration is the albedo of an area. The albedo (reflectivity) of a surface is a physical property defined as the ratio of reflected to incident electromagnetic radiation. Our perception of albedo with respect to visible light is commonly referred to as colour. The albedos of a range of typical rural and urban surfaces are compared in Table 2.2 where it can be seen that there is a great deal of similarity between man-made and natural materials. Trees have an identical albedo range to asphalt, and concrete lies within the typical albedo range of soil. It is also interesting to note that water can vary between being an almost perfect absorber and a perfect reflector, depending upon the incident angle of the radiation. It therefore seems unlikely that the urban-to-rural albedo differences are a prime factor in heat island initiation, although this does not mean that urban albedos are insignificant, as is discussed in Section 2.4.2 of this chapter.

Table 2.2: A comparison of the albedos of typical rural and urban surfaces (source: Oke, 1987)

	Surfaces	**Albedo range**
Rural	Soil	0.05 – 0.40
	Grass	0.16 – 0.26
	Trees	0.05 – 0.20
	Water (depending upon angle)	0.03 – 1.00
	Snow (old – fresh)	0.40 – 0.95
Urban	Asphalt	0.05 – 0.20
	Concrete	0.10 – 0.35
	Brick	0.20 – 0.40
	Stone	0.20 – 0.35
	Slate	0.10
Average for the Earth from space		**0.39**

2.3 Determining the presence of an urban heat island

It has been explained that urban heat islands are predominantly a result of differences in the thermal and geometrical characteristics of urban areas in comparison to the surrounding undeveloped countryside. Such differences tend to increase the overall efficiency with which built-up areas absorb and trap solar radiation and so it is not surprising that the effect is most readily identified by increased surface temperatures. Heat island occurrences can be visualised using infrared imagery techniques which reveal the raised temperatures of the city surfaces. The photograph and infrared image of a Tokyo district shown in Figure 2.3 illustrate what a typical city looks like when viewed in this way. The image was recorded late one afternoon in October once the building surfaces had begun to cool (Voogt, 2006). The exposed vertical surfaces of the high-rise tower blocks in the business district can be seen to be glowing yellow corresponding to surface temperatures of approximately 30 °C. In the foreground, the roofs of the low rise residential properties are generally much cooler with some down to as low as 15 °C. The effect of different building geometries and materials is very therefore very apparent.

Figure 2.3: A photograph and infra-red image of the Shinjuku area of Tokyo (source: Voogt, 2006)

Pedestrians will experience raised surface temperatures both directly as short-wave radiation and also indirectly as a resulting rise in local air temperatures. Hot surfaces warm the adjacent air which then rises in buoyant plumes, setting up convection currents within the street canyon. The second means by which the presence of an urban heat island may be detected is thus by the monitoring of local air temperatures. Air temperature heat islands tend to be more noticeable in calm weather during which there is little cool fresh air arriving to displace and mix with that warmed by the surfaces. Even the lightest winds will tend to destroy air temperature heat islands quite rapidly (Klysik and Fortuniak, 1999) and hence urban layouts which promote turbulent mixing at street level can be highly beneficial.

Such air temperature heat islands have been widely investigated in numerous cities around the world. They can be recorded by an array of fixed temperature sensors installed throughout the city's street network; a technique recently used to monitor the air temperature distribution in London (Watkins, 2002). Alternatively, a series of traverses can be made across a city using a single set of sensors mounted on a vehicle as was employed to measure the Montreal and Vancouver heat islands (Oke and Maxwell, 1974).

It is known from such measurements that the peak air temperatures tend to occur in the central high-rise core of a city where the greatest amount of heat becomes trapped (Sailor, 2002). Figure 2.4 shows a cross-section through a typical metropolitan area which includes the low-rise outer suburbs, medium-rise commercial districts and high-rise central core. The local air temperature is highly dependent upon the level of urbanisation and is also sensitive to factors such as the height and density of the buildings. The diagram shows a significant dip in air temperature between the suburban and urban residential districts. There are several features which have been shown to have such an affect. For example, London's many parks have a significant cooling effect on the city which often extends for some distance beyond their boundaries (Watkins, 2002). Similarly, the presence or large areas of water such as a lake or a river running through a city may also have an important cooling effect, thereby helping to regulate the overall temperature.

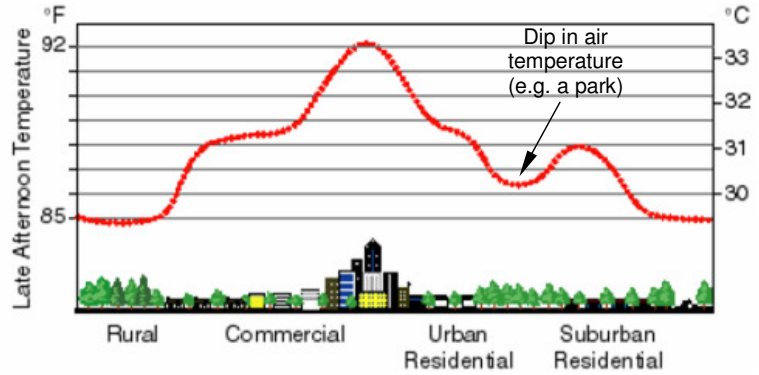

Figure 2.4: The formation of an air temperature heat island over a typical city (Sailor, 2002)

Whilst the actual air temperature distribution will vary from that illustrated during the course of a single day as well as with the seasons, the general trend remains similar. An air temperature rise of between 2 and 4 °C is typical for many cities worldwide (Oke, 1987). The deciding factor which determines whether these effects are of concern is likely to be the baseline temperatures on top of which the air temperature rise occurs. It must be remembered that at colder more northerly latitudes, a heat island that warms the city during winter may actually be a positive occurrence.

Surface and air temperature heat islands are clearly closely related, but it is important to note the distinctions between them. In sunny, breezy conditions it is possible to have raised surface temperatures without a significant rise in air temperatures. Similarly, regions of raised air temperatures may occur in isolation from heated surfaces where there is little solar influx but high anthropogenic output, for example at night-time in winter. However, it is most common for these two effects to occur in conjunction with each other since they share many of the same triggers and limiting factors. A third heat island type relates to ground (soil) temperatures, but since the primary significance of this effect is only for agriculture it will not be considered further in the current work

2.4 Ameliorating urban heat islands

A number of strategies have been proposed to help ameliorate the various consequences of urban heat islands. There is currently much debate concerning which of these is the most beneficial and cost effectiveness is often the deciding factor. Several cities have piloted schemes with varying levels of success. In reality, there is unlikely to be a single solution which can be universally applied to solve all instances of unintentional climate modification. Rather, a combined approach of several complimentary measured may be called for.

The most practical of these amelioration strategies will be discussed in the following paragraphs in order to better define current thinking. Much of this background knowledge was gained by the author at the 'North American Heat Island Summit' which was held in Toronto in May 2002. This conference brought together a wealth of leading academics in the field, along with town planners, politicians and health professionals to discuss the current state of the art.

2.4.1 Modification of the urban geometry

The geometry of street canyons has several important effects upon the local climate (see Section 2.2). As buildings become higher rise, the total surface area increases since the walls are in addition to the plan area of the site. Larger surfaces provide greater potential for the absorption of incoming solar radiation. Any radiation that is initially reflected from a surface has a high likelihood of hitting further adjacent surfaces. These multiple reflections ensure that the urban fabric absorbs a greater proportion of all incoming radiation than an equivalent area of countryside (Oke, 1988). A lower sky-view factor also means that reduced amounts of long-wave radiation exit the street canyon, thereby impairing night-time cooling. Consequently streets are able to maintain their raised temperatures into the night whilst the surrounding rural areas are cooling down.

For other street canyon geometries, the effect can be completely reversed. Rows of tall, closely spaced buildings allow little solar radiation to reach street level, except for a short period around mid-day when the sun is directly overhead. This shading can actually lead to negative heat islands in some cities where the temperature at street level can actually be lower that that in the surrounding open countryside. This approach has been employed in some hot climates for many centuries in order to provide cool street temperatures during the heat of the day. These contradictions emphasise the fact that there is no single best practice applicable to all urban environments.

The most significant factors when discussing the geometries of urban areas in this context are the proximity of the buildings to each other and the depth of the street canyon. These parameters are best described by the street's height-to-width ratio; simply the average height of the buildings divided by the spacing between them. As this value is dimensionless, it is independent of the actual building size. Therefore if the building height is doubled, the same canyon geometry may be obtained so long as the street width is also doubled. The height-to-width ratio also implies the sky-view factor (i.e. the amount of sky visible from the street) since this will be reduced for narrower canyons.

Increased levels of urbanisation generally relate to increased height-to-width ratios, with peaks around the city centre. As land values increase, buildings tend to become taller and more tightly spaced. The ratio can therefore also be a good indicator of the likelihood that a heat island will exist. Whilst it may not be possible to change the height-to-width ratios of existing streets, data relating to its effect on the local climate will allow architects and town planners to better design new developments. Such considerations must of course be taken in context with the various other factors affecting heat island occurrence as a single unilateral approach is unlikely to be successful.

2.4.2 Increasing the surface albedo

A more practical approach to reducing the solar flux into our towns and cities may be to increase the proportion of radiation that is reflected straight back into the sky. This can be achieved by careful selection of new building materials, or recoating of existing ones, so as to maximise their albedo. This is not a new idea; there is a tradition in many hot climes of whitewashing houses as part of a strategy to maintain cool indoor temperatures without the need for modern air-conditioning systems. This practice is not as common in the UK, largely because our temperate climate has previously allowed us to give preference to the aesthetics of our more traditional wall and roof constructions which tend to have relatively low albedos, as Table 2.3 demonstrates.

However, the combined effects of climate change and spiralling energy costs are beginning to alter public opinion. In California, the 'Title 24 Building Energy Efficiency Standards' (California Energy Commission, 2005) detail cool roof specifications for low-pitched roofs on non-residential buildings requiring them to have an albedo greater than 0.7 when new. Whilst residential properties currently lie outside the scope of this legislation, incentive is given to homeowners to install cool roofs by the prospect of a 10 to 30% reduction in air-conditioning running costs (Cool Roof Rating Council, 2008). However, when the new edition of 'Title 24' comes into effect in 2010 (California Energy Commission, 2008), cool roof requirements (albeit quite modest ones) will be extended to residential properties. A number of other US cities are also implementing similar cool roof programs, a selection of which are summarised in Table 2.4. It can be seen by comparing the values shown in Tables 2.3 and 2.4 that the albedos of traditional roofing materials are significantly lower than the new cool roof requirements.

White surfaces are almost perfect reflectors of radiation with albedos near unity, whilst black surfaces are almost perfect absorbers with albedos near zero. Since roofs constitute as much as a quarter of the total urban surface area (Akbari *et al.*, 2009), it follows that a dramatic decrease in heat island intensity could be brought about virtually overnight by painting all roof surfaces white. Whitewash has an albedo of 0.5 to 0.9; many times greater than unpainted concrete, corrugated iron and other such materials (see Table 2.3). Several companies have developed cool roofing products for large, low-pitched industrial and commercial roofs. The photographs shown in Figure 2.5 illustrate the typical reduction in surface temperatures resulting from the application of such a product. The left photograph shows the original untreated asphalt roof, whilst the right photograph shows an area treated with the 'Hydro-Stop PremiumCoat' waterproofing product. The two temperature readings were taken simultaneously on treated and untreated areas of the roof and show that an approximate 47 °C (85 °F) surface temperature reduction was achieved.

Table 2.3: The typical albedos of traditional urban surfaces
(source: Oke, 1987)

Surfaces	**Type**	**Typical albedos**
Roofs	Tile	0.10 – 0.35
	Slate	0.10
	Corrugated iron	0.10 – 0.16
	Tar and gravel	0.08 – 0.18
Roads and pavements	Asphalt	0.05 – 0.20
	Concrete	0.10 – 0.35
Paints	Whitewash	0.50 – 0.90
Urban average		**0.15**

Table 2.4: Requirements of various US 'cool roof' programs
(source: Cool Roof Rating Council, 2009)

City / State	**Policy title**	**Albedo requirement**
Austin, TX	Austin's 2006 Energy Code	Low slope: 0.70 Steep slope: 0.35
Chicago, IL	Energy Conservation Code	Low slope: 0.65 Medium slope: 0.15
Dallas, TX	Dallas Cool Roof Code	Initial: 0.65 Aged: 0.50
Florida	Florida Energy Code 2004 (Chapter 13)	0.65
Houston, TX	City of Houston Commercial Energy Conservation Code	Low Slope: 0.75

Figure 2.5: The reduction in surface temperature on a typical cool roof
(source: Hydro-Stop Incorporated, 2006)

Such treatments are popular for the flat and low-pitched roofs of industrial and commercial properties since energy minimisation is typically a more important factor than aesthetics. These surfaces are usually unseen from street level due to their shallow slopes and so the high-albedo roofs often go unnoticed. Homeowners however typically prefer darker colours for the coverings of their steep-pitched residential roofs. Significant research has therefore gone into developing cool roofing materials which have the same appearance as traditional products, but with notably higher albedos. Much of this research has been led by the Heat Island Group at Lawrence Berkeley National Laboratory in California. In particular, the ongoing 'Cool Colours Project' (LBNL, 2009) is a research and development collaboration between LBNL and sixteen industry partners sponsored by the California Energy Commission. The aim of this work is to develop non-white cool roofing products for the residential market. A number of manufacturers now have ranges of dark-coloured, high-albedo pigments with which to produce cool roofing materials. These pigments are being used in liquid coatings for metal roofs, in clay and concrete tiles, and in the multi-coloured granules from which shingles are produced.

Such cool roofing products often look identical to their equivalent low-albedo counterparts. The performance advantage is gained by considering the albedo characteristics of the pigments outside of the visible part of the electromagnetic spectrum (Levinson *et al.*, 2007). As Figure 2.6 illustrates, more than half of all sunlight falls within the near-infrared radiation (NIR) wavelength range. Two materials of similar appearance under visible light may have significantly different NIR reflectances. By selecting materials and pigments with the greatest NIR reflectances, cool roofing products are designed to reflect a greater proportion of the invisible incident sunlight. The potential gains are greatest for darker colours since their standard albedos are typically so low.

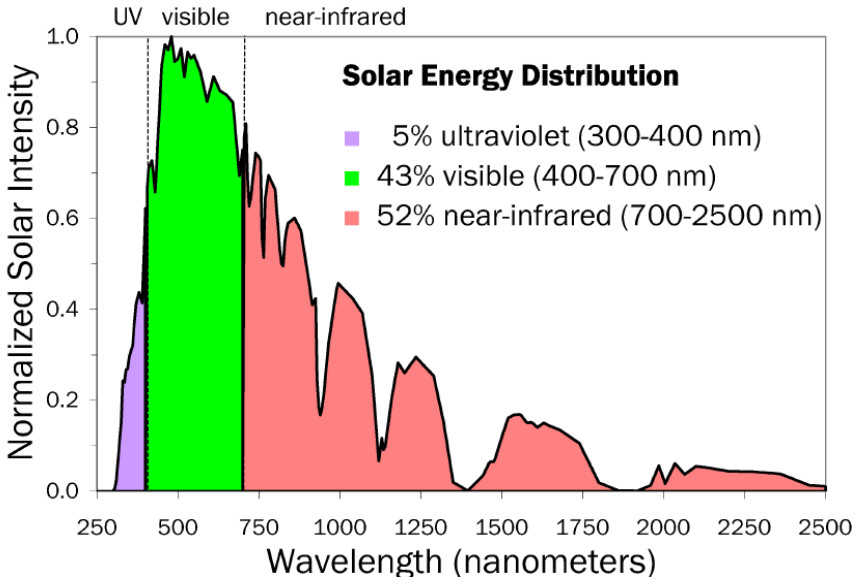

Figure 2.6: The composition of sunlight (source: Levinson, 2004)

A photograph illustrating a selection of the available colours from just one manufacturer (American Rooftile Coatings, 2006) is shown in Figure 2.7. The bottom row is comprised of standard roofing tiles whilst the top row shows the respective 'cool' equivalents. The reflectivities (R-values) of these new tiles are notably higher, especially for the darker colours which would traditionally absorb a high proportion of the incident radiation. Typical increases in the albedos are of the order of 0.2 to 0.3, but for black tiles the cool alternative will reflect more than ten times the amount of incident sunlight of the standard tile.

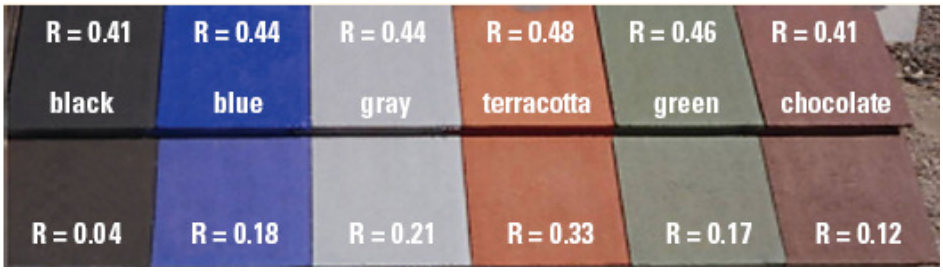

Figure 2.7: A range of 'cool roof' tiles in traditional colours
(source: American Rooftile Coatings, 2006)

The potential benefits of installing cool roofs are huge. They lower local air temperatures around the building and also reduce the requirement for air-conditioning inside. Levinson and Akbari (2009) estimated that retrofitting cool roofs to 80% of the US commercial building conditioned room area would result in an annual saving of 10.4 TWh of cooling energy worth $735m. As a result CO_2 emissions would also be reduced by 6.2 Mt per year; an amount equivalent to the output of 1.2 million cars. Cool roofs will normally also benefit from increased lifespans due to lesser ultra-violet degradation and reduced thermal stresses (CRRC, 2008).

Roofs are perhaps the most obvious urban surfaces to undergo such transformation since the building owner is likely to benefit from reduced cooling costs (in hot climates) and as such, has a greater incentive to fund the work. However, the same approach and technologies could equally well be applied to other urban surfaces such as car parks, roads and pavements. The latter of these surfaces may account for as much as 40% of the total urban surface area (Akbari *et al.*, 2009) and so the potential for increasing the average urban albedo is even greater than for roofs.

2.4.3 Increasing urban vegetation

Another approach to improving the albedo of an urban area is to make it appear more rural by increasing the amount of vegetation. This can take many forms including planting more trees, designing new developments to feature green open spaces and encouraging the use of gardens. The result goes further than simply increasing the average albedo of an urban area by improving the urban climate in a number of other important ways. Trees provide shade under which people can shelter from the sun, and also act as windbreaks to improve pedestrian comfort. By using deciduous species, there is the added benefit that in winter (when natural light levels are lower) the trees will have shed their leaves and so more light can reach street level and the windows below.

Urban areas are usually relatively dry due to the non-porosity of building materials and the efficiency of rainwater drainage systems. This means that there is often little opportunity for surfaces to be cooled by evaporation processes (Oke, 1987). Vegetation requires a porous substrate in which to grow (i.e. soil) and this in turn makes a greater amount of water available for evaporation by holding it near to the surface. Further cooling results from evapotranspiration through the leaves and local air quality may be improved by absorption of some forms of pollution.

A number of studies have demonstrated the thermal benefits of urban parks and green areas. In London, a series of field measurements across Primrose Hill (a park to the north-west of the City shown in Figure 2.8) revealed that temperatures were up to 1.1 °C cooler than the surrounding areas on warm sunny days (Graves *et al.*, 2001). It was also shown that the cooling effect extended 200 to 400 metres into the surrounding streets. In Singapore, a maximum temperature difference of over 4 °C was measured between urban and rural areas (Wong and Yu, 2005) and this was again shown to extend some distance into the surrounding built environment (Yu and Hien, 2006). An earlier study in Israel found that the partial shading provided by various urban wooded sites gave an average cooling of around 3 °C at midday (Shashua-Bar and Hoffman, 2000). The benefits of urban vegetation are therefore very clear.

Figure 2.8: The view across London from Primrose Hill
(source: WIKIPEDIA, 2003b)

This is not to say that increased urban vegetation is the perfect solution. Maintenance costs for looking after trees and planted areas must be carefully considered, as must the damage caused by roots to pavements and the problems associated with leaves blocking drains and gutters. There can, however, be little doubt of the aesthetic benefits which plants and trees bring to our metropolitan areas.

2.4.4 Installation of green roofs and façades

An alternative approach to transforming the roofs of buildings is to use this often unused space for the planting of vegetation. The idea of 'green roofs' was developed in Germany in the 1960s to provide additional space for home agriculture, but is now being increasingly used to improve the urban environment. Even further back in history, the Vikings used living grass roofs to provide additional insulation and blend their homes into the surrounding countryside. Green roofs are common in mainland Europe and use in North America is growing fast. However they still remain a relative novelty in the UK. The photographs shown in Figure 2.9 illustrate two very different examples of green roofs. The picture on the left shows traditional grass roofs in the village of Norðragøta in the Faroe Islands, and on the right is a modern, more intensive interpretation on top of a Manhattan apartment block.

Figure 2.9: Examples of green roofs in the Faroe Islands and Manhattan (source: WIKIPEDIA, 2003a)

Measurements made in a roof garden installation on top of Chicago City Hall found that surface temperatures on a hot summer's day were reduced by between 14 and 44 °C compared to an adjacent traditionally roofed building (Dawson, 2002). Ambient air temperatures above the roof were also found to be reduced by as much as 3.9 °C (Federal Energy Management Program, 2004).

A computer simulation exercise based upon the city of Toronto in Canada predicted that the addition of green roofs to 50% of the downtown buildings could cool the entire city by up to 0.8 °C (Liu and Bass, 2005). It was also found that by irrigating the green roofs, the maximum air temperature reduction could be increased to 2.0 °C and the geographic extent of this cooling significantly extended. The research therefore indicated that green roofs could play a significant role in ameliorating urban heat islands, especially if kept well watered. Other research reported that widespread adoption of green roofs across Toronto could account for annual building energy savings of 4.15 kWh/m^2 and a reduction of ambient air temperature of between 0.5 and 2.0 °C, depending on the time of the year (Ryerson University, 2005). A total initial city-wide saving of £139m was identified with further annual savings in the region of £16.5m. The insulation of the roof is greatly increased so that the building requires less heating in winter and air-conditioning in summer. A study conducted for *Environment Canada* showed that the energy required for each of these processes could be reduced by at least 23% when a green roof was installed (Bass and Baskaran, 2003).

Green roofs also have many additional benefits. They aid the management of storm water run-off by trapping up to an estimated 75% of annual precipitation that falls on them (Peck *et al*., 1999). This reduces the peak flow rate into the sewers following a rainstorm event so that the size of the required storm water infrastructure may be reduced. Evaporation of this water from the soil combined with evapotranspiration from the leaves of the plants helps to actively cool the roofs of buildings and the surrounding air. Any excess water trickles through the soil which acts as a filter removing pollutants such as nitrogen and phosphorus that are held in the soil as useful plant fertilisers (FEMP, 2004). Such roofs also provide valuable habitat for plants and animals that is otherwise rare in urban areas, acting as biodiversity corridors for birds, insects, butterflies and other wildlife. They provide quality outdoor amenity space for residents and office workers and promote horticultural therapy through gardening (Bass, 2002). Green roofs can also help to absorb urban noise; one study found that local traffic noise from nearby roads was reduced by as much as 46 dB (FEMP, 2004).

Urban gardens need not be restricted to just the roofs of buildings; the façades can also be made into 'green walls'. These might be formed by a simple creeper or vine covering over a traditional wall, or they may make use of one of the commercial planted wall systems that are now available. The photographs in Figure 2.10 show two such systems installed at the BRE Innovation Park in Watford. The system in the left photograph combines a series of ivy-covered mesh panels, whilst the one of the right features growing blocks made from recycled car tyres into which a wide range of plants may sewn. The wall therefore becomes an extension (or replacement) for the town garden. Green walls share many of the same benefits as green roofs, as well as providing shading around the windows of buildings to reduce solar heat gain in summer. Both of the systems illustrated in Figure 2.10 incorporated automatic watering systems which minimises maintenance whilst also ensuring the availability of water for evaporative and evapotranspirational cooling processes.

Figure 2.10: Examples of 'green walls' at the BRE Innovation Park, Watford

2.4.5 Increasing urban wind speeds

Research has shown that even the lightest of winds can rapidly disperse an air temperature heat island (for example: Klysik and Fortuniak, 1999; Watkins, 2002). Winds also reduce urban surface temperatures by convectively cooling the walls and roofs of buildings. It is therefore a logical progression to suggest that the urban heat island effect could be ameliorated by increasing the wind speeds within the urban area. However this would be in direct conflict with the preference for low street level wind speeds from a pedestrian comfort and safety perspective (Oke, 1988). In order to maximise convective exchange from their surfaces and to disperse polluted air from within the adjacent canyons, buildings would need to be designed and arranged to promote turbulent airflow along the streets. In contrast, pedestrians prefer a much calmer environment in which they can conduct their day-to-day activities without the nuisance, and perhaps even danger, of high winds (Lawson, 2001). In winter, wind chill can make it seem much colder that it actually is and hence the shelter traditionally provided by buildings is often rather welcome.

Wind speeds are most often discussed with reference to the Beaufort scale which was devised by a British Admiral in 1806. Although originally intended for use at sea, the scale has since been revised and extended to cover the effects of different wind speeds on land. Penwarden (1973) presented a summary of the Beaufort scale with respect to the effects felt by pedestrians which is reproduced in Table 2.5 below. The approximate wind speed range (in metres per second) corresponding to each Beaufort number is also shown. He concluded that on the basis of the mechanical (i.e. force) effects of the wind, the onset of pedestrian discomfort occurs at around 5 m/s (Beaufort 3), wind speeds greater that 10 m/s (Beaufort 5) are “definitely unpleasant” and those greater than 20 m/s (Beaufort 8) can be dangerous.

Table 2.5: The Beaufort wind scale and the respective effects on people (source: Penwarden, 1973)

Beaufort Force	Wind speed (m/s)	Noticeable effect of wind
0	< 0.5	No noticeable wind.
1	0.5 - 1.5	No noticeable wind.
2	1.6 - 3.3	Wind felt on face.
3	3.4 - 5.4	Hair disturbed and clothing flaps.
4	5.5 - 7.9	Hair disarranged.
5	8.0 - 10.7	Force of wind felt on body. Limit of agreeable wind on land.
6	10.8 - 13.8	Difficult to walk steadily. Umbrellas used with difficulty. Wind noise unpleasant.
7	13.9 - 17.1	Inconvenience felt when walking.
8	17.2 - 20.7	Progress impeded and great difficulty with balance in gusts.
9	20.8 - 24.4	People blown over by gusts.

Hunt *et al.* (1976) conducted a series of tests in which people were asked to undertake a range of activities whilst in the National Physical Laboratory's wind tunnel. Based upon the observations made and the subjective assessments of the volunteers, the researchers proposed a series of maximum wind speeds for various pedestrian criteria. The results presented for "gusty winds" (typical of those around buildings) are summarised in Table 2.6 and generally agree with the criteria proposed by Penwarden. Murkami *et al.* (1981) conducted further tests in both a wind tunnel and around real buildings in order to determine the effect that various wind speeds have on pedestrians. A summary of their "new criteria" is provided in Table 2.7; it can be seen that these are actually rather similar to those determined by the previous researchers.

Table 2.6: Maximum wind speeds for pedestrian comfort and safety (source: Hunt *et al.*, 1976)

Criteria for pedestrians	**Maximum wind speed**
For comfort and little effect on performance	6 m/s
Most performance unaffected	9 m/s
Control of walking	15 m/s
Safety of walking	20 m/s

Table 2.7: Wind effects on pedestrians (source: Murakami and Deguchi, 1981)

Wind speeds	**Effect on pedestrians**
< 5 m/s	Minor effects on hair and clothing.
5 - 10 m/s	Footsteps sometimes irregular. Hair and clothing considerably disturbed.
10 - 15 m/s	Walking irregular and difficult to control. Upper body bends windward.
> 15m/s	Dangerous for elderly people. Walking impossible to control. Body blown sideways or leeward.

However, the effects of the wind on pedestrians are subjective and will depend upon what an individual person is doing at the time. In order to take account of this varying perception, a series of user defined 'acceptability criteria' have been developed over time, mainly from observation of pedestrians in shopping centres in the south of England. The Beaufort scale alone is too coarse to use for such assessments and it is therefore usually combined with a probability of exceedence for each wind speed range. The acceptability criteria proposed by Lawson (2001) for various typical pedestrian activities are shown in Table 2.8. In this table '6% > B3' means wind conditions where Beaufort 3 is exceeded for more than 6 percent of the time. Where conditions are said to be 'Tolerable' for a given activity, the wind will be noticeable but will not prevent the activity taking place. However where conditions are 'Unacceptable' the wind will deter people from using the area for its designated purpose.

Table 2.8: Acceptability criteria (source: Lawson, 2001)

Pedestrian activity	Tolerable	Unacceptable
Sitting	4% > B2	1% > B3
Entrance doors	4% > B2	6% > B3
Pedestrian standing	6% > B2	6% > B3
Pedestrian walk-through	6% > B3	4% > B4
People around buildings	2% > B4	2% > B5
Roads and car parks	2% > B5	6% > B5

The 'Lawson Acceptability Criteria' often form the basis of pedestrian level wind environments studies conducted as part of a building's 'Environmental Impact Assessment' (EIA). Wind speed ratios measured in the wind tunnel at various locations around a building or development are combined within appropriate meteorological records which give the strength, direction and probabilities of winds at the site. These combined statistical results are then assessed against the applicable acceptability criteria to determine whether the pedestrian level wind conditions will be appropriate for their intended usage. Lawson also proposed a 'Distress Criterion' which may be used to assess the winds in an area for public safety. He recommended that an hourly average wind speed of 15 m/s (20 m/s in areas where no frail persons or cyclists are expected) should not occur more than once a year.

In summary, it is concluded that pedestrian level wind speeds around buildings should ideally be less than 5 m/s in order to maximise pedestrian comfort. Wind speeds between 5 and 10 m/s may be noticeably windy and might elicit adverse comments, but will generally not prevent use of the area. Wind speeds above 10 m/s are unpleasant for pedestrians and those above 15 m/s are potentially dangerous.

Whilst the suggestion of promoting increased urban winds in order to cool our cities is therefore not an entirely feasible one, the cooling effect of the wind is however a very important factor. Forced convection is the least well understood and most difficult to quantify of all the heat transfer processes which occur from buildings. Thermal simulation models of buildings and urban areas rely on the accuracy and appropriateness of the expressions which are used to define the thermal exchange. As demonstrated in the following chapter, these are often very simplistic equations derived from data for situations very dissimilar to those which actually take place in and around buildings. Consequently research is required to better determine the levels of forced convection which take place from typical building surfaces at varying wind speeds before any judgement regarding the use of wind to ameliorate heat islands can be made.

2.4.6 Reducing anthropogenic heat fluxes

Anthropogenic heat fluxes are those which are derived directly from human activities, including losses from buildings, traffic, street lighting and even from our own bodies. Whilst this heat flux may be small relative to the peaks in incoming solar radiation, it remains a significant factor in the urban energy budget. The magnitude of anthropogenic heat releases may exceed that of solar radiation at night or during the winter months. The flux is directly proportional to both the local population density and the requirements for spacing heating. Therefore it can range from as much as 265 W/m^2 in Manhattan during the winter, to as low as 3 W/m^2 in Singapore (Oke, 1987). Such heat inputs can often be directly felt by city inhabitants as they typically occur at the locations of our greatest activities. For example, blasts of hot, humid air may be felt by pedestrians in front of open shop doorways or when passing air-conditioning plant outlets.

With air-conditioning use on the increase in British cities (where traditionally very few commercial buildings and virtually no homes have had such appliances fitted), there is a potential risk of a vicious circle developing. Hotter local climates will necessitate wider and more prolonged use of mechanical cooling. This in turn heats the local air still further so that people feel the need for more cooling, and so on. However, efficient use of energy is becoming of ever increasing importance to both organisations and individuals alike. Measures such as low-energy light bulbs and high-efficiency water heaters are becoming the standard with various campaigns and grant schemes promoting their use. Recent increases in energy supply costs provide further motivation for minimising energy usage (DTI, 2007), as does the growing environmental conscience and sense of responsibility. A high proportion of buildings are now double-glazed and well insulated so that as well as conserving warmth during the winter, the buildings are also better kept cool during the heat of summer (DTI, 2002). Heat losses to the surroundings through the building fabric are kept to a minimum, benefiting households and the local climate alike. The infrared image shown in Figure 2.11 features two buildings; the one in the background (through the trees) glows yellow indicating heat losses through its walls, whereas the façade of the foreground building is significantly cooler.

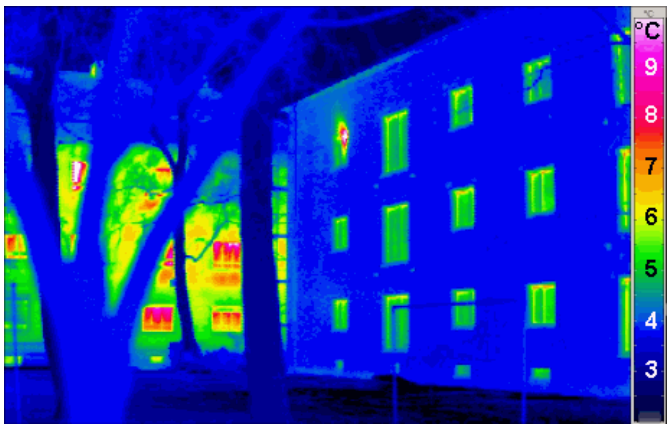

Figure 2.11: An infrared image of buildings with varying levels of insulation (source: WIKIPEDIA, 2003c)

The relative importance of anthropogenic heat influxes will clearly vary from city to city, and from season to season. Notwithstanding this wide variation, any reduction in anthropogenic fluxes will generally benefit the local environment both by lowering ambient air temperatures and from the cost benefits inherent in minimising energy consumption. However the greatest source of anthropogenic heat release into cities is often not from buildings, but from traffic. Vehicles crawling through gridlocked city streets emit vast quantities of heat from their engines along with a cocktail of chemical pollutants. Any attempt to reduce city centre traffic (such as London's Congestion Charge initiative) will also thereby have benefits for heat island reduction.

2.5 The consequences of an urban heat island

Urban heat islands are generally regarded as having a negative impact upon our towns and cities, in part due to the perceived connection with global warming. It has been shown by the wealth of existing data on heat island effects (see Table 2.1 for examples) that the location, climate, urban form and layout of the cities that are affected are wide and varied. Nearly all worldwide urban areas will experience some degree of climate modification; it is not just a phenomena restricted to a particular continent, latitude or landscape. In a presentation given at the 'North American Heat Island Summit' Oke (2002) summarised the social, economic and health implications of urban heat islands for both hot and cold climates. It can be see from Table 2.9 that whilst the effects for an already 'hot' city are negative, 'cold' urban areas may derive some benefit from the presence of a local heat island. In some arid environments, the presence of large areas of irrigated land within a city may result in cooler temperatures than in the surrounding dry areas (Grimmond, 2007). In practice however, the differentiation between 'hot' and 'cold' cities is likely to be far less clear and the significance of the various impacts quite variable.

Table 2.9: The socio-economic and health implications of urban heat islands (source: Oke, 2002)

UHI Impact	**In Hot Climates**	**In Cold Climates**
Energy usage.	Negative	Positive in winter Negative in summer
Water usage.	Negative	Negative
Human comfort and mortality rates.	Negative	Positive in winter Negative in summer
Air quality.	Negative	Negative
Biological activity.	Neutral (except perhaps disease)	Positive
Ice and snow.	n/a	Positive

The most important impacts of urban climate modification relate to energy usage. Research conducted in Athens has shown that the local UHI increases both the energy usage and peak energy demand for air conditioning (Hassid *et al.*, 2000). Investment in energy generation and distribution infrastructure is therefore required if previous summertime 'blackouts' are to be avoided. It has been calculated that London's heat island generates a 25% higher cooling load over the year, whilst heating load is reduced by 22% (Watkins *et al.*, 2002). This suggests that even modest heat islands in relatively cool cities with minimal air conditioning usage have a net negative effect on energy consumption. Furthermore, peak cooling demand typically occurs between noon and early afternoon when the power networks are often already overloaded.

Heat island effects may vary widely from one city to the next. Figure 2.12 shows the potential cooling and heating load reductions resulting from installation of a cool roof to a typical home in four US cities. It can be seen that Miami has a very high cooling load and minimal heating load, so the potential cool roof savings are high. The other three cities have a significant winter heating load which is increased as a result of lower solar gains through the roof (i.e. negative energy savings). In Burlington, the extra heating required in winter actually outweighs the reduction in summer cooling load giving an overall increase in energy usage. In this scenario the installation of a cool roof may actually be detrimental, although building heating is usually by relatively efficient means (e.g. gas) whereas air conditioning is powered by electricity.

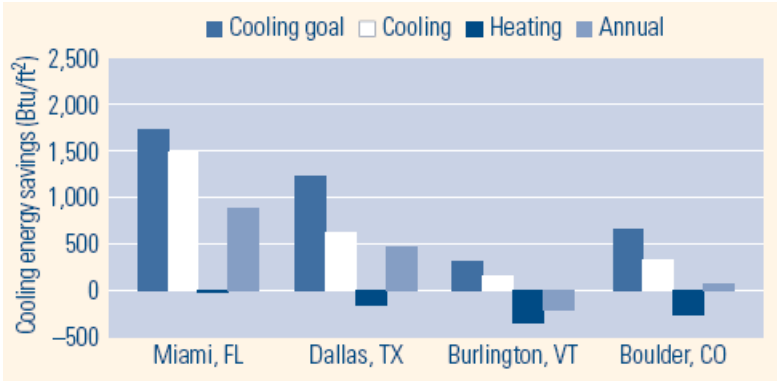

Figure 2.12: Cooling energy saving from cool roof installation in four US cities (source: State of California Energy Commission, 2005)

Increased use of air conditioning in itself adds to heat island intensity by increasing the anthropogenic heat flux into the city. However without it, heat related fatalities may soar. In Toronto it is estimated that there are at least 42 heat-related deaths on average each year (Sheridan, 2002) and exposure to extreme hot temperatures caused an annual average of 381 deaths in the United States between 1979 and 1996 (Sailor, 2002). In England and Wales, it was reported that the August 2003 heat wave resulted in an additional 2045 deaths compared to the months average from the preceding five years (Stedman, 2004). Atmospheric pollution is of further concern as this is directly related to air temperature. Therefore urban heat islands can be severely detrimental to public health, especially where these arise on top of already high summertime temperatures.

However in colder climates a mild increase in urban temperatures may actually be very welcome, particularly in winter. A weak heat island of up to 2 °C has been recorded in Reykjavik which helps to give the city a relatively low winter severity index (Steinecke, 1999). A few degrees increase in temperatures is likely to reduce heating costs and snow will melt more quickly reducing the cost of clearing roads and walkways. The urban form of Melbourne in Australia has been shown to inhibit early morning advection events of warm continent air giving rise to an urban cool island effect which can be as much as 3 °C (Morris and Simmonds, 2000). The city is thereby pleasantly cooler than the surrounding countryside.

Gardeners may see benefits from the milder winter temperatures resulting from an UHI in the form of an extended growing season and the ability to plant a wider range of crops. Wildlife may also flourish; some species of birds that would have historically migrated to warmer climes over the winter now make British cities their year-round home. Other research just published has found that urban populations of garden birds (such as robins and blackbirds) are able to start feeding later in the morning than their rural living counterparts (Ockendon *et al.*, 2009). Cold winter nights are a difficult time for small birds and they need to start feeding early to replace lost energy, but these pressures are not as strong for urban birds which use up fewer energy reserves overnight. Milder winters also allow a greater number of insects to survive providing additional food sources, although the consequential increase in the numbers of garden pests may not be so welcome.

In some circumstances an urban heat island may therefore have a positive influence on a cities microclimate from the point of view of its inhabitants. However, it is important to consider the net effect of climate modification over the course of a year so as to be able to weigh up the potential benefits and pitfalls in each of the seasons. The effects of global warning should also be considered; cities which are currently relatively cool may see temperatures climb over the coming decades with average global temperatures expected to rise by 2 to 3 °C with 50 years if current trends continue (Stern, 2006). Summer heat waves are also expected to become more frequent. Consequently what may now be regarded as a pleasant heat island effect could easily be transformed into a serious summertime concern. It is therefore essential that every city investigates the degree of climate modification and its likely future growth, taking action now where needed to ameliorate future effects.

2.6 Summary and conclusions

The urban heat island effect is a form of climate modification that has been shown to affect the majority of the world's towns and cities. Whilst the basic causations remain the same in each case, each occurrence will have its own individual characteristics and peculiarities depending upon the urban form, building materials, climate, landscape and a variety of other factors.

A range of heat island amelioration measures have been discussed, many of which have already been trialled and developed in various cities. Each may be more or less effective in different scenarios and there are of course also economic, practical and cultural considerations to take into account. A recent review by workers at the University of Hong Kong (Rizwan *et al.*, 2008) provides a useful comparison of the effectiveness of various mitigation measures proposed by other workers. Table 2.10 provides examples of the maximum temperature reductions that have been achieved (or shown to be possible by theoretical studies) for various mitigation strategies. This illustrates the conclusion that there is no single universal approach to minimising heat island effects that will be effective for all towns and cities.

Table 2.10: The effectiveness of some proposed UHI mitigation measures (source: Rizwan *et al.*, 2008)

Proposed mitigation measure	**Max. temperature reduction (°C)**
Vegetation, light coloured paving and cool roofs.	3.0
Vegetation and suitable albedo.	2.0
Planting and vegetation.	1.6
Reducing anthropogenic heat and vegetation.	1.2
Turning off air-conditioning.	1.0

It is therefore proposed that research should be directed at being able to predict the heat island effect and its related physical processes more accurately. With such capability in hand, the effects of measures such as changing albedos, reconfiguring geometries and planting vegetation in our urban areas could be better modelled. Such results would be of equal value in all cities worldwide, allowing better prediction and control of the local climate. Urban heat islands may then be promoted or reduced as appropriate to minimise energy consumption and maintain a desirable climate. Advances in modern computer technology have now made simulation and modelling of such scenarios practical, and to this end, several codes such as DOE-2 (Hirsh, 2006) have already been produced. The aim now is therefore to increase the capability and accuracy of such software by refining the basic equations and principles on which they are based. It is therefore anticipated that at least part of the outcome of this research work should be data that can be applied in such a way. Due consideration must therefore be given to the most appropriate way such findings may be presented, and this will largely depend on the objectives of the modelling package.

Chapter 3 Review of convective heat transfer

3.1 Overview of theory

Convective heat transfer occurs in two different forms; that of free convection (otherwise known as natural or buoyancy-driven convection) and that of forced convection. Free convection is driven by buoyancy forces generated as the heated fluid expands, becomes less dense and hence rises. Its magnitude is therefore primarily dependent upon the temperature and orientation of the heated surface as these factors determine the velocity of the local fluid movement. The overall height of a vertical surface is also significant since the cooling effect of the rising air plume lessens as its temperature increases.

In contrast, forced convection occurs when the fluid flowing around the surface is driven by some external mechanism unrelated to the heat transfer processes. Its magnitude can therefore be much greater than that of free convection as it is not solely reliant upon buoyancy effects to drive the flow. At all but the lowest fluid velocities, the free component of convection is likely to be negligible as forced convection dominates the heat transfer processes.

For wind speeds greater than around 3 m/s, the convective heat transfer coefficient is primarily dependent upon the wind speed. For wind speeds below around 0.75 m/s, it is typically a function of the temperature difference between the surface and surrounding air. At the intermediate wind speeds, conditions are characterised by 'mixed convection' in which the convective coefficient is dependent upon both the speed and the temperature difference.

A comprehensive review of convective heat transfer from the external surfaces of buildings was undertaken by Cole and Sturrock (1977). In summary, the rate of convective heat transfer from buildings can be related to five main factors:

a) Local wind speed across the building surface
b) Temperature difference between building surfaces and surrounding air
c) Relative direction of the wind across the building surface
d) Shape of the surface
e) Surface roughness

As both the temperature difference and the flow properties of the fluid are highly variable with respect to time, it follows that the rate of convective heat transfer must be similarly unsteady. The rate of energy transfer by these processes ($\partial Q/\partial t$) is proportional to both the area of the surface (A) and the temperature difference ($\partial\theta$) between surface and fluid.

By including a constant of proportionality (h_c) into the equation, the rate of energy transfer can be defined as:

$$\frac{\partial Q}{\partial t} = h_c \times A \times \partial\theta \qquad \text{(Eq. 3.1)}$$

Hence the heat transfer coefficient (h_c) may be defined as:

$$h_c = \frac{\Delta Q}{A \times \partial\theta} \qquad \text{(Eq. 3.2)}$$

Dimensional analysis can be used to show that a relationship exists in terms of the Nusselt (Nu), Reynolds (Re), Prandtl (Pr) and Grashof (Gr) numbers in the form:

$$Nu = f(Re, Pr, Gr) \qquad \text{(Eq. 3.3)}$$

In still conditions, no forced convection occurs and so the Reynolds number term can be neglected from Equation 3.3. However, in the more likely event that fluid velocities are significant, it is the gravitational forces which become weak and so the Grashof number can be omitted, hence:

$$Nu = f(Re, Pr) \qquad \text{(Eq. 3.4)}$$

By inclusion of the constants c, p and q into this equation, it is commonly re-written in the following form:

$$Nu = c \cdot (Re)^p (Pr)^q \qquad \text{(Eq. 3.5)}$$

This non-dimensionalised form of the convective heat transfer equation allows the pertinent terms to be identified for experimentation, and the results from such research to be presented in a form which permits more general application. Previous researchers have presented relationships in terms of both dimensional convective heat transfer coefficients (h_c) and non-dimensional Nusselt numbers. The appropriate choice of presentation for convective heat transfer data will depend upon the anticipated application of the results. Whilst non-dimensionalised data may be more readily compared to other data obtained under differing experimental conditions, it is usually more convenient for 'end-users' if relationships are presented in simpler dimensional forms. It is, after all, a single dimensional answer that the designer or engineer will typically require from such heat transfer calculations for practical applications.

3.2 Research to date

A considerable amount of work has been conducted into convective heat transfer over the last 80 years by a wealth of different researchers. This section includes a comprehensive chronological review of the most important and influential works so that gaps in the current state of the art may be identified. Unless otherwise stated, all formulations for the convective heat transfer coefficient presented in this Chapter are in the metric units of Watts per square metre Kelvin (W/m^2K).

Juerges (1924)

One of the first reported pieces of work on forced convective heat transfer from surfaces was conducted by Juerges in the early 1920s. For well over 80 years, this work has remained one of the most important and influential in its field. Indeed, many contemporary sources still make use of the correlations presented by the author, or derived from his data by subsequent workers. Written in German, the original work has been largely inaccessible to the English speaking academic community which has resulted in it often being misquoted. An English translation of the paper was provided by Allen working at the University of Nottingham as part of a research project into the validation of thermal models for buildings (BRE/SERC, 1988). Juerges stated that convective heat transfer from a surface was a function of the fluid velocity, the temperature of the fluid and of the surface, the size of the surface and the surface roughness. His aim was to determine the magnitude of forced convection, concentrating on the effects of velocity and surface roughness.

Experiments took place in a large, well insulated room. The air temperature in the room was maintained to within 0.1 °C during the experiments by opening and closing the doors and windows, and by use of a gas fired heater. A low pressure air pump was employed to provide the air stream. This was driven by a DC motor powered from a bank of rechargeable batteries. A variable resistor fitted in parallel to the motor allowed a consistent running speed to be maintained whilst the output of the batteries and temperature of the motor varied with time. After exiting the pump, the air passed through a diffuser into a 2.0 m long cylindrical chamber (1.1 m in diameter) which was fitted with guides to smooth the flow. A rounded nozzle then directed the air stream over the plate. This was located so that part of the flow passed behind the test specimen, thus allowing the starting point of the velocity boundary to be controlled. The size of the test surface was determined by the requirement for a uniform air stream. Therefore a 500 mm square test plate was selected which was surrounding by 50 mm wide insulation to give an overall size of 600 mm square (the same as the width of the air stream exiting the nozzle).

Several methods of heating the test surface were attempted before success was achieved using a 5 mm thick test plate with a 5 mm water bath attached to its rear. On the other side of the water bath was a 2.5 mm thick iron plate onto which electrical heating elements were fitted. Copper was chosen for fabrication of the test plate as its high thermal conductivity would provide an even temperature distribution. Surface temperatures were measured using ten copper-constantan thermocouples which were soldered into groves cut into the test surface.

Three further thermocouples were mounted onto the rear of the water bath and a further seven in the insulation surrounding the plate. These were all calibrated against a mercury thermometer for the range 10 to 130 °C. The maximum error was found to be 6% and the mean deviation from the calibration curve was 1.5%. In this way, the temperature of the plate was maintained at 30 °C above the ambient temperature of the room (20.4 °C) during the experiments. Air velocity was measured at a variety of locations and distances from the test surface using a Pitot-static tube.

The experimental procedure began by switching on the heating elements and allowing the water bath temperature to stabilise. The air pump was then run for approximately 4 hours before any readings were taken. Typically, a single set of readings would take around 40 minutes to collect. Readings were then repeated until identical values were recorded in two consecutive data sets signifying that steady-sate conditions had been reached.

Three surface roughnesses were investigated; Tests were initially conducted on a copper plate in its 'as-rolled' condition. The plate became heavily oxidised during preliminary trials and so it was later blasted with 2 mm diameter sand to remove the oxidisation and provide a rougher surface finish. Finally, the plate was highly-polished to a mirror finish and then lightly nickel plated to prevent re-oxidisation. Juerges expressly stated that the radiative component of heat transfer for each set of measurements had been determined and taken into account. The emissivity of the three test plates were individually measured by comparison of the radiation emitted to that of a blackened plate, the emissivity of which had been determined previously.

Plotting of the results onto logarithmic graph paper revealed virtually straight fit lines for velocities between 5 and 25 metres per second:

$$h_c = 7.14V^{0.780}$$ - for as-rolled surface (Eq. 3.6)

$$h_c = 7.52V^{0.784}$$ - for shot-blasted surface (Eq. 3.7)

$$h_c = 7.12V^{0.775}$$ - for highly-polished surface (Eq. 3.8)

At lower air velocities (less than 5 metres per second), the effect of free convection was evident as the buoyancy driven flow from the vertical plate was perpendicular to the air stream:

$$h_c = 7.14V^{0.780} + 5.35e^{-0.6V}$$ - for as-rolled surface (Eq. 3.9)

$$h_c = 7.52V^{0.784} + 5.85e^{-0.6V}$$ - for shot-blasted surface (Eq. 3.10)

$$h_c = 7.12V^{0.775} + 5.13e^{-0.6V}$$ - for highly-polished surface (Eq. 3.11)

For practical purposes, it was proposed that the following simplified versions of equations 3.6 to 3.11 would suffice:

For $0 < V \leq 5$ m/s:

$h_c = 5.81 + 3.95V$ - for as-rolled surface (Eq. 3.12)

$h_c = 6.16 + 4.19V$ - for shot-blasted surface (Eq. 3.13)

$h_c = 5.58 + 3.95V$ - for highly-polished surface (Eq. 3.14)

For $5 < V \leq 25$ m/s:

$h_c = 7.14V^{0.78}$ - for as-rolled surface (Eq. 3.15)

$h_c = 7.52V^{0.78}$ - for shot-blasted surface (Eq. 3.16)

$h_c = 7.12V^{0.78}$ - for highly-polished surface (Eq. 3.17)

These results show that the value of the convective coefficient rises with surface roughness. At the time, this finding was surprising as it was in contradiction to the only other data which existed. The convective coefficients for the sand-blasted surface were found to be 7% higher than those for the as-rolled surface. However, the patterns of these two data sets were similar.

Nusselt and Juerges (1928)

Juerges went on to continue his earlier research working with Nusselt. In their joint 1928 paper, also originally written in German, they aimed to determine the magnitude of the free convection from a surface. They employed the same highly-polished 500 mm square copper plate that Juerges had used in his previous research (Juerges, 1924). This plate was mounted vertically and so that it was flush with the surrounding insulation. It was heated to a temperature of 99.7 °C with an ambient room temperature of 26.5 °C.

The free convection coefficient was found to vary with the inverse of the fourth root of the vertical distance from the bottom edge of the plate. By integrating the results over the length (height) of the plate, the following expression was derived for the mean free convective heat transfer coefficient:

$h_c = 4.82L^{1/4}$ (Eq. 3.18)

where *'L'* is the plate length measured in metres.

Other workers have since shown that the Nusselt and Juerges equations are valid for perfectly smooth surfaces with friction coefficients of unity. It has been suggested that simple equations can therefore be derived for other materials by multiplication of their values by the relevant friction coefficient for the non-smooth material being considered.

Rowley, Algren and Blackshaw (1930)

Working in America, Rowley, Algren and Blackshaw undertook a comprehensive investigation into the variation of convective heat transfer coefficients. Although they employed essentially the same technique as Juerges with a test plate mounted flush in a wind tunnel, they extended previous work in several important areas. The most significant finding was that the effect of surface roughness was shown to be highly important. A variety of typical building materials were considered which featured a wider range of surface finishes than had been tested by Juerges previously. They included stucco, brick, concrete, smooth plaster, wood and glass. The range of convective heat transfer coefficients obtained from these tests was considerable, with that for stucco being almost twice that for glass for the majority of wind speeds.

The findings for smooth surfaces compared well with the work of Nusselt and Juerges, but results for rougher surfaces were found to be approximately 25% greater. This was attributed to greater turbulent exchange and a reduced laminar boundary layer resulting from increased friction between surface and fluid.

However, the researchers failed to make measurements of the radiative component of heat transfer in their experiments. Instead, they painted the inside of their wind tunnel dull grey in order to obtain what they referred to as *'average radiation conditions'*. The results presented therefore represent combined radiative and convective heat transfer from the plate, unlike those of Juerges for which the radiative component had been separately evaluated and subtracted.

The results presented in the paper only detail the calculations for the smooth plaster experiments. For this case, assuming an emissivity of 0.91 for the inside of the wind tunnel, it is possible to correct the values proposed by Rowley *et al.* to remove the radiative component. This results in the following equation for the convective heat transfer coefficient:

$$h_c = 5.3 + 3.3V \qquad \text{(Eq. 3.19)}$$

This equation is in approximate agreement with that presented by Jurges for a highly polished flat plate (see Equation 3.14). Without the intermediate data for the other experiments, it is not possible to apply the same correction technique to the correlations proposed for the other materials. However, the relative magnitudes of the correlations obtained from this research will be independent of the radiative component of heat transfer as so the effect of surface roughness illustrated by the data remains valid.

The research also showed that the effect of mean temperature difference between surface and air was measurable, but not significant. A higher temperature difference was found to give rise to a marginally higher heat transfer coefficient.

Rowley and Eckley (1932)

Rowley and Eckley noted that the majority of previous work had only been conducted for flow parallel to a heated plate. To investigate the effect that wind direction had upon the convective coefficient, they varied the angle of a 380 mm square test piece within a wind tunnel. The plate was fitted with a 300 mm extension to the front of the plate which directed flow over the surface and minimised disturbances at the leading edge.

The results appeared to show that the rate of convective heat transfer was actually surprisingly uniform for approaching flow angles between 15 and 90 degrees to the surface. These values were shown to be only slightly less than those obtained for parallel flow. The authors therefore concluded that for practical purposes, the effect of flow direction was not significant and that the parallel flow values obtained in previous studies were acceptable.

Several researchers have since questioned the experimental procedures used in this study, in particular in relation to the disregard of the three-dimensional aspects of the air flow over the surface.

Parmelee and Huebscherm (1947)

Parmelee and Huebscher conducted similar experiments on the magnitude of forced convection using a streamlined heated plate suspended vertically in a wind tunnel.

Their tests showed agreement with those of Rowley *et al*. In addition, they also found that the average value of forced convection along the plate decreased as the surface length increased.

Rich (1953)

Rich investigated the effect upon free convection of the inclination of a surface from the vertical. He used a small heated plate (91 mm wide by 405 mm long) to determine the average buoyancy-driven convection coefficient. The plate was uniformly heated to a temperature of approximately 47 °C and experiments were conducted for angles of inclination of up to 40 degrees from the vertical.

Air flow was shown to be laminar and two-dimensional along the length of the plate. The experimental results were shown to match the following correlation to within 10%:

$$Nu = 0.508\,Pr^{1/2}(0.952 + Pr)^{-1/4}(Gr \cdot \cos\theta)^{1/4} \qquad \text{(Eq. 3.20)}$$

where θ is the inclination from the vertical and the Nusselt, Prandtl and Grashof numbers are local values taken at a distance from the leading edge of the plate.

McAdams (1954)

Heat Transmission by McAdams has been the standard reference used in American literature for many years. It this book, the author references the forced convection correlations originally presented by Juerges from his work with copper plates. In particular, he quotes the equations for the sand-blasted and polished copper plates which are referred to as '*rough*' and '*smooth*' surfaces respectively.

McAdams emphasizes that free convection is predominant for low air velocities and presents the following correlations derived from theoretical analysis for such scenarios:

$$Nu = 0.13\,Pr^{1/3}Gr^{1/3} \quad \text{(for turbulent free convection)} \qquad \text{(Eq. 3.21)}$$

$$Nu = 0.59\,Pr^{1/4}Gr^{1/4} \quad \text{(for laminar free convection)} \qquad \text{(Eq. 3.22)}$$

Where the values obtained using Equations 3.21 and 3.22 are larger than those calculated using Juerges correlations for forced convection, McAdams suggests that his free convection values should be used.

Gates (1962)

Using dimensional analysis, Gates was able to demonstrate the same dependence of the rate of convection upon surface length found experimentally by Parmelee and Huebscher. He showed that the smaller the dimension of the surface is in the plane of the direction of air flow, the greater the average rate of turbulent heat transfer will be. This, he explained, was due to the air having the greatest cooling effect near to the leading edge of the surface. The further along a surface the air flows, the lesser its cooling effect will be. Therefore for long surfaces, the convective cooling effect of the air at the trailing edge may be significantly less than at the leading edge and so the average rate of convective transfer diminishes.

Sturrock (1971)

For his doctoral thesis at the University of Liverpool, Sturrock performed laminar wind tunnel tests which were more representative of urban geometries than any of the existing work. Rather than employing two-dimensional flat plates, Sturrock used cube-shaped models in an attempt to better understand full-scale convective heat transfer. He measured both the air velocity and convective heat transfer coefficients distribution around the cubes and found that these were very different to those for flat plates. Until this point, the effects of three-dimensionality had not been considered. However, as a laminar wind tunnel was used, the correct atmospheric velocity profile and turbulence spectra were not simulated for these tests.

The findings of this research were in direct contrast to the work of Rowley and Eckley (1932) who had found little dependence of the incident angle of the flow upon convection. Sturrock found that the rate of convective transfer from a surface was highly dependent upon the orientation to the wind. The greatest convective heat transfer occurred with an incident wind angle of around 30 degrees and the convection was also shown to be doubled when the surface was exposed compared to when it was sheltered.

The values of convective coefficients derived from Sturrock's wind tunnel tests were significantly greater than those presented in contemporary design guides. For the exposed vertical face of his test cube, the average convective heat transfer coefficient was shown to be proportional to the 0.58^{th} power of the wind velocity. This could be represented over the wind speed range 3 to 10 m/s by the following linear correlation:

$$h_c = 23 + 5.7V \qquad \text{(Eq. 3.23)}$$

Sturrock was able to show that the convective heat transfer coefficient profile (i.e. the variation of the convection coefficient across the building surfaces) is closely related to the local fluid velocities. The highest air movement and hence the greatest convective transfer was measured at the vertices of the cubes.

During the same research, Sturrock also conducted full-scale measurements of convective heat transfer coefficients from buildings. These were made using a heat flow meter which minimised, but was not able to completely eliminate, radiative heat transfer. Readings were taken at a number of locations on the side of a tower block during the night, so as to minimise the effects of solar irradiation. Measured values were found to be up to 30% higher than those that would have been determined using the 1970 IHVE Guidebook (IHVE, 1970). This confirmed the author's belief that flow direction was significant and that results obtained using heated flat plates were unlikely to be representative of full-scale buildings.

From these full-scale measurements, Sturrock proposed the following relationships may be more 'reasonable' than those determined from his wind tunnel experiments:

$$h_c = 11.4 + 5.7V \qquad \text{(for windward surfaces)} \qquad \text{(Eq. 3.24)}$$

$$h_c = 23 + 5.7V \qquad \text{(for leeward surfaces)} \qquad \text{(Eq. 3.25)}$$

Note the variation of these results from the authors own wind tunnel derived correlations (Equation 3.23).

Schwarz (1972)

The work of Schwarz into heat and mass transfer from external wall surfaces is largely unreported, mainly as it was originally written in German. An English translation has been provided by BRE Library (BRE, 1972) although it is not clear whether it is the translation or the original document which was produced in 1972. It is therefore possible that this work proceeded the full-scale testing of Sturrock (1971). Schwarz's work was concerned with the moisture absorption of exterior walls, both externally from driving rain effects and internally from condensation of room humidity. The moisture content of such walls has a significant effect upon their thermal properties and it is therefore desirable that moisture content be kept to a minimum. In order to investigate the drying properties of external walls, the author conducted a series of heat and mass transfer experiments; only the heat transfer sections are of current interest.

Measurements were made on the west face (the predominant wind direction) of a test house situated in an exposed site. A pair of 200 mm square rear-heated heat flux meters was mounted into the building façade. The dimensions of the building are not stated, but from a photograph provided, the 'house' appears to have been a single storey shed approximately 4 m wide by 3 m high and with a low-sloped, monopitch roof. The measurement panel seems to have been at a height of approximately 2 m near to the centre of the building. In order to account for radiative effects, one meter was brightly polished and the other blackened. The surface temperatures were held at 5 °C above the ambient air temperature and measurements were conducted during the night to minimise solar radiation. Wind speed was measured at a height of 10 m at a nearby weather station.

Schwarz presented two equations for windward and leeward wind directions respectively as is shown in Figure 3.1 below. Converted into standard metric units (where 1 kcal/m^{2}hK = 1.163 W/m^{2}K), these expressions are:

$$h_c = 11.05V^{0.51} \qquad \text{(for windward surfaces)} \qquad \text{(Eq. 3.26)}$$

$$h_c = 6.98V^{0.36} \qquad \text{(for leeward surfaces)} \qquad \text{(Eq. 3.27)}$$

Note that the wind speed is that measured at a height of 10 m at the nearby weather station. The author compared the correlations he derived against results from previous workers, including those of Juerges (1924), and found good agreement at low speeds (up to approximately 5 m/s). At higher wind speeds, Schwarz's data and correlations were seen to diverge from the existing relationships. He suggested that this was as a result of the variation in flow conditions between the respective experiments. It was also noted that the measured convective transfer rates remained below the values determined under laboratory conditions at model scale for parallel flow.

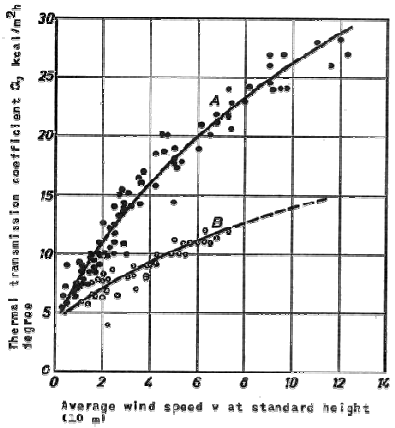

Figure 3.1: Experimental results presented by Schwarz
(source: Schwarz, 1972)

Cooper and Tree (1972)

An alternative approach was adopted by Cooper and Tree who presented an analytical technique for determining the rate of convection. Their research concerned the average value across a surface and considered its characteristic length and the incident angle of the flow. They assumed that both the velocity and thermal boundary layers would begin at the same point; the leading edge of the surface. When presenting their theoretical results, Cooper and Tree included a radiation component of 3.97 W/m^{2}K to take account of the inherent inclusion of radiation they perceived with experimental data. With this modification, good agreement was found between the values calculated by the analytical method and experimental values for smooth plaster. This confirmed that the work of Rowley *et al.* (1930) was actually a combined radiative and convective heat transfer coefficient. When the characteristic length of the surface was increased, the results showed a reduction in the average convective coefficient as had been previously described by Gates (1962). Greater angles of incidence of the air flow were also shown to give similar reductions in convective heat transfer.

The authors proposed that their analytical approach was more accurate than wind tunnel techniques and suggested a list of errors they felt were inherent in experimental derivations. Their analytical relationships indicated that the average heat transfer coefficient was highly dependent upon the length of the surface. Therefore results obtained during wind tunnel tests are only applicable to surfaces of similar dimensions, rather then being universal applicable as had been previously assumed. Also, Cooper and Tree noted that the thermal properties of air (i.e. thermal conductivity, specific heat capacity, thermal diffusivity, etc.) vary with temperature and are able to significantly affect results if this variation is not accounted for.

Ito, Kimura and Oka (1972)

Full-scale field experiments similar to those of Sturrock (1971) were also conducted by Ito, Kimura and Oka working in Japan. Measurements were made at the third, fourth, fifth and sixth storeys of a six storey office block, both at the centre and edge of the building. Each measurement location consisted of a pair of identical heat flow meters which were mounted side by side. The flow meters consisted of a 300W electrical heater and 100 junction thermopile embedded in 3 mm neoprene and faced with a 1 mm copper plate (painted black).

By maintaining the two devices at slightly different temperatures, Ito *et al.* were able to evaluate the radiative component of heat transfer so that this could be subtracted from the measurements to provide isolated convection coefficients. As a further precaution, measurements were conducted at night during the winter so as to minimise the effects of solar radiation. Summertime readings were attempted in order to determine the effect of free convection, but the frequent changes in incident radiation made accurate readings impossible.

The researchers realised the value of being able to relate local convective coefficients on the surface of buildings to the general free-stream wind speed and direction around the building. As such, they measured both the free-stream wind speed above the roof of the office block and also the wind speed at 300 mm above the measurement locations. The former was recorded using a propeller type anemometer with vertical tail and the latter using a calibrated hotwire anemometer. Measurements were recorded manually at one minute intervals.

The data were reduced in two stages; firstly the free-stream wind velocity above the building was related to the local velocities at the measurement locations. Then the convective coefficients were described with respect to the local wind velocity at the measurement locations. Whilst finding that the relationship between near-wall wind speed and convective transfer remained consistent, the researchers concluded that correlations derived from wind speeds measured above the building did not agree with conventional relationships. They pointed out that such correlations were likely to be highly dependent upon the form of the building and the nature of its surroundings. However, for a given free-stream wind speed, the convective coefficients were seen to increase both with height and with proximity to the edge of the building. For leeward surfaces, the effect of wind speed was only slight.

In still conditions, the lowest coefficient recorded at the fifth floor was 8.6 W/m^{2}K whereas it was as low as 5.8 W/m^{2}K for the third and fourth floors. This variation was attributed to differences in the buoyant air movement and temperatures at the different heights. The authors concluded that additional measurements during the summertime with redesigned heat fluxes meters were required to fully evaluate the effect of free convection.

Kelnhofer and Thomas (1976)

The first wind tunnel tests to measure convective transfer whilst attempting to simulate the correct atmospheric velocity and turbulence profiles were undertaken by Kelnhofer and Thomas working at 'The Catholic University of America' in Washington D.C.

Measurements were made using a 127 mm cube model which featured an array of nine heat flux units over one of its faces. The heater elements were made using SR-4 strain gauges which were cemented onto the back of a 25.4 mm diameter, 0.076 mm thick brass disc. A chrome-alumel thermocouple was then soldered normal to the rear of the brass disc and covered by a 0.127 mm mica disc. This whole assembly was then cemented into a hollow Lucite cylinder and mounted into the model so that the brass disc was flush with the surface. This arrangement was shown to give an even temperature distribution over the brass disc (to within 0.2 °C) from which all of the heat from the element was dissipated. The active face of the cube was interchangeable between the roof and side surfaces, and a turntable allowed the model to be rotated so that the heated face could be aligned at varying orientations to the flow.

The short upwind fetch of the open-return wind tunnel meant that it was not possible to grow a boundary layer of the required depth using roughness elements alone. Instead, a graded grid was installed upwind of the test section consisting of a series of 12.7 mm diameter aluminium tubes. These were mounted horizontally across the wind tunnel at spacings which increased with height. The resulting velocity profile was shown to be a good fit to the desired theoretical curve, but simulation of the turbulence spectra was less successful with a maximum turbulence intensity of 10% being obtained (full-scale values for urban areas are typically up to 50%, see Section 6.6). This deficiency was acknowledged and accepted for the initial investigations.

Experiments were conducted with both uniform flow, and with the graded grid arrangement installed to produce a more turbulent shear flow. With flow perpendicular to the windward face of the cube, the measured distribution of convection coefficients were shown to be symmetrical along the stream-wise axis of the model. Minimum values were observed near to the stagnation point on the front face of the cube with maximum values occurring close to the upper and side edges of this surface. Rates of convection from the roof and side walls, which were in areas of separated flow, were similar in magnitude to those on the windward face. The convection coefficients on the leeward face of the cube were more uniform and calculated to be approximately 30% less on average than those for the other faces. The local convective transfer distribution across the faces of an isolated cube was shown to vary with incident wind angle, but the average coefficient across all faces was shown to be virtually independent of wind direction. The authors did not expect that this would be the case for alternative model geometries.

The effect of upwind buildings was to reduce the convection occurring from the cubes surfaces. Unsurprisingly, this was dependent upon the height of the building providing shelter and its distance from the heated cube.

When comparing the results for uniform and shear flow conditions, the results for the latter were reduced by approximately 20%. This was attributed to the reduction in bulk flow passing the model since the velocity at any height is less for shear flow than for uniform flow.

In their concluding remarks, Kelnhofer and Thomas advocate conducting a series of systematic wind tunnel experiments to determine the effect of other velocity profiles representative of conditions such as open-country and city centres. They also felt that the shelter effects of surroundings buildings, as well as fences and trees, required further investigation.

Cole and Sturrock (1977)

This review paper presents a useful overview of convective heat transfer with specific reference to that which occurs at the surfaces of buildings. As well as general theory and an outline of the main factors affecting the rate of convection, the paper also describes research conducted over the 50 year period from the pioneering work of Juerges to the most recent (for 1977) full-scale field measurements by Ito *et al. (1972)*. Also included is a summary of the laminar wind tunnel experiments and full-scale field measurements undertaken by Sturrock (1971) as part of his doctoral thesis six years previously.

In the closing sections of their review, the authors attempt to assess the relative importance of convective heat transfer from the external surfaces of buildings. A computational model was used to determine the heat flows through building elements over the course of a typical heating season. A comparison is made between results obtained using convective correlations determined from the ASHRAE and IHVE Guides, with the two sets of resulting heat flows being very similar. Two significant conclusions are drawn from this comparison; Firstly, the effects of convective transfer is quite small when combined with the other components of heat transfer at the building surface. Secondly, the relative importance of the convective component increases as the overall thermal resistance of the building is reduced. It is suggested that ventilation may be the predominant factor affecting heat loss, and that this may also be the least well determined for naturally ventilated buildings.

It is asserted in the concluding discussions that the results of Juerges (1924) must inherently include a radiative component. This is incorrect since Juerges, unlike Rowley *et al.* (1930), took great care to evaluate and eliminate the radiative component from his experiments.

In their suggestions for further work, Cole and Sturrock noted that convective heat transfer is often regarded in practice as being uniform over the entire external surfaces of a building (despite a number of researchers having demonstrated patterns of surface variation). They suggest that this is likely to be an oversimplification as wind speed is generally predominant from a particular direction and its magnitude will vary with height and proximity to the edges of a building.

Nicol (1977)

In this paper, Nicol describes experiments conducted at the Canadian Arctic Research Station. The aim was to determine the convection occurring from the exterior surface of a window and the tests were conducted during the polar night so that incident solar radiation was negligible. The following correlation was derived from the experimental data:

$$h_c = 7.55 + 4.35V \qquad \text{(Eq. 3.28)}$$

Nicol concluded that there was general agreement with existing relationships. He found that the convective heat transfer from the window surface could be over four times that of radiation on overcast, windy days. In contrast, the convection coefficient fell to as low as 1.0 W/m^2K in still clear-sky conditions.

Watmuff, Charters and Proctor (1977)

In this one page technical note, Watmuff, Charters and Proctor adjusted the correlation originally presented by Rowley, Algren and Blackshaw (1930) in an attempt to exclude the radiative component. They therefore proposed the following equation for the isolated convective component of heat transfer:

$$h_c = 2.8 + 3.0V \qquad \text{(Eq. 3.29)}$$

It can be seen that this equation differs from the correct adjustment of the Rowley *et al.* correlation given previously as Equation 3.19. They then went on to make similar assumptions regarding the correlations proposed by Juerges (1924), despite the radiative component already having been evaluated and removed from the data by the original author. The following equation was therefore proposed which was seen to be comparable to the adjusted form of the Rowley equation given above:

$$h_c = 2.8 + 3.8V \qquad \text{(Eq. 3.30)}$$

The misinterpretation of the Juerges correlations was probably attributable to the original paper being written in German, which has meant that misquoting of the results and methods has been common place. Despite these significant errors, the adjusted relationships presented in this brief technical note have been used by several subsequent researchers and have also been included in a thermal model.

Sparrow, Nelson and Lau (1981)

In this research, wind tunnel tests were conducted by Sparrow *et al.* in order to evaluate the heat transfer rates from roof mounted solar collectors. The pitch angle of the roof was set at 45 degrees. Results for the windward and leeward roof surfaces were compared and it was found that the latter were approximately 10% lower.

Air flow measurements around the model showed that the flow was strongly three-dimensional and dependent upon the form of the simulated building. This meant that the subsequent application of the results to other building geometries is likely to be significantly flawed. A laminar flow wind tunnel was used so that the atmospheric turbulence and velocity profile were not modelled.

Alamdari and Hammond (1983)

In their introduction to this paper, Alamdari and Hammond cite the limitations placed upon the latest generation of dynamic building thermal models by uncertainties with the input data, especially that of the rate of convective heat transfer. They also note the errors inherent in existing two-part correlations where the abrupt transition zone between the two curves often lies at the exact point of interest for building calculations.

The authors derived improved correlations for free convective transfer (i.e. zero wind velocity) from internal building surfaces which provided a smooth fit to data across the full laminar, transition and turbulent flow ranges. These relationships were based on mathematical models presented previously by Churchill and Usagi (1972) which solved the problem of fitting curves to the laminar and turbulent asymptotes. In terms of the non-dimensional Nusselt number, the correlation was presented in the following form:

$$Nu = \left[\left(A \cdot Ra^{1/4} \right)^6 + \left(B \cdot Ra^{1/3} \right)^6 \right]^{1/6} \qquad \text{(Eq. 3.31)}$$

where for vertical surfaces A = 0.58 and B = 0.11, and for horizontal surfaces A = 0.54 and B = 0.14.

For free convection there is no wind velocity and hence there is no velocity (Reynolds number) term in the above equation. As the properties of air do not vary significantly in the temperature range which is of interest for building thermal models, the authors felt that it would be more convenient to simplify this relationship to give the convection coefficient in its dimensional form. This yielded the following expression:

$$h_c = \left[\left\{ a \left(\frac{\Delta\theta}{L} \right)^{1/4} \right\}^6 + \left\{ \left(\frac{\Delta\theta}{1} \right)^{1/3} \right\}^6 \right]^{1/6} \qquad \text{(Eq. 3.32)}$$

where for vertical surfaces a = 1.50 and b = 1.23, and for horizontal surfaces a = 1.40 and b = 1.63.

For stably-stratified conditions, for example below a heated horizontal surface, Alamdari and Hammond noted that recent experimental data showed that the Nusselt number was proportional to the 1/5 power of the Raleigh number. As such, a simplified dimensional expression was presented for use only in such stable conditions. The characteristic length (L) employed in this expression was based upon a value of four times the surface area, divided by its perimeter:

$$h_c = 0.60 \left(\frac{\Delta\theta}{L^2} \right)^{1/5} \qquad \text{(Eq. 3.33)}$$

The improved correlations were compared to a range of empirical data and good agreement was found. Slightly more scatter was seen with the dimensional form of the equation (Equation 3.32) and this was attributed to errors in the recovery of the convective coefficient. Notwithstanding the success of these correlations, it is suggested that building thermal modellers should allow for variations of at least ±20% in the coefficients thereby obtained. This is to account for factors such as draughts, thermal stratification of the room, non-uniform surface temperatures and the presence of fixtures and fittings within the room. They conclude by emphasizing that the equations presented are only applicable to naturally ventilated buildings, as mechanical ventilation will require the calculation of forced convective coefficients using more elaborate techniques.

Kind, Gladstone and Moiser (1983)

Kind, Gladstone and Moiser were also interested in the convective heat transfer from solar collectors. They recognised that the full-scale air flow around real buildings is turbulent and so placed roughness elements upstream of the model in the wind tunnel in an attempt to simulate these conditions.

The radiative component of heat transfer was not measured, but was estimated in order to provide convective only results. The coefficients that were obtained from these experiments were seen to be two or three times smaller than those calculated from the expressions of Juerges (1924) or the adjusted correlation of Rowley *et al.* (1930). The convection coefficients showed some dependence upon the incident wind direction but small architectural details (such as the addition of eaves to the model) were shown to have no measurable effect.

Sharples (1984)

This paper by Sharples provides a summary of the results obtained during his doctoral research at the University of Sheffield. He begins by explaining that the effects of wind are the most difficult to quantify when determining the overall energy performance of a building. However, building materials such as brick, concrete and timber have relatively high thermal resistances and so their response to convective cooling is small.

Single glazing on the other hand has low thermal capacity and negligible resistance and so convective heat loss is rapid. The author therefore proposes that a better understanding of the convective energy balances at building surfaces is required. Real buildings are not equivalent to Juerges flat plate experimental conditions and the equations presented in the design guides fail to consider the influences of building shape, wind direction or location on the façade. Sharples' comment regarding the extra weight added by rising energy costs is even more significant in the current climate.

In an attempt to determine more realistic convective heat transfer relationships for real buildings, Sharples conducted a series of full-scale measurements at locations at the centre of the 6^{th}, 14^{th} and 18^{th} storeys of the 78 metre tall Sheffield University Arts Tower. Measurements were also taken at the edge of the 18^{th} storey. Like previous workers, he employed two identical heat flow meters which were mounted side by side. Each meter was 250 mm square and consisted of an inner 2 mm copper plate that was electrically heated, a central heat flux meter constructed from 3 mm neoprene rubber, and an outer 2 mm thick copper plate which was painted matt black.

This assembly was mounted in a Perspex frame which was recessed into a plywood sheet. By installing the unit in an open window of the tower block, the meter could be fitted flush to the building surface. A constant temperature difference was maintained between the plates (to within 0.3 °C) and experiments conducted at night, so that radiative effects could be minimised and accounted for in subsequent correlations. Wind speeds were measured at 6 m above the buildings roof, 1 m from the active surface and also at a local weather station. The results presented are the culmination of 100 nights of measurements (each of 12 hour duration) at the four locations on the building façade.

Analysis of Sharples' results showed that the data for each location could be fitted with a linear regression. Power-law regressions were also attempted but showed no improvement to the fit over the more simple linear equations (even though theory indicates a power-law fit). The correlations with respect to the local wind speeds 1 m above the surface are reproduced in Table 3.1 below.

Table 3.1: Correlations with respect to local wind speed
(source: Sharples, 1984)

Location	Wind direction	Linear regression	Correlation coefficient
18th floor, central	Windward	$h_c = 1.3V + 4.7$	0.783
	Leeward	$h_c = 2.2V + 2.4$	0.830
18th floor, edge	Windward	$h_c = 1.7V + 4.9$	0.750
	Leeward	$h_c = 1.7V + 5.3$	0.416
14th floor, central	Windward	$h_c = 0.99V + 3.4$	0.716
	Leeward	$h_c = 1.7V + 0.1$	0.687
6th floor, central	Windward	$h_c = 0.65V + 1.9$	0.264
	Leeward	$h_c = 2.1V - 0.6$	0.726

Sharples was also able to determine linear correlations linking the convective coefficients to the meteorological wind speed recorded at a height of 10 m at a local weather station. These linear expressions are reproduced in Table 3.2 below.

Table 3.2: Correlations with respect to weather station wind speed
(source: Sharples, 1984)

Location	Wind direction	Linear regression	Correlation coefficient
18th floor, central	Windward	$h_c = 1.4V + 6.5$	0.670
	Leeward	$h_c = 1.4V + 4.4$	0.829
18th floor, edge	Windward	$h_c = 2.9V + 5.3$	0.592
	Leeward	$h_c = 1.5V + 4.1$	0.599
14th floor, central	Windward	$h_c = 1.6V + 3.3$	0.834
	Leeward	$h_c = 1.5V + 1.0$	0.657
6th floor, central	Windward	$h_c = 0.5V + 3.8$	0.163
	Leeward	$h_c = 1.4V + 1.7$	0.654

It can be seen from the correlation coefficients presented for the two sets of data in the above tables that the convection is more closely related to local wind speeds at the surface, than to the more remote weather station readings. This is not surprising since there will be a number of factors which may influence the wind speed ratio between these two locations. However, Sharples stated that local wind speed measurements are rarely available, whereas records from weather stations are widely accessible. Therefore, relationships expressed in terms of the meteorological wind speed may be more useful, if perhaps less precise, than those in terms of the local surface wind speeds.

Gandrille, Hammond and Melo (1988)

Following on from the earlier work of Alamdari and Hammond (1982) with an *'intermediate level'* model of free convection within rooms, Gandrille *et al.* developed an analogous approach to forced convection from external building surfaces. The resulting *'WIND-CHTC'* computer program was designed to address the wide divide between the simple expressions presented in the contemporary design guides, and complex high-level airflow models developed from computational thermofluid dynamics. The former of these fail to take into account factors such as the incident wind direction and surface length, and the latter required inappropriately high levels of computing power to arrive at a solution.

Instead, the proposed intermediate level approach used the computer as a means to generalise lower level correlations. This procedure was split into two main elements: Firstly, the wind speed profile around the building is determined. The effect of the variation of wind speeds with height was accounted for using a power law velocity profile. The exponent of this relation was varied to take account of the local topography and corresponded to that of either urban, suburban or open country conditions. By integrating the wind speeds over the height of the building of interest, a local speed was obtained. This was then employed in the second element of the procedure which determined the rate of convection from the external building surface. Four convection regimes were considered relating to different flow scenarios, each with its own convection correlation, as follows:

For boundary layer flow which typically occurs on the flat roof and side walls of a building which is aligned square to the approaching flow:

$$Nu_p = \left[\left(0.59 \cdot Re^{1/2}\right)^6 + \left(0.032 \cdot Re^{4/5} - 745\right)^6\right]^{1/6} \qquad \text{(Eq. 3.34)}$$

For completely separated flow such as that which occurs around the leeward face of a building:

$$Nu_s = 0.20 Re^{2/3} \qquad \text{(Eq. 3.35)}$$

For stagnation flow such as that which occurs on the windward face of a building:

$$Nu_{st} = 0.14 Re^{0.69} \qquad \text{(Eq. 3.36)}$$

For buoyancy-driven convection flow for vertical and horizontal surfaces in the absence of significant wind:

$$Nu_b = \left[\left(0.58 \cdot Ra^{1/4}\right)^6 + \left(0.11 \cdot Ra^{1/3}\right)^6\right]^{1/6} \quad \text{(vertical)} \quad \text{(Eq. 3.37)}$$

$$Nu_b = \left[\left(0.54 \cdot Ra^{1/4}\right)^6 + \left(0.14 \cdot Ra^{1/3}\right)^6\right]^{1/6} \quad \text{(horizontal)} \quad \text{(Eq. 3.38)}$$

At intermediate incident wind angles where the approaching flow impinged neither perpendicular nor parallel to the building surfaces, a simple cosine squared relationship was adopted in order to give a smooth transition between the separated/stagnation flows and the boundary layer flow. This expression took the following form:

$$Nu_f = \cos^2\theta \cdot Nu_{s/st} + \left(1 - \cos^2\theta\right) Nu_p \quad \text{(Eq. 3.39)}$$

When mixed convection was important (i.e. when neither buoyancy-driven nor forced convection was predominant), the geometric mean of the buoyancy-driven and forced convection correlations was taken:

$$Nu = \left(Nu_f^{\,3} + Nu_b^{\,3}\right)^{1/3} \quad \text{(Eq. 3.40)}$$

This approach was shown to determine convective coefficients which took into account the significant effects of both wind speed and incident wind angle. The intermediate level methodology was therefore advocated as offering the best balance between accuracy, economy and user-friendliness. The readiness with which these codes could be incorporated into building thermal models was demonstrated using a model developed by the American *National Bureau of Standards*. A variation of between 7% and 15% in the calculated energy usage of two test houses was demonstrated with the inclusion of the proposed code, whilst this was shown to have only a minimal effect upon overall computing times.

Comparisons were made with the full-scale data obtained for an 18 storey tower block (Sharples, 1984). The computed values were seen to be significantly higher than those measured by Sharples at the centre of the block, but lower then those recorded at the edge. Gandrille *et al.* explained that this was because the code calculated surface-averaged values for the façade which would inherently be less than those at the peak edge regions and greater than those at the centre.

A plot of the computed values alongside the data of Sharples and correlation from the ASHRAE and CIBSE guides is reproduced from the paper as Figure 3.2 below. The advantages proposed by the authors are clear. However, field measurements were not available at the time with which to compare and verify the results simulating the effect of intermediate wind angles.

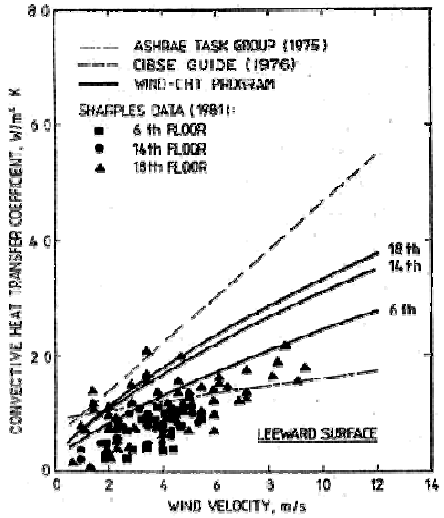

Figure 3.2: Comparison of the 'WIND-CHTC' code with full-scale data (source: Gandrille *et al.*, 1988)

Jayamaha, Wijeysundera and Chou (1996)

A test procedure was developed by Jayamaha *et al.* for determining the rate of convective heat transfer occurring from the external surfaces of buildings "under actual outdoor conditions". A 450 mm square heat balance plate was designed which was maintained at a constant temperature above ambient. By considering the energy balance of the plate and making a deduction for the estimated radiative heat transfer, it was thereby possible to determine the rate of convective heat transfer occurring. After testing and calibration in a wind tunnel, the heat balance plate was then installed outdoors at the centre of a vertical wall panel which measured 1.8 m by 1.2 m. Wind speed was measured at the top of the wall and all data was logged at 30 second intervals. Regression of the data obtained in this way gave a linear equation to correlate the CHTC with wind speed as follows:

$$h_c = 1.444V + 4.955 \qquad \text{(Eq. 3.41)}$$

Contrary to the findings of many other researchers (for example: Liu and Harris, 2007) it was noted that the dependence of the convective coefficient upon wind direction was not very significant. However, the results for flow parallel to the heated plate were found to be slightly higher than for flow directly perpendicular to it. This was attributed to the formation of a stagnation point at the centre of the wall (where the heat transfer measurements were made) when the flow was directly onto the wall. For other wind directions, the stagnation point was moved away from the sensor and hence the apparent convection coefficient was increased. However, the authors suggested that the overall CHTC would be highest for perpendicular flow as the average rate had previously been shown to be approximately 1.18 times that at the centre. The experimental uncertainty for the measurements was estimated to be ±6 to 7%.

Loveday and Taki (1996)

Loveday and Taki were keen to extend the previous full-scale measurements undertaken by workers such as Sharples (1984), Ito *et at* (1972), Nicol (1977) and Sturrock (1971). Their aim was to provide further full-scale experimental convection coefficient data, but at higher quality and accuracy than had previously been possible. One particular source of errors they identified in previous work was the difficulty of measuring surface temperatures accurately over the pairs of heat flux panels which were traditionally used. The authors concluded that, even allowing for a 30% uncertainty in the determination of long wave radiation, their chosen single panel approach would still provide more accurate data than the twin panel method.

Measurements were made on the south-eastern façade of the 8 storey Whitworth Building on the campus of Loughborough University. This building had an L-shaped ground floor, but all subsequent stories were rectangular of dimensions 21 by 9 metres. Their test panel was constructed from a mains powered electrical heater mat which was regulated using a transformer and measured 0.8m by 0.5 m. This was sandwiched between a 1 mm aluminium backing plate and a 2 mm copper heat spreader. A 1 mm thick heat flux meter was then mounted along with a 2 mm exterior copper plate which was painted matt black. Thermal paste was used at all interfaces and the sides and rear of the panel were well insulated. Aluminium tracks were mounted on the side of the building which allowed the panel to be slid down to its test location on the sixth floor from the roof. The panel protruded slightly beyond the building surface but 'air flow ramps' were fitted to minimise any step effects.

Wind speed measurements were recorded 1 m from the panel using an ultrasonic anemometer and at 11 m above the building height using a rotating-cup type anemometer and wind vane. The height of the latter was determined by considering the height required to reach undisturbed flow. Readings were sampled at 10 second intervals (later reduced to 5 minute averages) over a 12 hour period during the night. Wind directions were considered 'windward' if they arrived at an angle of between 0 and 180 degrees to the front of the panel, and leeward otherwise.

The data thus obtained showed good correlation both for the local surface wind speeds and for the free-stream wind speeds above the roof. In both cases, more scatter was apparent for windward directions than for leeward directions. The authors attributed this to local variations in the wind direction, especially at higher wind speeds.

The expressions presented with respect to wind speeds measured above the roof of the building (V_r) were:

$$h_c = 2.0V_r + 8.91 \quad \text{(for windward direction)} \qquad \text{(Eq. 3.42)}$$

$$h_c = 1.772V_r + 4.93 \quad \text{(for leeward directions)} \qquad \text{(Eq. 3.43)}$$

The expressions presented with respect to local wind speeds measured 1 m above the test panel (V_s) were:

$$h_c = 16.15 V_s^{0.397} \quad \text{(for windward direction)} \quad \text{(Eq. 3.44)}$$

$$h_c = 16.25 V_s^{0.503} \quad \text{(for leeward direction)} \quad \text{(Eq. 3.45)}$$

$$h_c = 16.21 V_s^{0.452} \quad \text{(average for windward and leeward)} \quad \text{(Eq. 3.46)}$$

Expressions were also presented relating the local surface wind speeds to those measured above the roof. The convection coefficient correlations obtained were compared with those from previous studies and were found to be generally consistent. Variations were attributed to effects such as differing building geometries, measurement conditions and the local climates. It was recommended that turbulence intensity measurements are taken in any future studies to help specify these particular conditions.

Taki and Loveday (1996)

The work conducted at Loughborough University was later extended to determine the effect that the recess depth of windows from the façade surface has upon the convective transfer. The same experimental arrangement of a 0.8 m by 0.5 m heat flux meter mounted on the sixth storey of a university hall of residence building was used, except that the panel was now fitted with a frame to simulate a variety of recess depths. These ranged from 33 mm up to 347 mm and corresponded to the range of frame protrusion depths identified in a survey of various UK commercial and municipal buildings.

Power law regression correlations were presented for each of the five recess depths that were tested, both in terms of the local wind speeds and those above the roof of the building. For windward conditions, the maximum rates of convective transfer were shown to occur for a 33 mm recess depth, which corresponded to the most common window framework geometry identified by the survey.

The trend for leeward wind directions was less pronounced, although the highest rates of convection were again measured at the shallow recess depths. The authors explained this phenomenon was due to the framework causing the flow to separate reducing convection at the edges but giving increased transfer at the reattachment point. The overall effect was to give higher average convective coefficients across the panels. For both flow directions, the minimum convective transfer was seen to occur for the deepest window recesses where the flow at the surface was sheltered by the frame.

It was suggested that lessons could be learned from this data that could be used to reduce the rate of convective transfer from the windows of buildings, but that such effects must be considered as part of the whole energy and cost balance of the building. Further full-scale tests, as well as laboratory experiments and computer modelling, were advocated in order to arrive at a more reliable model that would allow the geometry of window frameworks to be optimised.

Beausoleil-Morrison (2001)

This paper begins by highlighting the importance of developing accurate convective heat transfer algorithms for use in building thermal and air flow models. Reference is made to a recent study into the disagreement between models which found the treatment of surface convection as one of the primary factors. Sensitivity tests have shown that the choice of convection coefficient relationship can affect simulation results by up to 20 to 40% and may have an impact upon design decisions taken as a result.

However, the majority of building thermal models have been constantly evolving and are now broader in scope considering such aspects as building loads, plant equipment, day lighting and illumination. This evolution is expected to continue as more integrated and highly resolved models are required to handle real-world problems, and therefore refinement of the convection algorithms is essential. In particular, the author identifies the need for a procedure for dealing with the mixed convection regime which is important in many mechanically ventilated scenarios. He proposed that this should be an 'adaptive algorithm' consisting of a suite of equations with a procedure for selection of the most appropriate, which would be able to respond to local flow conditions.

In response to this requirement, the author presents a new approach to model mixed convection from internal building surfaces. This approach is based on two existing sets of equations; those of Alamdari and Hammond (see Equations 3.31 to 3.32) and those of Fisher (1995). The former of these are valid for buoyancy-driven (free) convection and the latter for mechanically-driven (forced) convection. Beausoleil-Morrison demonstrated that both of these regimes were significant in many real-world examples, and so neither of the two sets of correlations would be sufficient on their own. He used the technique demonstrated by Churchill and Usagi (1972) to blend these two sets of equations into a form which would include both the free and forced convective effects as follows:

$$h_{c\,(mixed)} = \left[\left(h_{c\,(forced)}\right)^3 + \left(h_{c\,(buoyant)}\right)^3 \right]^{1/3} \qquad \text{(Eq. 3.47)}$$

For conditions where the flow from mechanical ventilation is in opposition to buoyancy forces, the letter term is subtracted from (rather than added to) the former. Using this technique, the author presented a series of six correlations for mixed convection flow from walls, ceilings and floors.

Simulations of a simple one storey Canadian office block were conducted using the *ESP-r* thermal model to determine the respective annual building loads that would be predicted by the two existing models and the proposed mixed-convection algorithm. The new procedure predicted heating loads 9% and 11% higher and cooling loads 19% and 2% higher than the Alamdari *et al.* and Fisher correlations respectively. It was shown that such variations might have significant effects upon the building design decisions taken.

Meinders and Hanjalic (2002)

At first appearances, the recent work conducted by Meinders and Hanjalic concerning the cooling of printed circuit boards would seem to have little in common with convection from building surfaces. However closer scrutiny reveals a number of close similarities. Printed circuit boards, like urban environments, tend to consist of an array of bluff bodies. The authors noted that it was still difficult to determine the convective coefficients of these bodies accurately from current literature. Their aim was therefore to determine the local convective transfer rates for a pair of wall-mounted cubes which were arranged in a variety of inline and staggered configurations.

This was achieved using two 12 mm copper cubes into which heating elements were embedded. These copper cores were then coated with a uniform 1.5 mm outer layer of epoxy to produce 15 mm cubed test pieces. The surface temperature distribution over the five exposed surfaces of the cubes was determined using infrared imaging which was calibrated to give an accuracy of 0.4 °C. The surface temperatures and uniform copper core temperature were then used as boundary conditions from which the local temperature gradients through the epoxy coating could be obtained. Radiation was approximated from the surface temperatures. The convective heat flux was therefore obtained from a heat balance at the surface and the overall accuracy was estimated to be within 10%.

Tests were conducted in a closed-loop wind tunnel with fully developed flow at a speed of approximately 3.9 m/s. The flow fields around the various arrangements of cubes were measured using laser-dopler anemometry and visualised using pigmented oil-film techniques. Flow separation was shown to give convection maxima on the faces of the cube. Reattachment of the flow on the other hand was shown to give a reduction in the rate of convective exchange.

For inline arrangements of cubes, the results were found to be symmetrical across the central axis. As the spacing of the cubes was reduced, the authors reported that the interaction between the two bodies diminishes so that at zero spacings they behaved like a single (doubled-sized) block. With increased inline spacings, the interaction between the blocks was also seen to reduce as they became aerodynamically isolated. For intermediate spacings, the increased turbulence generated from the first cube was seen to influence convective transfer from the second cube, even when the mean flow field had fully recovered.

For staggered cube arrangements with small off-axis dimensions, the flow fields (and hence convective coefficients) were found to be significantly asymmetrical. Flow accelerated between the two cubes causing modification of the reattachment points on both the upwind and downwind blocks. However when the off-axis spacings were increased or the stream wise spacings increased for a given offset, the interaction between the cubes disappeared and they instead behaved as two isolated bodies.

In order to aid discussion of the complicated three-dimensional convection coefficients obtained, a plot showing the distributions over the vertical faces of the downstream cube for in-line arrangements is reproduced from the paper as Figure 3.3 below. Stream wise spacing of the cubes was represented by the ratio of cube spacing to their height (S/H). Larger values of ‘S/H’ represent greater stream wise spacings.

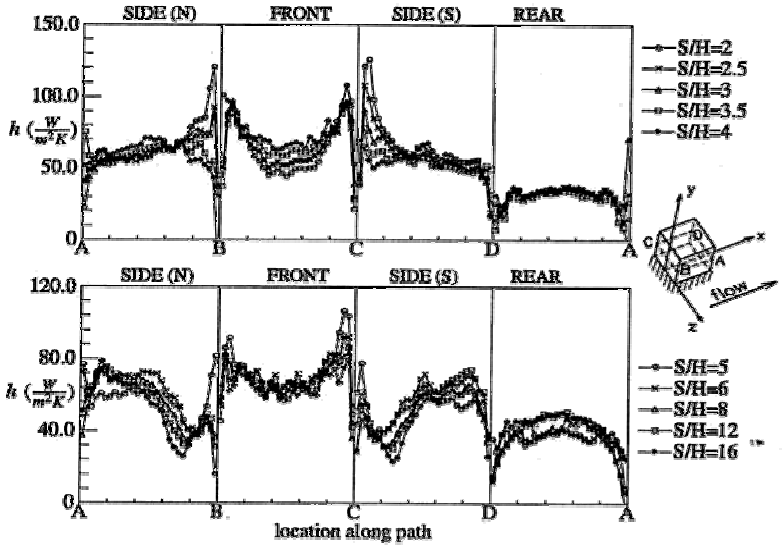

Figure 3.3: Convective coefficients on the upwind cube
(source: Meinders and Hanjalic, 2002)

Meinders and Hanjalic noted that the convection from the rear surface of the cube was largely independent of the spacing and attributed this to similar flow conditions existing in the wake region of the cube. The distribution over the front face of the cube was concave in shape with a minimum at the centre and peaks towards the edges.

The greatest differences between alternative spacings were determined at the leading edge of the side faces. For close cube spacings, the flow reattached to the wall in the absence of a separation region. Therefore peak convective transfer was measured at the leading edge and this decayed with distance along the side wall to a minimum at the trailing edge. This variation was attributed to heating of the air by the surfaces of the cube which in turn decreased the downstream heat flux. As the stream wise spacing of the in-line cubes was increased, the size of the recirculating vortices in the separation region at the leading edge of the side walls was seen to grow. This reduced the convective heat transfer and for the largest spacings (S/H > 4), a minimum convective coefficient was seen where there had previously been a maxima. The distributions of convective coefficients for the widest spacings were similar to those determined for the leading cube.

For the single air stream velocity tested (3.9 m/s), the surface averaged convective heat transfer coefficients were shown to be as much as 70 W/m^{2}K for the windward surface, down to as low as 30 W/m^{2}K for the leeward surface. The values for the other surfaces were shown to fall within this range, although mostly between approximately 50 and 70 W/m^{2}K.

Whilst the surface distribution of convective coefficients for the staggered arrangement of cubes showed greater variability, the authors were able to show that the cube-averaged coefficients were remarkably consistent. An average value of 59 W/m^{2}K was calculated which was shown to fit the data to within ±5%. The authors suggested that this was because the bulk airflow through the channel was the primary factor in determining overall convective transfer from the cubes.

Hagashima and Tanimoto (2003)

A series of full-scale convection measurements were performed on the flat roof of a two-storey building and on the vertical wall of a 'test dwelling' on top of the adjoining four-storey building. In the initial investigation, the surface distribution of CHTC's was demonstrated across the roof of the lower building using an array of sixteen surface heat balances. This distribution was shown to be affected by the adjoining higher-rise building and varied depending upon wind direction.

In subsequent experiments the three-dimensional components of wind velocity were measured at high frequency (10 Hz) using ultrasonic anemometers so as to be able to determine turbulence statistics. The head of the anemometer was positioned 13 cm from the surfaces. The root of the sum of the squares of the three wind speed components (V_{uvw}) was used as the wind speed for the correlations. For three measurement locations near to the centre of the flat roof, a linear regression of the experimental data yielded the following equation:

$$h_c = 3.96 V_{uvw} + 6.42 \qquad \text{(Eq. 3.48)}$$

The data for a fourth measurement point located close to the edge parapet of the roof was less easy to correlate. Two separate ranges of results were obtained depending upon the incident wind direction. The CHTC values were found to be greater than elsewhere on the roof when the wind direction was such that the measurement location was next to the parapet at the windward edge of the roof. This was attributed to separation and backflow conditions. For the vertical surface of the test building, the following correlating equation was derived:

$$h_c = 10.21 V_{uvw} + 4.47 \qquad \text{(Eq. 3.49)}$$

The gradient of this equation is much greater than that of the previous equation such that the resulting convective heat transfer coefficient is almost double at a wind velocity of 1.5 m/s.

Liu and Harris (2007)

Full-scale measurements of the rates of convection from the external surfaces of low-rise buildings were made using a heat balance method similar to those of Loveday (1996) and Sharples (1984). Although the title of the paper describes the test building as being "in sheltered conditions", the actual location was in rural pastureland. The shelter referred to belts of trees to the east, west and south sides of the site. The research therefore differed to that of the majority of previous workers in that it considered low-rise rural buildings rather than the typical high-rise urban ones.

CHTC correlations were presented for surfaces with respect to the local surface wind speed (V_s) measured with an ultrasonic anemometer, the rooftop wind speed (V_r) measured with a vane, and the free stream wind speed (V_{10}) measured at a nearby weather station at a height of 10 metres. A summary of these equations is provided in Table 3.3. It can be seen that the highest correlation coefficients were obtained with respect to wind speeds measured at the roof height and that the lowest were with respect to the weather station wind speeds.

Table 3.3: Convection correlations with respect to various wind speeds (source: Liu and Harris, 2007)

Wall orientation	Correlating wind speed	Linear regression	Correlation coefficient
Windward	V_s	$h_c = 6.31V_s + 3.32$	0.79
Leeward		$h_c = 5.03V_s + 3.19$	0.77
Windward	V_r	$h_c = 2.08V_r + 2.97$	0.83
Leeward		$h_c = 1.57V_r + 2.64$	0.79
Windward	V_{10}	$h_c = 1.53V_{10} + 1.43$	0.72
Leeward		$h_c = 0.90V_{10} + 3.28$	0.64

As well as the various wind speed measurement locations, results were also presented broken down by wind incidence angle. It was shown that this wind direction was highly critical and that a simple analysis based upon azimuth angle alone may not be sufficient due to the complicated flow patterns around the building.

Emmel, Adabie and Mendes (2007)

Noting that the choice of external CHTC's can lead to 20% to 40% variation in estimated building energy demands, this study has sought to predict appropriate values using computer modelling. The 'CFX' computational fluid dynamics (CFD) code was employed to model an isolated low-rise (single storey) rectangular building with a flat roof. The effects of free-stream wind speeds were thereby investigated for the wall and roof surfaces, for various approaching wind angles. The following equations were presented for the windward, leeward and roof surfaces for free stream wind speeds (V_∞) between 1 and 15 m/s:

$$h_c = 5.15V_\infty^{0.81} \quad \text{(for windward wall)} \quad \text{(Eq. 3.50)}$$

$$h_c = 3.54V_\infty^{0.76} \quad \text{(for leeward wall)} \quad \text{(Eq. 3.51)}$$

$$h_c = 5.11V_\infty^{0.78} \quad \text{(for flat roof)} \quad \text{(Eq. 3.52)}$$

The results were presented in the above format to permit easy integration into building energy simulation programs. Other correlating equations were also presented for intermediate wind directions and the effect of surface-to-air temperature differences was also considered. It was concluded that the CHTC correlations found in literature agreed well with the CFD based results, but that as an error of 10% in the selected value can lead to a 5% error in predicted building energy consumption, the use of accurate equations is critical.

Shao, Liu, Zhao, Zhang, Sun and Fu (2009)

In this recently published paper, the researchers describe full-scale measurements of convective heat transfer coefficients from the flat roof of a nine storey (46 m tall) building in Harbin, China. A variation of the naphthalene sublimation methodology was employed whereby a 100 mm square coated test piece was mounted on the roof of the building and the mass transfer rate measured by weighing the plate at five minute intervals.

These measurements were then converted to convective heat transfer coefficients using the mass – heat transfer analogy described in Chapter 8 of this thesis. Wind speed was measured using an ultrasonic anemometer mounted at a height of 1.6 m next to the test piece. The CHTC values varied from 7.6 to 36.4 W/m^2K as the wind speed varied from 0.72 to 4.93 m/s. A linear regression was fitted to the data and the following correlation presented for the CHTC with respect to wind speed:

$$h_c = 6.91V + 3.9 \qquad \text{(Eq. 3.53)}$$

Additionally, convective heat transfer coefficients were also obtained at the same roof location using the more traditional heat balance method for the purposes of comparison with and validation of the naphthalene sublimation results. The following correlating equation was presented for the results obtained:

$$h_c = 6.36V + 4.66 \qquad \text{(Eq. 3.54)}$$

It can be seen that these two linear relationships are comparable and have good general agreement at lower wind speeds (from 1 to 2 m/s). However at higher wind speeds (greater than 2.5 m/s) the naphthalene sublimation technique yielded greater CHTC values than those derived using the heat balance. It was suggested that the reason for this discrepancy could be the relatively slow response time of the heat balance (approximately 30 seconds) which was not able to react as quickly to the rapidly changing turbulent wind conditions on the roof. The uncertainty in the heat balance results was estimated to be 9.7% whereas that for the naphthalene sublimation measurements was 4.5%. It was thereby concluded that the novel measurement technique developed by the authors provided greater accuracy and faster response to changing wind conditions than the heat balance method used by many previous researchers (for example: Liu and Harris, 2007).

3.3 Design guidance

The design guide is the embodiment of the current state of the art and best practice, and as such it is often the designer's foremost point of reference. The techniques, data and calculation methods contained within such documents are considered to be the best available at the time. They are therefore constantly evolving in an attempt to keep pace with current thinking and leading research. For this reason, both current and historical (i.e. superseded) editions of some of the most prominent design guides are detailed in the following sections so that the evolution of the guidance can be seen.

IHVE Guide - Book A (1970 - Superseded)

The Institute of Heating and Ventilation Engineers' 1970 edition Guide Book A (IHVE, 1970) provides a single expression for the calculation of forced convection which appears to stem from the pioneering work of Juerges (1924) back in the early part of the twentieth century. Their equation appears to be an average of the three presented by Juerges (see Equations 3.12 to 3.14) and is shown below. The original correlations were valid for wind speeds below 5 m/s but the guidebook makes no reference to this limitation. For buoyancy-driven convection in the absence of forced air movement, the guide recommends that the fixed values shown in Table 3.4 should be used.

$$h_c = 5.8 + 4.1V \qquad \text{(Eq. 3.55)}$$

Table 3.4: Values for natural convection (source: IHVE, 1970)

Surface orientation	h_c (W/m^{2}K)
Vertical surfaces	3.0
Top side of horizontal surfaces	4.3
Underside of horizontal surfaces	1.5

Tables of internal and external surface resistances are also provided for 'sheltered', 'normal' and 'exposed' surfaces. These external values are based on the assumption that wind speeds are two-thirds of those measured at the roof height of the building. The surface resistances have been converted into combined radiative and convective heat transfer coefficients and are presented in Table 3.5 below for comparison with other values shown in this Chapter. It is interesting to note that the effect of emissivity (i.e. radiation) is not significant for exposed locations such as the upper floors of high-rise buildings.

Table 3.5: Combined heat transfer coefficients for outside surfaces (source: IHVE, 1970)

Building element	Emissivity	$h_r + h_c$ (W/m^{2}K)		
		Sheltered	Normal	Exposed
Wall	High	12.5	18.2	33.3
	Low	9.1	14.9	33.3
Roof	High	14.3	22.2	50.0
	Low	11.1	18.9	50.0

ASHRAE Handbook of Fundamentals (1981 - Superseded)

This edition of the *American Society of Heating, Refrigerating and Air-Conditioning Engineers*' handbook (ASHRAE, 1981) provides expressions for free and forced convection taken from McAdams (1954). The forced convection expressions are therefore originally based upon the early work of Juerges (1924) (see Equations 3.12 to 3.14).

CIBSE Guidebook (1986 - Superseded)

The Chartered Institute of Building Services Engineers' 1986 edition guidebook (CIBSE, 1986) gives the same values as in the IHVE guide (1970) for free convection (see Table 3.4), but with the addition of an average value of 3.0 W/m^2K. The same outside surface resistance table is also presented (see Table 3.5).

In Part C of this CIBSE guide, a series of non-dimensional relationships are listed in terms of the Nusselt number for both free (buoyancy-driven) and forced convection. These include expressions for various orientations of flat plates as well as for cylinders and wires.

BS EN ISO 12241 (1998 - Current)

'Thermal insulation for building equipment and industrial installations - Calculation Rules.'

This British Standard provides calculation rules for the evaluation of the thermal performance of building equipment and industrial installations, both inside and outside of buildings.

For plane vertical walls in the interior of buildings, the following expressions are presented for buoyancy-driven convection:

$$h_c = 1.32\left(\frac{\Delta\theta}{L}\right)^{1/4} \qquad \text{(for laminar flow)} \qquad \text{(Eq. 3.56)}$$

$$h_c = 1.74\left(\Delta\theta\right)^{1/3} \qquad \text{(for turbulent flow)} \qquad \text{(Eq. 3.57)}$$

For plane vertical exterior surfaces, the expressions presented for forced convection are:

$$h_c = 3.96\left(\frac{V}{L}\right)^{1/2} \qquad \text{(for laminar flow)} \qquad \text{(Eq. 3.58)}$$

$$h_c = 5.76\left(\frac{V^4}{L}\right)^{1/5} \qquad \text{(for turbulent flow)} \qquad \text{(Eq. 3.59)}$$

It is not currently clear what the origin of these expressions is, but considering the context of the Standard deals with building equipment and pipe work, it is expected that they have been determined outside the field of current interest.

CIBSE Guidebook (1999 - Superseded)

In the 1999 edition of the CIBSE guidebook, the values given for both free and forced convective heat transfer are those taken from BS EN ISO 6946 (BSI, 1997b). The values obtained from the forced convection equation (Equation 3.48) are tabulated alongside the 'traditional' values used in the UK for determination of U-values (see Table 3.5). The differences resulting from the two approaches are illustrated and it appears that for external surfaces, the calculated values of surface resistance correspond with the traditional values for a 'normal' exposure level.

BS EN ISO 13791 (2004 - Current)

'Calculation of internal temperatures of a room in summer without mechanical cooling - General criteria and validation procedures.'

This Standard provides the equations and procedures necessary for the determination of the internal temperature in a single room taking into account factors including construction type, solar gain, ventilation and most importantly (at least from the point of view of the current study), convection from the inner and outer surfaces. The same equation for forced convection and fixed values for free convection are given as per BS EN ISO 6946 (BSI, 1997b).

BS EN ISO 13792 (2005b - Current)

'*Thermal performance of buildings - Calculation of internal temperatures of a room in summer without mechanical cooling - Simplified method*.'

This document provides a simplified method for determining summertime room temperatures as per BS EN ISO 13791 (BSI, 2004). In this document, a fixed value of 8.0 W/m^2K has been taken for the external convective heat transfer coefficient, presumably by assuming a constant wind velocity of 1 m/s in Equation 3.48. The internal convective heat transfer coefficient is also condensed to a single value of 2.5 W/m^2K.

CIBSE Guidebook (2006 - Current)

The latest CIBSE guide reproduces the information given in BS EN ISO 6946 (BSI, 1997b) and it specifies that the values given for free convection (see Table 3.6) should only be used where the air velocity is less than 0.1 m/s. Alternative non-dimensional relationships for forced convection are given in later parts of the guide, but it is stated that the simplified expression (Equation 3.48) may be used to give a good approximation as long as the air velocity is above 1 m/s at the surface.

BS EN ISO 6946 (2007 - Current)

'Building components and building elements - Thermal resistance and thermal transmittance - Calculation method.'

This current British Standard gives the most comprehensive range of data for the calculation of rates of convection from buildings surfaces. At external surfaces, the following equation is provided where *'v'* is the wind speed adjacent to the surface (in m/s):

$$h_c = 4 + 4V \qquad \text{(Eq. 3.60)}$$

It can be seen that this expression is very reminiscent of that derived by Juerges, but with further simplification of the two constants. At internal surfaces, three values are presented for heat flow upwards and downwards from horizontal surfaces, and heat flow from vertical surfaces. These values are given in Table 3.6 below and it can be seen that the values are different from those presented in previous sources (see for example Table 3.4). A reference for the source of these new values is not provided.

Table 3.6: Values for natural convection (source: BSI, 2007)

Surface orientation	**h_c (W/m^{2}K)**
Vertical surfaces	2.5
Top side of horizontal surfaces	5.0
Underside of horizontal surfaces	0.7

The previous (now withdrawn) 1997 edition of this Standard (BSI, 1997b) also presented the same values and equation for the heat transfer coefficient.

3.4 Use in computational modelling

With recent increases in computing power and the development of a wide array of Computational Fluid Dynamics (CFD) codes, thermal modelling of buildings and local climates is becoming increasingly sophisticated. Such codes can be programmed with the various geometries and boundary conditions for a particular scenario and are then able to calculate a wealth of performance and environmental data. However, the turbulence models used in such simulations are generally not good and this topic is currently the subject of a great amount of research and development.

In order to accurately carry out the complicated calculations required for thermal modelling, it is important that the codes feature appropriate sub-routines for the determination of the various fundamental heat transfer processes. Whilst correlations for conduction and radiation are well documented, the rate of convective heat transfer cannot be determined as easily. It is anticipated that one of the main results from this research is the possibility to refine the existing equations used for convective heat transfer rates from external building surfaces.

It is therefore worth considering several existing building simulation codes and highlighting the methods by which they calculate and handle convective heat transfer from buildings.

'TAS' building simulation code by Environmental Design Solutions Limited

TAS is actually a suite of programs which enable the thermal simulation of new or existing buildings. Once the geometries and construction characteristics of the selected building have been input into the program, simulations can be run to determine the performance and environmental conditions within the building for a range of climate scenarios. The suite includes a database of hourly weather data (including wind speeds) which is used to calculate thermal inputs (e.g. incident solar radiation) and outputs (including convection from surfaces) at the various building boundaries.

Whilst this may seem quite sophisticated, closer examination of the program code reveals that the simulation is based on very simple correlations for the rate of convective heat transfer from building surfaces (EDSL, 2008). In particular, the code uses the equation $h_c=5.8 + 4.1V$ (Equation 3.47) to determine the rate of forced convection from external surfaces, as per the IHVE Guidebook (1970). It has been discussed previously that this relationship was originally obtained by Juerges (1924) using a flat plate mounted in a wind tunnel. It is therefore hard to believe that this equation is completely representative of heat transfer from three-dimensional buildings in a turbulent atmospheric boundary layer.

'DOE-2' code developed by Lawrence Berkeley National Laboratory

A similar building simulation program has been developed at the Lawrence Berkeley National Laboratory in conjunction with the US Department of the Environment (DOE). The latest version of this program, DOE-2, has many of the same features as the TAS programs and also includes input of energy costs to allow calculation of building running costs. A Microsoft Windows version of the software is also now available called 'eQUEST' which adds a graphical user interface and interactive wizards to the same underlying DOE-2 code.

The convective heat transfer coefficient subroutine used in the code (subroutine '*FILMU*') is slightly more advanced than that used by the *TAS* code as it also takes into account the building material of which a particular surface is constructed (LBL, 1982). This follows on from the work of Rowley, Algren and Blackshaw (1930) in which six typical materials were compared using 12 inch square plates in a wind tunnel. The correlation used is that documented in the 1977 ASHRAE Handbook of Fundamentals (ASHRAE, 1977) shown as Equation 3.53 below. The constants A, B and C are selected based upon the surface material type (or more precisely surface roughness) as shown in Table 3.7. These values have been converted from the original imperial units to their metric equivalents (where 1 Btu/hr.ft^2.°F is equal to 5.674 W/m^{2}K) so as to be directly comparable with the other values shown in this section.

$$h_c = A + (B \times V) + (C \times V^2) \qquad \text{(Eq. 3.61)}$$

Table 3.7: Constants used with Equation 3.53 in the DOE-2 CHTC subroutine (sources: LBL, 1982; ASHRAE, 1977)

Surface material	**A**	**B**	**C**
Stucco	11.57	3.04	0
Brick and rough plaster	12.48	2.09	0.00754
Concrete	10.78	2.16	0
Clear pine	8.23	2.06	-0.01508
Smooth plaster	10.21	1.59	0
Glass and painted pine	8.23	1.71	-0.00943

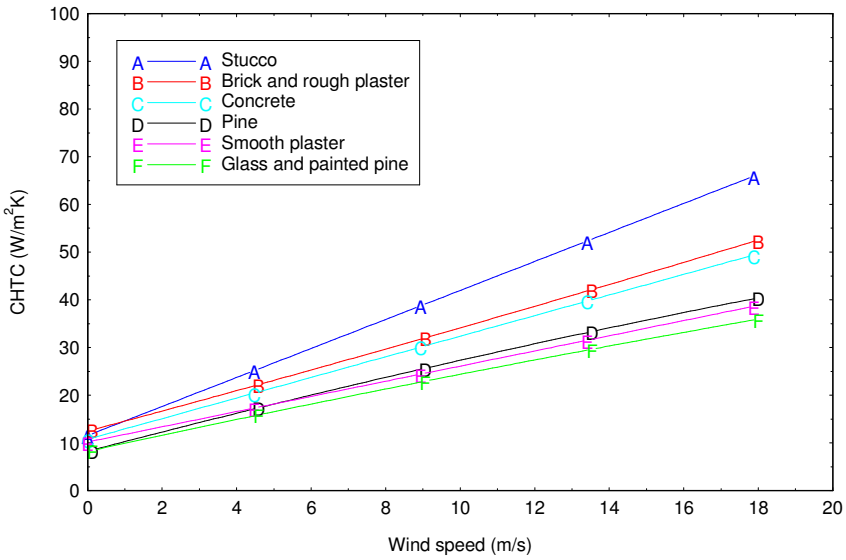

Figure 3.4: The convection coefficients for different building materials (drawn from Equation 3.53 and Table 3.7)

A plot showing the equations for the six different surface materials derived from Equation 3.53 and Table 3.7 above is shown in Figure 3.4. It can be seen that there is considerable variation with surface roughness, with the smoothest materials (glass and pine) exhibiting the lowest convective heat transfer coefficients.

3.5 Summary and conclusions

The main conclusion that can be drawn from the preceding literature review is that the mechanisms which drive convective heat transfer from building surfaces are the least well understood of all the thermal processes. However, it is important that these values are determined accurately since they can have a large influence upon the overall energy balance of buildings (Shao *et al.*, 2009). The method of calculation of the rate of convective transfer has been shown to be the primary cause of disagreement between a number of thermal models. Sensitivity analyses indicate that the selected convective heat transfer coefficient could affect the results of the simulation by up to 20%, or possibly even by as much as 40% (Emmel *et al.*, 2007). Such a variation can have dramatic consequences on the design decisions taken based upon the results obtained, and could therefore lead to inappropriate specification of building components. The heat transfer through windows is especially sensitive to the rate of convection since glass has a low heat capacity and negligible thermal resistance.

The basic correlations for convective heat transfer presented by a number of researchers are often too simplistic as they are unable to account for factors such as wind direction, flow regime or surface orientation. In contrast, high level results which are able to consider these factors are often too complex and processor-intensive to permit practical incorporation into simulation codes. Therefore 'intermediate level' approaches such as those advocated by Alamdari and Hammond (1983) or Beausoleil-Morrison (2001) can often offer the best compromise between the conflicting requirements of building thermal simulations.

The rate of free convection occurring from a building surface is primarily dependent upon the temperature difference between the surface and fluid. It has also been shown to be dependent upon the size of the surface, reducing along its length (height) as the fluid itself becomes heated. Therefore the average free convective coefficient over a large surface may be significantly less that that at its edge, or the average over a smaller surface. Forced convection on the other hand is mainly a function of wind speed, with the points of maximum velocity and peak convection often coinciding. The effect of surface roughness can also be significant with rougher surfaces giving rise to higher rates of heat transfer as a result of increased levels of local turbulence.

The pioneering work of Juerges (1924) has led the way in convective heat transfer research, with the expressions he derived still forming the backbone of current guidance. Along with a number of following researchers, Jurges employed heated flat plates in a laminar wind tunnel to derive correlations relating the convective coefficients to variables including wind speed and surface roughness. Despite the lack of consideration of the effects of atmospheric turbulence and three-dimensional flow, these correlations have remained in use for the calculation of the rates of convection from buildings for more than eighty years.

Only a few wind tunnel studies have been conducted to measure the rate of convection which occurs from more representative three-dimensional models of buildings. The most notable of these is the work completed by Sturrock (1971) and by Sparrow *et al.* (1981), both working in laminar flow wind tunnels. Fewer still wind tunnel studies have replicated the appropriate atmospheric boundary layer simulations for urban areas, although the effects of turbulence are known to be highly significant. Kelnhofer and Thomas (1976) used a series of exponentially spaced horizontal tubes in an attempt to generate the correct atmospheric boundary layer profiles in a short-fetch wind tunnel. Whilst they succeeded in developing a representative velocity profile, they were only able to generate a maximum turbulence intensity of approximately 10%. Whilst this is significantly more than that in a laminar-flow wind tunnel (turbulence intensities typically <0.1%), it is well below the values of up to 50% measured at full-scale in urban areas.

A number of researchers have undertaken full-scale measurements using heat flux meters to determine the rate of convective transfer from real building surfaces. However it is not clear how applicable these findings are to alternative geometries since the test buildings used were often of unusual, non-generic shapes. There is also little reference to the surrounding building densities, topography or land usage accompanying these results; all of which may have a significant effect upon the flow conditions and hence upon the measured convection coefficients. Loveday and Taki (1996) suggested that turbulence intensity data should be presented alongside all future full-scale experiments in an attempt to quantify these effects.

These issues are compounded by variation in the heights and locations at which the 'free-stream' wind velocities around each test building have been recorded. The most clear convection correlations have been found to be in respect of the local wind speeds adjacent to the surface, rather than more remote above-roof or weather station measurements. This is not surprising since it is known that the rate of forced convection is heavily dependent upon the wind speed. However, such expressions may not be of great usefulness to designers and engineers since the exact surface wind speeds around a particular building are rarely known. So, whilst free-stream correlations are more difficult to determine due to the effects of wind direction and surface orientation, they are nevertheless more useful since rates of convection can be calculated using readily available meteorological wind speed data.

A selection of the most notable expressions derived from full-scale convection measurements on windward surfaces have been plotted together in Figure 3.5. The relationship proposed by BS EN ISO 6946 (BSI, 2007) (see Equation 3.52) has also been included to permit direct comparison with the experimental data. This Figure illustrates the vast range of convective heat transfer coefficients which may be determined using just some of the currently available correlations. These do not include theoretical expressions, those determined from model-scale measurements or those for other surface orientations (e.g. leeward). These additions would increase the range of values that may be obtained still further.

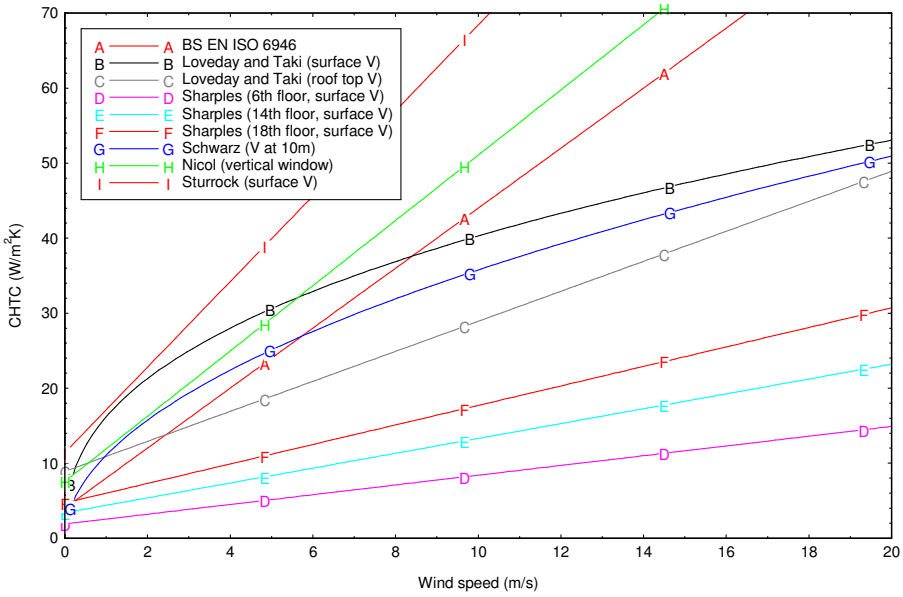

Figure 3.5: Comparison of expressions for convection from a windward surface

A further problem which has been evident in a large number of the studies is that of eliminating the radiative component of heat transfer from the results. Some researchers have been able to measure and subtract the appropriate value, but typically the rate of radiative transfer has been calculated or approximated for the experimental setup. This has led to confusion in interpretation of the data by subsequent workers, some of whom have wrongly corrected for radiative effects where this had already been carried out by the original author.

It is therefore concluded that existing guidance for the rates of convective heat transfer from building surfaces is limited, particularly for external surfaces where wind effects are significant. The values presented in BS EN ISO 6946 (BSI, 2007) and reproduced in the latest CIBSE Guide (2006) are the most recent and are therefore considered to be the current 'state-of-the-art'. Other applicable Standards have been noted which are more recent, but these still draw their data for convective heat transfer from BS 6946.

The effect that wind direction has upon the rate of convection for a particular surface is unclear. Kelnhofer and Thomas (1976) showed that the average convective coefficient across all faces of a cube was virtually independent of wind direction, whereas Sturrock (1971) found wind direction to be highly critical for his full-scale measurements. Kelnhofer and Thomas also concluded that the rates of convection from the roof and sides of a cube were similar to windward surface, and that those on the leeward face were more uniform and around 30% less. Limited research has been conducted to date into the role that urban form and layout has in determining the rate of convection occurring from the surfaces of buildings. The effects of variables such as the spacings of building or street width are therefore largely unknown. Meinders and Hanjalic (2002) investigated the interactions between two adjacent cubes when investigating the heat transfer from printed circuit boards. This work sees many analogies with heat transfer from urban areas since both problems involve consideration of the flow over arrays of bluff bodies.

When buildings are very closely spaced, they tend to behave as one larger building. Their interaction also diminishes at greater distances as they become aerodynamically isolated. However at intermediate spacings, the interaction of the flow between the buildings gives rise to raised levels of turbulence and to local flow accelerations. These effects are likely to increase the rate of convection. Alternative results have suggested that the rate of convection occurring from leeward surfaces is independent of building spacing, since the flow conditions in wake region remain constant. The data presented by Meinders and Hanjalic indicated that the average coefficient over all surfaces of a cube is consistent for a variety of spacings. The role that the urban form and geometry plays in determining convective heat transfer coefficients is therefore currently unclear.

Similarly, little data is available from which to assess the spatial variation of the convection coefficients across the surface of a building. Wind tunnel experiments have typically generated only surface averaged data and full-scale measurements have only been conducted at a limited number of discrete locations on each test building. Therefore the surface distribution of convection coefficients is largely unknown, except that is has been noted that minimum convection coefficient tend to occur at the centre of the windward façades, with maximums towards the edges.

Two examples of computational building thermal models have been briefly discussed to illustrate the fact that the sub-routines used to calculate convective heat transfer are often much less advanced than those used for other aspects of the models. Similar computer simulations are being developed for local-scale climate forecasting and these will be invaluable in predicting the effects of urban heat islands and determining appropriate mitigation strategies. It is likely to be even more important to accurately determine the convection coefficients when considering the external urban climate, since a large proportion of incident solar radiation will be transferred from the surfaces to the air by this mechanism. Such codes require correlations expressed in dimensional terms to permit easy integration (Emmel *et al.*, 2007).

Chapter 4 The naphthalene sublimation technique

4.1 Introduction to the technique

During initial background research for this project, a technique was highlighted by a paper written by Barlow and Belcher (2002) working at the University of Reading's Meteorology Department. The technique employs naphthalene - a white, crystalline chemical - with which scale models of buildings are coated. These models are then placed in a wind tunnel and, as naphthalene sublimates at room temperature, a reduction in the thickness of the coating occurs. By measuring this thickness change and employing an analogy between mass and heat transfer, it is then possible to deduce the respective convective heat transfer coefficient. Comprehensive reviews of the experimental technique were presented by Souza Mendes (1991) and Goldstein and Cho (1995).

Using the sublimation of naphthalene to measure convective heat transfer has several important advantages over traditional techniques such as heat flux meters. The most important of these is that it allows convection to be isolated from the other heat transfer processes of radiation and conduction. Experimental techniques which measure convection directly from a heated source inevitably also include radiative and conductive effects. Measurements (or sometimes just estimates) of the rates of these processes must then be deducted from the measured overall heat transfer, adding uncertainty to the results. By employing mass transfer as a direct analogy to convective heat transfer, both the radiative and conductive components are inherently eliminated. Mass has no effects analogous to radiation and (when the model is constructed from a non-porous material), absorption (i.e. conduction) is also eliminated.

When working with a heated wind tunnel model, it is difficult to maintain the required isothermal and adiabatic boundary conditions. However, these can be imposed with ease when the naphthalene sublimation technique is employed. A surface coated with the chemical corresponds to an isothermal boundary condition since the naphthalene vapour remains saturated. A constant temperature surface can therefore be modelled with ease. Similarly, an uncoated, inactive surface corresponds to an adiabatic boundary condition since there is no flow of mass (i.e. heat) either to or from the model. It is possible to change discontinuously from isothermal to adiabatic regimes simply by virtue of whether or not the surface is coated with naphthalene. More complex geometries are also made possible as the fabrication of models is not hindered by the necessity for insulation or thermocouple junctions to maintain temperature boundaries.

However, as with all experimental techniques, there are several limitations of the naphthalene sublimation methodology that must be noted. Most critical of these is that the saturation vapour pressure of naphthalene is very sensitive to temperature. A one degree Celsius change in surface temperature results in an approximate ten percent change in the vapour pressure (Goldstein and Cho, 1995). This makes it vital to either maintain the coated model at constant temperature throughout the duration of the experiment, or else to minimise run times so that variations due to ambient conditions are kept to a minimum.

There are also constraints on the maximum wind tunnel speed that may be used. At particularly high air velocities, localised heating of the model may take place as a result of the recovery effect (Goldstein and Cho, 1995). The heat generated by viscous dissipation may also be sufficient to have a large impact upon results in such circumstances. However, the typical running speeds used to generate a boundary layer simulation within a typical atmospheric wind tunnel are not thought to be high enough for this effect to be significant.

Another important consideration is that the sublimation of the surface coating will affect the size and geometry of the model. The impact of this may be minimised by selecting the largest feasible model scale so that any dimensional change resulting from sublimation is relatively small. The length of experiments must be determined to balance the conflicting requirements of maximising the reduction in coating thickness (in order to minimise measurement errors) and ensuring that the geometry is not significantly altered (Souza Mendes, 1991).

The technique has been previously employed by a number of researchers to investigate heat transfer resulting from flows in ducts, external flows, impinging jets, natural convection and rotating surfaces (Souza Mendes, 1991). It has also been used to model the dispersion of scalar sources such as heat from street canyons (Barlow *et al.*, 2004; Pascheke *et al.*, 2008) and the rate of convective heat transfer from grain storage silos (Finnigan and Longstaff, 1982). Other applications include determination of convective heat transfer in pipes (Silva L.F. *et al.*, 2001), in degraded nuclear reactor cores (Dutra *et al.*, 1991) and around holes in flat plates (Cho *et al.*, 1997). Research just published describes a novel approach to the full-scale measurement of convective heat transfer coefficients on a flat roof using naphthalene sublimation (Shao *et al.*, 2009). The results obtained were shown to have half the estimated uncertainty of the more traditional heat balance technique and were more able to respond to rapidly changing wind conditions.

4.2 About naphthalene

Naphthalene is a white, crystalline substance with the chemical formula $C_{10}H_8$, as illustrated in Figure 4.1 below. It can be seen that naphthalene molecules are composed of two fused benzene rings and accordingly, naphthalene is classified as a benzenoid *polycyclic aromatic hydrocarbon* (PAH). It is a volatile substance which forms a flammable vapour. A photograph showing examples of the snowflake-like crystal structures formed as naphthalene vapour condenses on a metal jar lid is shown in Figure 4.2. Naphthalene is also known by a wide variety of pseudonyms including *naphthene, naphthalin, naphthaline, tar camphor, white tar, moth flakes* and *albocarbon.* It should not however be confused with naphtha.

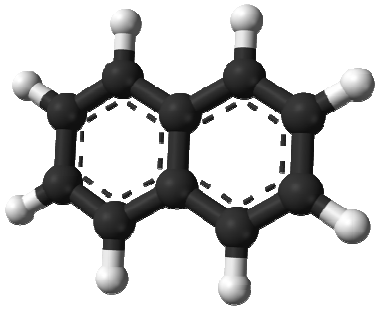

Figure 4.1: The structure of naphthalene $C_{10}H_8$ (source: WIKIPEDIA, 2002)

Most naphthalene is derived from coal tar, which itself is the liquid by-product of the distillation of coal to make coke. Typical coal tar contains about 10% naphthalene by weight, but industrial processing can yield crude naphthalene which is around 95% pure. Some of the chemical and thermal properties of naphthalene are summarised in Table 4.1.

Table 4.1: The Chemical properties of naphthalene
(source: Goldstein and Cho, 1995)

Chemical property	**Value for naphthalene**
Chemical formula	$C_{10}H_8$
Molar mass	128.17 g/mol
Melting point	80.2 °C
Normal boiling point	217.993 °C
Enthalpy of sublimation	70.36 kJ/mol
Density of solid	1175 kg/m^3

The single largest use of naphthalene is in the production of *phthalic anhydride* for the manufacture of plastics and dyes. However, it is best known for its use as an insecticide and household fumigant, especially in mothballs from where most people will have become familiar with its distinctive odour. When placed in a wardrobe or chest of drawers, naphthalene vapours build up to levels which are toxic to both the adult and larval forms of many textile-destroying moths. Other fumigant uses of naphthalene include use in soil as a fumigant pesticide, and in attic spaces to repel rodents.

Research conducted at Louisiana State University and published in the journal Nature (Chen *et al.*, 1998) suggests that certain species of termite may have found a similar use of naphthalene as a repellent against ants, poisonous fungi and nematode worms. Trace amounts are also produced by magnolias and certain types of deer (WIKIPEDIA, 2002).

In humans, exposure to large amounts of naphthalene is harmful and may damage or destroy red blood cells. This could cause the body to have too few red blood cells resulting in fatigue, lack of appetite, restlessness and pale skin. Exposure to large amounts of naphthalene may cause nausea, vomiting, jaundice and potentially fatal renal failure. For these reasons, good ventilation, appropriate personal protection and exposure monitoring are essential when working with naphthalene.

Figure 4.2: Naphthalene crystal formation on the lid of a storage container

For the purposes of this work, naphthalene's most important characteristic is that it sublimates readily at ambient temperatures. This is the basis of the experimental technique proposed and allows mass transfer to be used in direct analogy to convective heat transfer.

4.3 Overview of experimental methodology

The basic methodology of the naphthalene sublimation technique is well documented and can be broken down into five key stages:

1. A scale model is first coated in a thin layer of naphthalene.
2. The quantity of naphthalene is measured either by weighing the model or by taking local thickness measurements at discrete points.
3. The coated model is then placed in the air stream of a wind tunnel for a set duration.
4. The naphthalene coating is then re-measured and this subtracted from the initial readings to give the mass or thickness change(s).
5. The convective heat transfer coefficient can then calculated by employing an analogy between mass and heat transfer.

Whilst this procedure may appear relatively straight forward, the practicalities provide several significant challenges. The first of these is how the model is to be coated with an even layer of naphthalene of the required thickness. Previous researchers have employed a variety of techniques ranging from the casting of solid models in a mould (Goldstein and Cho, 1995) through to adhering naphthalene granules with thermal paste (Barlow and Belcher, 2002).

The second important consideration is how to accurately measure the mass or thickness of the naphthalene coating so that the mass transfer rate may be deduced. Once more there have been a number of methods suggested. These range from simply weighing the model using a sensitive mass balance through to complex measurements using a Linear *Variation Differential Transformer* (LVDT). Each of these techniques has advantages and disadvantages, and the selected technique will have a large impact on both the quality and quantity of the data that may be obtained.

Each of these issues will be discussed in more detail in the following sections and a novel approach will be suggested which it is hoped will greatly extend the scope of the naphthalene sublimation technique.

4.4 The heat / mass transfer analogy

Every physical quantity has a dimension which is related to (but not identical to) the concept of units. The choice of units for each quantity is arbitrary and many different alternatives are usually available. For example, we may consider length using either metres, feet, miles, inches or yards as our chosen unit. Conversion factors may be used to interchange between different units of the same quantity (e.g. 1 metre = 3.280 feet = 39.37 inches). However each quantity has only a single, unique dimension.

Table 4.2: The fundamental physical quantities

Physical quantity	Symbol	SI Units
Length	L	metre
Mass	M	kilogram
Time	T	seconds
Temperature	θ	Kelvin

The quantities shown in Table 4.2 above are regarded as the 'fundamental quantities'. They can neither be broken down into a more fundamental form, nor derived from one another. In contrast, other quantities of interest are referred to as 'derived quantities' as they are defined by reference to some or all of the above fundamental quantities. The units of velocity, for example, are defined in reference to length and time, and so this is considered to be a derived quantity.

Dimensional analysis is a tool which allows us to formulate hypotheses concerning complicated physical processes which can then be tested by experimentation. It helps us to identify the important physical quantities for a particular process. Buckingham's π theorem forms the basis of dimensional analysis. This theorem states that where a physically meaningful equation consists of 'n' variables formed from 'm' fundamental quantities, then a total of 'n' minus 'm' dimensionless parameters may be found.

The theorem will now be applied to both heat and mass transfer scenarios. The two dimensionless groups obtained will then be compared and it will then be shown that they are of similar form. This is the basis of the analogy between heat and mass transfer which is employed when utilising the naphthalene sublimation technique.

4.4.1 Heat transfer

The dimensions of importance for heat transfer are shown in the Table 4.3 below, along with their dimensions in terms of the four fundamental units of length, mass, time and temperature.

There are thus seven independent variables and four primary dimensions, and so using Buckingham's π theorem there must be three dimensionless groups.

Table 4.3: Quantities and dimensions for heat transfer

Physical quantity	Symbol	Dimensions
Heat transfer coefficient	h_c	$M\,T^{-3}\,\theta^{-1}$
Length	l	L
Density	ρ	$M\,L^{-3}$
Viscosity	μ	$M\,L^{-1}\,T^{-1}$
Specific heat capacity	C_p	$L^2\,T^{-2}\,\theta^{-1}$
Thermal conductivity	K	$M\,L\,T^{-3}\,\theta^{-1}$
Fluid velocity	V	$L\,T^{-1}$

The important independent variables are 'h_c', 'V' and 'C_p' and the scaling variables are 'l', 'ρ', 'μ' and 'K'. Hence three π-groups may be formed as follows:

$$\pi_1 = l^{a_1}\rho^{b_1}\mu^{c_1}K^{d_1}h_c$$

$$\pi_2 = l^{a_2}\rho^{b_2}\mu^{c_2}K^{d_2}V$$

$$\pi_3 = l^{a_3}\rho^{b_3}\mu^{c_3}K^{d_3}C_p$$

The first π-group may be solved as follows:

$$\pi_1 = L^{a_1}\left(\frac{M}{L^3}\right)^{b_1}\left(\frac{M}{LT}\right)^{c_1}\left(\frac{ML}{T^3\theta}\right)^{d_1}\left(\frac{M}{T^3\theta}\right)^{1}$$

Length	$0 = a_1 - 3b_1 - c_1 + d_1$
Mass	$0 = b_1 + c_1 + d_1 + 1$
Time	$0 = -c_1 - 3d_1 - 3$
Temperature	$0 = -d_1 - 1$

Solving these equations gives $a_1 = 1$, $b_1 = 0$, $c_1 = 0$ and $d_1 = -1$, thus:

$$\pi_1 = l^1\rho^0\mu^0K^{-1}h_c$$

$$\pi_1 = \frac{h_c\,l}{K}$$ which is the Nusselt number (Nu). (Eq. 4.1)

The second π-group may be solved as follows:

$$\pi_2 = L^{a_2}\left(\frac{M}{L^3}\right)^{b_2}\left(\frac{M}{LT}\right)^{c_2}\left(\frac{ML}{T^3\theta}\right)^{d_2}\left(\frac{L}{T}\right)^{1}$$

Length	$0 = a_2 - 3b_2 - c_2 + d_2 + 1$
Mass	$0 = b_2 + c_2 + d_2$
Time	$0 = - c_2 - 3d_2 - 1$
Temperature	$0 = -d_2$

Solving these equations gives $a_2 = 1$, $b_2 = 1$, $c_2 = -1$ and $d_2 = 0$, thus:

$$\pi_2 = l^1\rho^1\mu^{-1}K^0\,V$$

$$\pi_2 = \frac{\rho V l}{\mu}$$ which is the Reynolds number (Re) (Eq. 4.2)

The third π-group may be solved as follows:

$$\pi_3 = L^{a_3}\left(\frac{M}{L^3}\right)^{b_3}\left(\frac{M}{LT}\right)^{c_3}\left(\frac{ML}{T^3\theta}\right)^{d_3}\left(\frac{L^2}{T^2\theta}\right)^{1}$$

Length	$0 = a_3 - 3b_3 - c_3 + d_3 + 2$
Mass	$0 = b_3 + c_3 + d_3$
Time	$0 = -c_3 - 3d_3 - 2$
Temperature	$0 = -d_3 - 1$

Solving these equations gives $a_3 = 0$, $b_3 = 0$, $c_3 = 1$ and $d_3 = -1$, thus:

$$\pi_3 = l^0\rho^0\mu^1K^{-1}C_p$$

$$\pi_3 = \frac{C_p \mu}{K}$$ which is the Prandtl number (Pr). (Eq. 4.3)

It is known that in still conditions, the Nusselt number is a function of the Reynolds and Prandtl numbers, thus:

$$Nu = f(Re, Pr)$$ (Eq. 4.4)

By inclusion of the constants ‘C’, ‘m’ and ‘n’, an equation for the Nusselt number may therefore be obtained in the following form:

$$Nu = C \cdot Re^m \cdot Pr^n$$ (Eq. 4.5)

4.4.2 Mass transfer

The dimensions of importance for mass transfer are shown in the Table 4.4 below, along with their dimensions in terms of the four fundamental units of length, mass, time and temperature.

Table 4.4: Quantities and dimensions for mass transfer

Physical quantity	Symbol	Dimensions
Mass diffusivity	D	$L^2 T^{-1}$
Density	ρ	$M L^{-3}$
Length	l	L
Diffusion rate	k_c	$L T^{-1}$
Velocity	V	$L T^{1}$
Viscosity	μ	$M L^{-1} T^{-1}$

There are thus seven variables and four primary dimensions, and so there must be three dimensionless groups (using Buckingham's π theorem).

The important independent variables are 'k_c', 'v' and 'μ' and the scaling variables are 'D_v', 'ρ' and 'l'. Hence:

$$\pi_1 = D^{a_1} \rho^{b_1} l^{c_1} k_c$$

$$\pi_2 = D^{a_2} \rho^{b_2} l^{c_2} V$$

$$\pi_3 = D^{a_3} \rho^{b_3} l^{c_3} \mu$$

The first π-group may be solved as follows:

$$\pi_1 = \left(\frac{L^2}{T}\right)^{a_1} \left(\frac{M}{L^3}\right)^{b_1} \left(\frac{L}{1}\right)^{c_1} \left(\frac{L}{T}\right)^{1}$$

Length $\quad 0 = 2a_1 - 3b_1 + c_1 + 1$

Mass $\quad 0 = b_1$

Time $\quad 0 = -a_1 - 1$

Solving these equations gives $a_1 = -1$, $b_1 = 0$ and $c_1 = 1$, thus:

$$\pi_1 = D^{-1} \rho^{0} l^{1} k_c$$

$$\pi_1 = \frac{k_c l}{D}$$ which is the Sherwood number (Sh). (Eq. 4.6)

The second π-group may be solved as follows:

$$\pi_2 = \left(\frac{L^2}{T}\right)^{a_2}\left(\frac{M}{L^3}\right)^{b_2}\left(\frac{L}{1}\right)^{c_2}\left(\frac{L}{T}\right)^{1}$$

Length $0 = 2a_2 - 3b_2 + c_2 + 1$

Mass $0 = b_2$

Time $0 = -a_2 - 1$

Solving these equations gives $a_2 = -1$, $b_2 = 0$ and $c_2 = 1$, thus:

$$\pi_2 = D^{-1}\rho^0 l^1 V$$

$$\pi_2 = \frac{lV}{D} \qquad \text{(Eq. 4.7)}$$

The third π-group may be solved as follows:

$$\pi_3 = \left(\frac{L^2}{T}\right)^{a_3}\left(\frac{M}{L^3}\right)^{b_3}\left(\frac{L}{1}\right)^{c_3}\left(\frac{M}{LT}\right)^{1}$$

Length $0 = 2a_3 - 3b_3 + c_3 - 1$

Mass $0 = b_3 + 1$

Time $0 = -a_3 - 1$

Solving these equations gives $a_3 = -1$, $b_3 = -1$ and $c_3 = 0$, thus:

$$\pi_3 = D^{-1}\rho^{-1} l^0 \mu$$

$$\pi_3 = \frac{\mu}{\rho D} \qquad \text{which is the Schmidt number (Sc).} \qquad \text{(Eq. 4.8)}$$

Further, π_2 can be divided by π_3 to give:

$$\frac{\pi_2}{\pi_3} = \left(\frac{lV}{D}\right)\Big/\left(\frac{\mu}{\rho D}\right)$$

$$\frac{\pi_2}{\pi_3} = \frac{\rho V l}{\mu} \qquad \text{which is the Reynolds number (Re).} \qquad \text{(Eq. 4.9)}$$

It is known that the Sherwood number is a function of the Reynolds and Schmidt numbers, thus:

$$Sh = f(Re, Sc) \qquad \text{(Eq. 4.10)}$$

Again, by including the constants 'C', 'm' and 'n', an equation for the Sherwood number may be obtained in the following form:

$$Sh = C \cdot Re^m Sc^n \qquad \text{(Eq. 4.11)}$$

4.4.3 Comparison of heat and mass transfer

It has been shown in the previous two sections that the heat and mass transfer can be described by the following equations:

$Nu = C \cdot Re^m Pr^n$ - for heat transfer.

$Sh = C \cdot Re^m Sc^n$ - for mass transfer.

When written in this form, the similarities between these two equations are evident. Division of the Nusselt number by the Sherwood number yields the following equation:

$$\frac{Nu}{Sh} = \frac{C}{C}\left(\frac{Re}{Re}\right)^m \left(\frac{Pr}{Sc}\right)^n \qquad \text{(Eq. 4.12)}$$

Which reduces to:

$$\frac{Nu}{Sh} = \left(\frac{Pr}{Sc}\right)^n \qquad \text{(Eq. 4.13)}$$

Therefore:

$$Nu = \left(\frac{Pr}{Sc}\right)^n \times Sh \qquad \text{(Eq. 4.14)}$$

The Prandtl number is known for air, the Schmidt number can be determined for naphthalene and the value of the exponent 'n' is known empirically for different flow regimes (see Section 8.1). The Sherwood number is calculated from the mass transfer rate measured during the naphthalene sublimation experiment and hence the Nusselt number may therefore be determined. The convective heat transfer coefficient (h_c) can then be calculated.

Chapter 5 Preliminary trials of the naphthalene technique

5.1 Experimental methodology

A series of preliminary experiments were conducted in order to assess the feasibility and suitability of the naphthalene sublimation technique for the current research project. These tests allowed a practical understanding of the methodology to be acquired and therefore highlighted areas where development or modification of procedures would be needed. Prior to the commencement of testing, a number of important decisions were required regarding the method by which the naphthalene technique would be implemented. These considerations are discussed in the following sections, and the reasoning behind the decisions taken is explained.

5.1.1 Measurement of the naphthalene coating thickness

One of the primary considerations when planning the tests was the method by which the rate of sublimation of the naphthalene coating would be measured. Previous researchers used a variety of techniques which can broadly be divided into two groups; (a) those which provide surface averaged results and (b) those which involve measurements at an array of discrete locations over the model.

The surface average approach is typically the most straightforward and has therefore been selected by a number of previous researchers including Barlow and Belcher (2002) at the University of Reading. The mass transfer rate can be measured directly by weighing the model before and after a test and calculating the variation. High levels of accuracy may be achieved using this technique provided that the test is run over several hours so as to allow a significant mass of naphthalene to sublimate. An accurate and sensitive mass balance is also critical. In this way, the average convective heat transfer coefficient across the coated surfaces of the model can easily be obtained. If the model is constructed of several parts which can be separated prior to weighing, average values across discrete surfaces may be obtained (e.g. over the roof or a particular wall of interest). Whilst the relative simplicity of this methodology had obvious advantages, the limited data acquired from each experiment would have restricted the level of understanding developed. It would have been difficult to investigate the underlying physical processes taking place around the model without having been able to resolve any spatial variation across the individual surfaces. Consequently the required guidance regarding the significance of building geometry, urban form, orientation, etc. could not have been derived from such limited data.

It was therefore necessary to acquire an array of individual measurements at discrete locations across each surface of interest in order to determine special variation across surfaces. If required, such results can of course be combined to provide surface average data as per the weighing method previously discussed. The results from particular sub-sections of a model or surface may also be averaged in this was so that different regions of the building surface may be compared.

An example of where such an approach may be beneficial is to allow convective heat transfer data for a pitched roof to be compared with the wind loading data provided by documents such as BS EN 1991-1-4 (BSI, 2005a). Winds loads, like the rate of convective heat transfer, are a function of air velocity. The Standard prescribes particular areas of known susceptibility to high wind loads (see Figure 5.1) and it is feasible that the same areas may also experience high rates of convective heat transfer. Particular areas of the building of interest (e.g. those corresponding to windows, roof lights or sections of a façade system) could be isolated to provide dedicated design guidance. The ability to select particular regions of the model for separate analysis therefore had very clear benefits for determining the detailed thermal performance of individual elements in realistic situations. However, the primary benefit derived from taking measurements across a regular array of points was that the variation of heat transfer across the surfaces could be determined. By presenting results as contour plots, it become clear where areas of high and low heat transfer were located and so the effects of model geometry became apparent.

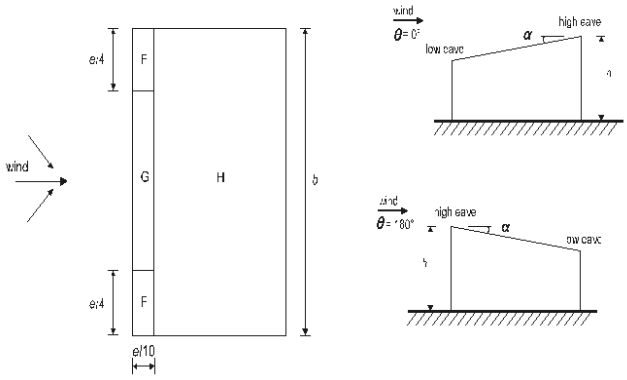

Figure 5.1: Sub-sections of a monopitched roof considered for wind loading (source: BSI, 2005a)

Some researchers have used *linear variation differential transformers* (LVDT's) to measure the surface profile of the naphthalene coating around the model (Goldstein and Cho, 1995). Such devices give a voltage output proportional to the deflection of a stylus and are therefore able to determine the thickness of a naphthalene layer along rows of points as the stylus is traced across the surfaces. Automated scanning of a surface can be accomplished using a computer-controlled positioning system. A practical setup of this nature can achieve high resolution and accuracy but is only suitable for flat plates or simple three-dimensional solids (e.g. cylinders). Measurement times in the order of an hour or more introduce errors as a result of extraneous sublimation of the naphthalene coating. For these reasons, this particular technique was not judged suitable for the current work. A novel approach was therefore required which would allows the thickness of a naphthalene coating to be measured rapidly at an array of locations over a three-dimensional solid.

Initial consideration was given to using laser distance measuring devices which could be used to determine the distances to various points on the model from a fixed datum position. By scanning the model in this way before and after the experimental run it was anticipated that the change in naphthalene thickness could be determined. Investigation of the specifications for off-the-shelf devices found that their measurement inaccuracy was several orders of magnitude greater than the anticipated changes in naphthalene thickness (e.g. ±1.5 mm typical accuracy for the Leica Disto A8 unit).

Internet based research identified a technology which permits the measurement of the thickness of thin coatings applied to metal substrates. Such devices are commonly used in certain industry sectors where they have applications in quality control and inspection. They are typically employed to monitor the thickness of applied paint, galvanising or powder coatings during manufacturing processes to ensure that the results are maintained within acceptable tolerances. Two variations on the technology are available depending upon the type of substrate. For magnetic (i.e. ferrous) substrate materials, devices use the electromagnetic induction principle. A coil in the measurement probe is powered by a sinusoidal signal which induces an alternating magnetic field around the probe. Two further coils (one behind and one in front of the primary coil) are used to detect this alternating magnetic field. The induced magnetic field around the probe is uniform when it is in free air. As the probe is brought closer to a ferrous substrate, the magnetic material influences the magnetic field causing it to become unbalanced and thus more of the field cuts the coil which is nearest to the substrate than cuts the furthest coil. This produces a net voltage difference between the two detector coils which can be calibrated as a direct measure of the distance to the substrate, and hence of the coating thickness.

A similar process is used for non-ferrous metal substrates except that the probe operates using eddy-current induction principles. The measurement probe features a single coil powered by a high frequency signal which generates an alternating field in the non-ferrous metal substrate. The field causes eddy currents to circulate in the substrate which have magnetic fields of their own. These fields influence the probe and cause changes to the electrical impedance of the coil that are dependent upon the distance to the metal substrate, and hence the coating thickness may again be determined.

Examples of surface coatings which are commonly measured with such devices include rubber, glass fibre, epoxy and enamel. However discussions with the leading manufacturer of these units confirmed that a naphthalene coating had not been previously tried or tested. Their technical representative explained that there was no theoretical reason why the thickness of a naphthalene layer could not be determined in this way as the principle of operation remained the same. It was therefore agreed that a loan unit would be supplied for trial.

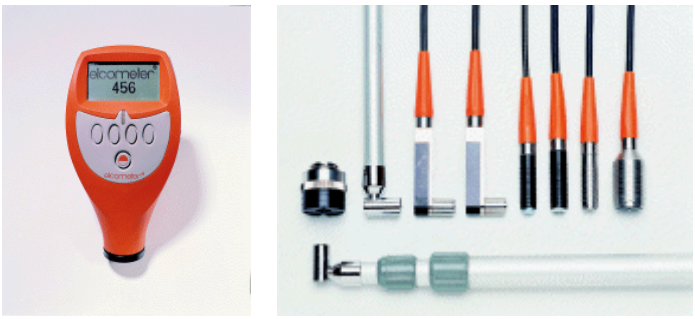

Figure 5.2: Elcometer 456 coating thickness gauge and probe options
(source: Elcometer Limited, 2009)

The Elcometer 456 coating thickness gauge (shown in Figure 5.2) costs approximately £750 + VAT including a non-ferrous probe. Specifications for the device are provided in Table 5.1 below. In summary, it offers a maximum accuracy of ±2.5 µm at a resolution of 0.1 µm, over a range of 0-1500 µm. The accuracy can be maximised by calibrating the gauge close to the required measurement range using supplied foils of known thicknesses. As measurements can be made almost instantaneously whilst the model remains in-situ in the wind tunnel, errors due to continued sublimation are minimised. Assuming an average sublimation depth of 0.25 mm occurs from the model, the maximum error would equate to only 1.0%. This is significantly less than other known sources of error within the technique, such as the estimation of properties of naphthalene.

Table 5.1: Specifications of the Elcometer '456' coating thickness gauge
(source: Elcometer Limited, 2009)

Specifications		**Description**
Part number - Gauge - Probe		Elcometer 456 Top FNF Standard T456FNF1S
Measurement range		0-1500 µm
Accuracy		±1 to 3%, or ±2.5 µm
Resolution		0.1 µm up to 100 µm 1 µm 100-1500 µm
Minimum Substrate Thickness		Ferrous: 0.3 mm (12 mils) Non-Ferrous: 0.1 mm (4 mils)
Operating Temperature		Ferrous: Up to 150 °C Non-Ferrous: Up to 80 °C
Minimum Convex Surface Diameter		Non-ferrous mode: 38 mm Ferrous mode: 4 mm
Minimum Concave Surface Radius		Non-ferrous mode: 25 mm Ferrous mode: 25 mm
Headroom		Non-ferrous mode: 88 mm Ferrous mode: 88 mm
Minimum Sample Diameter		Non-ferrous mode: 8 mm Ferrous mode: 4 mm

An additional feature of the device is that it has a large memory capacity which allowed sets of readings from a number of experiments to be stored in discrete batches for later download and analysis. The unit comes with either a built-in probe or with a separate probe and cable; the latter option was selected for the current study because it allowed easier access to the various model surfaces. A number of probe options are available for various ferrous or non-ferrous applications. The material from which the wind tunnel models were to be constructed was not known at the time of purchase and there a dual ferrous / non-ferrous type probe was selected to allow later flexibility.

5.1.2 The wind tunnel model

Models tested in the BRE boundary layer wind tunnel are typically at scales of between 1:100 and 1:500. This scale range is dependent upon the wind tunnel simulation techniques employed and therefore has fixed limits. It was desirable to maximise the size of the naphthalene coated model so that changes in dimension resulting from sublimation are negligible compared to the overall dimensions. A larger scale model also permits more measurement locations per surface and hence more detailed measurement of the variation of mass transfer rates across surfaces. A linear scale of 1:100 was therefore selected for the models used in this study, this being the largest scale at which the wind tunnel simulation remains representative of full-scale atmospheric boundary layer conditions. A 100 mm cube model was initially selected in order to provide an approximate representation of a typical three storey, 10 metre high, flat-roofed building at this scale. However limitations imposed by standard material dimensions required the model size to be reduced slightly to a 94 mm cube.

Assuming that this arrangement of a 94 mm high row of model buildings extends across the full 2 metre width of the wind tunnel, this corresponds to a blockage ratio of approximately 6.3%. However the BRE boundary layer wind tunnel was designed to be ‘blockage-tolerant’ up to blockage ratios of around 30% by the inclusion of aerofoil-slats in both the walls and roof of the working section (Parkinson and Cook, 1992). Flow acceleration around the models as a result of their blockage effect was therefore not significant.

The use of the Elcometer 456 coating thickness gauge to measure the naphthalene layer required the coated model to be made from a metallic substrate. As a dual mode ferrous / non-ferrous probe had been selected, the choice of metal could be made based on practical and fabrication considerations alone. In consultation with the model maker, it was decided that aluminium would be used as this was easier to machine into the specified dimensions and would not oxidise (rust) between tests. Aluminium possesses a relatively high thermal conductivity (237 W/m.K) and specific heat capacity (24.20 J/mol.K) which helped to ensure stable and uniform temperatures across the model surfaces. The primary wind tunnel model was therefore fabricated as a 94 mm solid aluminium cube and the surrounding buildings were formed from 94 mm solid softwood cubes.

5.1.3 Naphthalene coating technique

A number of techniques for coating the model with a layer of naphthalene have been proposed and developed by previous researchers. Some of the most recent research using this experimental technique has been performed at Reading University in the UK (Barlow and Belcher, 2002; Pascheke *et al.*, 2008). Researchers here employed what is perhaps the most straightforward coating method of all; a thin layer of thermal paste was applied to the surfaces of the aluminium models and then fine naphthalene powder was then sprinkled on top. The paste acted as an adhesive and also a thermal bond ensuring that an even temperature was maintained across the entire model during the test periods. Whilst this coating method benefits from not requiring any prior preparation of either the model or naphthalene, it is not possible to produce a uniform coating thickness across the model. This made it unsuitable for use with the Elcometer coating thickness gauge. Additionally, contact of the probe with the coated surface when taking measurements would have disturbed the delicate naphthalene layer, thereby affecting subsequent measurements at the same location.

An alternative methodology which is more suited to complicated geometries is to spray naphthalene directly onto the model. Neal *et al.* (1970) demonstrated that this can be achieved by dissolving naphthalene in a solvent whilst Lee (1986) developed a spraying method using heated compressed air. Both techniques permit a thin layer of naphthalene to be built up around even the most complicated geometries, although the finish may not be as smooth as expected due to recrystallisation of the naphthalene. There are also significant health and safety hazards to spraying a naphthalene / solvent mixture, including fire risk and increased levels of naphthalene inhalation resulting from the fine droplet size. Whilst the heated compressed air option removes the need for a solvent, inhalation and fire concerns remain and such facilities were not available at BRE. For these reasons, the spraying method was also discounted for the current experimental work.

A colleague's suggestion that molten naphthalene could be painted onto a model using a brush was investigated, but preliminary trials using aluminium sheets revealed that there were issues with the naphthalene solidifying on the brush. Even when these difficulties were partially overcome, the surface finish was found to be poor and streaky due to rapid solidification of the molten naphthalene upon contact with the cold metal sheet. For these reasons the method was soon abandoned.

Another technique which has been popular with some previous researchers has been that of casting the test piece (Goldstein and Cho, 1995). The naphthalene powder is heated to above its melting point (~80 °C) until it is fully liquid and is then poured into a mould. This method may be used to produce either solid naphthalene test pieces or ones cast around an internal base. The outer mould must be highly polished in order to achieve a very smooth surface and to give precise model dimensions. A smooth finish also aids removal of the test piece from the mould once the cast naphthalene has cooled and solidified. The casting method benefits from its relative simplicity and lack of requirement for complicated equipment which, combined with the precision mentioned previously, made it a potentially feasible option for this study.

A final alternative was to dip the wind tunnel model into a heated bath of molten naphthalene. This may be done once, or repeated several times (similar to the traditional technique for making candles) in order to build up a thicker surface coating. This approach is both simple and convenient and is also useful when a large number of small pieces require coating. Like casting, it requires little specialist equipment and has the additional benefit of not requiring a precision polished mould. With careful preparation and control of the temperature of the model and molten chemical, it is possible to achieve a coating thickness of the required uniformity (although isolated runs and drips are likely, especially near to the vertices of the model). The model must be non-porous to prevent absorption of the molten chemical and ease cleaning between tests; the metallic substrate required by the Elcometer coating thickness gauge met this requirement. The necessary equipment to heat and melt the naphthalene were readily available and the simple model could be fabricated quickly and at low cost. Therefore the dipping technique was selected for preliminary trials which aimed to establish both the practicalities of the methodology and the quality of finish that could be obtained. The slightly more complex casting procedure was reserved as a fallback option should the desired results not have been achieved by casting.

5.2 Preliminary experiments

After fabrication of the required solid aluminium cube models, preliminary trials of the proposed technique were commenced. In order to ensure that the naphthalene coating adhered to the model it was necessary to remove all traces of grease. This was achieved by cleaning the model using ethanol and then wearing gloves during subsequent handling to prevent recontamination. It was decided that a grid would be drawn on each surface of the model in order to aid rapid and accurate positioning of the thickness measurement probe at the desired measurement locations. Fine-tipped waterproof marker pens were used which would remain visible through the semi-translucent naphthalene coating. A different colour was used on each of the five exposed surfaces in the first trial in order to determine which was the most effective. Permanent marking (e.g. with painted dots) was avoided as this would provide additional coating thickness and so could have influenced the measurements.

It was important that the measurement locations were not too close to the vertices of the model as the probe required a minimum diameter of surrounding substrate to function correctly (8 mm for non-ferrous materials, see Table 5.1). A five-by-five array of measurement locations was chosen to meet the conflicting requirements of detail versus minimising measurement times. This gave a total of 125 measurement locations across the five exposed model surfaces (the base obviously not being included). Regular spacing of these locations across each 94 mm x 94 mm surface determined a 16 mm interval between points both horizontally and vertically, except for at the edges where this would be 15 mm. The model mark-up pattern is shown schematically in Figure 5.3. Each face of the cube was marked in an identical manner.

With the model marked up, the process of coating the model was started. High purity naphthalene powder* was transferred to a 160 mm diameter cylindrical metal storage container with sealable lid. The container was then placed in a hot-water bath which was maintained at approximately 95 °C for several hours until the naphthalene had fully melted. It was found that the water-bath temperature needed to be at least 15 °C above the melting point of the naphthalene (~80 °C) in order to achieve complete melting of the powder including that above the water line. This posed the additional problem of a rapid loss of water from the bath by evaporation which required constant top-ups that temporarily lowered the bath temperature. This was alleviated by using hollow plastic ball devices (about 25 mm in diameter) which float on top of the water providing an insulating layer and hence minimising evaporation. The water temperature was also maintained at just below boiling point and the lid of the water bath closed so that condensate would run back into the bath. The lid of the naphthalene container was left loosely fitted to prevent water droplets contaminating the chemical.

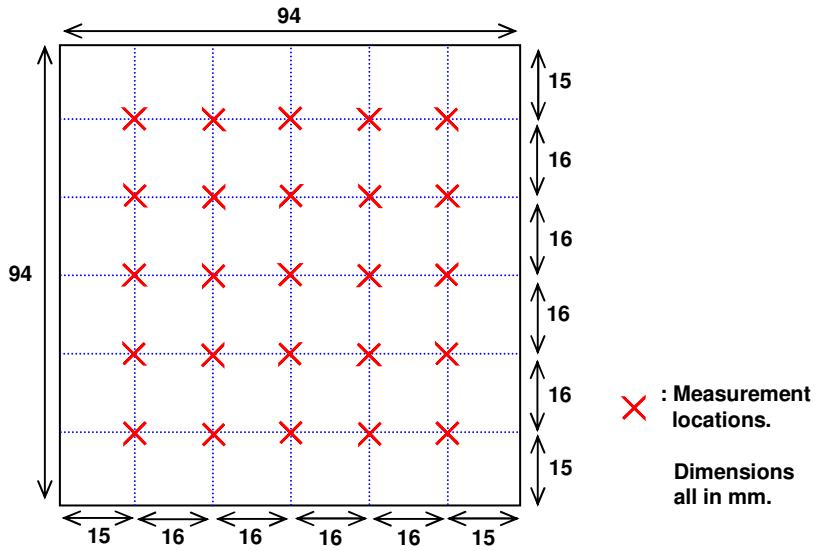

Figure 5.3: The array of measurement locations over each cube's surface

In order to permit easier and safe handling of the model cube during the coating process, threaded holes were tapped into four corners of its base. Two lengths of studding were screwed into a pair of diagonally opposite holes by which it was then possible to handle the model safely and lower it into the molten naphthalene. All of the preparation involving molten naphthalene was conducted in a fume cupboard to minimise health and fire risks from the build-up of chemical vapours. A photograph of this initial setup is shown in Figure 5.4 in which the aluminium cube model (with handling rods installed) and the container in which the naphthalene was melted can be seen.

* Supplied by Fisher Scientific Limited, chemical reference code N/0150/53, assay (GLC) greater than 99%, residue after evaporation less than 0.05%.

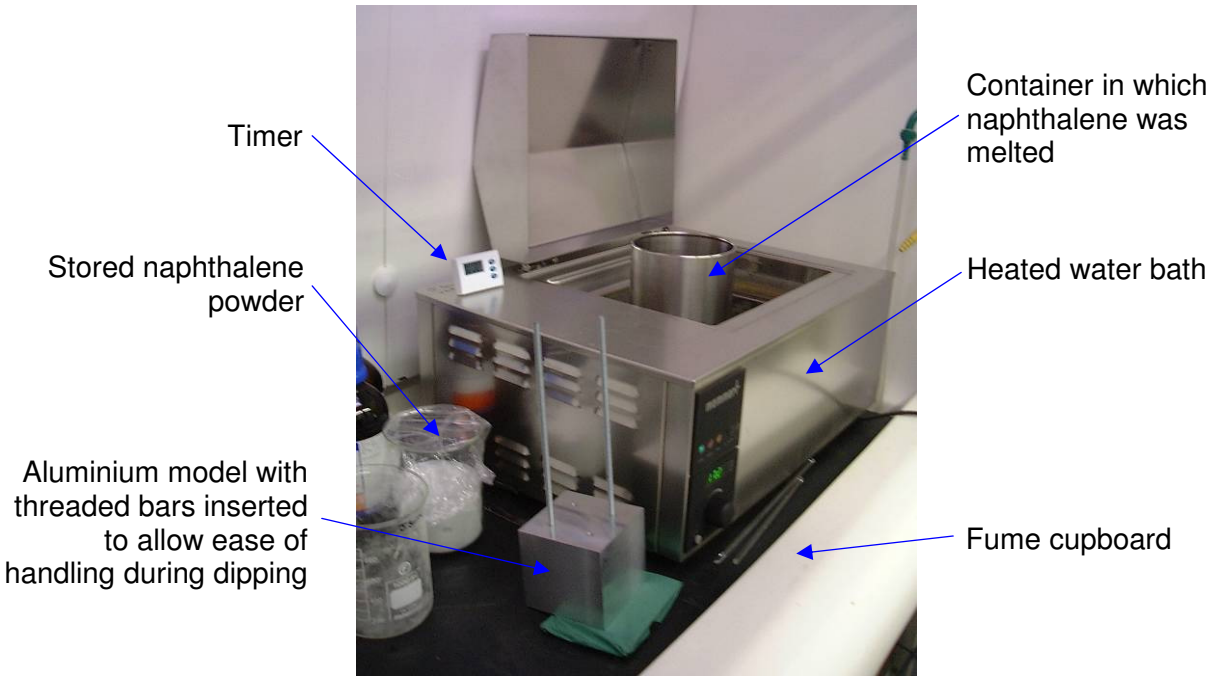

Figure 5.4: The preliminary naphthalene coating setup

An initial attempt at dipping the model directly into the molten naphthalene failed as the solid aluminium cube rapidly cooled the chemical, causing crystallisation and solidification. The result was a particularly rough and lumpy surface coating that was unsuitable for measurement with the Elcometer coating thickness device. The model was therefore cleaned and the coating process reattempted after first submersing the model in the hot water bath for a few minutes to bring its temperature close to that of the naphthalene. By raising the temperature of the aluminium cube, the temperature of the molten naphthalene didn't drop when the model was introduced and therefore it did not recrystallise. The molten naphthalene flowed smoothly around the cube as it was dipped into the container and the desired smooth finish was achieved. However as the cube still retained a considerable amount of latent heat, the newly formed naphthalene coating began to sublimate very quickly. The result was that the coating had completely sublimated from several large areas of the cube by the time it had cooled to room temperature and the areas that were still coated were particularly thin. It was obvious that a compromise between the conflicting requirements of a hot model for smooth coating and a cool model to minimise unwanted sublimation would be required.

In subsequent trials, the aluminium cube was dipped into the hot water bath for approximately 20 seconds prior to coating in order to raise the temperature of its outer surface, but without significantly heating the inner core. The molten naphthalene flowed smoothly around the model giving an even coating finish. Whilst some unwanted sublimation took place initially, the model cooled back to room temperature much more rapidly leaving a suitably thick coating over the whole model.

The freshly coated model was transferred to the BRE boundary layer wind tunnel. Measurements of the coating thickness at each of the 125 predetermined points were made using the Elcometer 456 coating thickness gauge. A standard measurement order was adopted to ensure that subsequent measurements at the same locations would correspond in the resulting data files. All measurements were repeated twice to verify repeatability of readings and allow averages to be taken for greater accuracy. Comparison of these two data sets showed that the depth of sublimation which occurred during the measurement time (typically 2 to 3 minutes) was an order of magnitude smaller than the maximum accuracy of the Elcometer thickness gauge. Extraneous sublimation during this period was therefore shown to have negligible impact upon the results obtained.

The model was then placed at the centre of the wind tunnel turntable and arranged at the centre of a long row of cubes aligned perpendicular to the approaching wind. Similar rows of cubes were also arranged on either side of the model to form a series of street canyons. A wind tunnel speed of 5 m/s was selected for the first trial as this would allow safe entry to the working section to observe the model during the test period. This air speed was measured at 300 mm above the tunnel floor using a Pitot-static tube.

Figure 5.5 shows the thickness of the naphthalene coating averaged over the entire model at various times during this first preliminary experiment. The red line on this plot corresponds to the average sublimation rate during the experiment which was calculated to be 0.23 µm per minute (13.8 µm per hour). The total sublimation depth over the two hour period was 27.6 µm. The rate of sublimation is dependent upon temperature, however the air temperature in the laboratory during this experiment (approximately 18 °C) was representative of that which was expected during subsequent experimental runs. Assuming the worst case errors in the before and after thickness measurements, the greatest potential inaccuracy was 5 µm which corresponded to approximately 18% of the measured sublimation. This was higher than would have been preferred, but was by no means an unacceptable level of error. Consideration was given to increasing the total sublimation depth during subsequent tests by lengthening the run time to 3 or 4 hours.

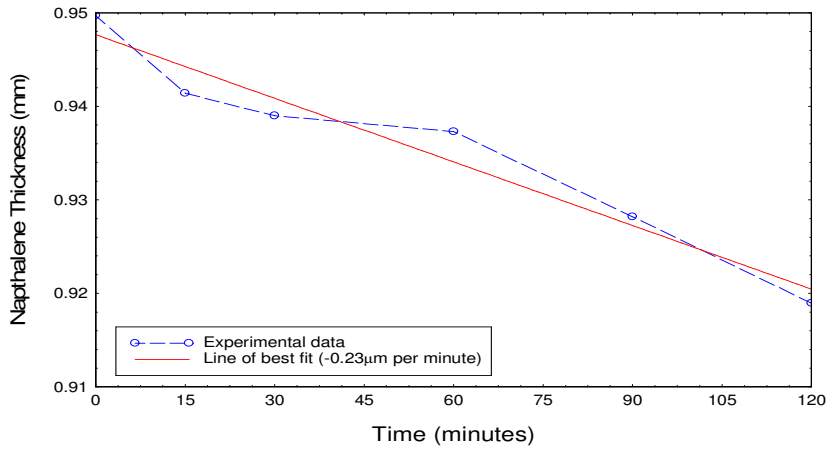

Figure 5.5: Reduction in average naphthalene thickness with time

The measured reductions in coating thickness were also averaged over each of the windward, leeward and roof surfaces in order to provide surface-average values. Additionally, the measurements over the top two rows of measurement locations on the windward and leeward surfaces were averaged in order to provide localised data for the most exposed position of each wall (the so-called 'top-floor' values). These results are presented in Table 5.2 below alongside results for a second test which was conducted at a higher wind tunnel speed of 10 m/s.

Table 5.2: Preliminary surface average heat transfer coefficient data

	CHTC (W/m^2K)	
Location on model	**Slow speed (5 m/s)**	**Fast speed (10 m/s)**
Windward surface	23.4	39.7
Windward surface (top-floor)	32.1	47.2
Roof surface	22.2	32.7
Leeward surface	18.0	35.8
Leeward surface (top-floor)	6.4	18.9

In order to verify the accuracy of this preliminary data, it was compared with existing full-scale experimental data produced in independent studies by Sturrock (1971), Taki and Loveday (1996), Sharples (1984) and Nicol (1977). This comparison is presented in Figure 5.6 with the leeward surface plotted separately from the roof and windward surfaces to aid clarity.

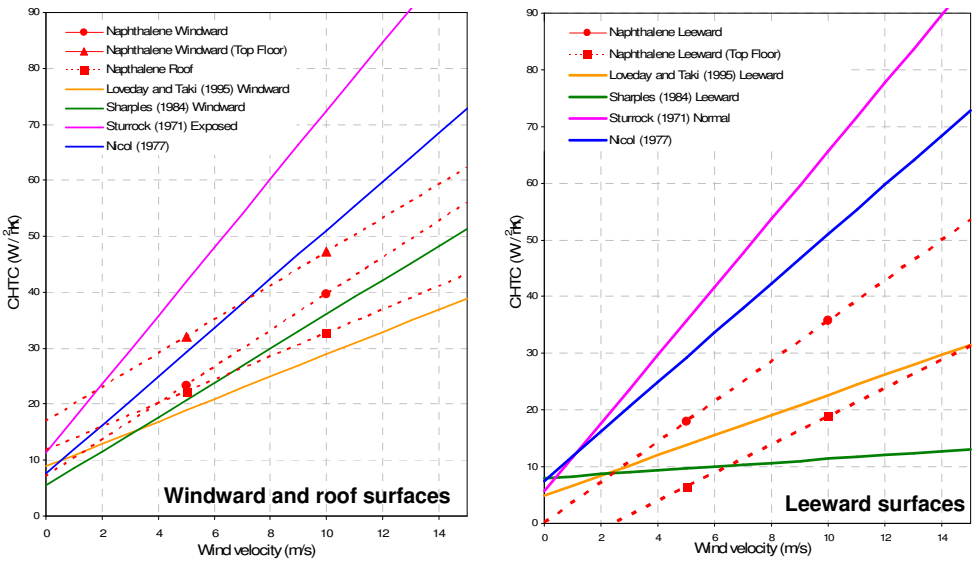

Figure 5.6: Preliminary convective heat transfer coefficients for building surfaces

It can be seen from Figure 5.6 that the preliminary experimental results obtained correlates well with the existing full-scale experimental data. For the windward face in particular, the surface-averaged data lies in the middle of the four full-scale relationships and shows especially good agreement with the data presented by Sharples for windward surfaces. When only the top two rows of measurement points are considered (the so-called 'top-floor' data), the average convective heat transfer coefficient is noticeably higher. In this case, good agreement is seen with the data of Nicol, but the results are still significantly less than those proposed by Sturrock for exposed surfaces. The Sturrock correlation is generally regarded as giving unrealistically high results due to errors with the measurement technique and these first naphthalene sublimation results would seem to support that conclusion. The averaged roof surface data is marginally less than that for the windward face, but also shows good agreement with both the Sharples and Loveday correlations for windward surfaces.

The second plot in Figure 5.6 compares the results obtained for the leeward surface of the cube with existing full-scale experimental correlations by the same researchers. Once more, the surface-averaged result lies at the centre of the four full-scale relationships although there would appear to be larger disagreement at lower (<3 m/s) wind speeds. The 'top floor' data for the leeward face of the cube shows less agreement with the existing data, particularly at low wind speeds. This could be as a result of the geometry of the cube providing particular shelter to this region, or equally a measurement or experimental error for this surface. It could also be due to differences in the heights and locations at which the winds speeds are measured.

The equations of the linear fits through the pairs of data points for the three surfaces have been calculated and are shown in Table 5.3 below. These results can be compared with the convective heat transfer coefficient expression given in BS EN ISO 6946 (BSI, 2007) which is $h_c = 4 + 4v$ (Equation 3.48). It is evident that there is wide variation in the first term of the equation which relates to the free component of convection. The experimental values ranged from a maximum of 17.0 down to 0.2 W/m^{2}K. The significance of this variation was further examined by subsequent experiments. However it is reassuring to note that experimental values for the second term of the equation (relating to the effect of wind speed) are all remarkably close to the value presented in the Standard. In particular, the value for the roof (3.6) is very similar to the stated value (4.0) which may imply that the equations in the Standard are for parallel, rather than impinging flow conditions.

Table 5.3: Experimental convective heat transfer correlations

Location on model	**CHTC (W/m^{2}K)**
Windward surface	$h_c = 17.0 + 3.0v$
Roof surface	$h_c = 0.2 + 3.6v$
Leeward surface	$h_c = 11.7 + 2.1v$

These preliminary correlations were based upon only two measurement points at wind speeds of 5 and 10 m/s and so are prone to inaccuracy. This was especially true for the value of the y-axis intercept which represents the free component of convection. The derived correlations were however indicative of the fact that results obtained using the naphthalene mass-transfer technique are representative of the convective heat-transfer from full-scale building surfaces. This finding provided the required confidence in the technique needed to justify its continued implementation and development.

These preliminary trials also demonstrated other strengths that the developed experimental methodology has over those employed by previous researchers. The measurement of the naphthalene layer using the Elcometer coating thickness gauge meant that the results were not limited to surface averaged values. It was also possible to show the distribution of the convective heat transfer coefficients (CHTC's) across the building by recording thickness measurements over an array of 25 locations on each model surface. Contour plots of the calculated CHTC's are shown in Figure 5.7. These plots represent opened-out nets of the windward, leeward and roof surfaces of the test cube, with the windward surface at the top (as shown in the left-hand diagram).

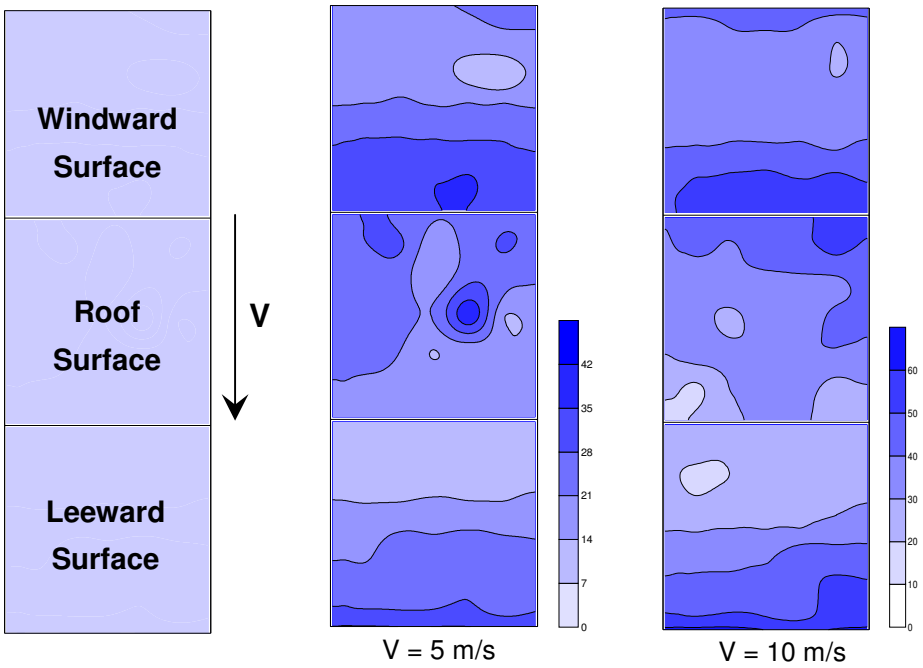

Figure 5.7: CHTC contour plots at wind speeds of 5 and 10 m/s

The plots correspond to two wind speeds over the same cube model and as such, the patterns on the windward and leeward faces are very similar. A region of high convective heat transfer can be seen at the top of the windward face of the cube. The prevailing wind is likely to hit this exposed area of the building and be driven down to form a vortex within the upstream canyon. Some of the flow impinging upon this exposed corner will be driven up and over the cube resulting in the higher CHTC's seen at the windward edge of the roof. As the flow separates over the roof, the convective heat transfer is also seen to diminish.

These preliminary results were presented at the 2004 Wind Engineering Society (WES) conference at Cranfield University. The paper which accompanied this presentation is provided in Annex I of this thesis and was also bound into the conference proceedings (Smith, 2004).

5.3 Improvements to the methodology

Preliminary investigations identified several potential areas of improvement for the naphthalene sublimation technique. Firstly, the high thermal mass of the solid aluminium model made coating via the dipping method difficult. A cold model caused rapid cooling and solidification of the molten naphthalene resulting in an irregular and unsatisfactory coating. In contrast, if the model was heated to the approximate temperature of the molten naphthalene (95 °C) a smooth and uniform coating was achieved but this soon sublimated before the model cooled back to ambient temperature. A compromise was reached by dipping the model in the hot water bath for approximately 20 seconds in order to heat only its outer surfaces. It was also noted that on particularly cold days (the preliminary tests were conducted in January and February), the sublimation rate of the naphthalene would drop which then required run times to be extended to 6 hours or more.

In order to overcome these two issues, a new hollow model was fabricated to replace the original solid aluminium cube. This provided two main benefits: Firstly a significant reduction of the thermal mass of the cube to aid the dipping procedure and secondly, to permit the model to be filled with warmed water. This latter advantage allowed the temperature of the model (and hence of the naphthalene coating) to be controlled and maintained during subsequent tests. The hot water bath previously used for melting the naphthalene featured a digital temperature control system which was able to maintain the required temperature to the nearest tenth of a degree Celsius. This was therefore used as a source of warmed water which was circulated through the model using a submersible electric pump.

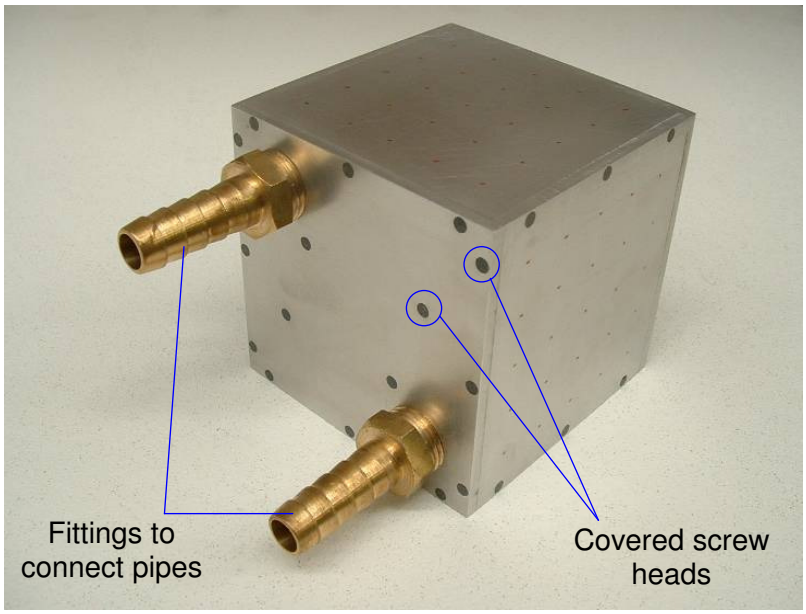

Figure 5.8: Revised hollow wind tunnel model design showing hose connections

The new wind tunnel model was fabricated using 4 mm aluminium plate. The six component faces were screwed together for strength and then the screw holes filled with a high aluminium content filler to smooth the surface and prevent 'cold-spots' over the screw heads. A narrow bead of the same filler was also applied to the internal vertices to seal the cube. A photograph of the hollow cube model is shown in Figure 5.8. The dark spots on the cubes surface are where screw holes have been filled and the two brass hose-tails were fitted into the base for connection of the water pipes.

In order to ensure that an even circulation of heated water was achieved throughout the entire inside area of the model (necessary for uniform heating), internal 'walls' were installed into the cube. These were constructed from the same 4mm aluminium plate and were designed to guide the water in a zigzag pattern from inlet to outlet. Without them, water flow would have favoured the shortest path leaving 'dead-spots' in the opposite corners. The two internal walls were screwed to the base of the model and positioned to divide the model into approximate thirds, as shown in the schematic plan view diagram of Figure 5.9. Gaps were left between the walls and the outer surfaces of the model (except the base) so that the entire internal surface would be in direct contact with the heated water. The walls were also staggered in order to guide the majority of the water flow around the zigzag path indicated in by the arrows in the diagram. However smaller amounts of water were still able to flow through the gaps between the inner and outer walls and roof. In this way the entire cube was heated equally by the circulating water.

The first submersible garden pond pump that was used to circulate the water from the bath to the model had a maximum head rating of 2 m. However, the constrictions of the pipes and fittings reduced this so that the pump was barely able to raise the water the approximate 1 m to reach and fill the wind tunnel model. This raised concern that there might be air left inside the upper corners of the model which would result in an uneven surface temperature distribution. Therefore a significantly larger 'Clarke CSE1' submersible unit was installed in its place which featured a 135 litre per minute maximum flow rate and 7 metre maximum head. This pump circulated the water through the model much more quickly and with greater force, and it was noted that all of the trapped air was rapidly flushed out of the model.

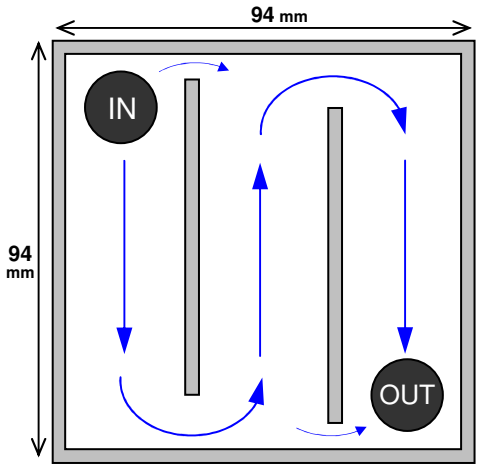

Figure 5.9: Plan view of hollow model showing inner walls and water flow path

With the hot water bath now located under the wind tunnel to supply warmed water to the model, it was necessary to find another means by which to melt the naphthalene for the dipping operation. Naked flames had to be avoided because of the inflammability of the naphthalene and its vapour. Instead, a 1500/1200 Watt dual electric hotplate was purchased. This allowed the naphthalene to be heated more quickly than by the water bath (reducing preparation time) and to a higher temperature resulting in less crystallisation when the model was dipped.

For the preliminary tests, the original solid aluminium cube had been marked with a five-by-five grid on each of the five active surfaces. It was found that the red marks were (surprisingly) the most visible through the naphthalene coating. This colour was therefore selected for all subsequent marking up of the model. However, drawing the grids on each face ready for each test was proving time consuming and the amount of ink used was contaminating the naphthalene preventing reuse. Instead, the grid was lightly marked onto the surfaces using a sharp scriber and then small dots marked with the red pen at the intersections to denote the measurement locations. Figure 5.10 shows the hollow cube model coated with naphthalene; the array of red dots on each face is clearly visible.

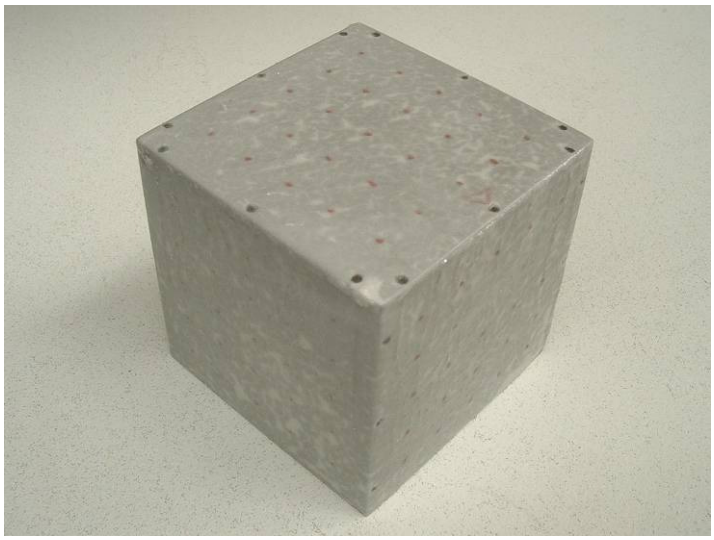

Figure 5.10: Coated model showing red measurement point markers

It was also noted that minor imperfections in the naphthalene coating were smoothed after a short duration in the wind tunnel. Accordingly, a ‘conditioning period’ of around 15 minutes was incorporated at the beginning of the wind tunnel tests before the initial thickness measurements were recorded.

At higher wind tunnel speeds, it was found that the wind loading on the models (especially the upstream canyon models) caused them to slide and rotate across the working section during the tests. The galvanised steel floor of the wind tunnel allowed this to be overcome without affecting the model geometry by the use of small but powerful magnets. These were placed on the ground immediately behind the upwind models and were able to resist the wind-induced movement. Other more permanent fixing types such as glue or tape were not appropriate due to the damage caused to the models during removal; it was important to preserve their condition for later tests.

Sublimation from the model prior to testing was minimised by keeping the model in an airtight container until the point of testing. Initially, this was achieved using cling film which was wrapped tightly around the cube. However it was found that the coating was often damaged (especially at the corners) during removal and so sealable plastic food bags were employed instead. An unexpected result of having the model less tightly wrapped was that the smoothness of the surface coating was found to improve over time. It appeared that the naphthalene from imperfections (such as runs or dimples) sublimates more quickly than the 'flat' surfaces and so the small amount of air left inside the bag soon becomes saturated with naphthalene vapour. Consequently very little sublimation from the flat surfaces was found to occur during storage and any imperfections from the dipping became smoothed out.

Extraneous sublimation prior to testing was further reduced by storing the models in a small freezer at approximately -5 to -10 °C between coating and testing. The vapour pressure of naphthalene is highly dependent upon temperature (see Section 4.2) and hence reducing the temperature to this level greatly reduced the sublimation rate. In preliminary tests, the chilled model was installed straight into the wind tunnel. When the warmed water was introduced to the hollow model, it was found that the inner layer of naphthalene melted resulting in the remaining coating falling from the model in large 'sheets'. This made the model unusable and led to the abandonment of several early tests. It was therefore necessary to remove the model from the freezer approximately one hour before testing and allow it and its naphthalene coating (still sealed in the storage bag) to gradually warm to room temperature.

In warmer weather, it was noted that the temperature of the water in the bath would occasionally rise above the preset limit even when the digital temperature control unit had not turned the heater element on. This was attributed to the heat input from the water pump and the problem was ameliorated by installing a desk fan blowing over the water bath in order to increase the rate of heat loss. In this way, the temperature could be more accurately regulated by the water bath controls and hence the precise temperature required was maintained.

5.4 Summary of experimental methodology

The naphthalene sublimation methodology which was developed during the course of the preliminary trials featured a number of significant improvements and refinements. A summary of the specific procedures employed for the main series of naphthalene sublimation experiments is given in the following paragraphs. The basic stages of the experiment are also shown in flowchart form in Figure 5.16. However, a full step-by-step account of the developed experimental procedure is described in Annex A of this thesis. It was this experimental methodology which was used to derive the convective heat transfer relationships detailed later in this thesis.

A series of three identical hollow aluminium cube models were fabricated for the main series of experiments in order that several experiments could be run consecutively. The uncoated models are shown in Figure 5.11 alongside an example of a coated model (note the red measurement locations dots visible through the coating). The models were coated by dipping into a molten tin of naphthalene heated on an electric hotplate in a fume cupboard, as shown in Figure 5.12. After coating, the models were cooled with cold water, carefully dried and then sealed in plastic bags. They were then stored in a freezer for approximately 24 hours prior to testing, being brought out to slowly warm to room temperature one hour prior to installation in the wind tunnel.

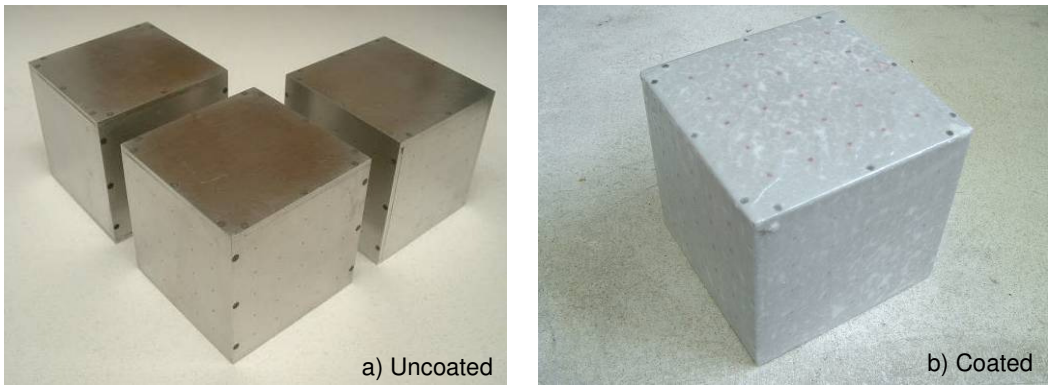

Figure 5.11: The wind tunnel models prior to and after coating with naphthalene

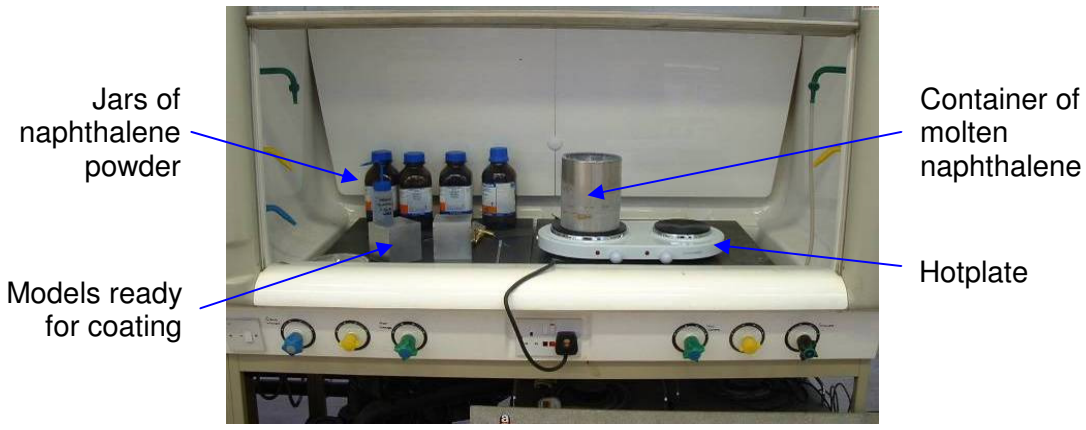

Figure 5.12: Preparations for dip coating the models in a fume cupboard

Immediately prior to testing, the naphthalene coated model was removed from its plastic bag and attached to its baseboard before being fitted into the wind tunnel turntable. Hoses were then fitted to the underside of the model to connect this to a submersible pump immersed in a heated water bath. In this way, water at a fixed temperature of 40 °C was circulated through the model and back into the water bath. A desk fan was positioned to blow air over the water bath to remove excess heat. Without this it had been found that the temperature of the bath would occasionally rise above the required 40 °C as a result of additional uncontrolled heat input from the submerged pump unit. With the fan in place, the water baths temperature controller was more able to accurately regulate the temperature. Photographs of this setup beneath the wind tunnel working section are shown in Figure 5.13 and Figure 5.14 below.

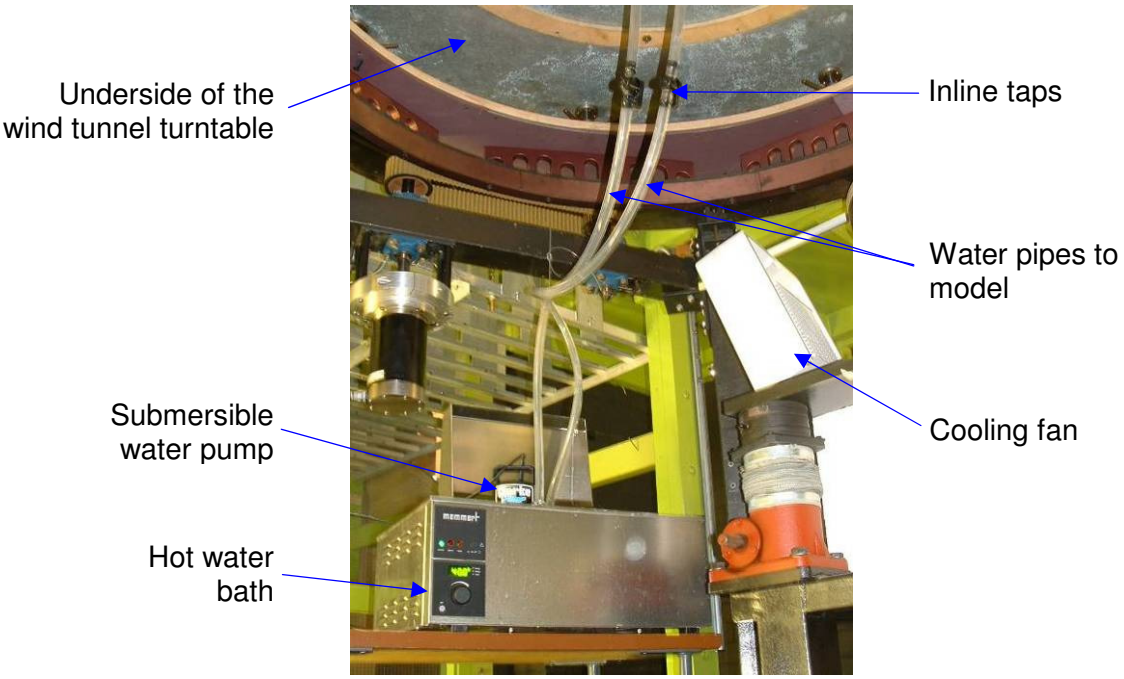

Figure 5.13: Hot-water bath, pump and underside of the model

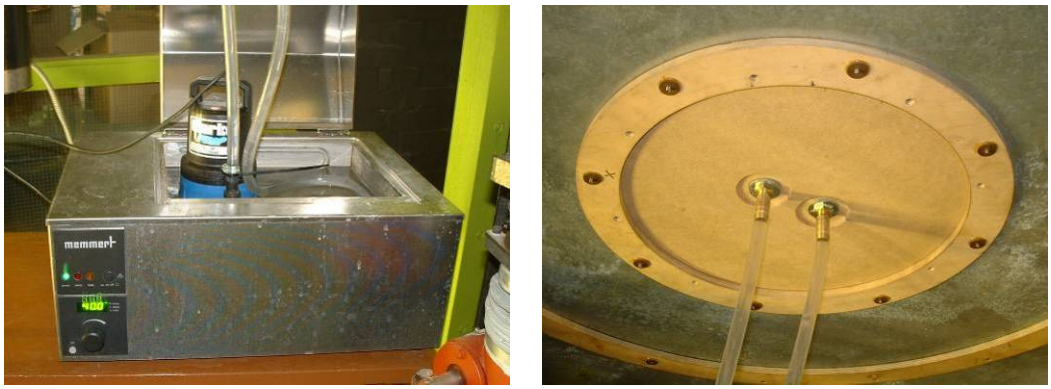

Figure 5.14: Detail of the water bath, pump and hose connections to the model

With the naphthalene coated model installed and connected, the surrounding models were then arranged at the required street canyon geometry, spacing and approaching wind angle. Measurements were then made of the coating thicknesses of each of the exposed model surfaces using the Elcometer 456 device described in Section 5.1.1. A total of 25 measurements were made across each surface in a standardised order, and this procedure repeated twice to allow later cross-checking and averaging where necessary. Figure 5.15 shows photographs of the model installed at the centre of the turntable and during the initial coating thickness measurements.

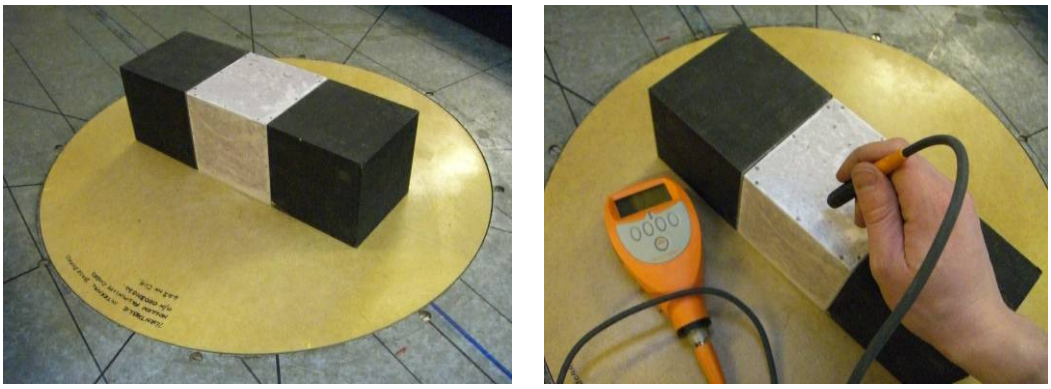

Figure 5.15: The coated model in the wind tunnel and during measurements

The wind tunnel was then started and the speed increased to the required setting, at which point a time was started. The laboratory conditions (i.e. air temperature, atmospheric pressure and relative humidity) were recorded and monitored through the test. The typical test duration was two to three hours, except for low wind speeds runs where the duration was extended to four hours, or high speed runs where it was sometimes reduced to one hour. The model was continually monitored during this time to ensure that the sublimation depth was maximised but without completion sublimation occurring at any locations. At the end of the test, the wind tunnel was stopped and the measurement procedure repeated in order to determine the final coating thickness.

Before processing the data obtained, the two sets of readings (start and end measurements) were inspected to ensure that the two repeat measurements were consistent. Any anomalies found were removed at this stage by ignoring the erroneous measurement and using only the other reading, otherwise both readings were averaged. Processing of the verified data was then conducted using a custom spreadsheet based program. The change in coating thickness is determined by subtraction of each final measurement from its initial equivalent. The spreadsheet thereby calculated the convective heat transfer at each location, as well as several surface averages, using the mass – heat transfer analogy described previously in Section 4.4. The appropriate chemical properties and coefficients were automatically determined by the spreadsheet based upon the recorded laboratory conditions during each experiment.

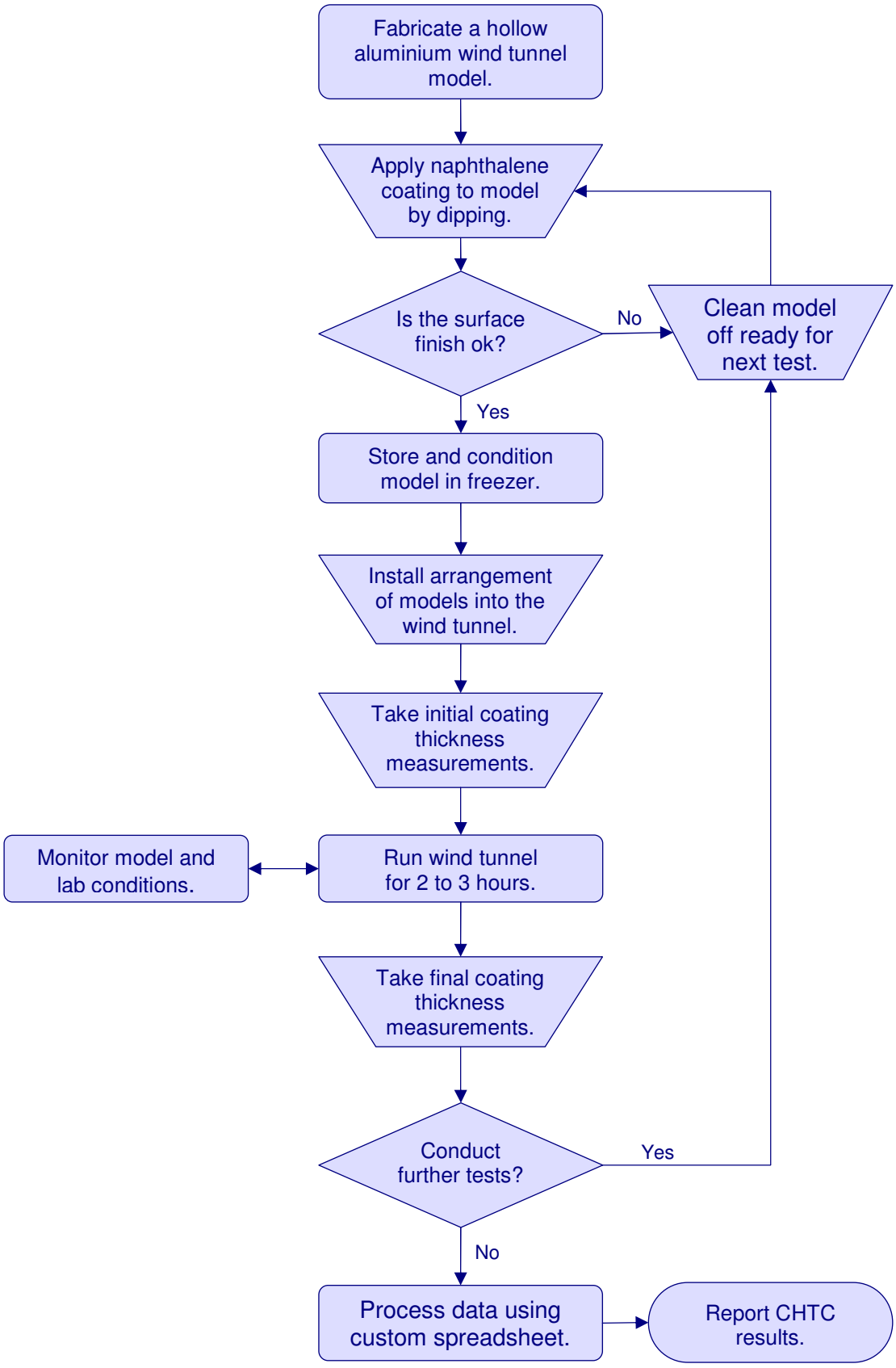

Figure 5.16: Simplified naphthalene sublimation methodology flowchart

Chapter 6 Development of a wind tunnel simulation

6.1 The BRE boundary layer wind tunnel

The BRE boundary layer wind tunnel was constructed in 1992 as an upgrade to previous facilities and is one of two wind tunnels currently in operation (the other being a low speed tunnel predominantly used for dispersion modelling). Air flow is provided by an electrically driven centrifugal fan which forces air through and along the 1.5 m high by 2.0 m wide tunnel. The building itself forms the return path of what is basically a closed-loop system. The wind tunnel is capable of achieving outlet speeds of up to 50 m/s for full-scale testing of roofing products when the flow conditioning devices are removed and a nozzle fitted at the outlet to reduce the cross-sectional area. However, model scale testing is typically limited to around 20 m/s by the practicalities of such tests. A photograph of a $1/17^{th}$ scale model of the facility (used to calibrate the wind tunnel design before construction) is shown in Figure 6.1 below. Air is forced from left to right through the tunnel by the fan.

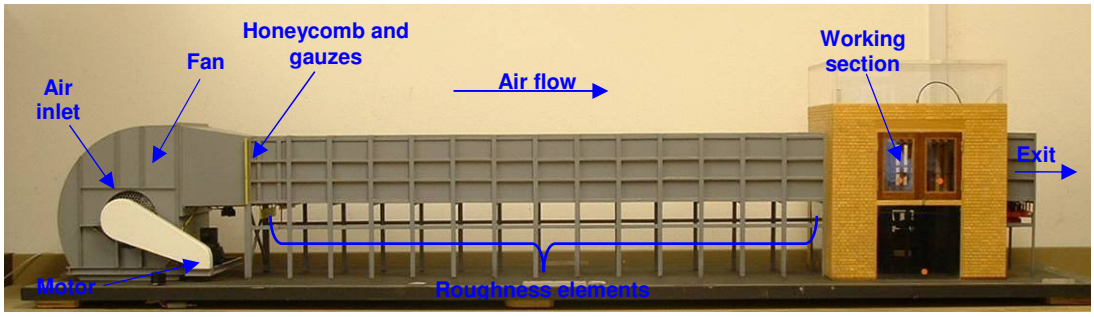

Figure 6.1: A $^{1}/_{17}{}^{th}$ scale model of the BRE boundary layer wind tunnel

After entering the wind tunnel through the fan, the air stream first encounters a series of two fine gauzes. These smooth the airflow across the cross sectional area of the tunnel and remove local irregularities resulting from the fan. A honeycomb section further smoothes the air stream before it enters the main upwind fetch of the tunnel.

A velocity boundary layer is grown over the upwind stretch using techniques developed by Cook (1973). His method of simulating only the lower third of the urban atmospheric boundary layer helps to meet the conflicting requirements of wind tunnel size and model scale. In this way, larger scale models can be tested within (relatively) small facilities allowing more detailed results to be obtained. The BRE wind tunnel employs a 14 metre long upstream array of roughness elements to generate the atmospheric boundary layer. The roughness elements are in the form of staggered arrays of flat plates arranged in 14 groups along the length of the wind tunnel. Each group consists of 60 plates and may be independently adjusted in height so that a variety of simulations (from open sea to dense urban) at a range of model scales may be generated.

Growth of the required boundary layer using surface roughness alone would require an unfeasibly long upwind fetch. Instead, the BRE wind tunnel uses a triangular castellated wall before the roughness elements to create a momentum deficit at ground level and hence jump-start boundary layer growth. This technique allows the wind tunnel to be much shorter than would otherwise be required. A wooden grid is also used to help generate the required large-scale turbulence within the flow. The yellow grid, red fence and silver roughness plates can clearly be seen in Figure 6.2.

This method yields a good approximation of the mean flow and turbulence characteristics in both scale and intensity. Comparison of such a simulation with full scale data shows good agreement and hence variants of this technique are employed in both BRE wind tunnels. Provided that the wind is fully turbulent (which occurs at wind tunnel speeds above about 1 m/s), the wind tunnel can be run at any nominal speed setting.

The two metre working section features a computer controlled turntable and overhead 3-axis traverse system. The top and sides of the working section are formed by removable aerofoil slats which provide tolerance to blockages. This allows larger models to be tested by maintaining streamlined flow in the working section, whilst at the same time allowing the pressure to vent into the outer plenum chamber.

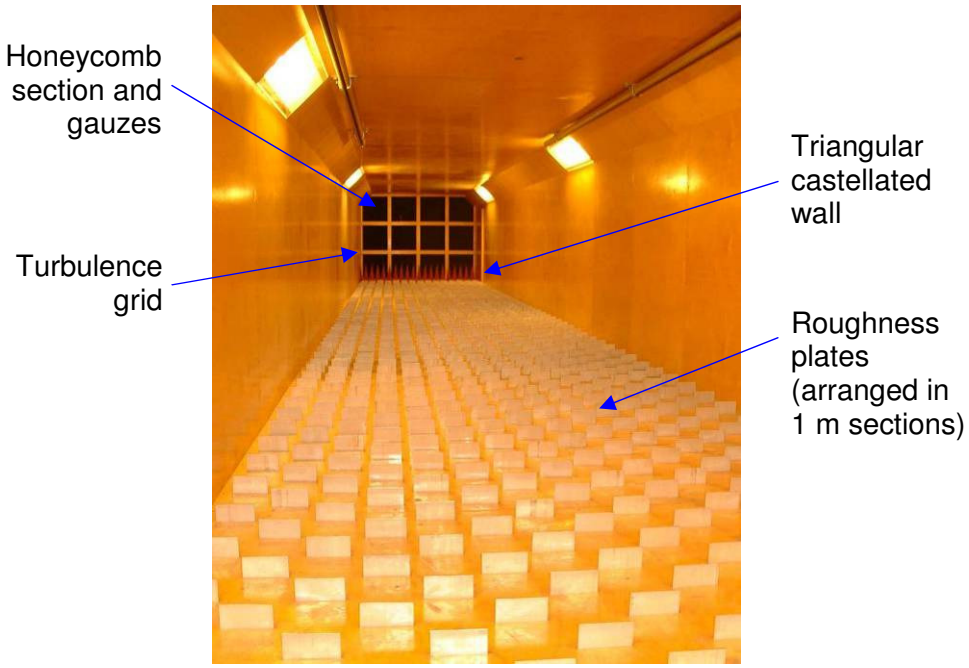

Figure 6.2: The upwind fetch of the BRE boundary layer wind tunnel

There are three important aspects of the atmospheric boundary layer which are simulated for wind tunnel experimentation. These are the:

- Vertical in-wind mean velocity profile
- Turbulence intensity profile
- Turbulence integral length

These criteria are discussed in the following sections.

6.2 Vertical mean velocity profile

A vertical traverse of the BRE wind tunnel was made using a *constant temperature anemometry* (CTA) probe. Samples were taken at a rate of 200 Hz and the signal fed via a 100 Hz low-pass filter to a computer running custom BRE data logging software. A diagram of the Dantec CTA probes used is given in Figure 6.3 and further details are provided in Annex H.

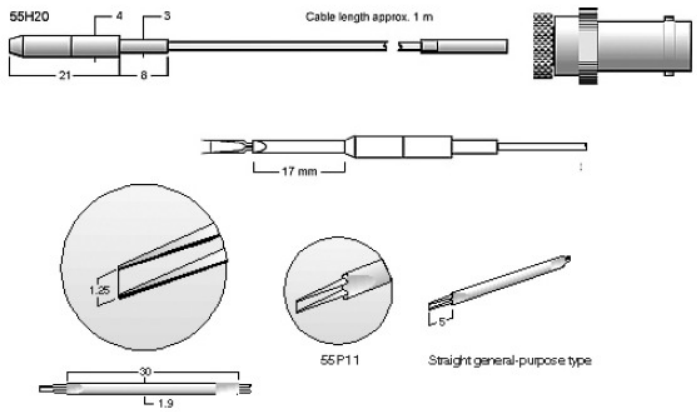

Figure 6.3: Dantec 55P11 CTA probe and 55H20 probe holder
(source: Dantec Dynamics Limited, 2006)

The traverse was made at a location in the centre of the wind tunnel 300 mm downstream from the final row of roughness elements. The vertical mean velocity data is recorded in Table 6.1 below and the profile is plotted in Figure 6.4. It can be seen that the velocity (V) increases with height (z) above the tunnel floor to a maximum value above which the velocity begins to decrease. This is as a result of the boundary layer which has grown along the roof of the wind tunnel. Similar boundary layers also exist along the sides of the tunnel and therefore measurements near to the edge of the turntable should be avoided.

Table 6.1: Wind tunnel velocity profile data

Height z (mm)	Velocity V (m/s)	Height z (mm)	Velocity V (m/s)
0	0	300	5.34
5	1.98	400	5.80
10	2.08	500	6.16
15	2.19	600	6.48
40	2.55	700	6.68
60	2.81	800	6.79
80	3.13	900	6.84
100	3.44	1000	6.85
150	4.14	1200	6.78
200	4.66	1400	5.93

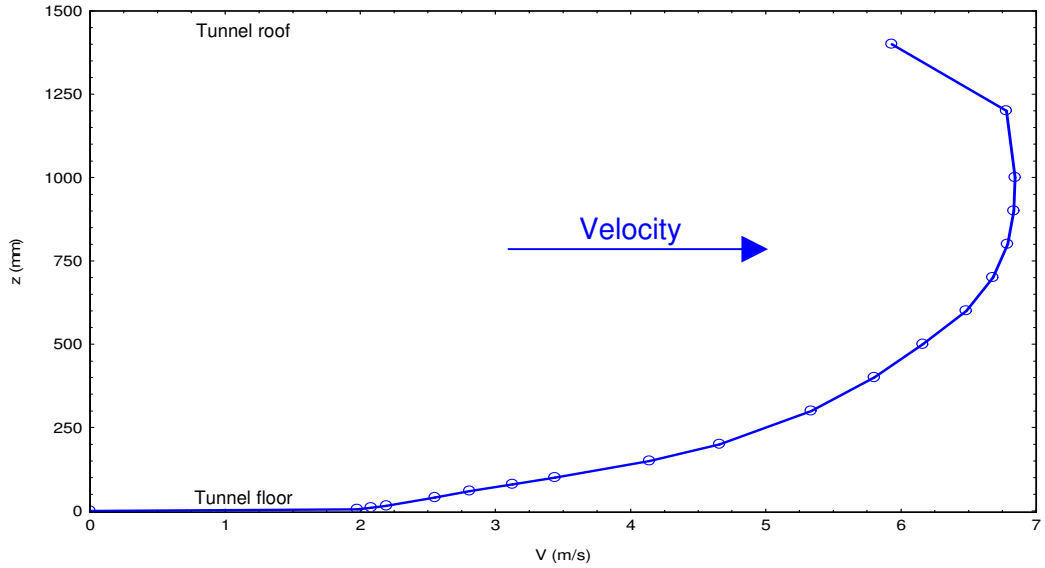

Figure 6.4: The horizontal velocity profile in BRE wind tunnel

The maximum mean horizontal velocity of the flow has been seen to occur at a height of approximately 1000 mm. This maximum measured horizontal mean wind speed is therefore taken to be the reference wind speed (V_{ref}) and the measured velocities may be non-dimensionalised by dividing through by this value. The height of 1000 mm is also taken to be the reference height (z_{ref}) and data above this point will be ignored.

A simple empirical model for representing atmospheric boundary layers is referred to as the log-law model and takes the following form:

$$V = \frac{u_*}{\kappa} \ln\left(\frac{z-d}{z_0}\right) \qquad \text{(Eq. 6.1)}$$

where: u_* = Friction velocity
κ = Von Kármán constant
d = zero plane displacement
z_0 = aerodynamic roughness length

The Von Kármán constant (κ) has a value of 0.40 and therefore the equation is more commonly written as:

$$V = 2.5u_* \ln\left(\frac{z-d}{z_0}\right) \qquad \text{(Eq. 6.2)}$$

The normalised velocity profile measurements (i.e. V / V_{ref}) from the wind tunnel are plotted in Figure 6.5 below. A curve in the form of Equation 6.2 has been fitted to the linear portion of the experimental data and is presented as the dotted red line. Values for the three unknown quantities are therefore obtained from the equation of this curve as u_*/V_{ref} = 0.0954, d = 4.15 mm and z_0 = 11.4 mm. Multiplication by the reference velocity (V_{ref}) provides the friction velocity (u_*) as 0.653.

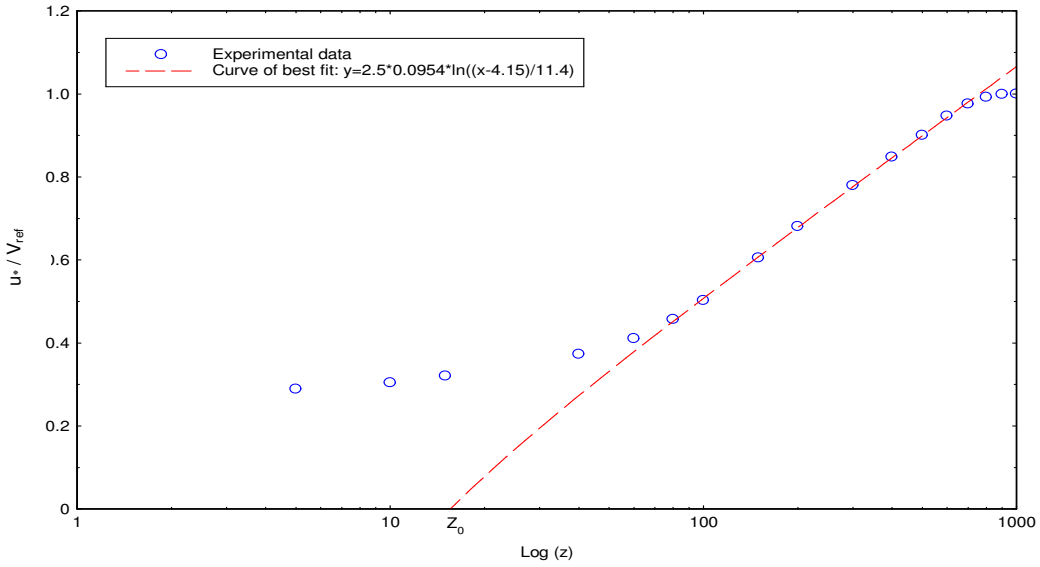

Figure 6.5: Log-law fit to wind tunnel velocity profile

Table 6.2 shows the range of values for the surface roughness parameter (z_0) and zero plane displacement (d) appropriate to various terrain types, as detailed in the ESDU data sheets (ESDU International, 2002).

Table 6.2: Approximate values of z_0 and d for various terrain types (source: ESDU International, 2002)

Description of terrain upwind of site	**z_0 (m)**	**d (m)**
Centres of large towns and cities, forests	1.2 - 0.7	25 - 15
Centres of small towns	0.7 - 0.5	10 - 5
Fairly level wooded country	0.5 - 0.4	10 - 5
Suburbs	0.4 - 0.3	10 - 5
Many trees and hedges, few buildings	0.3 - 0.1	10 - 5
Farmland, long grass	10^{-1} - 10^{-2}	2 - 0
Large expanses of water	10^{-2} - 10^{-4}	0

The value of the roughness length (z_0) obtained from the boundary layer profile measurements was 11.4 mm. Assuming a model scale of 1:100, this gives a full-scale value of 1.14 metres. From the Table 6.2 it can be seen that this corresponds to the value expected at the centres of large towns and cities. Similarly, the value of the zero plane displacement (d) scales to 0.42 metres which typically represents open farmland or long grass conditions. In subsequent tests additional cubes were arranged around the primary model to simulate surrounding buildings. The local zero plane displacement is raised as a result. Depending upon the spacing of the 100 mm models, this was expected to be in the range of 50 to 100 mm (5 to 10 metres full-scale) which corresponds to conditions typical of small towns. Therefore the atmospheric boundary layer simulation generated in the BRE wind tunnel was appropriate for low-rise, urban areas.

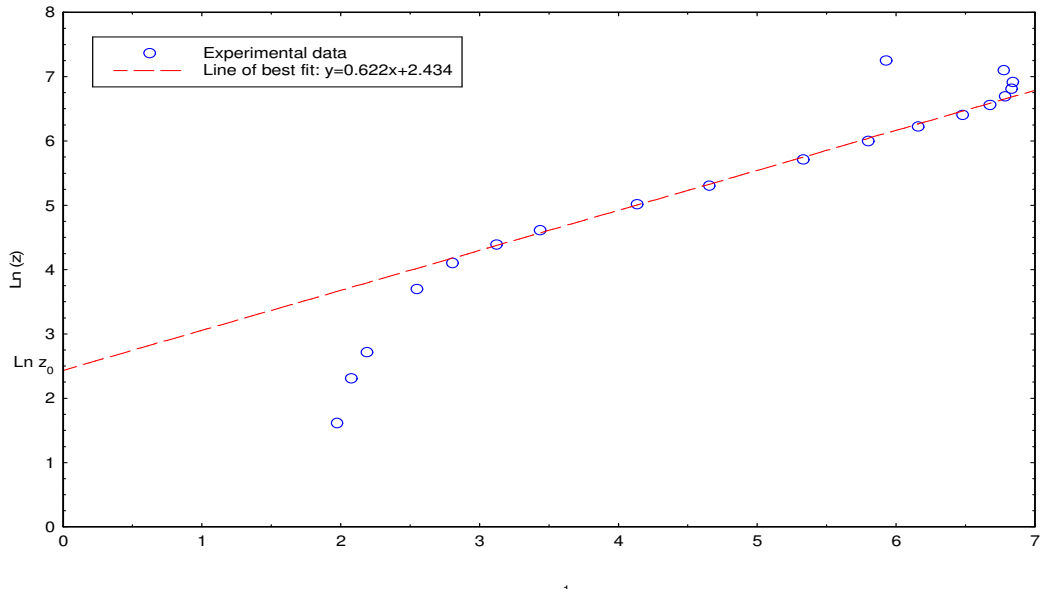

Figure 6.6: The velocity profile plotted against a logarithmic axis

An alternative presentation of the measured velocity profile data is shown in Figure 6.6, with velocity (V) plotted against natural log of height (z). If the zero plane displacement is neglected, Equation 7.2 may be rearranged into the following form:

$$\ln z = \frac{1}{2.5u_*} V + \ln z_0 \qquad \text{(Eq. 6.3)}$$

By comparison of this form of the log-law model with the equation of the line of best fit shown in Figure 6.6 it can be seen that natural log of z_0 equals 2.434, and hence z_0 itself equals 11.4 mm as previously. Similarly, the reciprocal of $2.5u_*$ equals 0.622 and hence the friction velocity (u_*) is calculated to be 0.643. The small variation from the previously obtained value of 0.653 is likely to be as a result of errors in the fitting of the respective curves.

As a result of these measurements it was confirmed that the mean velocity profile simulated in the wind tunnel was an accurate representation of the profile for large town or city terrain at a scale of 1:100. Using this knowledge of the mean velocity profile, the velocity at any given height through the boundary layer may be calculated based upon a single velocity measurement at a different known height. From Equation 7.2, it was possible to determine an equation for the velocity ratio (V/V_{ref}) as a function of only the heights (z and z_{ref}) and the roughness length (z_0). This is given as Equation 6.4 below.

$$\frac{V}{V_{ref}} = \frac{\ln z - \ln z_0}{\ln z_{ref} - \ln z_0} \qquad \text{(Eq. 6.4)}$$

For the boundary layer simulation measured, the roughness length (z_0) is known to be 11.4 mm and the equation can therefore be further simplified to the form shown in Equation 6.5.

$$\frac{V}{V_{ref}} = \frac{\ln z - 2.434}{\ln z_{ref} - 2.434} \qquad \text{(Eq. 6.5)}$$

Figure 6.7 shows a plot of the velocity scaling factors for heights within the wind tunnel boundary layer with respect to a reference velocity reading taken at 900 mm. This particular height was selected as the reference as it was a more convenient position for the CTA velocity probe using a simple retort stand arrangement. To position a velocity probe at a reference height of 1000mm (the height of maximum wind velocity in the BRE wind tunnel, see Figure 6.4) would have required use of the overhead traverse system which was less convenient. Multiplication of the measured reference velocity by these factors gives the wind velocity at the respective height. This relationship was employed in latter experiments where it was necessary to convert from reference velocities taken at practical locations in the wind tunnel, to local velocities at or near the building height.

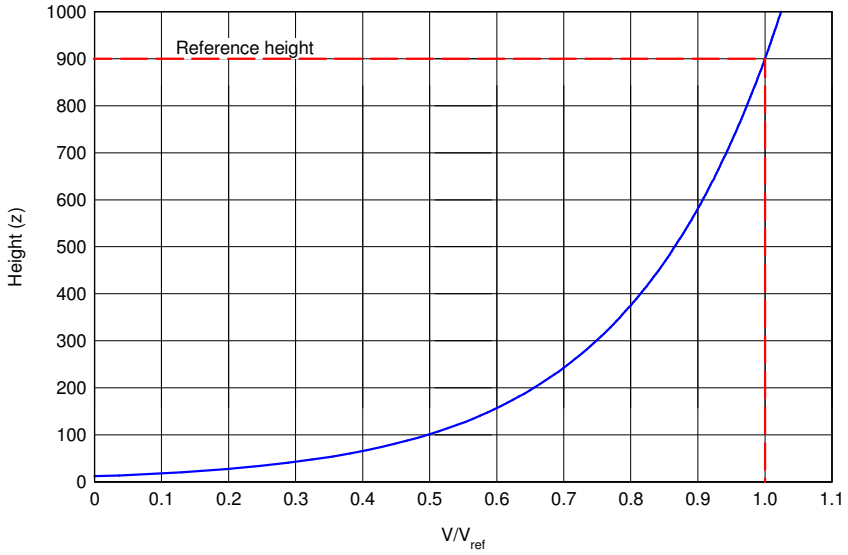

Figure 6.7: Velocity scaling factors with respect to the reference velocity

6.3 The development of the boundary layer

The boundary layer simulation technique proposed by Cook (1973) employs a castellated wall at the start of the wind tunnel to jump-start boundary layer growth. Whilst this allows wind tunnels to be shorter than would be otherwise required, it raises concerns that the boundary layer may not be fully developed (i.e. stable) by the time it reaches the working section. If it was found that the boundary layer varied across the measurement area, it may mean that results might vary depending upon the location of the model. The change from 50 mm roughness plates to 94 mm upwind buildings will also result in the formation of a secondary, deeper boundary layer. Such effects may confuse any results obtained.

In order to asses the effect of these factors, velocity profile measurements were made at a number of locations across the wind tunnel working section using a constant temperature anemometry (CTA) probe. Seven rows of cubes were arranged on the turntable perpendicular to the flow, to form a series of street canyons with a row spacing equal to the model height. The model layout and the measurement locations (labelled A to G) are shown in Figure 6.8 where wind flow is from left to right. The primary location was in the street canyon immediately upstream of the central test cube shown in white in the diagram (i.e. the location where the naphthalene coated model would be placed). Boundary layer profiles were also made in two canyons further upstream and two canyons downstream of this point. Further measurements were made both within and immediately after the roughness elements so that any variation between the primary and secondary boundary layers could be identified. All boundary layer profiles were taken along the centreline of the wind tunnel.

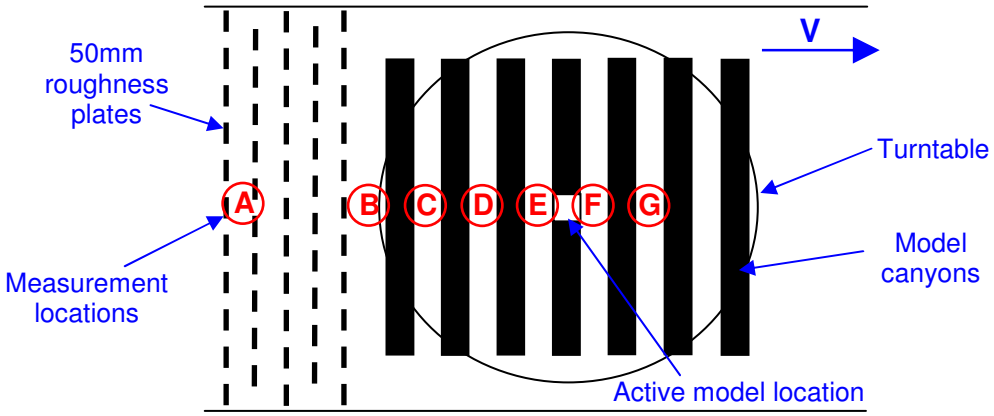

Figure 6.8: Plan view diagram showing profile measurement locations

The mean velocity data from the seven boundary layer profiles are provided in Table 6.3 and are plotted in Figure 6.9. It can be seen that there is little variation between the velocity profiles across any of the five street canyons. However, the profiles measured within and immediately following the roughness elements (the orange and green lines respectively) are noticeably shallower near to the ground than those within the canyons. This was to be expected due to the variation in roughness height between the 50 mm roughness elements and 94 mm models. Any variation rapidly decreases with height, and at a height of 900 mm all of the profiles have reached the free stream velocity.

Table 6.3: Velocity profile measurements at locations across the wind tunnel working section

	Wind velocity (m/s) at measurement locations						
Height (mm)	**A**	**B**	**C**	**D**	**E**	**F**	**G**
5	0.637	0.686	0.447	0.438	0.439	0.326	0.450
50	1.122	1.465	0.599	0.574	0.603	0.652	0.732
100	3.486	2.814	2.087	2.124	2.063	1.974	1.869
150	4.017	3.568	3.769	3.434	3.006	3.214	3.091
200	4.407	4.325	4.542	4.081	4.270	4.001	3.526
300	5.003	5.162	5.036	4.810	5.007	4.911	5.123
600	6.299	6.313	6.358	6.282	6.168	6.201	6.418
900	6.863	6.858	6.839	6.858	6.863	6.878	6.897

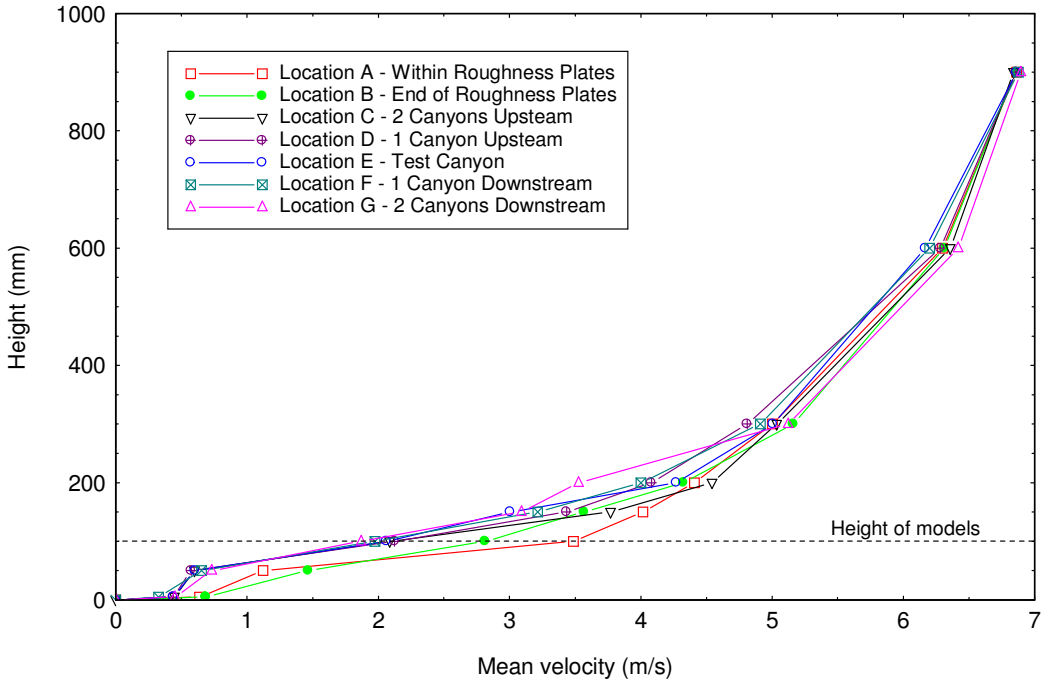

Figure 6.9: Development of the boundary layer along the wind tunnel test

Several conclusions may be drawn from these results. Firstly, as predicted, the growth of a secondary boundary layer is initiated by the rows of model street canyons. The variation of this boundary layer along the length of the working section is small and so unlikely to affect measurements. However, this confirms the suggestion that it is necessary to model a number of canyons both up and downstream of the model in order to obtain the correct, equilibrium flow regime at the location of the active model.

6.4 The effect of wind tunnel velocity

One of the fundamental premises on which wind tunnel modelling is based is that the shape of the velocity profiles is independent of velocity. This means that measurements taken in a wind tunnel at any velocity may be scaled up to full-scale results at another velocity. The benefit of this is that a tunnel speed may be selected based solely upon practical considerations of the equipment used.

In order to verify this assumption for the current simulation, velocity profile measurements were obtained at a number of wind tunnel running speeds. The data obtained is provided in Table 6.4 below and the profiles are plotted in Figure 6.10. The wind tunnel speed is noted as a percentage of full running speed.

Table 6.4: Wind tunnel velocity profile data (in m/s) at various running speeds

	Wind velocity (m/s) at various tunnel settings				
Height (mm)	**10%**	**20%**	**30%**	**40%**	**50%**
5	0.075	0.439	0.786	1.291	1.841
50	0.212	0.603	1.027	1.480	2.097
100	0.799	2.063	3.207	4.239	5.016
150	1.551	3.006	4.856	6.465	8.600
200	1.960	4.270	6.032	7.423	10.055
300	2.209	5.007	6.889	9.083	12.740
600	3.142	6.168	9.179	11.723	16.020
900	3.463	6.863	9.969	12.665	17.409

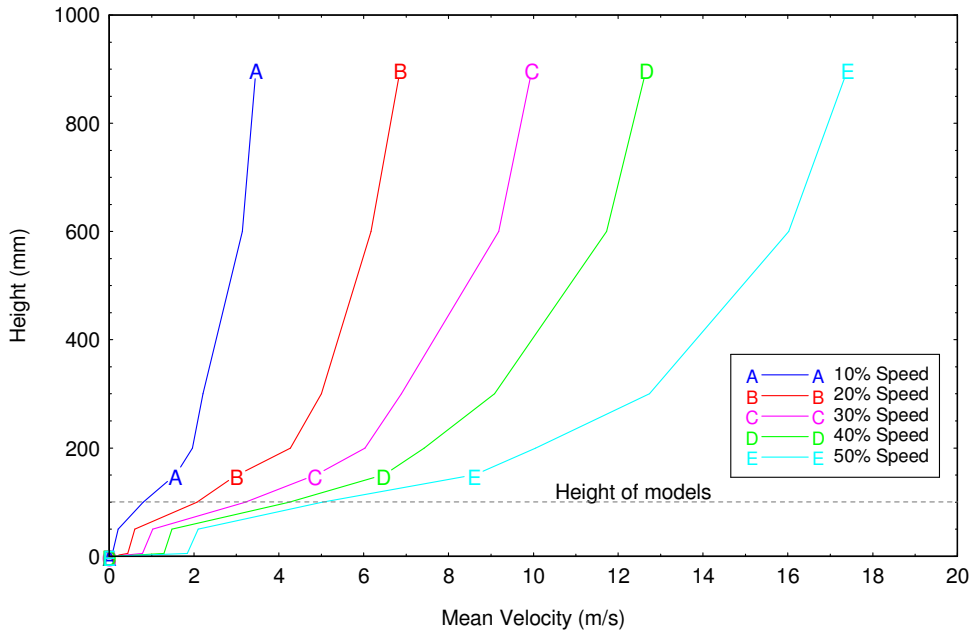

Figure 6.10: Wind tunnel velocity profiles at various speed settings

Two clear regions of these boundary layers can clearly be identified; that above the models where free-stream velocities vary from 3.5 to 17.4 m/s and that within the street canyons where variations are more restricted. By dividing each measurement by the free-stream velocity for that tunnel speed, velocity profile ratios may be obtained.

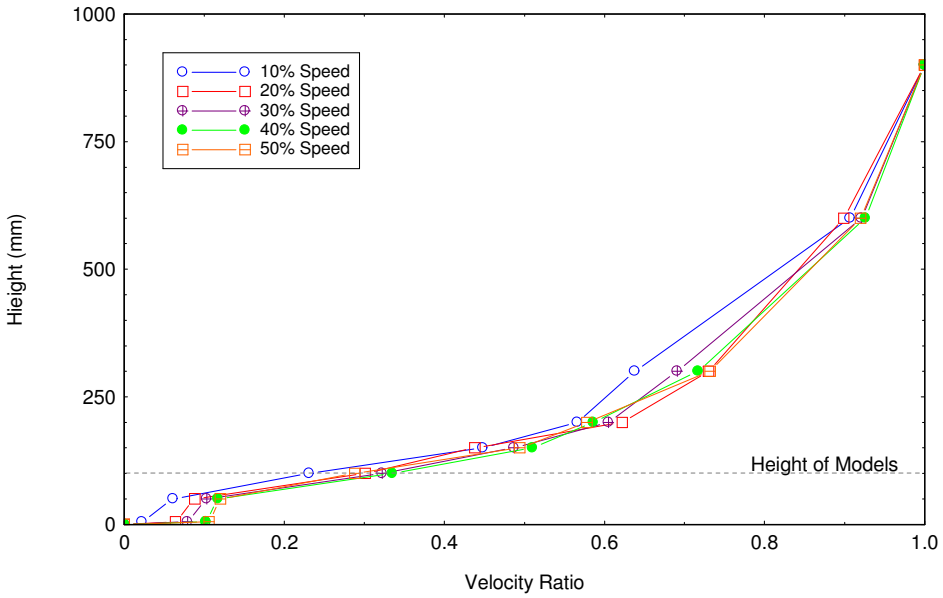

Figure 6.11: Velocity profiles expressed as ratios of velocity at 900 mm

By expressing each measurement as a velocity ratio in this way, it can be seen in Figure 6.11 that the five profiles collapse onto a single curve. The variations at the 10% speed setting are likely to result from the greater significance of experimental error as a percentage of the lower velocities being measured.

It should be noted that measurement locations at a height of less than 100 mm are within the wake-interference flow regime of the model canyons. The CTA probes used for these measurements are unable to distinguish flow direction; only its magnitude. It is likely that the flow pattern within the canyons will be unstable and the effect of windward vortices in front of the models may drive flow back upwind near to the ground. These effects are likely to be the cause of the variation between the various series of measurements taken at height below 100 mm which can be identified in Figure 6.11.

6.5 Reynolds numbers

The Reynolds number (Re) is a non-dimensional parameter which represents the ratio of inertial to viscous forces in a flow. It is defined by the following equation where 'ρ' is the density of the fluid, 'V' is the velocity, 'l' is the length of a body within in the flow and 'μ' is the dynamic viscosity of the fluid:

$$Re = \frac{\rho V l}{\mu} \qquad \text{(Eq. 6.6)}$$

The primarily importance of this parameter is to characterise the flow as being either laminar (low Reynolds numbers where viscous forces dominate) or turbulent (high Reynolds numbers where inertia forces dominate). This in turn affects how the flow separates when flowing around an immersed body. The Reynolds numbers of full-scale buildings are typically greater than 10^6 (Lawson, 2001), however it is not normally possible to simulate such conditions in the wind tunnel. For similarity at model scale the product of the length and velocity scales would have to be unity; for a length scale of 1:100 the velocity scale would therefore need to be 100:1. Consequently a full-scale wind speed of 10 m/s would require a wind tunnel velocity of 1000 m/s which equates to approximately Mach 3.

Snyder (1972) proposed that the roughness Reynolds number (Re_{z_0}) is a more appropriate parameter to use for wind tunnel modelling of groups of buildings. Reynolds number independence of the flow over an aerodynamically rough surface is assured if the following equation is satisfied (ACSE, 1999) where 'u_*' is the friction velocity, 'z_0' the roughness and 'v' the kinematic viscosity or air:

$$Re_{z_0} = \frac{u_* z_0}{v} > 2.5 \qquad \text{(Eq. 6.7)}$$

For the values of the friction velocity and roughness length derived for the current wind tunnel simulation in Section 6.2 and taking a typical value of the kinematic viscosity from Table 8.1, this equates to:

$$Re_{z_0} = \frac{0.653 \times 0.0114}{1.5313 \times 10^{-5}} = 486 \qquad \text{(Eq. 6.8)}$$

This result is therefore two orders of magnitude greater than the value prescribed in Equation 7.7 and consequently Reynolds number independence is assured.

The Reynolds numbers for the current wind tunnel studies have been calculated in Annex C4. The length variable for these calculations was taken as the height of the model cubes used in both the pressure measurement (see Chapter 7) and naphthalene sublimation (see Chapter 8) tests which is 94 mm. The wind tunnel velocity used is that measured at approximate model roof height (100 mm). The results for the building height Reynolds number (Re_H) are summarised in Table 6.5; the range for the current experiments is therefore 8.2×10^3 to 5.7×10^4.

Table 6.5: Summary of Reynolds numbers for current tests

Wind tunnel speed setting	Reynolds number (Re_H)
7.5%	8,174
15%	16,674
30%	32,653
45%	44,589
60%	57,474

For comparison, the Reynolds numbers presented for naphthalene sublimation experiments conducted by Barlow and Belcher (2002), Pascheke *et al*. (2008) and Finnigan and Longstaff (1982) are presented in Table 6.6. All values were calculated using the building height as the length dimension (except for Longstaff *et al*. when grain bin diameter was used, although this was equal to building height for the example presented below). The wind speeds used were those at building height.

Table 6.6: Comparison of Reynolds numbers from various experiments

Source	Notes	Reynolds number Min.	Max.
Barlow and Belcher	EnFlo wind tunnel	2068	5545
	Reading Uni. wind tunnel	1057	72744
Pascheke *et al*.	'C10S' configuration	1200	3520
	'RM10S' configuration	933	2880
Finnigan and Longstaff	100 mm grain storage bin	61900	138000
Current experiments	BRE wind tunnel	8174	57474

Quoted values for the critical Reynolds number (Re_{Hcrit}) for flow around model buildings range from 2100 to 7500 (Uehara *et al*., 2003). Meroney *et al*. (1996) and Pavageau and Schatzmann (1999) required that the Reynolds number based upon building height should exceed 3400. Standard wind tunnel practice is to assume that the Reynolds number effects can be ignored if the models are all sharp-edged (not rounded) as separation of the flow will always occur at the sharp corner (Lawson, 2001). This was presumably the assumption made for the various experiments detailed in Table 6.6 where the suggested critical Reynolds numbers were not exceeded. However, it has been shown that even the lowest Reynolds number for the current naphthalene sublimation tests exceed all of these criteria and also those for the minimum roughness Reynolds number (Re_{z_0}) described in Equation 7.7. The current results are therefore assumed independent of Reynolds number effects.

6.6 Turbulence Intensity

Turbulence intensity (I) can be considered a measure of how smooth or turbulent a flow is. Low turbulence intensity means that the flow is smoother and more laminar. It is defined as being the root-mean-squared (RMS) velocity divided by the mean velocity, thus:

$$I = \frac{\sigma}{V} \qquad \text{(Eq. 6.9)}$$

$$\text{where: } \sigma = \left[\frac{1}{n} \sum_{n=1}^{n} \left(v(t) - v^{-2} \right) \right]^{1/2}$$

It should also be noted that the quantity σ^2 is equal to a property known as the variance.

The turbulence intensities at a range of heights through the wind tunnel boundary layer have been calculated based upon mean and RMS velocity measurements made using a constant temperature anemometry (CTA) probe. The results of these calculations are presented below in Table 6.7.

Table 6.7: Measured turbulence intensity in the BRE wind tunnel

Height z (mm)	Turbulence intensity (%)	Height z (mm)	Turbulence intensity (%)
0	-	300	17.34
5	50.34	400	13.11
10	48.44	500	10.76
15	45.78	600	8.15
40	41.35	700	5.87
60	41.32	800	4.24
80	38.65	900	3.31
100	36.18	1000	2.77
150	28.52	1200	2.89
200	22.42	1400	7.31

Full-scale turbulence intensity data for a range of typical urban and rural terrains is provided by Cook (1985). For the current wind tunnel simulation, the data presented for aerodynamic roughness categories 4 and 5 are most appropriate for comparison (see Table 6.8 below for further details). Both the results of measurements made in the BRE wind tunnel and the data presented by Cook for roughness categories 4 and 5 are plotted below in Figure 6.12. It can be seen that the largest turbulence intensities measured in the wind tunnel were in the order of 50% at ground level; this is the maximum level which a CTA probe it able to record. The value decreases with height down to a minimum value of approximately 3%. The subsequent rise above a height of 1 m is due to the effects of the ceiling of the wind tunnel.

Table 6.8: Aerodynamic roughness categories (source: Cook, 1985)

Category	z_0	Description
4	0.3m	Dense woodland and domestic housing typically between 10% and 20% plan-area density
5	0.8m	City centres, comprising mostly four storey buildings, or higher, typically between 30% and 50% plan-area density

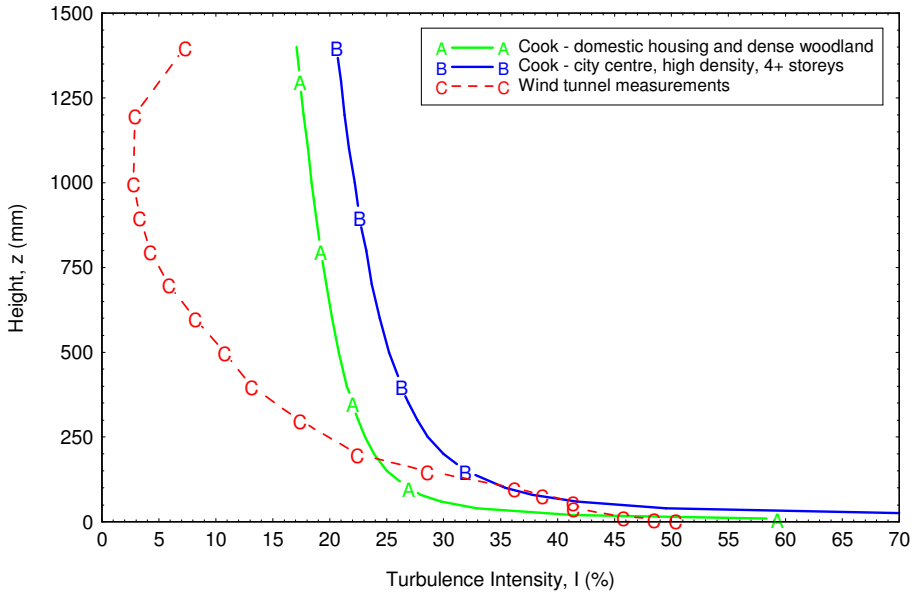

Figure 6.12: Turbulence intensity in the BRE wind tunnel

Comparison with the data presented by Cook shows that the wind tunnel simulation follows the trend of the full-scale values for dense city centre areas up to a height of approximately 150 mm. It is not possible to simulate full-scale turbulence levels throughout the full wind tunnel boundary layer due to the conflicting requirements of other aspects of the simulation (e.g. the mean velocity profile). As models typically sit within the lower part of the boundary layer which replicates the levels of turbulence seen above urban areas, this compromise is usually accepted.

It should also be noted that measurements were made in the BRE wind tunnel without any models in place. When the naphthalene sublimation experiments were conducted, the turntable area was covered by the array of models. This increases the turbulence intensity levels in the lower part of the simulation and it is therefore likely that the agreement with the data of Cook existed to a greater height in the boundary layer.

6.7 Turbulence integral length

In any turbulent flow, there will exist a range of eddies which each influence and take their energy from each other. This is illustrated by the following verse penned by the physicist Lewis Richardson to summarise his paper entitled *'The supply of energy from and to atmospheric eddies*' (Richardson, 1920). Richardson was the first to apply mathematic techniques to make accurate predictions of the weather.

"Big whorls have little whorls
That feed on their velocity,
And little whorls have lesser whorls
And so on to viscosity."

The turbulence integral length can be thought of as being the average eddy size, or the eddy size at which most of the energy of the flow is located. It is an important property as it determines how the flow will envelop the model and hence how it will affect the nature of the wake region downstream.

The turbulence integral length can be defined by the power spectral density, sometimes referred to as simply the spectral density. This is often presented as a graph of the power spectral density (*S(n)*) versus frequency (*n*) on natural logarithm axis, as shown in Figure 6.13.

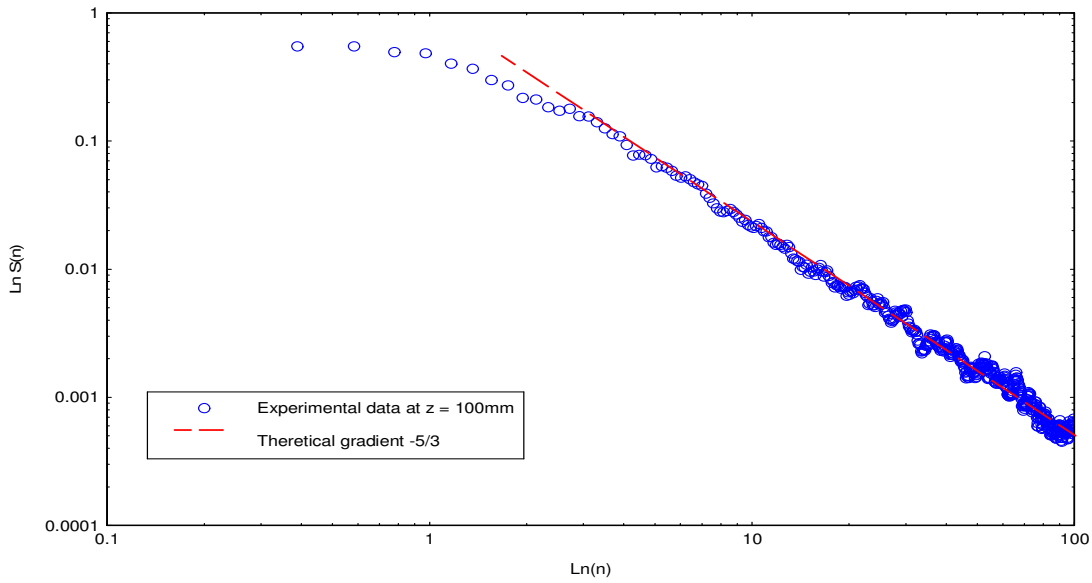

Figure 6.13: Power spectral density at z = 100 mm plotted on log-log axis

Theoretically, the plotted data should be linear (see dashed red line) representing the smooth cascade of energy from larger eddies to ever smaller ones. The gradient of this theoretical line should be approximately -5/3. In practice, this would require averaging of a very large data set, and hence the experimental data (blue points) are not completely linear.

The area under the graph shown in Figure 6.13 is equal to the variance (σ^2) thus:

$$\int_0^\infty S(n) \cdot dn = \sigma^2 \qquad \text{(Eq. 6.10)}$$

This provides us with a useful check as the variance can also be calculated from velocity in the time domain (see Section 6.6). An alternative presentation of this information is provided by non-dimensionalising the y-axis, as can be seen in Figure 6.14 below. Power spectrum plots for data recorded at other heights in the BRE wind tunnel are provided in Annex A at the end of this thesis. A modified Von Kármán spectrum of the form shown in Equation 7.8 may be fitted to the experimental data.

$$\frac{n \cdot S(n)}{\sigma^2} = 4 \frac{n L_{x_u}}{V} \Bigg/ \left[1 + 70.8 \left(\frac{n L_{x_u}}{V} \right)^2 \right]^{5/6} \qquad \text{(Eq. 6.11)}$$

where: L_{xu} = along-wind integral length

This presentation format has the advantages of both showing clearly where the energy of the flow is concentrated (i.e. the peak) and also emphasizing the important low frequencies (as a result of the logarithmic x-axis).

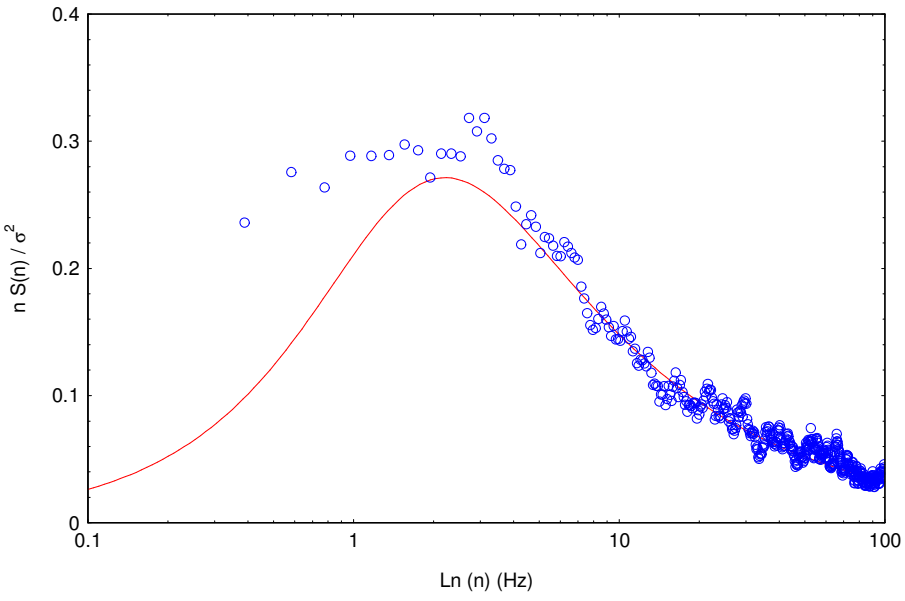

Figure 6.14: Turbulence power spectrum at a height of 100 mm

By fitting a curve of this form to the experimental data, the value of the along-wind integral length (Lx_u) may be obtained. In the case shown above, Lx_u equals 0.226 metres. Values determined from measurements taken at other heights in the wind tunnel boundary layer are detailed in Table 6.9. Using this information it is possible to determine the turbulence scale factor at each height and hence assess the appropriateness of the wind tunnel simulation to the selected model scale (Cook, 1978).

The following empirical relationship is presented by ESDU (1974):

$$L_{x_u} = 25(z-d)^{0.35} z_0^{-0.063} \qquad \text{(Eq. 6.12)}$$

At full-scale, the appropriate terms in the above equation will be multiplied by the scale factor (*S*). A solution for the scale factor may therefore be obtained by rearrangement of the factored equation into the following form:

$$S = \frac{91.3 \times (z-d)^{0.491}}{L_{x_u}^{1.403} \times z_0^{0.088}} \qquad \text{(Eq. 6.13)}$$

With knowledge of the values of zero plane displacement (d) and roughness length (z_0) derived at model scale in Section 6.2, and the along-wind turbulence integral length (Lx_u) obtained from the graph shown above, the turbulence scale factor may be calculated. The full derivation of Equation 7.13 and an example calculation of the scale factor are given in Annex C. The values obtained in this way for each of the measurement heights in the wind tunnel are listed in Table 6.9 and shown in Figure 6.15 and Figure 6.16.

Table 6.9: Calculated properties of the wind tunnel turbulence simulation

Height z (mm)	**Integral length Lx_u (mm)**	**Scale S**
15	72	588
40	85	844
60	126	601
80	192	387
100	226	345
150	330	250
200	359	256
300	392	277
400	330	407
600	323	513
800	191	1236
1000	181	1488

At lower levels, turbulent effects are damped by the ground and therefore more of the flow's energy is transferred to the along-wind direction. The turbulence integral length reduces, signifying that eddies in this region are relatively smaller than in the full-scale atmospheric model. The calculated model scale is therefore higher to take account of this. Above around 600 mm, the wind tunnel is not able to simulate the large scale eddies that typically occur in the atmospheric boundary layer, and hence the calculated model scale again begins to rise.

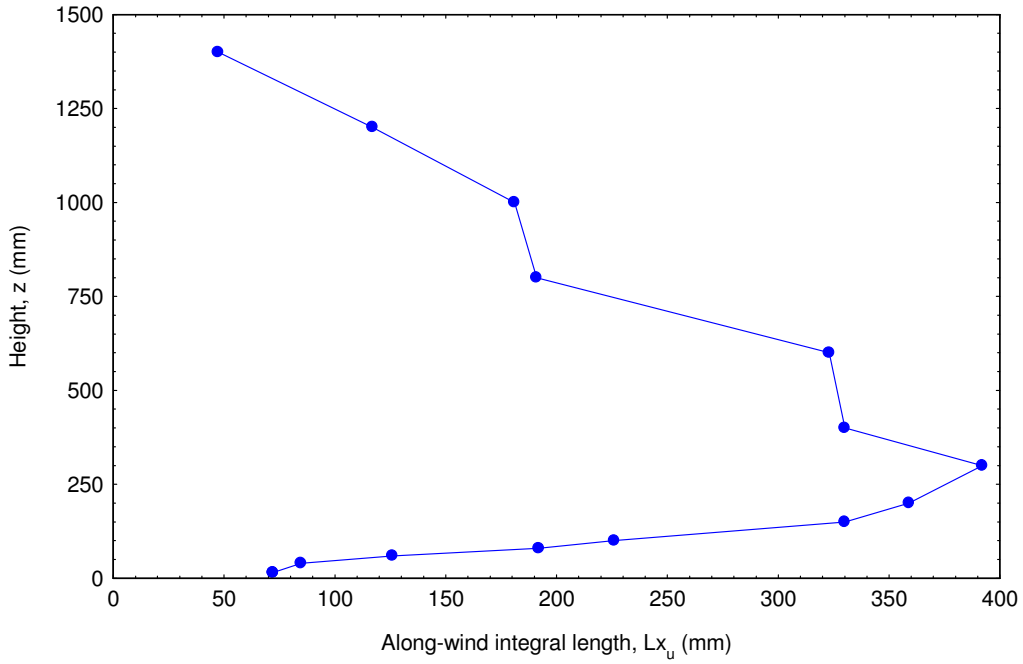

Figure 6.15: Along-wind integral length

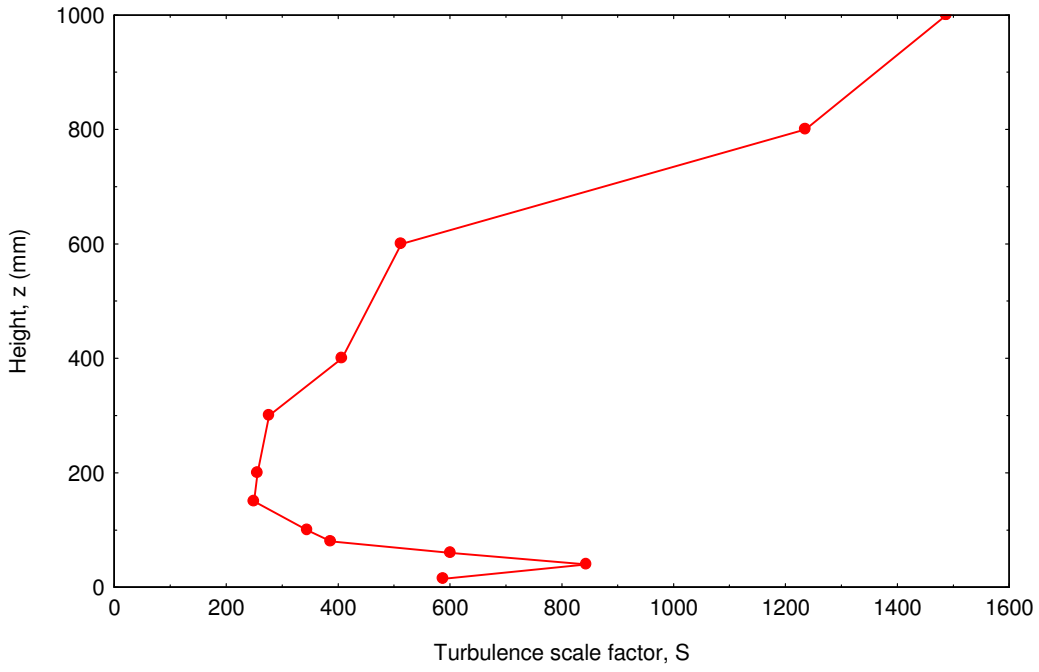

Figure 6.16: Turbulence scale factor

For dynamic wind loading work, such a mismatch of scales between the wind tunnel simulation and the atmospheric boundary layer may prove problematic leading to incorrect dynamic responses of load or deflection. However, the naphthalene sublimation technique deals only with time-averaged measurements and hence such problems are not encountered. BS 6399-2 (BSI, 1997a) specifies that the geometric scale of the model may be up to a multiple of three times the simulated turbulent length scale for the measurement of overall cladding loads. With the incorporation of this allowance, the turbulence length scale is acceptable between heights of 150 and 300 mm, immediately above the model street canyons.

The latest ESDU datasheets (ESDU International, 1985) give an improved empirical formulation and suggest that larger turbulence length scales are required. However, such scales can not be readily simulated in wind tunnels and so standard practice remains to work with the scales proposed by Cook (1978).

6.8 Conclusions

This Chapter has described the development and measurement of a 1:100th scale atmospheric boundary layer simulation within the BRE wind tunnel facility. The relatively large model scale required to permit an array of measurements to be made across each model surface is greater than is typically used for commercial wind environment studies. Therefore additional development of the standard atmospheric simulation was required in order to ensure that the modelled velocity profiles and turbulence levels were within acceptable limits.

A series of wind speed measurements were made in the working section of the wind tunnel using a sensitive constant temperature anemometer device. The mean velocity profile thus obtained was shown to be representative of that documented at full-scale at the centres of large towns and cities. A power-law curve was fitted to the data and this enabled wind speeds measured at particular heights in subsequent naphthalene sublimation experiments to be factored to give the respective wind speed at alternative heights within the boundary layer.

Measurements were also made of the turbulence intensity at various heights through the boundary layer. It was shown that these results are similar to those recorded at full-scale up to a model height of approximately 150 mm, although this height limit was likely to be increased with the addition of the surrounding models to the turntable area. The flow patterns immediately around the model therefore possessed the appropriate amount of turbulence. Above this height, it was not possible to maintain the high turbulence levels due to various conflicting requirements, such as the priority given to maintaining the correct mean velocity profile. This compromise is however usually accepted for wind tunnel studies as it is acknowledged that precisely simulating every characteristic of the atmosphere is impractical.

The turbulence length scale measured in the wind tunnel was shown to be of appropriate magnitude for model-scale heights of between 150 mm to 300 mm (i.e. directly above the roofs of the models). Values below a height of 150 mm are not of concern since these are directly affected by the flow pattern around a particular arrangement of models. Above a height of 300 mm, the lower levels of turbulence (compared to full-scale data) which it was possible to simulate in the wind tunnel lead to turbulence length scales above that of the model scale. This was acceptable for the proposed time-averaged naphthalene sublimation measurements, particularly given that the turbulence directly above the models was of the appropriate scale.

Further series of constant temperature anemometry measurements were made across the baseline arrangement of models arranged perpendicular to the wind. From these results, it was confirmed that the flow regimes and patterns around the models were independent of wind speed and so the wind tunnel could be run at any speed (above a minimum threshold). This permitted the relationship between convective heat transfer and wind speed to be determined in subsequent experiments using the naphthalene technique. These measurements also showed that the mean velocity profile is stable across the wind tunnel turntable, and so the location of the active cube within this area did not affect the results obtained. The confidence in the wind tunnel simulation given by these preliminary series of tests meant that results obtained in the main naphthalene sublimation tests were representative of the conditions experienced by full-scale buildings.

Chapter 7 Air flow in urban street canyons

The rate of convective heat transfer from the surfaces of buildings has been shown in previous chapters to be directly proportional to the magnitude of the local wind speeds. It follows that knowledge of the local wind speeds and flow patterns in and around an urban street canyon may indicate the nature and magnitude of the convective heat transfer.

One technique widely used in wind engineering is to employ a pressure tapped scale model of the building (or buildings) of interest. Arrays of pressure taps are located over the model surfaces and sampled by a series of precision pressure transducers. This technique is often used to determine the cladding loads which may be experienced by full-scale structures to aid the design of safe and economical façades. However, such pressure distributions over building surfaces are also indicative (when combined with knowledge of the principles of building aerodynamics) of the flow patterns adjacent to the surfaces. Velocity and pressure are interrelated by Equation 8.1, where ρ is the density of air. It can be seen that pressure (P) increases with the square of the velocity (V) and hence it is possible to accurately determine the velocity of impinging jet by measuring the surface pressure.

$$P = \tfrac{1}{2} \rho V^2 \qquad \text{(Eq. 7.1)}$$

An alternative technique, and one which provides immediate visual feedback, is to introduce smoke into the air stream to highlight specific flow patterns. Whilst this generates no quantitative data for either velocities or pressures, it does offer a unique opportunity to witness otherwise invisible air movements around the model buildings.

To this end, a series of surface pressure measurements and smoke visualisation studies were conducted in parallel with the main naphthalene sublimation experiments. By combining the results of these three independent techniques, a deeper understanding of the interrelated flows and heat transfer processes was acquired. The pressure and smoke studies are discussed in the following sections and comparisons made with results from naphthalene sublimation experiments later in this thesis.

7.1 Methodology

A pressure tapped model was constructed specifically for the purposes of these tests. The model took the form of regular cube with sides each 94 mm long. The hollow structure was fabricated from 5 pieces of 5 mm thick clear Perspex sheet, with the base left open to allow connection of the pressure tubes. A total of 100 pressure taps were located over the cube with 20 taps in a 4 by 5 array on each face. The tappings were formed from lengths of brass tubing (1 mm internal diameter) mounted flush with the external surfaces of the model so as not to influence the flow. The cube was mounted on a 470 mm diameter circular wooden baseboard which allowed it to be mounted at the centre of the turntable. A photograph of the model installed in the BRE wind tunnel in shown in Figure 7.1 below.

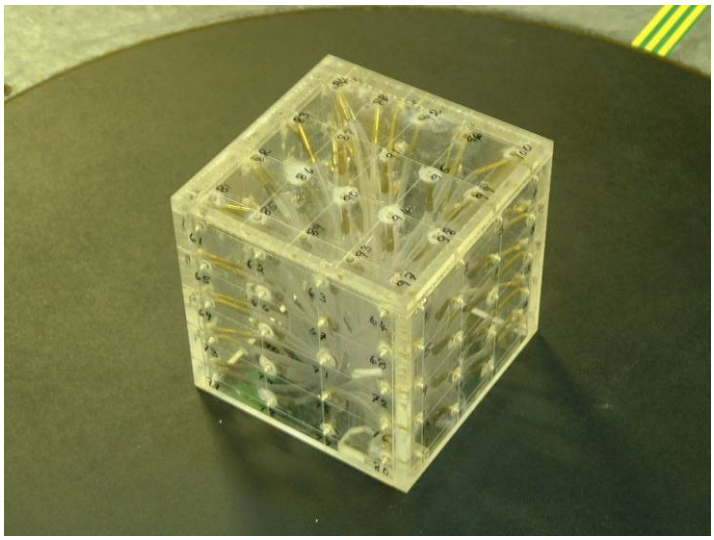

Figure 7.1: Pressure tapped cube model

Each of the one hundred pressure taps were individually connected to ports on miniature pressure transducers via 400 mm lengths of urethane tubing of 1 mm internal diameter. These tubes were calibrated to give a flat frequency response up to 100 Hz by inserting a brass restrictor at the mid-point. The pressure transducers enabled simultaneous measurements to be made at each of the 100 pressure taps. Pressure signals were also recorded from a Pitot-static tube positioned at a height of 300 mm immediately upwind of the model in order to provide reference wind speed information with which to normalise the results. The pressure taps were numbered sequentially from 2 to 101 as illustrated in Figure 7.2 below. The static pressure from the Pitot-static tube was connected to port 0 and the total pressure to port 1.

The pressure transducers were 'ZOC' (Zero, Operate, Calibrate) type pressure scanners manufactured by *Scanivalve* (see web site: Scanivalve Corporation, 2006). These units are piezo-resistive differential sensors with a sampling rate of up to 20 kHz and a pressure range of ±10 inches of water (±2488 Pa).

The modules are extremely compact, multi-pressure scanners with either 32 or 64 individual silicon pressure sensors. They include a high speed multiplexer (maximum 20 kHz) and instrumentation amplifier, and are specifically designed for use in wind tunnel testing. Pressure transducer models *ZOC33* and *ZOC22B* were used for this study. The transducers were operated by a *DSM3200 digital service module* control unit which fed data via a TCP/IP network connection to a standard personal computer. Custom BRE programs were used to log, process and analyse the pressure data before this was output to a Microsoft Excel spreadsheet.

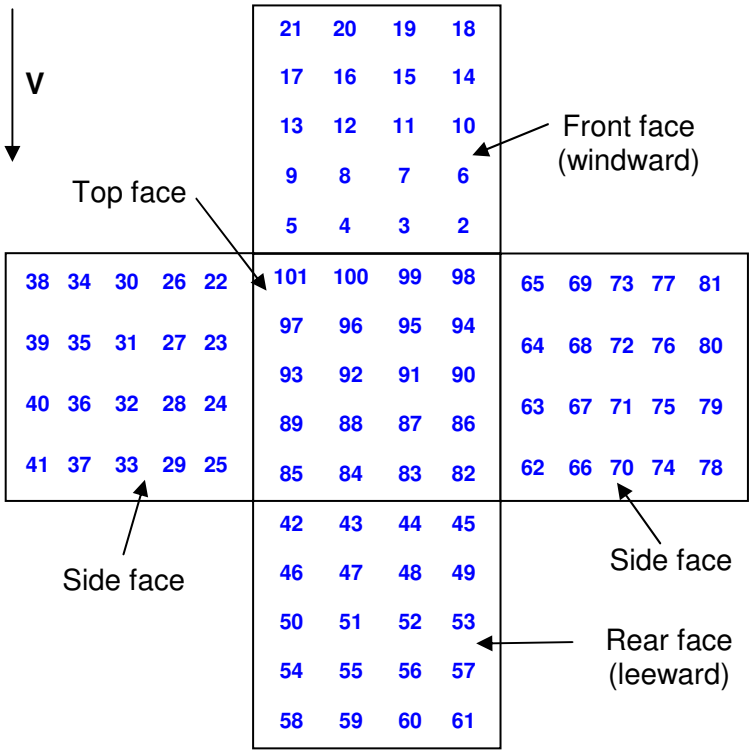

Figure 7.2: A diagram showing tap locations and numbering on the cube model

Figure 7.3 shows the underside of the pressure tapped model when installed in the BRE wind tunnel. The five bundles of pressure tubes can be seen (each bundle of 20 tubes is connected to a different face of the cube) as can the brass flow restrictors. The tubes are connected to the pressure transducers via 'Scanivalve Series D' 48-way connector rings which permit fast connection (and disconnection) of each bundle between tests.

The pressure tapped model was located at the centre of the wind tunnel turntable, as shown in Figure 7.4. The surrounding buildings which formed the street canyons were simulated using wooden blocks (painted black in the photograph below) of the same height and depth as the active model. Wooden spacers were fabricated to aid rapid positioning of the surrounding blocks at the required height-to-width ratios, eliminating the need for repeated measurements.

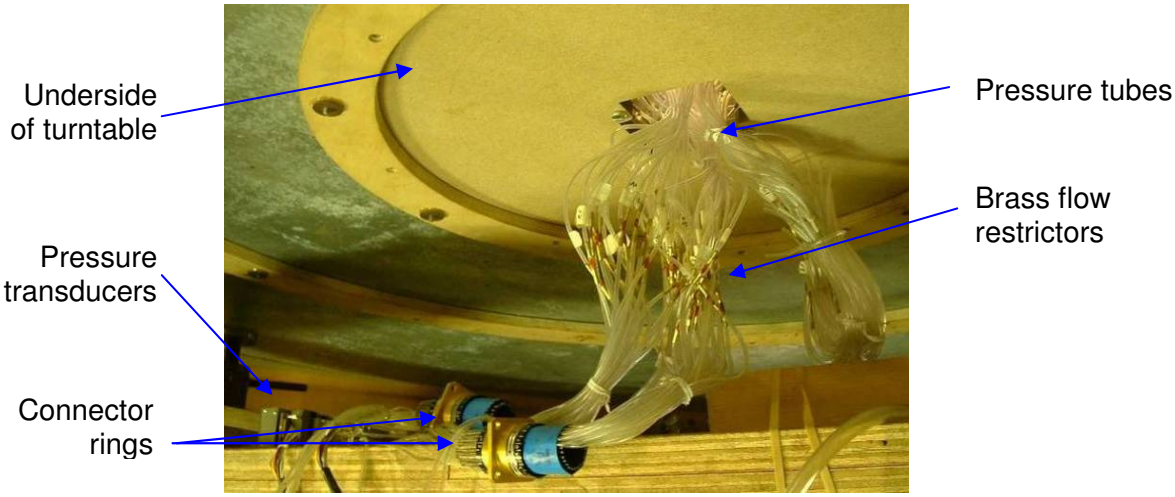

Figure 7.3: The underside of the pressure tapped model in the wind tunnel

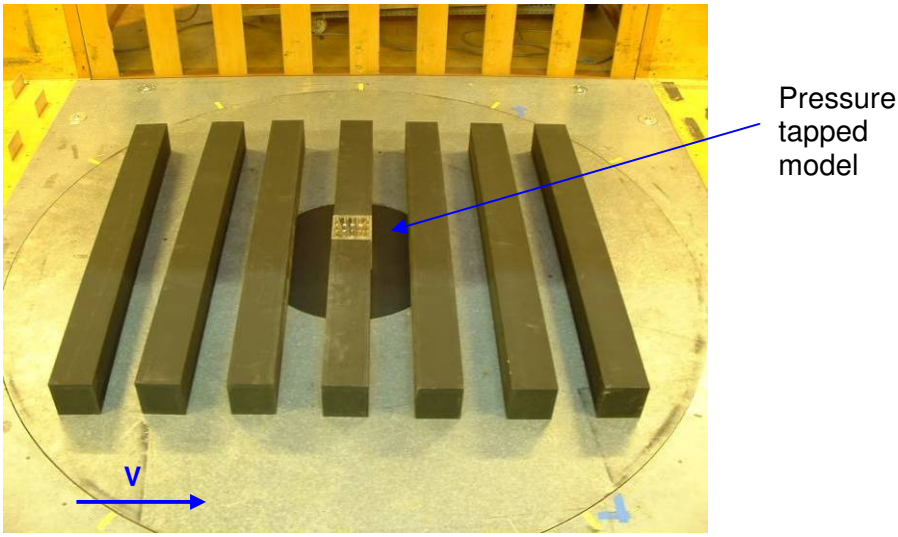

Figure 7.4: Arrangement of pressure tapped model within street canyons

The wind tunnel turntable is 1.75 m in diameter and is able to continuously rotate in either direction. It was therefore possible to test each particular arrangement of models at a variety of approaching wind angles without the need for manual reconfiguration.

7.2 Processing of data

Data from the pressure tapped model and Pitot-static tube were sampled at a time interval of 2.5 ms and the average of each consecutive batch of 4 samples was then calculated. This provided data at the required 100 Hz sample rate, with the over-sampling and averaging giving greater confidence than would a straightforward 10 ms sample interval. With a model length scale of 100 and a velocity scale of 1, the time scale for the experiment was therefore 100 and hence the full-scale sampling rate was 1 Hz. This frequency is known to be the highest to which building cladding elements will react (e.g. when calculating cladding loads) and was adopted for the current tests for the same reason. Additionally, the pressure tubing and flow restrictor arrangement described earlier has been developed to provide a flat response up to this frequency. A total of 10,000 samples (100 seconds at 100 Hz) were recorded at each location simultaneously so as to provide sufficient data for statistical analysis. This sampling duration also ensured that all long-period turbulent fluctuations within the wind tunnel were captured.

To process the data, the mean static pressure recorded during the test (as measured at the Pitot-static tube) was first subtracted from each measurement to remove any variation due to changing ambient conditions. The data was then non-dimensionalised by division by the mean dynamic pressure measured at the Pitot-static tube. The resulting pressure coefficients (C_p) were non-dimensional and thus independent of both length scales and wind velocities.

The choice of reference height was an important consideration. The maximum height of the building would usually be employed for high-rise or isolated building scenarios. However, this is impractical when the model under test is of similar height to the surroundings because the Pitot-static tube would have been submerged within the local highly-turbulent boundary layer thus influencing the measured values. Instead, a reference height of 300 mm was selected for the current study. With knowledge of the mean horizontal velocity boundary layer profile (as described in Section 6.2) it was possible to scale the wind speed measured at this reference height to that at any other height as required. The choice of Pitot-static tube height was therefore largely academic and hence based on ease of access and positioning considerations.

Pressure coefficients are widely used in wind engineering as when combined with local metrological conditions, ground topography data, etc. they permit calculation of the wind loads experienced on buildings and building elements (for example: Blackmore and Tsokri, 2006). Much experimental data is available at both model and full-scales and this permits validation of the present measurements (for example: Sill *et al.*, 1989; Robertson *et al.*, 1998).

The street canyon scenarios considered in this thesis were two-dimensional. Long canyons were selected to remove end effects from the results, and the numbers of up and downstream buildings were chosen in order to ensure a uniform approaching flow. In most conditions, the mean pressures measured at any of the four taps across each horizontal row are (approximately) equal. By averaging the results for the four taps at each height, a single pressure coefficient value was obtained for each row. It was considerably more straightforward to plot results of this type on a two-dimensional plot, and comparisons can also be more easily made between alterative data sets.

The results from the pressure measurement tests are presented in the following sections as x-y plots, where the x-axis gives the pressure coefficient in respect to the row number shown on the y-axis. Figure 7.5 details the groups of taps which have been combined to give each row averaged result.

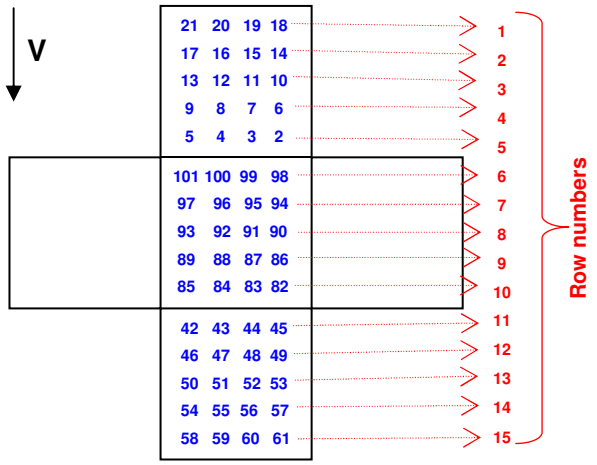

Figure 7.5: Tap row numbering system on pressure tapped cube

The top of this diagram relates to the bottom of the windward face of the cube, with the other faces opened out into a net below. The central square depicts the roof of the cube building, whilst the left and right squares are the two sides which adjoin the neighbouring models and hence were unused in these particular tests. The numbering system for the rows of pressure taps starts at number 1 at the base of the windward face and ends at number 15 at the base of the leeward face, as shown by the red numbers in the diagram above. The blue numbers show the individual tap numbers taken from the model. For clarity, an overview of several of the important row numbers is given in Table 7.1 along with a description of their respective positioning on the model building.

Table 7.1: Description of notable pressure tap row numbers

Row Number	Tap numbers	Description
1	18, 19, 20, 21	Base of windward face.
5	2, 3, 4, 5	Top of windward face.
6	98, 99, 100, 101	Windward edge of roof.
10	82, 83, 84, 85	Leeward edge of roof.
11	42, 43, 44, 45	Base of leeward face.
15	58, 59, 60, 61	Top of leeward face.

7.3 Tests to determine the repeatability of results

Preliminary tests were conducted to determine the repeatability of results obtained from the pressure tapped cube. The model was arranged in the wind tunnel with surrounding street canyons at a height-to-width ratio of unity, and tested with both perpendicular and parallel flows. In each case, four identical tests were conducted in succession. The pressure coefficients are plotted on the lower x-axis and the standard deviations of the results from the four runs are plotted on the upper x-axis. The row numbers detailed in the previous section are plotted on the y-axis. Figure 7.6 shows the results obtained from the perpendicular (0 degree wind angle) flow and Figure 7.7 shows the results for the parallel (90 degree wind angle) flow.

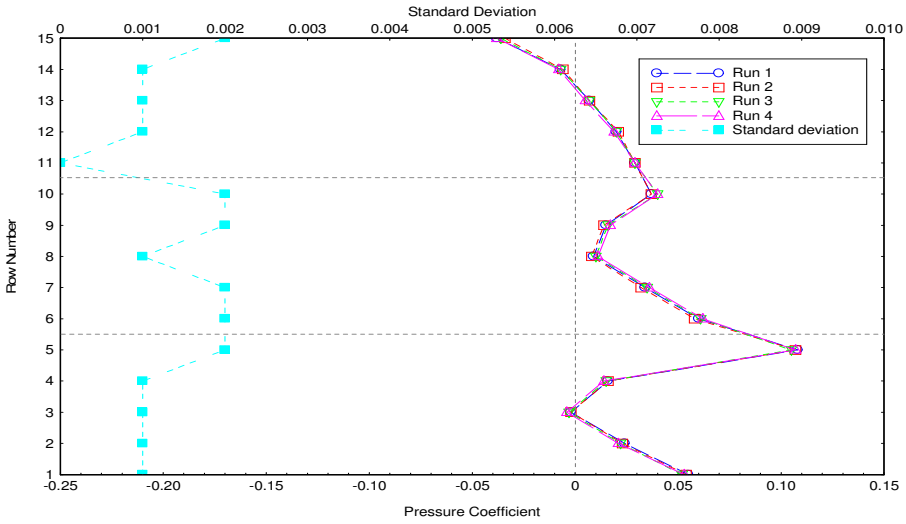

Figure 7.6: Repeatability of results for perpendicular flow

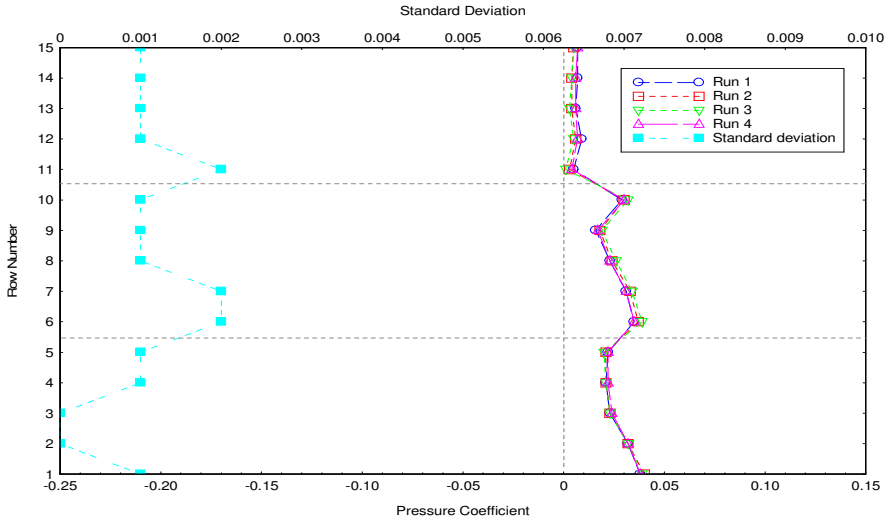

Figure 7.7: Repeatability of results for parallel flow

It can be seen in these figures that the results obtained from the pressure measurements are highly repeatable, with maximum standard deviations of the pressure coefficients in each case of 0.002.

For winds blowing along the canyon, it is to be expected that the pressures on the two vertical façades would be identical and that those over the roof would be symmetrical across the centre line. The results shown in Figure 7.7 do not exhibit these characteristics. This is due to the models being slightly angled to the flow in the wind tunnel and this result therefore highlighted the need to ensure accurate model arrangements in subsequent tests (both with the pressure tapped cube and for naphthalene sublimation tests).

7.4 Arrangement of models

When selecting the urban geometries that were to be simulated at model scale, it was important that these were representative of a typical town or city layout. The buildings in such areas are generally low-rise residential properties arranged along linear streets. It was also important that the chosen arrangement could be compared with other studies and so it needed to be of a generic form which was not specific to a particular scenario. Consequently the selected geometry for this research was a long street with continuous buildings on each side. Such geometries are often referred to as ‘street canyons’ as the street forms a sheltered void between the rows of buildings. This type of urban form is typical of large towns and cities where land is at a premium and hence buildings are built abutting their neighbours (e.g. rows of shops, terraced houses, and long office buildings).

In order to eliminate the influence of the ends of these rows of buildings and make the flow purely two-dimensional, Oke (1987) suggested that it is necessary to have a canyon length of at least eleven times the height of the building. From the perspective of air flow around such two-dimensional street canyons, the most important factors are the height and spacing of the rows of buildings. These two quantities may be combined and non-dimensionalised by dividing the height (H) of the building by the width (W) of the street to give the ‘height-to-width ratio’ (H/W). Oke determined that one of three flow regimes may exist when flow is perpendicular to the street canyon. When street canyons are wide (i.e. H/W less than 0.30), the wind profile is able to recover after reaching each successive row of buildings. The wind profile around each street is therefore similar to that of an isolated row of buildings, as shown in Figure 7.8.

When street canyons are particularly narrow (i.e. H/W greater than 0.65), the majority of the air flow passes over the roofs of the buildings with little interaction with the street canyons. This so called ‘skimming flow’ regime is particularly relevant to towns and cities which have a higher building density and is illustrated in Figure 7.9.

Between these two height-to-width ratios (i.e. $0.30 < H/W < 0.65$), an intermediate regime exists know as ‘wake interference flow’. Figure 7.10 shows how a complex pattern is formed by the interaction of the wake from upwind obstructions with winds driven down into the canyon by the windward surfaces of subsequent buildings.

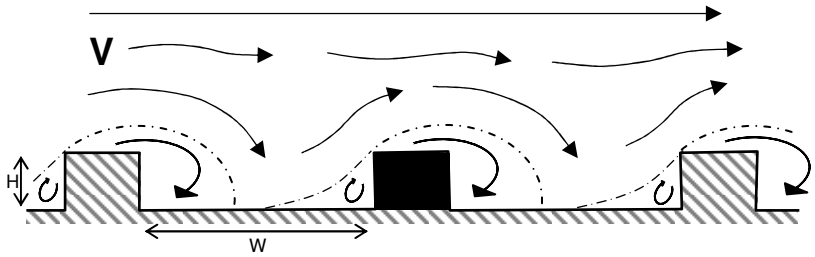

Figure 7.8: Isolated flow regime at a height-to-width ratio of 0.33

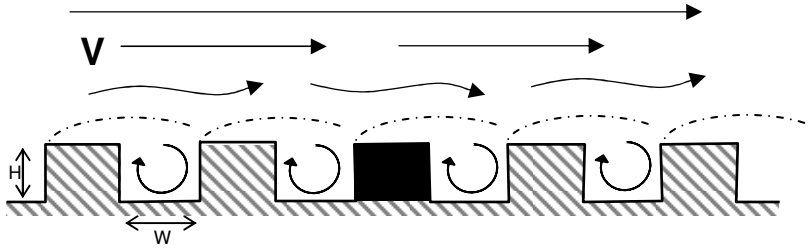

Figure 7.9: The skimming flow regime at a height-to-width ratio of 1.0

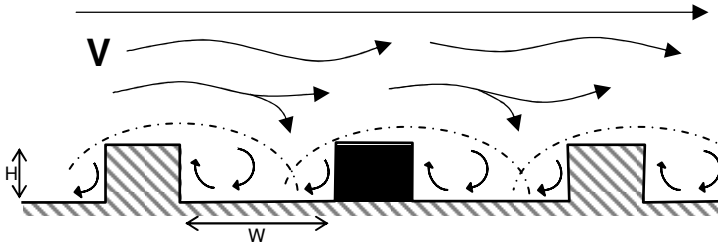

Figure 7.10: Wake interference flow regime at a height-to-width ratio of 0.5

These three flow regimes and their relative ranges of occurrence are shown in Figure 7.11 below. It was desirable to make measurements in each of these flow regimes with the skimming flow region being of particular relevance to urban areas. It was therefore decided that measurements would be made with model street canyons arranged in rows with height-to-width ratios of 0.25 (isolated flow), 0.50 (wake interference flow), and 1.00 (skimming flow). The red figures and arrows show how these points fit within the three flow regimes ranges.

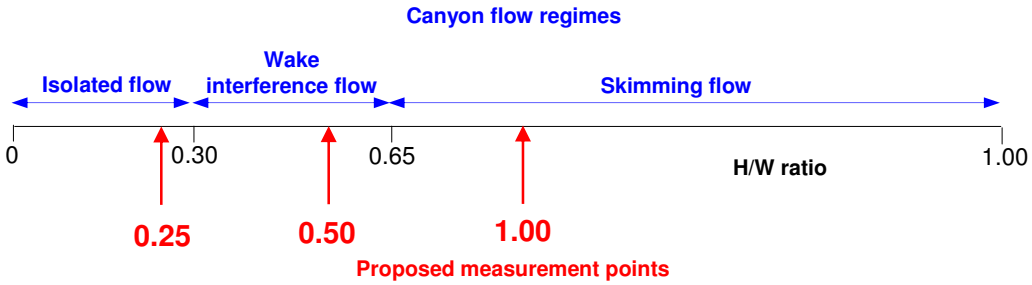

Figure 7.11: Canyon height-to-width ratios and flow regimes

The three canyon flow regimes described exist only when the approaching flow is perpendicular to the street. At other angles, the rotation of air within the canyon illustrated in Figure 7.9 is given a sideways component and hence begins to move along the canyon in a spiralling motion. The angle of the approaching flow determines the form of this 'cork-screw' with more acute angles giving rise to faster flow along the canyon and hence to a more elongated spiral. Small angles of incidence give rise to little flow along the canyon and therefore lead to tight spirals, ultimately reducing to the stationary rotation associated with perpendicular flow. When the flow approaches the buildings parallel to their rows, no shelter is provided at street level and wind may be channelled along the canyon. With wider streets (i.e. lesser H/W ratios), the flow along these canyons will revert to conditions more similar to open terrain.

7.4.1 The effect of canyon length

It is suggested in the literature (Oke, 1987) that in order for the flow around a canyon to be considered two-dimensional (i.e. for effects perpendicular to the approaching flow to be neglected), the canyon must have a length of eleven or more times its width. In order to put this theory to the test for the particular canyon geometry considered in this study, a series of parametric experiments were conducted using the pressure tapped cube model described earlier.

Surface pressure measurements provide a useful means by which the time-averaged flow patterns around the model can be determined. By conducting a series of experiments with the models arranged in different row lengths, the relative differences in pressure distribution became evident and hence the effect of these variations was determined. The effect of adding additional blocks to the end of a row of buildings is initially significant, but then diminishes to a point above which further lengthening of the canyon has no effect. By determining the particular length at which this occurred, it was possible to ensure that the surrounding buildings were modelled to a sufficient extent as to remove local end-effects from the simulation.

The case of flow perpendicular to the street canyons (0 degrees) was the most dependent upon end effects. The configuration to be tested using the naphthalene sublimation technique was a canyon 11 units long (where one unit is equal to the height of the model). This is illustrated by the grey blocks in Figure 7.12 below; the red block represents the pressure tapped active model. Surface pressure measurement experiments were therefore conducted on this configuration in order to provide a baseline case for comparison. Further measurements were then made with the addition of between one and four extra cubes at both ends of the canyons, as illustrated by the blue blocks in the diagram below. The maximum canyon length tested was 19H with 4 extra cubes at each end of the standard 11H long canyon.

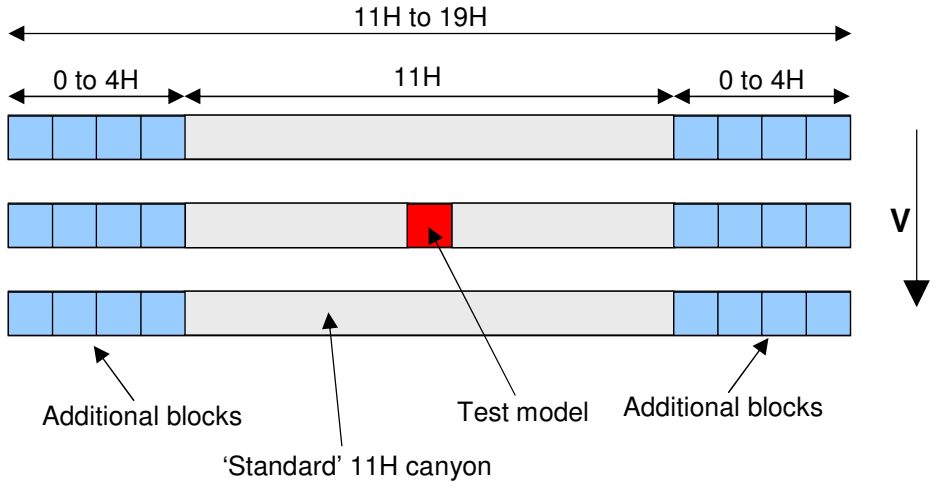

Figure 7.12: Arrangement of models to determine the effect of canyon length

For each of these tests, the height-to-width ratio was unity and the wind tunnel speed setting was maintained at 40%. The measured mean pressures were converted to non-dimensional coefficients by division by the reference pressure recorded using a Pitot-static tube at a height of 300 mm in the undisturbed air stream immediately upwind of the models. The average mean pressure coefficients along each row of measurements locations are plotted for the five experiments in Figure 7.13 below. The plot area is divided by dotted lines to signify the windward (bottom of graph), roof (middle) and leeward (top of graph) surfaces.

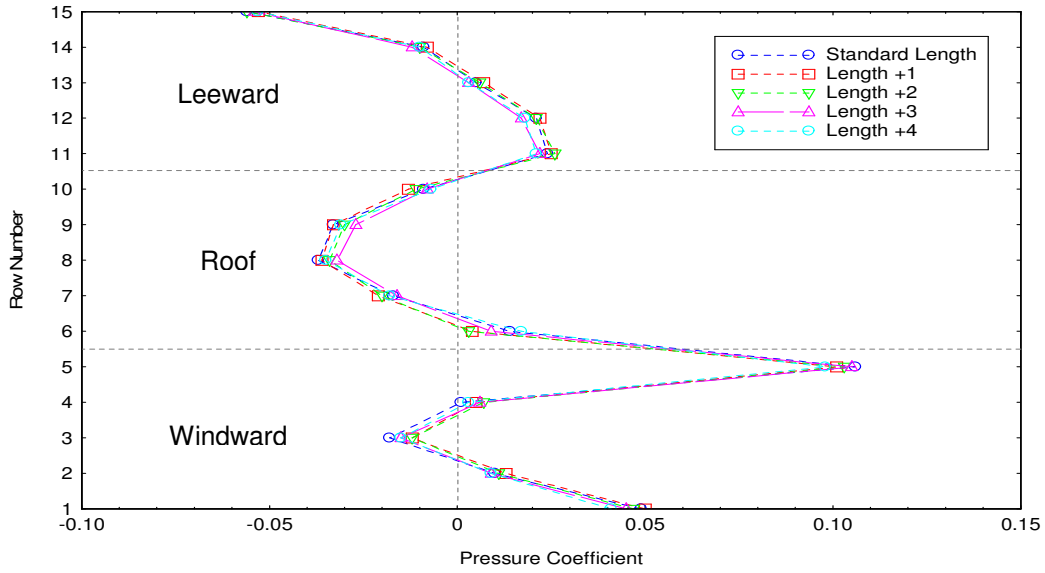

Figure 7.13: The effect of canyon length on surface pressures at 0 degrees

The pressure coefficient results presented in Figure 7.13 show that the effect of adding additional units of length to the ends of the street canyons was negligible. A small amount of variation was seen between the various test runs (most notably for a length of plus three units) but these were within the levels of experimental error; the actual variations are in fact very small. It was therefore concluded that the proposed street canyon length of eleven times the building height was sufficient to remove the end effects from the measurement location at the centre of the canyon, thereby ensuring two-dimensional flow in this region. The model arrangement for the following naphthalene sublimation was thus confirmed as being the active model at the centre of the turntable, with five further 'dummy' cubes on either side to give the required length of eleven units.

7.4.2 The effect of the number of surrounding canyons

Another important variable which needed to be considered was the extent of the surrounding models that were used in the wind tunnel simulation. A number of dummy cubes were employed to form additional up and downstream canyons identical to the one in within which the active model was located. The number of these canyons installed affects the flow patterns around the models. Sufficient rows were required in order that the desired wake-interference, isolated or skimming flow regimes were fully developed at the active model location.

A series of tests were therefore performed using the pressure-tapped cube in order to determine the minimum number of canyons that were required on either side of the model. It was decided that the same number of canyons would be used on both the windward and leeward sides so that the arrangement of models was symmetrical about the centreline of the active cube. A baseline experiment was initially conducted with a single isolated canyon of length 11H perpendicular to the approaching wind (see grey blocks in Figure 7.14 below). Further tests were then conducted with the addition of between 1 and 4 extra upwind and downwind canyons (the blue blocks in diagram below) arranged at a height-to-width ratio of one to the central canyon.

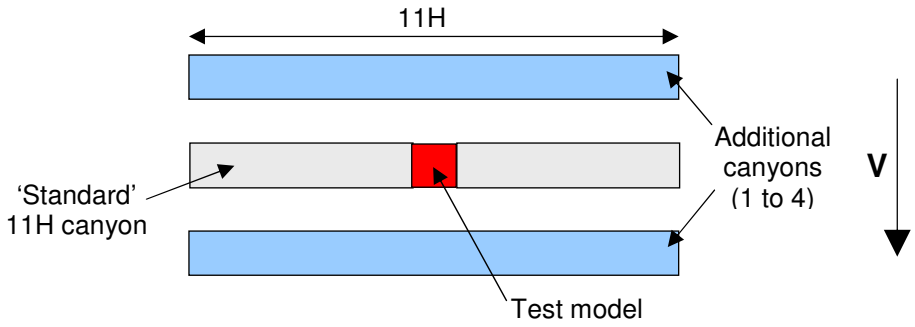

Figure 7.14: The arrangement of models in the wind tunnel

The measured mean pressures were again converted into pressure coefficients as in previous tests. The average mean pressures calculated for each horizontal are plotted in Figure 7.15 below. As previously, the plot area had been divided to indicate the three surfaces of the model.

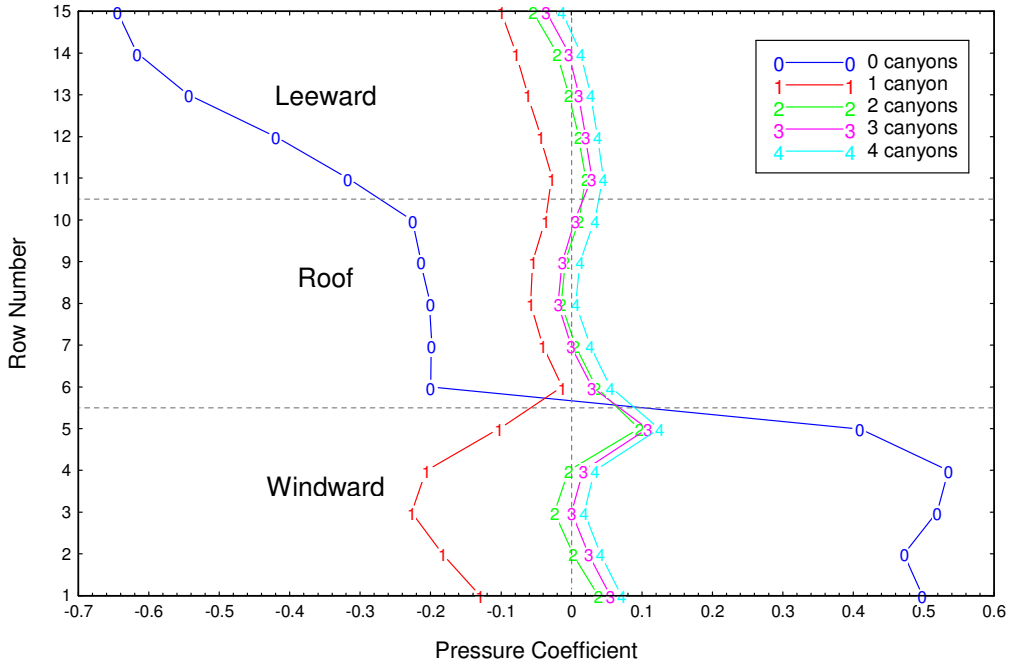

Figure 7.15: The effect of the number of upwind and downstream canyons

It can be seen that the results for the isolated single row of models (the dark blue line) are significantly different from those where shelter is provided by adjacent rows of models. The pressure coefficients measured on the central cube are typical of those for an isolated building; the pressures on the windward surface are positive with a maximum at the stagnation point at approximately two-thirds the height of the model. The pressures across the flat roof are negative and relatively uniform and the pressures across the leeward surface are also negative in the wake region.

When an additional row of buildings was modelled on each side of the active canyon (the red line on the plot), the results became more representative of a typical street canyon. The pressure coefficients over the roof and leeward surfaces remained negative, but were smaller in magnitude and also less variable than previously. The pressures over the windward surface were also negative for this particular arrangement. This was due to the formation of a large separation region by the single upwind row of buildings which engulfed the street canyon on the windward side of the active cube in a negative pressure wake region.

The results for two or more surrounding canyons were reasonably similar and the addition of further up and downstream canyons appeared to have only marginal effect. When two surrounding rows of buildings were simulated, negative pressures were still noted in the central portion of the windward face. It was therefore concluded that in order to simulate a large area of uniform low-rise buildings, at least three rows of buildings needed to be simulated on either side of the active row. For closer building spacings, four rows of buildings were employed in order to span the full diameter of the wind tunnel turntable. Further experiments by the author (but not documented in this thesis) indicated that the number of downstream canyons was less significant that those upstream. However for the sake of simplicity and ease of documentation, the same numbers of canyons were arranged on both sides of the central measurement cube.

7.4.3 Summary of the selected model arrangements

In summary, the results of the pressure tapped model tests determined that the baseline arrangement of models was to be the central active row of cubes with four additional dummy rows on either side. The height-to-width ratio of the canyons was to be a half (in order to simulate the wake-interference flow regime typical of urban areas) and the baseline wind direction was to be perpendicular to the canyons (0 degrees).

Additionally, canyon height-to-width ratios of a quarter and of one were also to be used to simulate isolated and skimming flow regimes respectively. A height-to-width ratio of two was also included to investigate the effect of very close building spacing, although this arrangement was not used in the later naphthalene sublimation tests. The effect of wind direction was to be determined by conducting further experiments with flow parallel to the street canyons (90 degrees) and also at an intermediate (45 degrees) incident angle. Photographs showing the wind tunnel models arranged in the four height-to-width ratio configurations selected are shown in Figure 7.16. The models are shown arranged in the perpendicular flow (0 degrees) orientation. Photographs of the model arranged at the intermediate (45 degrees) and parallel flow (90 degrees) wind directions are shown in Figure 7.17.

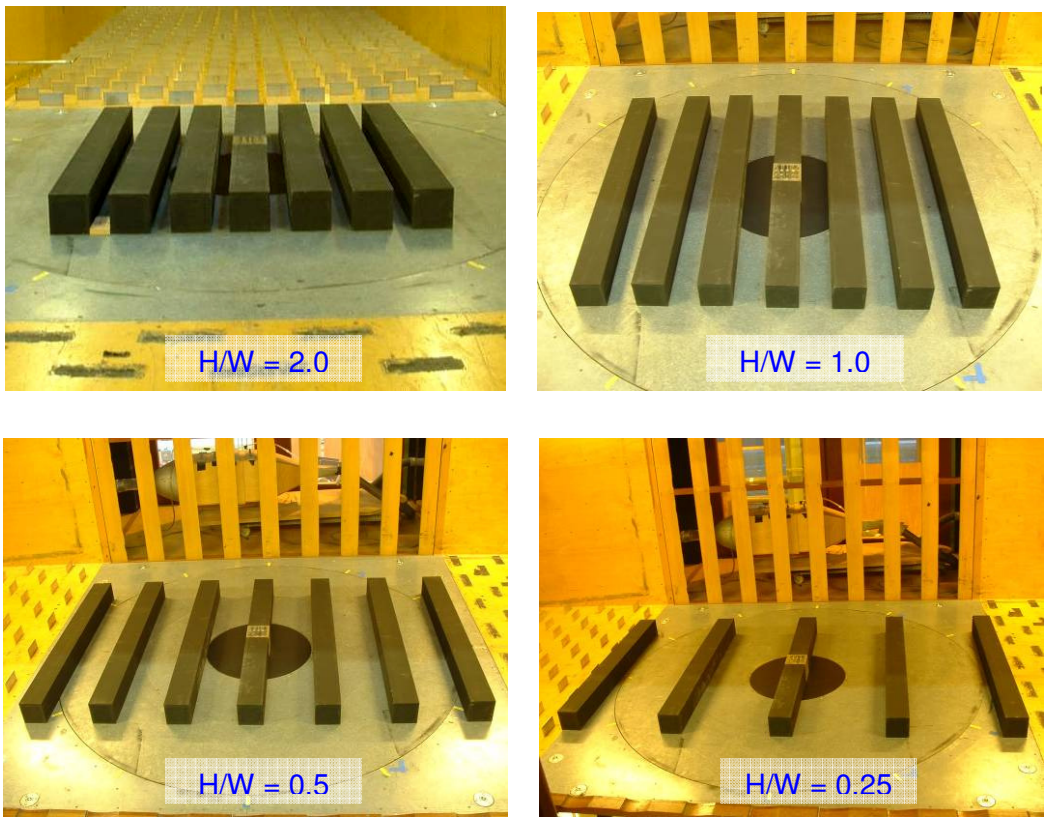

Figure 7.16: Models at H/W ratios of 2.0, 1.0, 0.5 and 0.25 respectively

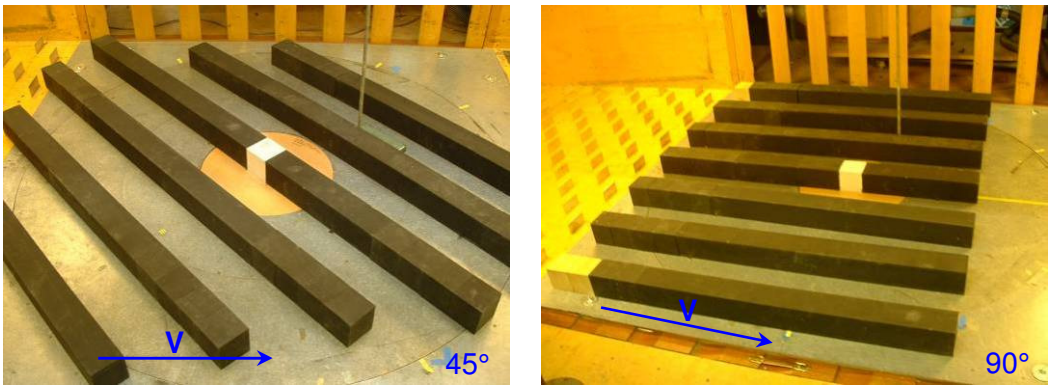

Figure 7.17: Models arranged at 45 and 90 degrees (H/W = 0.5)

It was necessary to extend the canyons arranged at the parallel and intermediate wind angles using additional cubes in order to ensure the necessary upwind fetch of buildings in front of the test model, as can be seen in Figure 7.17. This removes any end effects which may otherwise have compromised the simulation of a large urban area.

7.5 Experimental results

The case of wind approaching perpendicular to the street canyon was considered first, followed by flow parallel to the street canyons and then flow approaching at an intermediate angle. The three height-to-width ratios of 0.25, 0.50 and 1.00 determined in Section 7.4 were simulated, as well as an additional height-to-width ratio of 2.00 which provided an even more closely spaced configuration. A height-to-width ratio of zero was also considered representing an isolated row of buildings with no immediate surroundings (e.g. a terrace of houses next to parkland).

7.5.1 Flow perpendicular to the street canyon

The pressure coefficient data obtained from the experiments with flow perpendicular to the canyon are shown as contour plots in Figure 7.18 below for each of the five height-to-width ratios (H/W) considered. These plots each represent the three opened-out exposed faces of the model (i.e. windward, roof and leeward). The windward face is shown as the lower square, the roof the middle square and the leeward face the top square. The five plots are each to the same scale allowing direct comparisons to be made between the results.

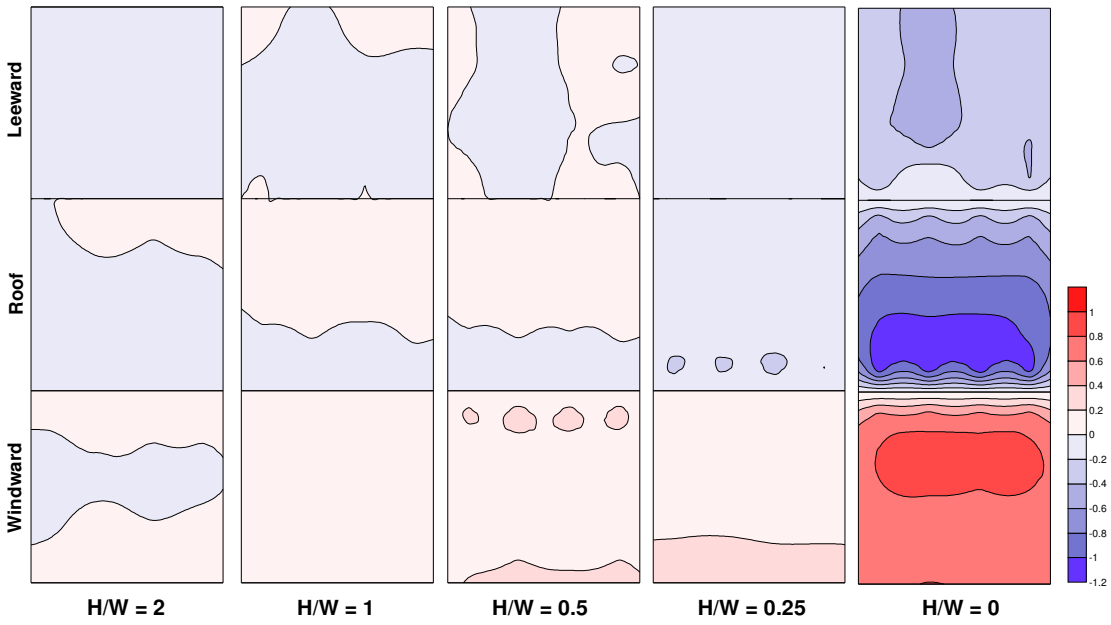

Figure 7.18: Pressure coefficient plots for perpendicular flow

In order to help understand these results, a smoke visualisation study was undertaken in parallel with the pressure measurements. An *Aerotech SGS-90* smoke generator unit was employed to introduce smoke at discrete locations around the models. This device uses an electrically heated element at the end of a wand to burn crushed walnut oil, producing a constant and controllable smoke flux. By careful positioning of two or more studio projection lamps and experimenting with digital camera shutter speeds, it was possible to freeze-frame an image of the highly turbulent flow in and around the street canyons. The black painted models and a matt black background help to make the white smoke clearly visible.

The same model arrangements were tested as per the pressure cube experiments, except that the tapped cube was replaced by a 'dummy' wooden model to prevent clogging of the pressure taps by walnut oil residue. The wind tunnel speed was also greatly reduced so that the individual vortices could be captured; it has already been shown in Section 6.4 that the flow patterns are independent of wind speed.

It can be seen in Figure 7.18 that the greatest variation in pressure coefficients was measured when the building was isolated (H/W = 0). In such scenarios, the building is subjected to the full unsheltered force of the prevailing wind. The variation at the vertical edges of this Figure are as a result of the way the contour plotting program deals with the lack of data on either side of the model. In reality the pattern along the majority of the length of the two-dimensional street canyon will be similar to that seen along the centreline of this plot. A smoke visualisation photograph of the same scenario is shown in Figure 7.19 below. A stagnation point (labelled 'A') occurs on the windward face at roughly two-thirds of the height of the building. The approaching flow is brought to rest at this point which results in the high positive pressure region at approximately two-thirds the height of the windward face of the cube seen in the contour plot.

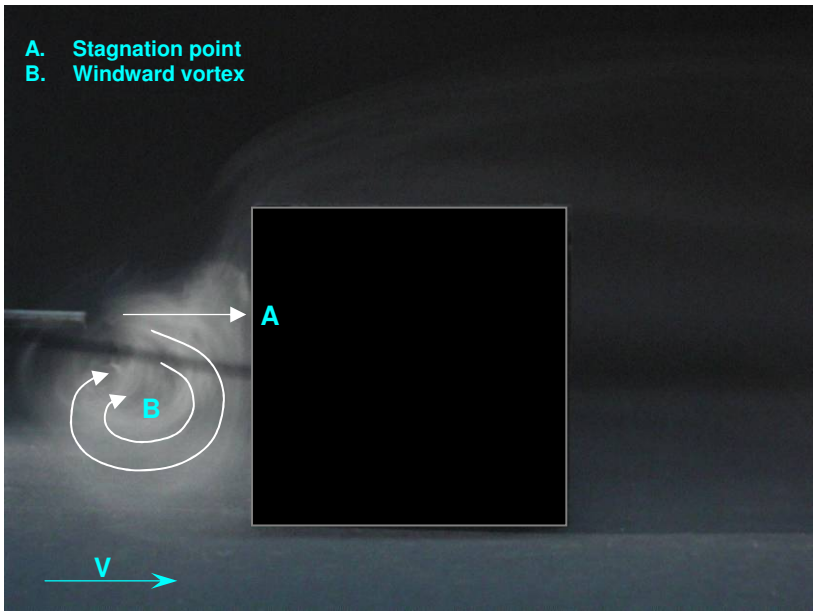

Figure 7.19: Smoke visualisation of flow recirculating in the windward vortex

Below the stagnation point, the approaching flow is driven downwards towards the ground and recirculates in what is known as the 'windward vortex'. This phenomenon maintains the moderate positive pressure over of the lower windward face of the building and can clearly be identified in Figure 7.19 (labelled 'B'). In the street canyon scenario modelled, the majority of the approaching flow was forced up and over the roof of the building as shown in Figure 7.20. The flow detached from the leading edge of the flat roof resulting in the high negative pressure separation region (labelled 'C' in Figure 7.20) seen in the contour plots. The flow then reattached to the roof at a later point (labelled 'D') leading to a loss of the suction by the leeward edge of the roof.

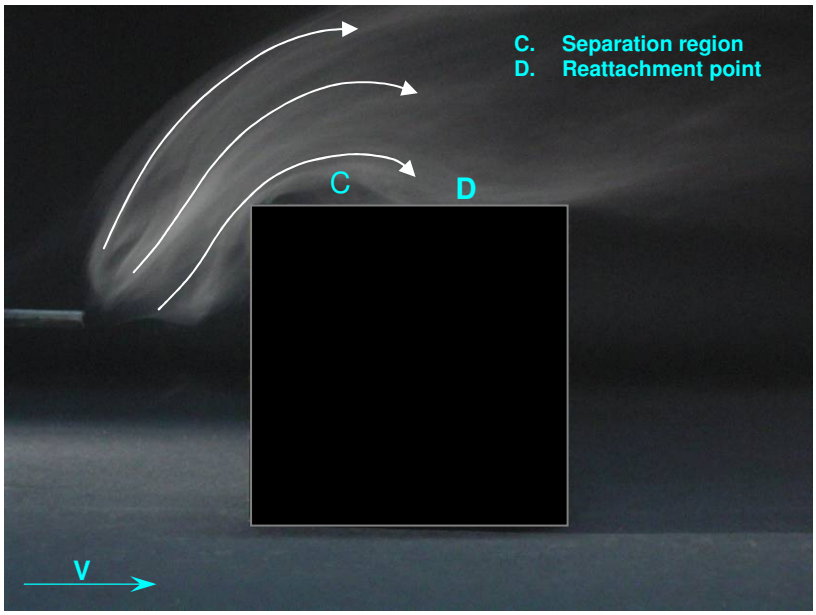

Figure 7.20: Smoke visualisation showing the separation on the roof

Typical pressure distributions over the windward and leeward façades of a building are shown in Figure 7.21 below (Cook, 1985). These data were obtained from wind tunnel experiments in which a low-rise building was placed upstream of a high-rise building on which measurements were made; this accounts for the variation in the contours at the base of the windward face. The similarity of these plots with the experimental data for a height-to-width ratio of zero (an isolated row of buildings) shown in Figure 7.18 is clear. The variation in magnitude and horizontal contour distribution between the two plots is as a result of the differing model geometries.

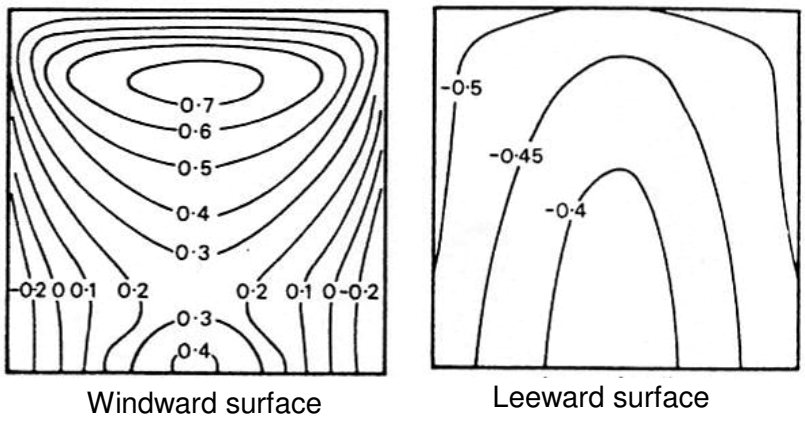

Figure 7.21: Typical pressure distributions over building surfaces (source: Cook, 1985)

Flow around the models in the wind tunnel is, like that around full scale buildings, inherently turbulent and unstable. These images therefore represent only 'snapshots' in time of a flow pattern that is rapidly fluctuating. The two smoke visualisation photographs on the previous pages were taken only a fraction of a second apart and yet exhibit very different flow patterns. This is further illustrated by the time-series photographs shown in Figure 7.22 below which were taken at 0.25 seconds intervals using a digital camera. Each row of four images therefore represents a one second time period and the full series of sixteen images represents a total of four seconds. The probe of the smoke generator was held steady so all fluctuations in the smoke pattern were due only to variations in the flow patterns. The unstable nature of the turbulent flow is therefore evident with the smoke trail rapidly fluctuating between the windward vortex in front of the cube and the separated flow above the roof. This switching of the flow pattern actually occurs at a much greater frequency than has been captured by these quarter second intervals; several oscillations may have occurred between each quarter of a second frame.

Figure 7.22: Time-series photograph for flow visualisation around a cube model

The effect of turbulence within the wind tunnel (as well as in the atmosphere) is to modify the flow patterns around the buildings. Such rapid fluctuations in the flow would not be seen in a laminar flow wind tunnel and the location of the reattachment points would typically be further downstream on the model. This justifies the concerns raised earlier in this thesis regarding the use of convective heat transfer results obtained in laminar flow experiments being employed for turbulent scenarios around buildings.

7.5.2 Flow parallel to the street canyon

When flow approached the street canyons parallel to their length (90 degrees), a completely different local flow regime and pressure distribution was seen around the model. Results from these experiments are displayed in the contour plots shown in Figure 7.23 for the various canyon spacings considered. These plots show little variation between the five different height-to-width ratios. It is likely that the same phenomena seen previously for perpendicular flow (e.g. stagnation points, windward vortices, reattachments points) still occurred, but only at the leading edges of the canyons. These effects would have dissipated by the time the flow reached the pressure tapped model half way along the row of buildings. The pressures measured were relatively uniform across the three cube surfaces and are unlikely to have varied significantly until the end of the canyon.

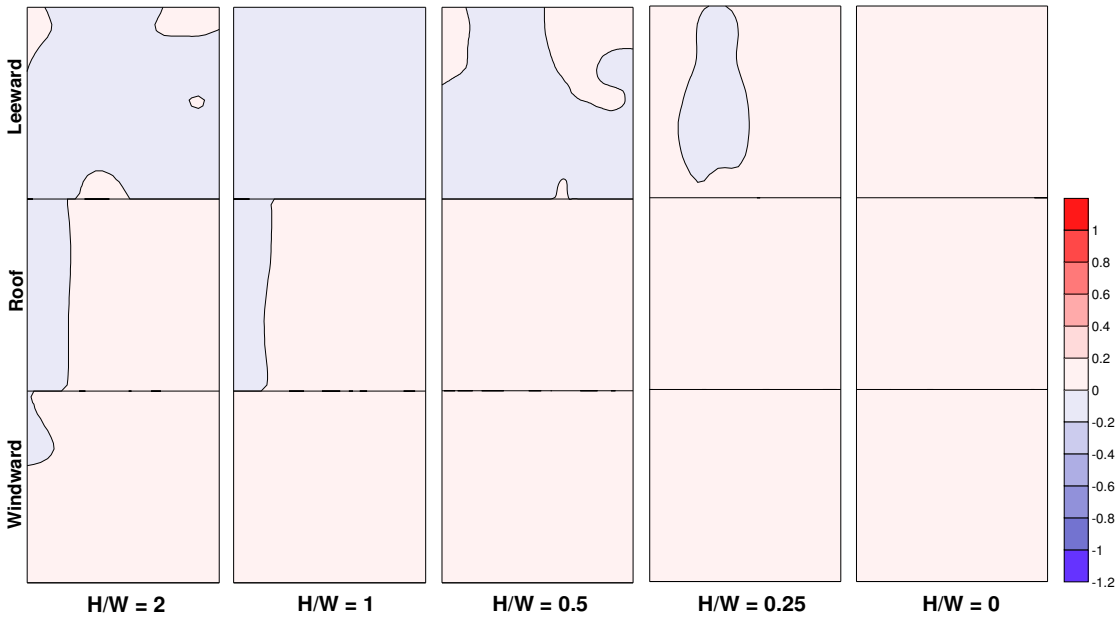

Figure 7.23: Pressure coefficient plots for parallel flow

7.5.3 Flow from intermediate angles

The final scenario that was considered was flow approaching the canyons at an intermediate 45 degree angle, halfway between the previously investigated parallel and perpendicular flow patterns. The pressure distributions measured across the surfaces of the cube during this experiment are plotted in Figure 7.24. It can be seen that the pressure distribution pattern is a combination of the features of the parallel and perpendicular flow cases. The stagnation point is not as pronounced as in the perpendicular flow case as wind is now more able to pass the building obstruction laterally, rather than being brought to a halt. However the high positive pressure region of the windward vortex on the front face of the cube remains; Oke (1987) suggested that this vortex moves down the canyon in a corkscrew motion. The low pressure region at the leading edge of the roof also remains evident.

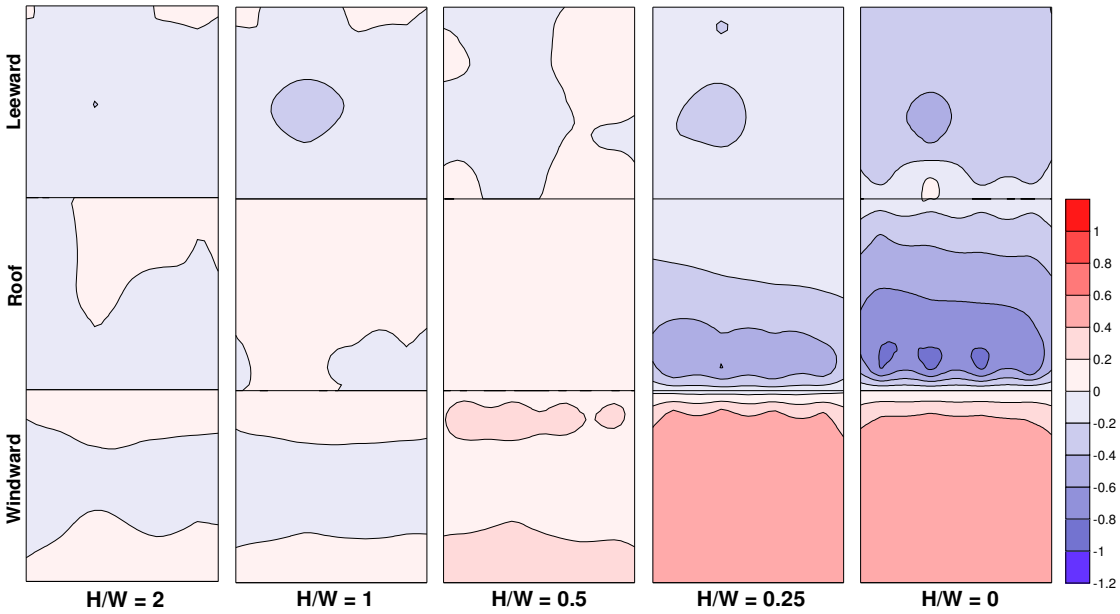

Figure 7.24: Pressure coefficient plots for intermediate angle flow

7.6 Conclusions

With an appropriate 1:100th scale wind tunnel simulation developed, a practical arrangement of models for the various proposed naphthalene sublimation tests has been discussed. A parallel row arrangement of model cubes was selected to represent the long streets of buildings which are typical of urban areas. Row spacings were selected to correspond with the isolated, wake-interference and skimming flow regimes documented in the literature. The wake-interference regime (in which the flows around successive rows of buildings interact) is most typical of urban areas and therefore formed the baseline case. Literature suggested that a canyon length of eleven times the building height was required in order to ensure that the surrounding flow was purely two-dimensional (i.e. to avoid end-effects). Tests conducted with canyon lengths of 11, 13, 15, 17 and 19 times the building height found little variation in the pressure distribution over the central active cube and thus the proposed 11H length was shown to be of sufficient length.

Chapter 8 Naphthalene sublimation measurements

8.1 Calculation of convective heat transfer coefficients

The basis of the naphthalene sublimation methodology is that there exists an analogy between heat and mass transfer such that the Nusselt and Sherwood numbers may be expressed in the following similar forms:

$$Nu = c\,Re^{m}\,Pr^{n} \qquad \text{(Eq. 8.1)}$$

$$Sh = c\,Re^{m}\,Sc^{n} \qquad \text{(Eq. 8.2)}$$

By dividing Equation 9.1 by Equation 9.2, an expression for the Nusselt number may be obtained in the form:

$$Nu = \left(\frac{Pr}{Sc}\right)^{n} \times Sh \qquad \text{(Eq. 8.3)}$$

The Prandtl and Schmidt numbers are known to be based on the properties of air and naphthalene respectively. The Sherwood number may be obtained from wind tunnel experiments during which the sublimation of naphthalene from models in the wind tunnel is measured. An appropriate value for the exponent 'n' is determined from the literature based upon empirical data. An example calculation is presented in Annex C.

Determination of the Prandtl number

The Prandtl number may be obtained with knowledge of the thermal diffusivity (k_a) and kinematic viscosity (v_a) of air as follows.

$$Pr = \frac{v_a}{k_a} \qquad \text{(Eq. 8.4)}$$

The kinematic viscosity of air (v_a) may be calculated by the following formula derived by Cho (1989):

$$v_a = 0.1556\left(\frac{\theta_a}{298.16}\right)^{0.17774}\left(\frac{1.013\times10^{5}}{P_{atm}}\right) \qquad \text{(Eq. 8.5)}$$

Values at a range of typical air temperatures at an atmospheric pressure of 1013 mb were presented by Goldstein and Cho (1995). Values for a wider range of temperatures and atmospheric pressures are pressures in Table 8.1. It can be seen that there is significant variation of the values across this table and it is therefore critical that air temperature and pressure variation were taken into account in the results.

Table 8.1: The kinematic viscosity of air (from Equation 9.5)

	Kinematic viscosity of air (v_a) (m^2/s x10^{-5})				
Temperature (K)	**1000mb**	**1005mb**	**1010mb**	**1015mb**	**1020mb**
285	1.4547	1.4475	1.4403	1.4332	1.4262
290	1.5004	1.4929	1.4855	1.4782	1.4710
295	1.5467	1.5390	1.5313	1.5238	1.5163
300	1.5936	1.5856	1.5778	1.5700	1.5623
305	1.6411	1.6329	1.6248	1.6168	1.6089
310	1.6892	1.6808	1.6725	1.6642	1.6561

The thermal diffusivity may be calculated using Equation 9.6 and the properties of air shown in Table 8.2.

$$k_a = \frac{K}{C_p \times \rho} \qquad \text{(Eq. 8.6)}$$

Table 8.2: The properties of air (source: Rogers and Mayhew, 1995)

Property of air	**Value**
Thermal conductivity (K)	0.02624 W/m.K
Specific heat capacity (C_p)	1004.90 J/kg.K
Density (ρ)	1.177 kg/m^3

The Prandtl number of air at various temperatures and atmospheric pressures are detailed in Table 8.3. It can again be seen that the values depend upon both atmospheric pressure and air temperature, hence the importance of logging these parameters during experiments.

Table 8.3: Range of typical values for the Prandtl number (source: Rogers and Mayhew, 1995)

	Prandtl number at various pressures				
Temperature (K)	**1000 mb**	**1005 mb**	**1010 mb**	**1015 mb**	**1020 mb**
285	0.656	0.652	0.649	0.646	0.643
290	0.676	0.673	0.670	0.666	0.663
295	0.697	0.694	0.690	0.687	0.683
300	0.718	0.715	0.711	0.708	0.704
305	0.740	0.736	0.732	0.729	0.725
310	0.761	0.758	0.754	0.750	0.746

Determination of the Schmidt number

The Schmidt number may be calculated as a function of the naphthalene temperature (in degrees Kelvin) as follows:

$$Sc = 2.28 \times \left(\frac{\theta}{298.16} \right)^{-0.1526} \qquad \text{(Eq. 8.7)}$$

The Schmidt numbers calculated using this equation over the typical laboratory temperature range are listed in Table 8.4.

Table 8.4: Values of the Schmidt number (from Equation 9.7)

Temperature (K)	Schmidt number
290	2.290
300	2.278
310	2.266
320	2.256

Determination of the Sherwood number

The Sherwood number may be determined as follows:

$$Sh = \frac{M \times L}{D} \qquad \text{(Eq. 8.8)}$$

The value of 'L' has been taken to be 0.094 m (i.e. the height / width / depth of the naphthalene coated model). Values for the mass diffusivity of naphthalene (D) are known for various temperatures and are given in Table 8.5 below.

Table 8.5: Values of the naphthalene mass diffusivity constant
(source: Goldstein and Cho, 1995)

Temperature (K)	D (m^2/hr)
290	2.3238×10^{-2}
295	2.4016×10^{-2}
300	2.4808×10^{-2}
305	2.5614×10^{-2}

The mass transfer rate (M) can be calculated from Equation 9.9 where '∂T' is the measured reduction in thickness of the naphthalene coating on the wind tunnel model and 't' is the experimental run time.

$$M = \frac{\partial T \times \rho_n}{t \times (\rho_v - \rho_a)} \qquad \text{(Eq. 8.9)}$$

where: $\rho_n = 1175\ \text{kg/m}^3$ (at 20 °C)

ρ_a = assumed zero due to large air volume of wind tunnel building

$$\rho_v = \frac{P}{R \times \theta} \qquad \text{(Eq. 8.10)}$$

where: P = 44.61 Pa

R = 64.89 J/Kg.K

Goldstein and Cho (1995) recommend employing the correlation presented by Ambrose *et al*. (1975) for calculation of the saturated vapour pressure of naphthalene in air. This correlation is as follows:

$$\theta \log P = \left(a_0 / 2 + \sum a_x E_x \right) \qquad \text{(Eq. 8.11)}$$

where: $E_1 = x$ and: $a_0 = 301.6247$

$E_2 = 2x^2 - 1$ $a_1 = 791.4937$

$E_3 = 4x^3 - 3x$ $a_2 = -8.2536$

$x = \frac{(2T - 574)}{114}$ $a_3 = 0.4043$

The value of the exponent 'n'

It has been shown that the Nusselt number may be calculated using the following equation:

$$Nu = \left(\frac{Pr}{Sc}\right)^{n} \times Sh \qquad \text{(Eq. 9.12)}$$

The Prandtl and Schmidt numbers may be selected from Table 8.3 and Table 8.4 respectively and the Sherwood number is measured during the naphthalene sublimation experiment. The appropriate value of the exponent 'n' has been determined by previous researchers based upon empirical data and limited theoretical models. It has been shown to be in the range of 0.33 to 0.40. The maximum error in the value of the Nusselt number which could result from selection an inappropriate value of 'n' from within this range can be calculated using Equation 9.13 (Finnigan and Longstaff, 1982):

$$Error = \frac{Q^{0.40} - Q^{0.33}}{Q^{0.33}} \qquad \text{(Eq. 9.13)}$$

where 'Q' is calculated using data from Table 8.3 and Table 8.4 (at 295 K and 1010mb) as:

$$Q = \frac{Sc_n}{Pr_a} = \frac{2.290}{0.670} = 3.418 \qquad \text{(Eq. 9.14)}$$

The maximum potential error in the value of the derived Nusselt number is therefore 9% (Finnigan *et al.* used Sc = 2.53 and Pr = 0.71 in their calculation; however the resulting error value was almost identical).

Mills (1962) presented a Nusselt number correlation based upon experimental results under fully developed conditions in which n = 0.33. This value has been successfully employed to correlate experimental data for a wide range of forced convection scenarios (Souza Mendes, 1991) and both Finnigan *et al*. (1982) and Barlow *et al*. (2002) employed this value for their studies. Shao *et al.* (2009) assumed a value of n = 0.4 for their full-scale measurements on a building surface in turbulent flow conditions.

Goldstein and Cho (1995) suggested that an appropriate value to take for such naphthalene sublimation wind tunnel tests is n = 0.34. Thus this was the value of 'n' that was selected for the current naphthalene sublimation experiments.

8.2 Selection of experimental variables

It is clear that there is a wide array of variables that might be considered when investigating convective heat transfer from the surfaces of buildings in urban environments. It was not practical, or indeed desirable, to include all of these factors within the scope of the current study and so it was important to determine those of most importance and interest within the context of the urban heat island phenomenon. Numerous variables have been identified and these can be broadly divided into the following three categories:

a) The urban form and geometry of surrounding buildings
b) The geometry of the particular building of interest
c) Local wind and flow conditions

Within each of these categories are a series of individual variables which may exhibit a greater or lesser effect on the rate of convective heat transfer from a particular building. In the following paragraphs, each category is considered in turn and the factors deemed most significant identified.

It has been discussed previously in this thesis that the majority of the existing convective heat transfer coefficient correlations applied to the external surfaces of buildings have been derived using (potentially) unrepresentative flat-plates. For the purposes of the current research, it was therefore desirable to investigate the heat transfer processes which take place when the important aspects of the local urban environment are taken into account. The following list, although not exhaustive, details the factors which are generally used to describe a local urban environment for the purposes of categorisation and simulation:

- Plan area density of the surrounding buildings
- Street width (W)
- Building height (H)
- Building spacing along the row (S)
- Local topographical effects (e.g. hills, valleys, cliffs)
- Vegetation (e.g. trees, hedges)
- Terrain roughness (e.g. country, town, city)

The plan area density of buildings is defined as the total footprint area of the buildings as a proportion of the total ground area and consequently is a good indicator of the level of urbanisation. It is often employed in pollutant dispersion studies where it is the blockage of flow by the buildings rather than the individual geometries which is of primary interest. The plan view area tends not to be a good descriptor of building geometry as it does not take into account the number or dimensions of particular structures. To illustrate this Figure 8.1 shows three urban layouts with the shaded areas representing building footprint area. The first of these is a staggered array of cubes, the second consists of long rows of terraced buildings and the third more unusual cross-shaped buildings. All of these layouts have a plan area density of 37.5% and yet it is obvious that the flow patterns (and hence the CHTC's) around each type of building will be very different. Accordingly the plan area density was not used as the primary indicator of urban layout for the current research.

Instead, the surrounding urban form was defined by the spacing of the buildings along the street (S) and the width of the street canyons (W) as shown in Figure 8.2. These factors allow for a more useful definition of the arrangement of individual buildings along a particular street or complex. In practice, very few urban areas are completely regularly spaced and so it may be necessary to take typical or average values for these spacings when considering a town or city as a whole.

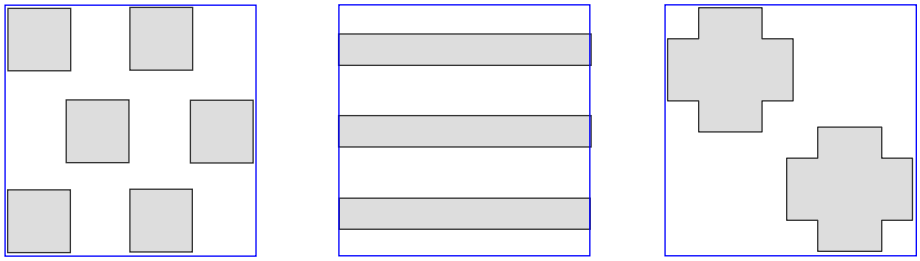

Figure 8.1: Comparison of building layouts with the same plan area density

Local topographical factors (such as the presence of hills and valleys) are known to have a significant impact on the local wind speeds around a location. As such, scaling factors are presented in the UK wind loading code BS 6399-2 (BSI, 1997a) to take account of the local flow modification effects of these features on the general wind conditions. It was not however practical to conduct the vast array of tests that would have been necessary to establish the effect (if any) of each of these features on convective heat transfer. As such, local topographical features were not simulated in the current wind tunnel studies. It may be possible to apply equivalent scaling factors to those presented in the existing wind loading codes to the CHTC results, although this has not been considered in the current research. It was similarly impractical to consider the effect of local vegetation within the urban fabric. The shelter effect provided by trees is typically limited to their immediate vicinity and does not have significant effect upon the upper stories of buildings. Furthermore the shelter effect varies greatly throughout the year; in summer when the trees are in leaf, winds tend to be deflected around and under the canopy layer giving rise to localised flow acceleration. Maximum amelioration of winds by deciduous trees usually occurs in the winter when the bare branches dissipate the winds energy. For this reason, trees and vegetation are normally omitted from pedestrian level wind environment studies conducted in the wind tunnel in order to provide baseline information.

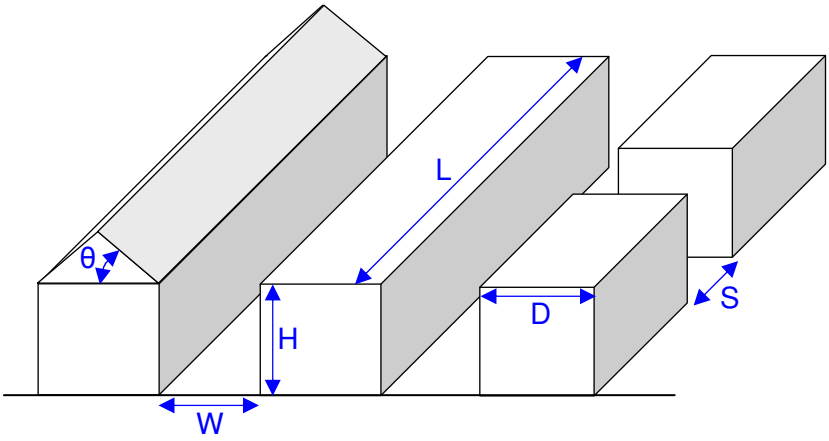

Figure 8.2: Typical street canyon geometries and notation

Let us now consider the geometry of the individual buildings (or rows of buildings) for which convective heat transfer data is required. Whilst buildings come in an almost infinite range of layouts and sizes, there are a number of common factors which can generally be used to describe them, as Figure 8.2 illustrates. These are:

- Height of the building (H)
- Depth of the building (D)
- Length of the building or row of buildings (L)
- Roof type (e.g. pitched, flat, hipped)
- Roof pitch angle (θ)
- Surface finish or roughness
- Surface features (e.g. doors, windows, balconies)

The primary dimensions of the building (i.e. its height, length and depth) are the most important descriptors of its shape and size. These lengths determine the effective area of the building 'seen' by the wind and hence the area over which convective heat exchange with the surroundings can take place. However it is not the actual dimensions that are of concern; rather it is the ratios of the dimensions that are of importance. If two buildings are considered, one having dimensions that are all exactly double that of the other, then the flow conditions around the two buildings will be similar. This dimensional similarity is the basis of wind tunnel testing of real buildings at model scale.

The height-to-width (H/W) property of street canyons was discussed in an earlier section of this thesis (see Section 7.4). This ratio relates the height of buildings to the spacing between then and thereby indicates how the wind will flow in and around the street canyons. Neither the height nor the spacings of the buildings alone is particularly useful, but the combined H/W property is. As a ratio, it also has the benefit of reducing the number of variables that are required to describe a particular situation. Building height is typically taken as the base dimension of such ratios and hence most other geometrical factors are related back to this length.

In a similar manner, the height-to-depth ratio of a building (H/D) provides an indication of the slenderness of a structure. A typical residential dwelling will have a height-to-depth ratio of approximately unity whilst a high-rise office block may have a ratio of five or more. The depth of a building has implications regarding the wake region which exists in the lee of the building; as the depth of building increases so the drag exerted on the building by the wind decreases. However, the height-to-depth ratio is perhaps not as significant as the height-to-width ratio of a building from the perspective of convection heat transfer. Therefore its value was fixed at unity for the current study in order to limit the number of experimental variables. The height and depth of the model was therefore equal.

The length dimension of a row of buildings can also be non-dimensionalised by relating it to the building height. Dividing the height of the building by the length of a long terrace, for example, would result in small decimal values. As a result the length of a row of buildings is more commonly expressed as a factor of the building height; a row of buildings 30 metres long of height 6 metres would therefore be said to have a length of 5H.

As a result of the land premium in central London, streets are typically lined with continuous rows of buildings on either side to maximise property density. This forms long street canyons which are often only broken up by adjoining roads. It is therefore convenient to think of these canyons as purely two-dimensional whereby the effect of length (presuming it is above a certain threshold level) is insignificant. This eliminates another of the experimental variables regarding the building geometry. Literature suggests a canyon length of 11H (i.e. eleven times the building height) as being the point at which the flow in the street becomes irrespective of length (Oke, 1987). This was also verified by the current author in Section 7.4.1 of this thesis. The length of the street canyons modelled in the current study was therefore held constant above this threshold value.

The roofs of buildings are also found in a wide range of styles and types. Some of the most common roof types are shown in Figure 8.3 below, with gable-ended, flat monopitched and hipped roofs being the most common in the UK. Additional variation is added by the pitch angle of the roof which typically varies from around 30 to 60 degrees from the horizontal. Horizontal flat roofs are also very common, especially on higher-rise inner city apartment and office blocks.

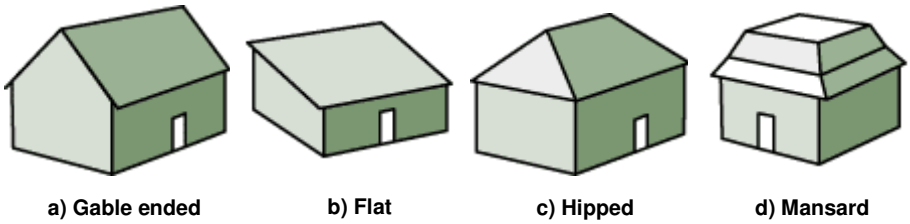

Figure 8.3: Some common roof types (source: BobVila.com, 2001)

Because of this wide variation it was decided that the case of flat roofed buildings (pitch angle of zero) would form the basis of the current research. This provided a simple arrangement with which to evaluate and develop the naphthalene sublimation methodology and also minimised the number of experimental variables which could have otherwise become overwhelming. Comparisons with existing data (e.g. the pressure distributions over a building) were also made clearer by the simple geometry of the flat-roofed model design.

It is not possible to accurately simulate the surface roughness seen on full-scale buildings when working at model scale in the wind tunnel. The surface roughness of the naphthalene coated model was determined by the coating process and was not expected to represent real-life values. A simple rule of thumb with regards to wind tunnel modelling of surface features is to assume that features with primary dimensions less than 0.5 m at full-scale have little significance on results at model scale. Accordingly features such as windows, doors and chimneys are not typically represented on wind tunnel models. It was similarly not viable to investigate the effect of such features using the proposed naphthalene sublimation technique. However, as such features typically have only a second-order effect on convective heat transfer when compared to other aspects of building design, this was not of great concern. Therefore neither the surface roughness nor surface features (such as windows and doors) were considered further in this study.

The third category of experimental variable identified at the beginning of this section was that regarding the prevailing wind conditions. These were considered previously in Chapter 6 when the wind tunnel simulation of the atmospheric boundary layer was discussed. In summary, there are five factors which are of primary importance as follows:

- Wind speed
- Approaching wind angle
- Mean vertical velocity boundary layer profile
- Turbulence intensity
- Turbulence length scales

The rate of convective heat transfer is primarily dependent upon the local wind speeds, as was shown by the sole dependence on this variable of the majority of the correlations presented in Chapter 3. The primary objective of this research was to present correlations for convective transfer as a function of wind speed. It was therefore critical that the naphthalene sublimation experiments were conducted at a range of wind speeds so that this dependence could be investigated. It was shown in Section 6.4 that tests could be successfully accomplished in the BRE wind tunnel at settings of between 10% and 50% of full speed; the maximum speed range is actually slightly wider than this. The low wind speed boundary is determined by the requirement to maintain turbulent flow and is satisfied by speeds above around 1 m/s (5% wind tunnel speed). The maximum speed is limited by the physical forces on the models and can be up to around 20 m/s (60% wind tunnel speed) depending upon the particular model arrangement.

Naphthalene sublimation results were therefore conducted at speed settings of 7.5%, 15%, 30%, 45% and 60% of full tunnel speed. These settings equated to wind speeds at the reference height (z = 900 mm) of approximately 2.6, 5.3, 10.4, 14.2 and 18.3 m/s respectively for the current boundary layer simulation. The corresponding building height Reynolds numbers (Re_H) for these experiments ranged from 8,174 to 57,474 based upon the model dimensions (94 mm) and the wind velocity at roof height. This provided a sufficient range of data from which to draw correlations between convective heat transfer and wind speed, whilst staying within the limits of the experimental procedures.

The approaching wind direction is particularly significant to the flow patterns around buildings when considering long two-dimensional street canyons. The flow regimes promoted by flow perpendicular and parallel to the streets are significantly different, with intermediate angles being a combination of these two extremes. The parallel and perpendicular flow scenarios were therefore essential to this study. An intermediate 45 degree prevailing wind direction was also included in order to quantify the relationship with the other two limiting cases. Previous surface pressure measurement studies suggested that the variation between other wind angles should be smaller and hence of lesser importance than the three key scenarios identified.

By selecting to simulate an inner-city urban scenario, the mean velocity and turbulence variables were fixed by the requirement for developing the correct urban boundary layer profile. With this research set in the context of inner-city urban heat island formation, convective heat transfer in rural or coastal locations is of lesser interest as the phenomenon, by definition, does not occur in such situations. Therefore a boundary layer simulation was developed which reproduced appropriate mean velocities, turbulence intensities and turbulence length scales for an urban area (see Chapter 6 for further details).

The selected experimental variables and their range of values for this research are summarised in Table 8.6 below. The factors that were maintained as constants throughout the experiments are summarised in Table 8.7.

Table 8.6: The selected experimental variables

Variable	**Values**
Wind tunnel speed settings	7.5, 15, 30, 45 and 60%
Wind angles	0, 45 and 90 degrees
Height-to-width ratios	0.25, 0.50 and 1.00

Table 8.7: Experimental constants

Constant	Value
Canyon length (L)	11H (or more)
Building depth (D)	1H (H/D = 1)
Roof pitch angle (θ)	0 degree (flat roof)

Although the plan area density of buildings was not to be used as a descriptor of the urban form in this study, it may be useful to note the values for the selected street canyon widths for comparison with other research. Table 8.8 shows the values calculated for the four height-to-width ratios tested using the naphthalene sublimation technique. It can be seen that a wide range of plan area densities was modelled from 20% up to 50% which covered the majority of typical urban and sub-urban scenarios.

Table 8.8: Street canyon geometry ratios

Street canyon width	Height-to-width ratio	Plan area density
1.0H	1.00	50%
2.0H	0.50	33%
4.0H	0.25	20%

8.3 Sensitivity analysis

In order to establish the sensitivity of the calculated convective heat transfer coefficients to the various input parameters and experimental variables, a sensitivity analysis was undertaken. Each of the parameters and variables, as listed in Table 8.9, were in turn increased by 10% and subsequently reduced by 10% from their 'standard' values. These baseline values were taken as those corresponding to naphthalene sublimation experiment number 2 as shown in Annex F. The recalculated convective heat transfer coefficients were noted and the percentage change evaluated. The results are presented in Table 8.9.

All convective heat transfer coefficient results in this thesis have been rounded off to two decimal places. This level of accuracy was selected based upon the accuracy of the values used in the various calculations. It provides an appropriate compromise between carrying forward rounding errors into subsequent (e.g. percentage change) calculations and not overstating the anticipated accuracy of the experimental results. It is expected that calculated convective heat transfer coefficients would in practice be stated to only one decimal place or less to reflect the likely errors inherent in such values.

The baseline convective heat transfer coefficient (i.e. that calculated using the 'standard values' measured during the experiment) was 36.39 W/m^2K.

The most significant experimental factor was found to be the temperature of the water bath, which in turn determined the temperature of the model and its naphthalene coating. A ±10% variation in the temperature (from 36 to 44 °C) gave a variation of between -28.4% and +41.1% in the calculated convective heat transfer coefficient. However, the water bath employed for this research features a digital control which regulates temperature to within ±0.1 °C of the required level. Also, the large flow rate of the water pump used ensured that there was minimal temperature drop at the model. Assuming an estimated maximum variation in water temperature of ±0.2 °C, this would correspond to a variation of ±1.7% in the resulting convective coefficient; this level is much more acceptable.

The next most significant factors were those of the measured reduction in thickness of the naphthalene coating on the model, and length of the experimental run time. Both of these properties affect the Sherwood number which is proportional to the change of coating thickness per hour. They are therefore also proportional to the Nusselt number and hence to the convection coefficients thereby calculated.

The properties of naphthalene were shown to be directly proportional to the convective coefficients obtained. A variation of ±10% in the density of the naphthalene or of the naphthalene gas constant gave an identical rise in the convective heat transfer coefficient. This is because each of these properties are used in the calculation of the Sherwood number to which the Nusselt number (and hence convection coefficient) are directly related. The case of the mass diffusivity coefficient of naphthalene vapour in air is similar.

Table 8.9: Sensitivity analysis for ±10% change in input values

	Standard value[a]	Variation in calculated CHTC			
		+10% value		-10% value	
Measurement		h_c	%	h_c	%
Thickness reduction[b]	283µm	40.03	10.0%	32.75	-10.0%
Experimental run time	3hrs	33.08	-9.1%	40.43	11.1%
Air temperature	18.8 °C	36.46	0.2%	36.31	-0.2%
Model (water) temperature	40.0 °C	26.06	-28.4%	51.33	41.1%
Air pressure	1012.5 mb	36.39	-	36.39	-
Relative humidity	32.4%	36.39	-	36.39	-
Air Constants					
Thermal conductivity	0.02526 W/m^{2}K	38.76	6.5%	33.94	-6.7%
Specific heat capacity	1004.4 J/kg.K	37.59	3.3%	35.11	-3.5%
Mass diffusivity coefficient	0.0232 m^2/h	33.14	-8.9%	40.50	11.3%
Gas constant	287.1 J/kgK	35.24	-3.2%	37.72	3.7%
Water vapour constants					
P_{sat} of water vapour	1704 Pa	36.39	-	36.39	-
Gas constant	461.5 J/kgK	36.39	-	36.40	-
Naphthalene constants					
Density	1175 kg/m^3	40.03	10.0%	32.75	-10.0%
Gas constant	64.89 J/kg.K	40.03	10.0%	32.75	-10.0%
Other					
Exponent 'n'	0.34	35.15	-3.4%	37.68	3.5%

The experimental results were largely insensitive to environmental conditions. Changing air temperatures gave a small variation (less than 1%) in the convection coefficients but this was not significant in comparison with other sources of experimental error. The temperature measurement primarily affects the calculation of air density, but it is also required for correct selection of values for the other properties of air from the appropriate tables. It would therefore be unwise not to record average values during the experiments.

Relative humidity and atmospheric pressure both had particularly negligible effects upon the data. Increasing the relative humidity to 100% (completely saturated air) would have given only a 0.1% rise in the convective coefficient since its only effect is via a small modification of the density of the air.

[a] Standard values were those recorded for Experiment 2 (see Annex F).
[b] Average thickness change in naphthalene coating during experiment on windward face.

Variation of atmospheric pressure over the likely range at which experiments may be conducted (say 950 to 1050 mb) had no effect upon the results obtained. Similarly the values employed for the gas constant and saturation pressure of water vapour were also unimportant; not surprising since these are used in the same air density calculations as relative humidity and atmospheric pressure. Recording of all four of these parameters could therefore be omitted in future studies.

Other properties of air, such as the thermal conductivity, specific heat capacity and gas constant were shown to be more critical. However, the values of these quantities were taken from published tables (Rogers and Mayhew, 1995) and are therefore known with confidence.

The value of the exponent ‘n’ in the heat-mass transfer analogy is determined by consideration of the respective parameters with values given in the literature ranging from 0.33 to 0.40. In their review of the naphthalene sublimation technique, Goldstein and Cho (1995) suggest that a value of 0.34 should be taken and so this value has been employed in the current work. Barlow and Belcher (2002) employed a similar value for ‘n’ of 0.33 for their work. The dependence of the results upon the magnitude of this exponent is relatively low. A variation of ±10% in the value (n = 0.31 to 0.37) covers the majority of the range of values given in the various literature, but results in a variation of the resulting convection coefficient of less than ±3.5%.

8.4 Assessment of measurement accuracy

Whilst the values calculated in the previous section provide an indication of the sensitivity of the results to variation in each variable, they do not take into account the actual accuracy with which measurements can be obtained. This will primarily depend upon the accuracy of the measurement instruments, but may also be affected by experimental procedure.

The maximum resolutions and accuracies of each of the seven main experimental variables which were recorded during the naphthalene sublimation tests are tabulated in Table 8.10 below.

Table 8.10: Measurement accuracies for experimental variables

Measurement	Units	Maximum resolution	Measurement accuracy
Thickness of naphthalene	µm	1 µm	±2.5 µm
Experimental run time	seconds	1 s	±1 s
Air temperature	°C	0.1 °C	±0.3 °C
Model (water) temperature	°C	0.1 °C	±0.2 °C
Air pressure	mbar	1 mb	±1 mb
Relative humidity	%RH	0.1%	±1.5% RH
Wind speed	m/s	0.1 m/s	±0.3 m/s

Whilst the stop watch used to record the experimental run time is accurate to the nearest whole second, the actual precision with which the test may be timed is dependent on more practical factors. These include the time taken for the wind tunnel to reach the required running speed and that taken for it to stop, the time required to measure the coating thicknesses using the Elcometer gauge and any delays whilst the models are setup and arranged into the required configuration. Therefore the actual error in the measurement of the experimental run time is likely to be significantly larger than one second, and is estimated to be up to approximately 5 minutes. The maximum resolutions and accuracies for the remaining measurements are determined as per the BRE calibrations of the respective devices.

The maximum instrument inaccuracies listed in Table 8.10 have each been entered into the calculation spreadsheet to determine its effect upon the 'standard' results defined in the preceding section. These results are noted in Table 8.11 as both the modified convective heat transfer coefficient (h_c) and the percentage change from the standard value. In this way, the actual effect upon the derived convective coefficient resulting from each potential measurement inaccuracy can be ascertained. The baseline value for the convective coefficient obtained using the standard values is, as before, 36.39 W/m^{2}K.

Table 8.11: The effect of measurement (instrument) inaccuracies

Measurement	Standard value	Maximum value		Minimum value	
		h_c	%	h_c	%
Thickness reduction	283 μm	36.71	+0.9	36.20	-0.5
Experimental run time	3 hrs	37.43	+2.9	35.41	-2.7
Air temperature	18.8 °C	36.38	0	36.40	0
Model (water) temperature	40.0 °C	37.01	+1.7	35.78	-1.7
Air pressure	1012.5 mb	36.39	0	36.39	0
Relative humidity	32.4 %	36.39	0	36.39	0

By combining the effects of each of these individual maximum measurement errors, it is possible to obtain a maximum overall error which would be obtained if each individual maximum inaccuracy occurred simultaneously. Such a calculation has been performed for both positive and negative errors, in order to give the maximum and minimum values for the convective coefficient. The results are shown in Table 8.12 below.

Table 8.12: Maximum potential errors

	h_c (W/m^{2}K)	% variation
Baseline value	36.39	-
Minimum value	34.50	-5.2
Maximum value	38.41	+5.6

The results shown in Table 8.11 reveal that the largest source of experimental error is likely to be attributed to the measurement of the experimental run time. Since the convective heat transfer coefficient is a measure of the rate at which convection occurs, this dependence is not surprising. Variation in the length of the naphthalene sublimation experiments may be as a result of the speed-up and slow-down times of the wind tunnel, and the time required to take naphthalene thickness measurements. A total, maximum value for these factors has been estimated to be five minutes, although this may actually be shorter in practice.

It can be seen in Table 8.12 that assuming that all of these errors occur simultaneously, the range of possible values for the convective heat transfer coefficient may vary between 34.50 and 38.41 W/m^{2}K. The baseline value for the convection coefficient (calculated using the 'standard' experimental data) is 36.39 W/m^{2}K. This variation therefore accounts for a percentage variation of between -5.2% and +5.6%.

These values represent the likely error for a typical set of experimental data. The actual significance of the errors may vary depending upon the environmental conditions and details of the specific test. However, an overall typical experimental error in the derived convective heat transfer coefficient of ±6% is proposed as encompassing the majority of likely scenarios.

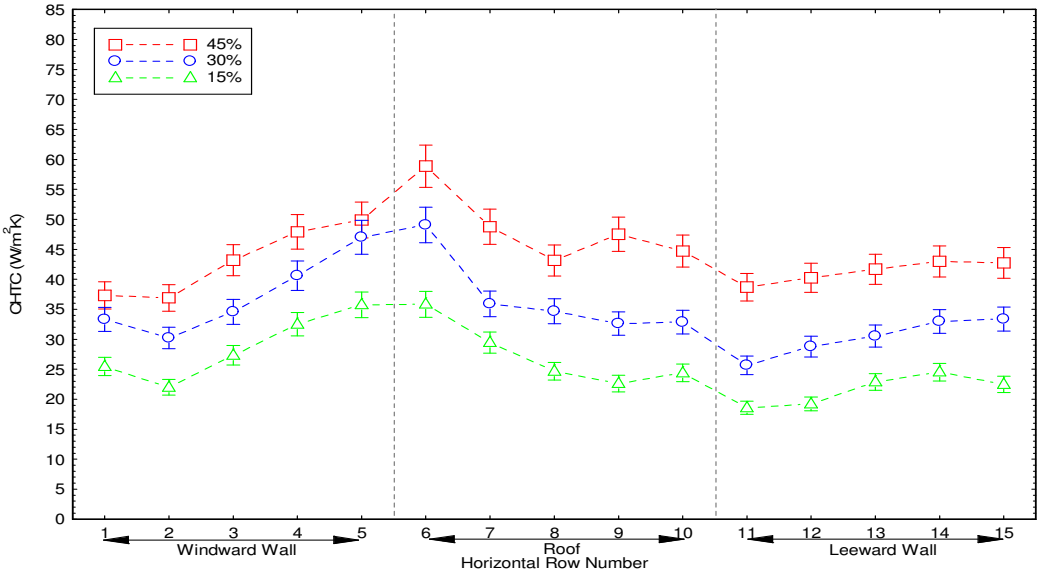

Figure 8.4: Typical experimental results for H/W = 0.50 showing ±6% error bars

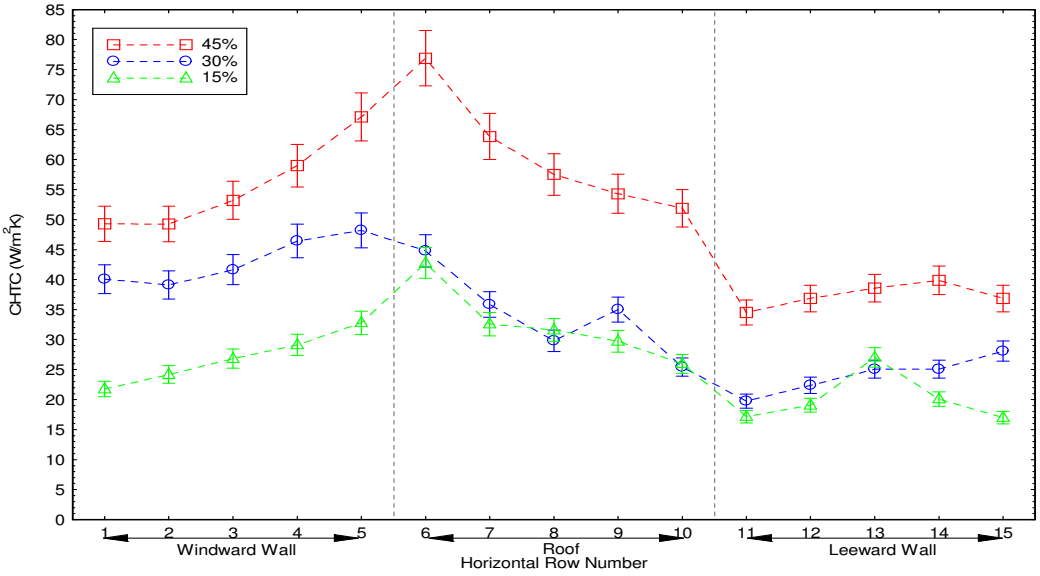

Figure 8.5: Typical experimental results for H/W = 0.25 showing ±6% error bars

Figure 8.4 above shows the results from tests conducted at a height-to-width ratio of 0.50 with the canyon orientated perpendicular to the flow. The error bars shown represent a variation in the presented convection coefficients for each wind speed of ±6%. Similarly, the plot shown below in Figure 8.5 shows the error bars attributable to data for tests conducted at a height-to-width ratio of 0.25. It is evident in both of these cases that the experimental errors which have been identified in this chapter are not significant to the overall patterns in the convective coefficients, or the relative magnitudes between alternative surfaces. The proposed maximum error of ±6% is considerably lower than may be attributed to other experimental techniques, particularly ones in which the effects of radiation or factors such as maintaining constant surface temperatures (e.g. using heat flux meters) are considerable.

8.5 Assessment of measurement uncertainties

The 'Guide to the Expression of Uncertainty in Measurement' (ISO, 2008) was first published in 1993 and is more usually referred to by its 'GUM' acronym. The text of the latest ISO GUM document has been republished by a number of organisations, most notably in the form of the Joint Committee for Guides in Metrology's 'JCGM 100' document (JCGM, 2008a) and the accompanying 'JCGM 101' supplement (JCGM, 2008b). However, a more practical guide to determining experimental uncertainty for laboratory workers is provided by the United Kingdom Accreditation Service in the document 'M3003: The Expression of Uncertainty and Confidence in Measurement' (UKAS, 2007). This text is fully consistent with the original ISO document in terms of both its methodology and terminology.

An overview of the methodology described in the 'GUM' and its related documents is provided in Annex D of this thesis. This methodology represents the current 'state-of-the-art' with regards to the assessment of uncertainty in experimental measurements and has therefore been used to assess the results of the current naphthalene sublimation technique. The full calculation of the measurement uncertainty in the convective heat transfer coefficients is provided in Annex D. As in previous sections, the data obtained from experiment number 2 (see Table 8.9 and Annex F for further details) were used as the basis for this calculation.

The combined standard uncertainty in the value of the convective heat transfer coefficient for a typical naphthalene sublimation experiment has been calculated to be ±1.029 $W.m^{-2}K^{-1}$ with a normal probability distribution function. The expanded uncertainly (taking k = 2 for 95% confidence level) is therefore ±2.058 $W.m^{-2}K^{-1}$, but this should only be quoted to two significant figures.

The value for the typical convective heat transfer coefficient result obtained in naphthalene sublimation experiment number 2 is therefore 36.4 ± 2.1 $W.m^{-2}K^{-1}$. This value equates to an error of ±5.8%.

This result obtained using the 'GUM' methodology is almost identical to the uncertainty obtained from the basic assessment of the worst case instrument inaccuracies detailed previously in Section 8.4. Whilst this similarity is perhaps surprising, it does not imply that the two methodologies are in any way equivalent. It does however mean that the two plots provided previously to show the relevance of a ±6% uncertainty in the naphthalene sublimation results (see Figure 8.4 and Figure 8.5) are also illustrative the findings of the current 'GUM' analysis.

Chapter 9 The effect of wind speed upon convective transfer

9.1 Introduction

It was noted previously in Chapter 3 that convection from surfaces is typically a mixture of both free and forced heat transfer components. The free (or natural) component of convection is that which occurs in the absence of an externally driven flow, or in the case of the urban environment, in the absence of wind. In such circumstances the fluid gains upward velocity as a result of the buoyancy forces which arise when its temperature increases. This reduces the density of the fluid relative to its surroundings and so it begins to rise.

In contrast, when the flow over a surface is driven by some external mechanism (for example, on a windy day), the convective removal of latent heat becomes much more effective. In such circumstances free convection may become insignificant since the rate of forced convection is typically several orders of magnitude greater. It is therefore evident that the local wind speeds around a building will have a significant impact upon the rate of convective heat transfer occurring at its external surfaces.

A series of naphthalene sublimation experiments have been conducted in order to investigate the relationship between the wind speeds in and above a street canyon, and the convective heat transfer which occurs from the building surfaces. Measurements were made over an array of points covering the windward, leeward and roof surfaces of a cube-shaped wind tunnel model. This was positioned at the centre of a long row of buildings (L = 11H) and the resulting street canyon was orientated perpendicular to the wind (a prevailing wind angle of 0 degrees).

The height-to-width ratio of the street canyon was set at 0.5, which is to say that the spacing between the rows of cubes was twice the model height. At this spacing, the wake interference flow regime illustrated in Figure 9.1 is expected to occur whereby the flow around each subsequent row of buildings is influenced by and mixed with that from the upwind rows.

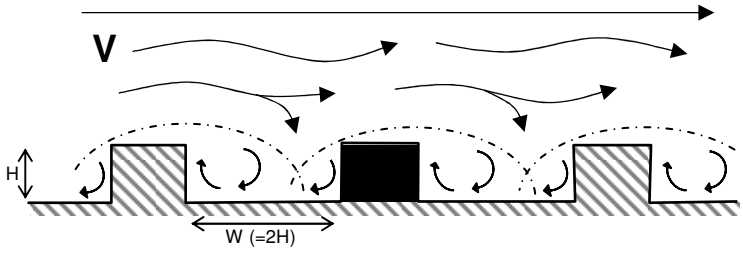

Figure 9.1: The wake interference flow regime at height-to-width ratio of 0.5

In order to assess the effect of wind speed upon the rate of convective transfer, experiments were conducted with the wind tunnel running at speed settings of 7.5, 15, 30, 45 and 60 percent of full speed. These settings equate to wind speeds at the reference height (z = 900 mm) of approximately 2.6, 5.3, 10.4, 14.2 and 18.3 m/s respectively for the current boundary layer simulation. The wind speeds at other heights in the boundary layer may be calculated with knowledge of the wind tunnel velocity profile; these are detailed as required in the following discussions.

The range of wind speeds in which experiments could be conducted was limited by the practical requirements of wind tunnel testing and the need to maintain the correct turbulent boundary layer conditions. Below a tunnel speed setting of approximately 5 percent (≈1 m/s), the flow is unlikely to exhibit fully-developed turbulence and hence the required atmospheric boundary layer simulation is not attained. Kelnhofer and Thomas (1976) showed that low levels of turbulence can have a significant impact upon the flow patterns occurring around the models and therefore upon the rate of convection from the surfaces. It is therefore important to test at wind speeds above this level.

Above a speed setting of approximately 60% (≈18 m/s), the resultant high wind loads are such that damage is likely to occur to the flow conditioning elements of the wind tunnel. The models may also be moved by the wind making it difficult to maintain the desired test geometries. Another concern is localised heating of the model as a result of the recovery effect; this would affect the rate of sublimation of naphthalene since its vapour pressure is highly dependent upon surface temperature. As a result of these factors, wind tunnel speed settings of between 7.5 and 60 percent have been selected as being the optimum range over which the naphthalene sublimation tests should be conducted.

A further naphthalene sublimation experiment has been conducted at zero wind speed (i.e. with the wind tunnel turned off) in order to establish the magnitude of the free convection coefficients over the surface of the cube. The results from this experiment are initially presented as a separate case, but are later combined with the forced convection results in order to aid determination of the overall relationships.

The long street canyons modelled in these experiments can be considered to be two-dimensional for perpendicular wind directions. Therefore, away from the ends of the canyon, the convective heat transfer coefficients are likely to be uniform at a given height along the surfaces of the cubes. The average convective coefficient for each row of measurement points has therefore been calculated. Variation in the results along each of these rows should be minimal with perpendicular flow and so this averaging thereby gives greater accuracy and confidence in the experimental data. It also has the advantage of making the data easier to understand and compare as it may then be presented in two-dimensional plots, without the complication of considering the third-dimension along the canyon. Further confidence in the experimental data has been obtained by repeating each set of naphthalene thickness measurements twice; these have been compared and averaged to ensure the accuracy of the raw data. Any obviously erroneous results were removed from the data prior to processing.

The results obtained from these experiments have been plotted as graphs of the convective heat transfer coefficients versus the location on the model. The x-axis of the graphs gives the row number of the measurement locations as explained in Figure 7.5. These rows are numbered from 1 (at the base of the windward surface of the model) through to 15 (at the base of the leeward surface). The windward edge of the roof therefore lies between rows 5 and 6, and the leeward edge between rows 10 and 11. The respective surfaces are also labelled next to the x-axis to aid understanding of the presented results. The y-axis of the graph gives the calculated convective heat transfer coefficient (in W/m^2K) averaged over each row of measurement points.

Full details of the environmental conditions and variables for each experiment are provided in Annex F at the end of this thesis. A full point-by-point breakdown of the experimental data (including the measured reductions in naphthalene coating thickness and the Nusselt numbers / CHTC's thereby calculated) is tabulated in Annex G. The summarised results presented in this Chapter will allow the underlying relationships between wind speed and convective transfer to be established more clearly.

9.2 Free convection results

In order to establish the free components of convective transfer occurring from the model, an experiment was conducted in which the wind tunnel remained switched off. All other variables remained as per the main series of tests outlined previously, except that the run time was extended to a total of four hours to account for the lower rate of free sublimation of the naphthalene coating. The results from these tests are displayed in Table 9.1 and shown graphically in Figure 9.2 below. The standard deviations of the five measurements in each row are also shown as an indication of the inherent variation. Overall surface averages are also given.

Table 9.1: The results of the free convection experiment

Windward surface		
Row number	CHTC (W/m^2K)	St. dev.
1	7.01	1.28
2	6.34	2.36
3	5.73	2.06
4	6.68	1.81
5	5.43	1.27
Avg.	**6.24**	**1.76**

Roof surface		
Row number	CHTC (W/m^2K)	St. dev.
6	6.59	2.40
7	7.53	3.51
8	4.98	1.02
9	7.01	2.30
10	6.34	1.80
Avg.	**6.10**	**2.38**

Leeward surface		
Row number	CHTC (W/m^2K)	St. dev.
11	6.50	0.62
12	4.93	1.35
13	4.51	2.49
14	6.40	1.05
15	5.94	2.41
Avg.	**6.32**	**1.94**

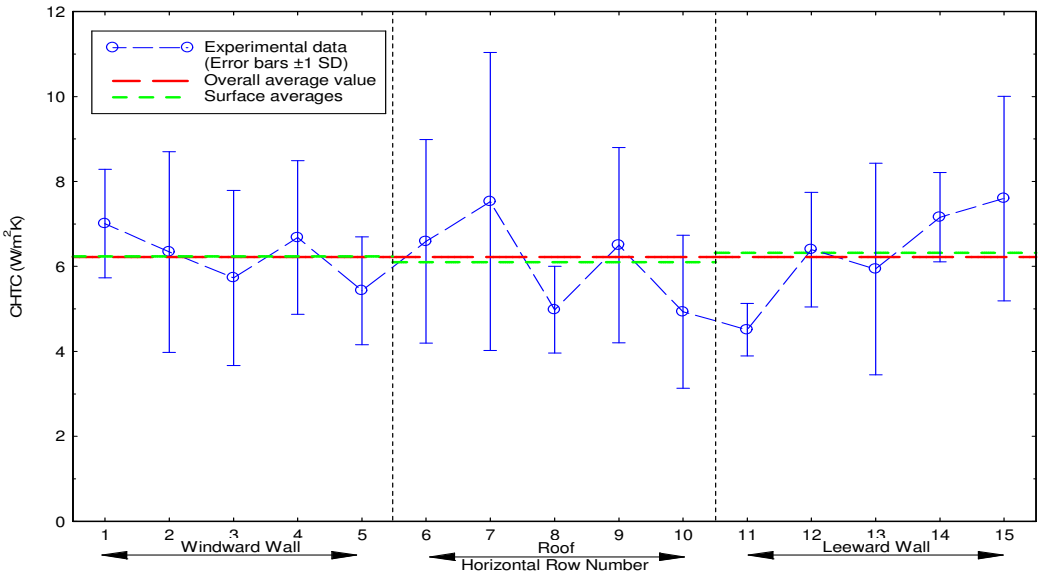

Figure 9.2: Free convection coefficients derived from zero wind speed test

From this plot, it is evident that the free convection coefficients remain relatively constant over the whole surface of the model, with values varying between approximately 4.5 and 7.5 W/m^2K. The average value across all three surfaces of the model has been calculated to be 6.22 W/m^2K; this is shown on Figure 9.2 as the red (long-dashed) line.

The three green (short-dashed) lines show the average convection coefficients across each of the individual surfaces. It can be seen that the surface averages for the windward (6.24 W/m^{2}K), leeward (6.32 W/m^{2}K) and roof (6.10 W/m^{2}K) faces are very similar and within 0.1 W/m^{2}K of the overall average value. There is little distinction between the horizontal and vertical surfaces.

There is clearly some variation in the results across the fifteen rows of measurements points, although it is difficult to positively identify any specific spatial trends. The error bars shown in Figure 9.2 indicate a range of plus and minus one standard deviation from the mean values. In the majority of cases, these ranges include the respective surface and model averages. The only significant exception is row 11 which has both the lowest average value and smallest standard deviation. This data point lies well below the averages in comparison to the other data points. No clear explanation for this anomaly has been found and it is therefore probably attributable to error in the measurement processes.

Notwithstanding the relatively small variations between measurement rows and the significant standard deviations, there does appear to be a slight trend across these two vertical surfaces. The convective heat transfer coefficients are greatest at the bottom of these two surfaces (rows 1 and 15) and then decrease with height towards the roof. Whilst this trend is admittedly slight, such an effect was predicted in the review of existing convective heat transfer research documented in Chapter 3. The rate of free convection was shown to be dependent upon the length of a vertical surface and is greatest at its base since the surrounding fluid's ability to cool the adjacent surface reduces as it is heated and rises. Similarly, air at the base of the wind tunnel model also has the greatest ability to absorb naphthalene since the vapour concentration is less. As the air rises (due to heat supplied by the heated model) and becomes more saturated with naphthalene vapour, so its ability to absorb more of the chemical reduces. The convection coefficient thereby reduces with height. The effect is quite small in this particular instance and this is probably due to the limited length (94 mm) of the surfaces involved. This would suggest that the current free convection value represents the maximum rate which will occur near to the base of a larger vertical surface and that the average value over such an area may therefore be significantly lower.

The current surface averaged results suggest that an appropriate value for the convective heat transfer coefficient in still conditions should be between 6.1 to 6.3 W/m^{2}K. A summary of the free convection coefficients proposed by previous researchers is given in Table 9.2 below. These results are calculated from the linear (low wind speed) expressions determined by each author where a value of zero has been taken for the wind speed. The values have been ranked in order of their magnitude and the current experimental result is highlighted in bold text.

The correlation presented by Watmuff *et al*. (Equation 3.29) has been neglected from this list due to the author's erroneous subtraction of the radiative component, resulting in relatively low convection coefficients. The range of the values tabulated can be seen to vary from just 2.5 W/m^{2}K (from BS EN 6964 for a vertical surface) to 11.4 W/m^{2}K (from Sturrock for a windward surface). The current average value of 6.22 W/m^{2}K over the three model surfaces lies almost at the centre of this range. The range of values for the individual rows presented in Table 9.1 (4.51 to 7.53 W/m^{2}K) corresponds with all but the outlying values.

Table 9.2: Summary of the Range of values for the free convection coefficient

Source	Surface type	Reference	CHTC (W/m^{2}K)
BS EN 6946	Vertical surfaces	Table 3.6	2.50
BS EN 6946	General equation	Eqn. 3.52	4.00
Loveday and Taki	Leeward	Eqn. 3.42	4.93
BS EN 6946	Horizontal surfaces	Table 3.6	5.00
Rowley *et al*.	Smooth plaster	Eqn. 3.19	5.30
Juerges	Polished plate	Eqn. 3.14	5.58
Sturrock	Leeward	Eqn. 3.25	5.70
Juerges	As-rolled plate	Eqn. 3.12	5.81
Juerges	Shot-blasted plate	Eqn. 3.13	6.16
Current work	**Overall average**	Table 9.1	**6.22**
Nicol	From a window	Eqn. 3.28	7.55
Loveday and Taki	Windward	Eqn. 3.41	8.91
Sturrock	Windward	Eqn. 3.24	11.40

The result of the current work is similar to the results proposed by Juerges for his three plate roughnesses, especially those for the shot-blasted finish. This is a significant result since Juerges' values have been the basis for many of the convection correlations still in use today. It is likely to be indicative of the similarity in length scales of the models used in the two experimental techniques. The proposed value is also close to that derived by Nicol for a window and by Sturrock for leeward surfaces. It is interesting to note the large variation in the results given by Sturrock's leeward (5.7 W/m^{2}K) and windward (11.40 W/m^{2}K) expressions when the wind speed is taken as zero. In such circumstances it would normally expected that both expressions give a similar result since without wind, there is no differentiation of windward or leeward surfaces. Sturrock's windward expression is generally regarded as giving vales which are too high; both comparisons with the other values shown in Table 9.2 and with the current result would certainly support this conclusion.

The fixed coefficient given in BS EN 6946 for vertical surfaces is the lowest of those tabulated at only 2.50 W/m^{2}K. The next lowest value is that calculated from the equation provided in the same Standard, although presumably the free convection constants should be used in preference to the calculated values in the absence of wind. This result is significant as it implies that the latest guides (e.g. the CIBSE 2006 Guide which features values derived from BS EN 6946:1997) are providing designers and engineers with convection rates which are significantly lower than those determined by the majority of heat transfer research, including the current study. Such an underestimate of the rate at which convective heat transfer occurs could have significant impact upon the overall thermal design and functioning of a building.

The values for free convection obtained from this experiment will also be used to provide a zero-intercept value for correlations relating convective coefficients to wind speed in subsequent sections of this thesis.

9.3 Forced convection results

The results obtained in the series of naphthalene sublimation experiments at various wind speeds are presented in Figure 9.3 below. The 'row averaged' data for the five wind speeds are presented together on the graph to allow direct comparison of the various values of convective heat transfer coefficient.

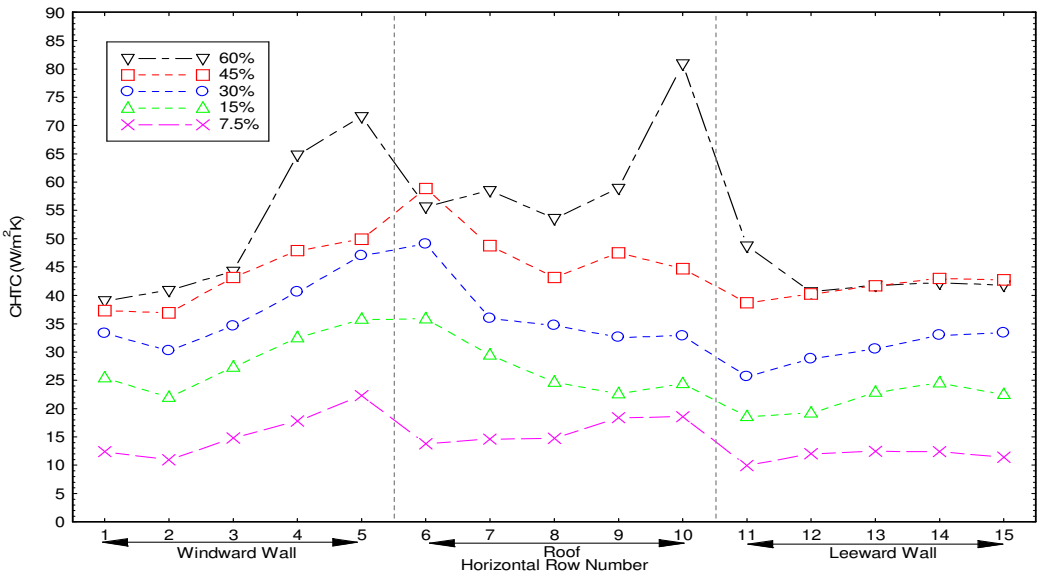

Figure 9.3: The measured CHTC's across the two-dimensional model

Setting the two large peaks in the 60% data to one side for the moment, it can be seen that the overall trends and patterns in the convective coefficients for the five sets of data are largely similar. This confirms that the flow patterns over the models must be independent of wind speed. As expected, the highest rates of convective transfer occur at the fastest wind speed and the lowest rates at the slowest wind speed.

The highest rates of convective transport were typically measured on either side of the windward edge of the roof (rows 5 and 6) for all but the 60% speed experiment. This was to be expected since the leading edge of the roof is the most exposed area of the models, and also the area of highest local velocities as the flow accelerates up and over the roof. It is likely that there exists a peak coefficient along this vertex which exceeds the measured values on either side, but which it was not possible to measure. The Elcometer gauge employed to measure the thickness of naphthalene layer needed to be a minimum distance from the edge of the metal substrate in order to function correctly. This meant that measurements could not be made directly adjacent to the vertices of the model and hence this peak value could not be determined.

It is however possible to identify such regions of peak convective transfer by returning the model to the wind tunnel after the main sublimation test has ended. By noting the areas at which the metal substrate of the model becomes exposed first, the regions of peak sublimation (and therefore maximum convective heat transport) can be identified. This theme is discussed further in Chapter 12 of this thesis.

In contrast to the other two surfaces, the calculated convective coefficients on the leeward face of the model are relatively uniform, as illustrated by the smoothness of the curves shown in Figure 9.3 over this region. This is because the flow directly adjacent to the rear face of the model is less turbulent and thus by definition, more homogenous across the surface. Wake regions are typically low speed, low pressure areas and therefore the scouring effect of the wind will be less than at the windward surface. The localised peaks noted on other surfaces are not present on this face of the model, although a small reduction in convection was noted at the very top of the leeward surface.

The actual convective heat transfer coefficients calculated from the naphthalene experiments (as graphed in Figure 9.3) are presented as the row averages in Table 9.3 below. The result sheets detailing the environmental conditions, wind tunnel simulations and processed data (from which Table 9.3 is summarised) are provided in Annex F at the end of this report.

Table 9.3: Convective heat transfer coefficients presented by row number

		CHTC's (W/m^2K)				
	Row number	**Low speed (7.5%)**	**Slow speed (15%)**	**Medium speed (30%)**	**Fast speed (45%)**	**High speed (60%)**
Windward	1	12.41	25.44	33.32	37.32	39.05
	2	10.96	21.98	30.22	36.92	40.89
	3	14.80	27.32	34.59	43.18	44.26
	4	17.80	32.50	40.60	47.91	64.77
	5	22.29	35.76	47.02	49.90	71.59
Roof	6	13.80	35.84	49.07	58.87	55.64
	7	14.61	29.45	35.92	48.78	58.52
	8	14.76	24.67	34.68	43.16	53.58
	9	18.40	22.62	32.62	47.51	58.93
	10	18.56	24.40	32.86	44.72	80.87
Leeward	11	9.96	18.58	25.66	38.69	48.71
	12	12.03	19.20	28.79	40.25	40.62
	13	12.47	22.88	30.52	41.69	41.78
	14	12.41	24.54	32.96	42.98	42.20
	15	11.43	22.48	33.38	42.73	41.82

In order to make it easier to visualise the convective coefficients results, this same data has been re-plotted in Figure 9.4 with the convective heat transfer coefficients shown versus the wind speed for each of the 15 rows of data points. Several things are obvious from this graph: Firstly it confirms that the highest rates of convective transfer generally occur from the areas at the leading-edge of the roof (row 6) followed by the top of the windward face (row 5 and to a slightly lesser extent row 4). These three curves are clearly higher than the others for the majority of the wind speed range.

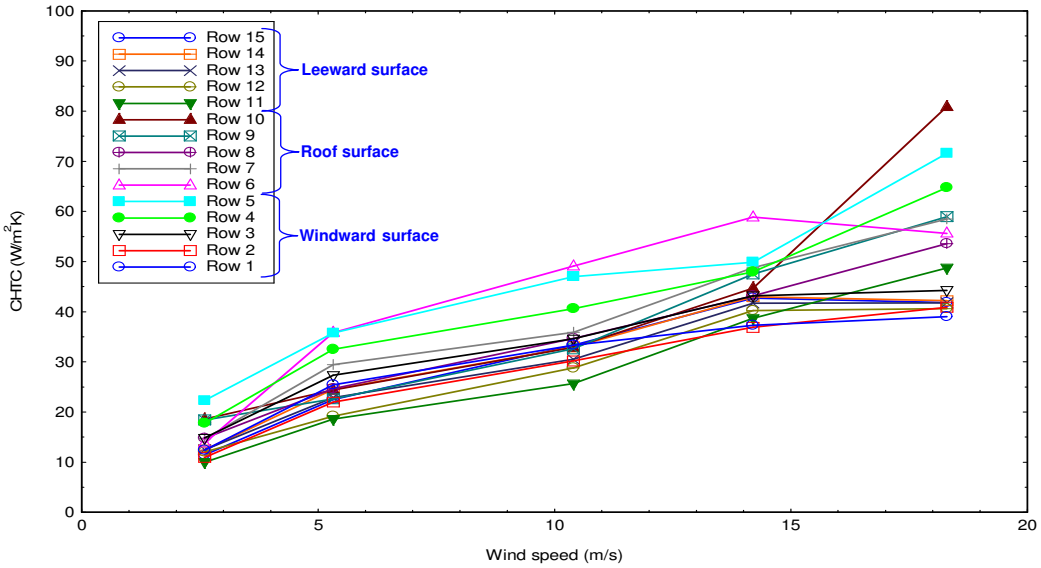

Figure 9.4: Variation of CHTC by row with wind speed

The majority of the data lines are clustered closely together at similar ranges of convective heat transfer coefficients. The lowest rates of convective transfer are seen to occur at the top of the leeward surface of the model (rows 11 and 12) which is thought to be the area around the model at which the flow will be the most sheltered and least turbulent. With the exception of the rows already identified, the majority of the data points around the model are surprisingly similar and frequently overlap. This implies that there is actually relatively little variation in the rates of convective transfer from buildings for a given wind speed, apart from at a few exposed areas where localised peaks have been shown to occur. This finding will make it easier to present representative expressions for use in building thermal simulations since a range of correlations for each particular region of the building may overly complicate the required calculation process. The results so far obtained indicate that it may be possible to identify expressions for the average convective coefficients across each surface, and possibly even across the whole building, which are more representative than those currently employed by recent design guides.

A large peak in the convective coefficients at the leeward edge of the roof (row 10) is evident for the fastest wind speed shown in Figure 9.3. Whilst a peak in this region is typical of the majority of data sets, the dramatic rise from the previous (45%) wind speed appears to be disproportional. This feature of the results can also be seen in Figure 9.4 as a dramatic rise in the convective coefficient at the right-hand end of the curve for row 10. Whilst an upward slope in this part of the graph is again typical for most of the rows, the magnitude of the gradient for this particular row is much higher than that of its counterparts.

A similar (but much more slight) rise in the convective coefficients was seen in this area for lower wind speeds and is attributed to the reattachment of the flow which separated at the leading edge of the roof. However, at this highest speed setting, the effect is significantly more pronounced and the increase above the next fastest wind speed results is significantly greater than was measured elsewhere on the model. A comparable effect can also be seen at the top of the windward wall (rows 4 and 5). This region of the model is also relatively exposed, being above the shelter layer provided by the upwind row of buildings and is hence subjected to the higher speed winds flowing above the models. It is these high local velocities which result in the relatively large convective heat transfer coefficients at the windward edge which have been noted for all of the wind tunnel speeds tested. However, the disproportional peak seen at the fastest (60%) speed setting is very much outside the anticipated range when compared to the increases seen at other locations.

These two unexpected peaks indicate that a secondary effect (or effects) may be occurring to assist in the naphthalene removal from this particular area of the cube. Mechanical erosion of the chemical by the high-speed flow is an obvious possibility and is undesirable since it has no analogous heat transfer process. Another possible cause is that the jet of impinging air at the reattachment point may also have raised the local surface temperature via the recovery effect. As the vapour pressure of the chemical is highly dependent upon temperature (see Section 8.3), this would result in a rise in local convection coefficients not seen at lower wind speeds.

These factors were considered during the design stage of the naphthalene sublimation experiments and were key to the selection of the maximum running speed. This finding confirms that it is not possible to run naphthalene sublimation experiments at higher wind tunnel speeds. The exact maximum will depend upon factors such as the model geometry and ambient temperatures. However, it seems in this instance that a speed setting of 60% in the BRE wind tunnel (approximately 18 m/s free-stream wind speed) is on the limit; the most exposed locations are beginning to be affected by the secondary naphthalene removal processes, but the majority of locations are unaffected.

9.4 Derivation of equations with respect to the free-stream velocity

Expressions for convective heat transfer coefficients have traditionally been presented as either linear (i.e. $h_c = ax + b$) or power-law (i.e. $h_c = ax^b$) relationships. The linear form is the most common and has the advantage that the free convection coefficient of heat transfer is represented by the intercept on the y-axis. In contrast, a power-law equation ultimately has a zero intercept and therefore free convection is effectively neglected from the expression. Whilst this issue may be overcome by specifying a minimum value of convection which should be substituted in conditions where the equation gives a lower value, it is usually preferable to have a single expression for all scenarios.

However, power-law expressions have the advantage that they typically represent the convective coefficients at higher wind speeds more accurately since the rate of increase begins to tail off. Linear expressions have the same rate of increase of convective coefficient irrespective of wind speed and thereby predict ever-increasing levels of forced convection. In reality, there is an upper limit to the rate of convective heat transfer that can be achieved for any given surface and geometry.

To overcome these issues, some researchers (for example Juerges, 1924) have chosen to represent convection at low wind speeds (say below 5 m/s) with a linear expression, and that at higher wind speeds with a power-law curve. This combination of several simple expressions has allowed them to achieve the desired representation of their data over the required wind speed range without the need for more complicated, higher-order expressions.

The current naphthalene sublimation results for each of the five wind speeds are shown in Table 9.4. In addition to the familiar surface averaged results, an ‘exposed edge’ value has also been calculated. This is the combined average of the top row of the windward face (row 5) and the leading edge row along the front of the roof (row 6). These regions of the cube were highlighted in the previous Section as being the regions in which peak convective heat transfer will typically occur. Hence this exposed area average is included alongside the surface averaged data to allow comparison of the peak heat transfer region with the wider results for each of the surfaces and the building as a whole. Such a value may also be more appropriate for comparison with results presented by previous researchers (e.g. Sturrock, 1971) working at full-scale who have presented relationships for so called ‘exposed locations’ on buildings which protrude significantly above their surroundings.

The reference wind speed (V_f) for each test was recorded at a height of 900 mm in the wind tunnel boundary layer using a Constant Temperature Anemometry (CTA) probe (see Chapter 6.2). This measurement represents the free-stream velocity in the wind tunnel away from the local influences of the ground, roughness elements and models. It is therefore directly comparable with the results for alternative building configurations discussed in latter sections of this thesis as it is far enough above the ground to be unaffected by the model layout.

Table 9.4: Experimentally obtained convective heat transfer coefficients

		Wind tunnel speed setting ← Slowest Fastest →				
Measurement	**Units**	**7.5%**	**15%**	**30%**	**45%**	**60%**
Average CHTC over all surfaces	(W/m^2K)	14.44	25.84	34.81	44.31	52.21
Average CHTC over windward surface	(W/m^2K)	15.65	28.60	37.15	43.05	52.11
Average CHTC over roof surface	(W/m^2K)	16.03	27.40	37.03	48.61	61.51
Average CHTC over leeward surface	(W/m^2K)	11.66	21.54	30.26	41.27	43.03
Average CHTC over 'exposed edge' area	(W/m^2K)	18.05	35.80	48.05	54.39	63.62

The data obtained in still conditions and at the five wind speeds have each been plotted and both linear and power-law curves fitted to the data points. The equations of these best-fit curves have been obtained, as well as the statistical measures of the coefficient of determination (*R^2 value*) and the maximum deviation. These are assessed a later point in order to help determine the most suitable format for the presentation of the experimental results relating wind speed to the rate of convective transfer.

Separate graphs are presented for the following data sets in Figure 9.5 to Figure 9.9 on the following pages (the respective measurement location rows for the relevant surfaces are given in parentheses):

- Average convective coefficient over all three surfaces (rows 1 to 15)
- Average convective coefficient over the windward surface (rows 1 to 5)
- Average convective coefficient over the roof surface (rows 6 to 10)
- Average convective coefficient over the leeward surface (rows 11 to 15)
- Average convection coefficient over the exposed edge (rows 5 and 6)

In each case, the y-axis of the graph indicates the measured convective heat transfer coefficients and the x-axis the wind speed measured at the free-stream reference height of 90 m full-scale (900 mm at model-scale in the wind tunnel). The dashed blue lines represents the linear best-fit relationships and the solid red lines represent the best-fit power-law curves. The green data points show the actual convective heat transfer coefficients obtained from the naphthalene sublimation experiments at each of the wind speeds tested.

The equations of both the linear and power-law correlations obtained from the data are noted in the legend of each plot. They are later summarised in Table 9.5 (for linear relationships) and Table 9.6 (for power-law relationships) to aid comparison and discussion.

Both types of curves have been fitted to the experimental data using the *EasyPlot* graphing program written by Spiral Software. This employs the *downhill simplex method* for polynomial curve fits and also calculates the coefficient of determination and maximum deviation as part of its curve fitting routine.

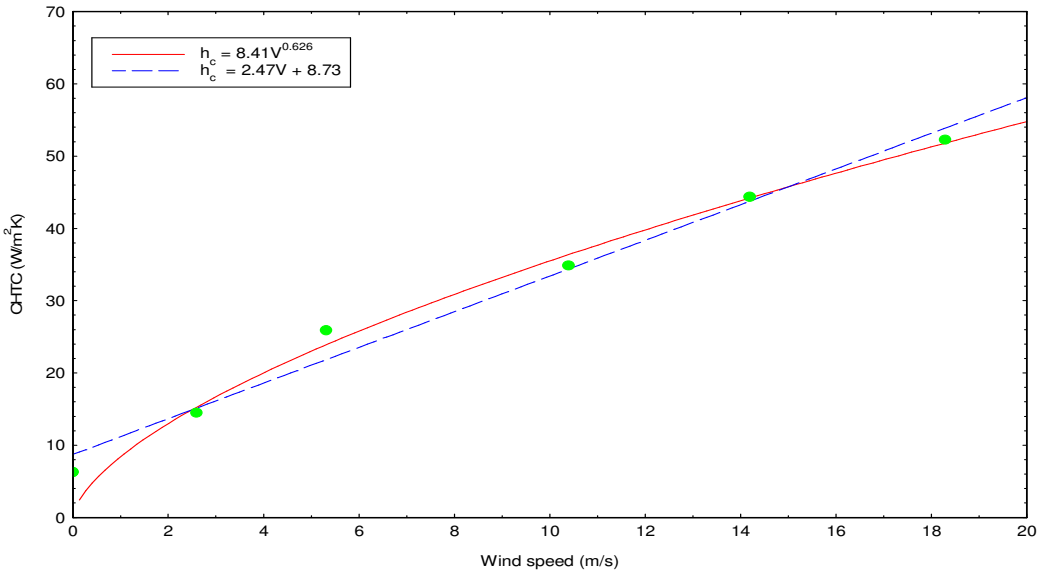

Figure 9.5: Average convection coefficient data across all surfaces

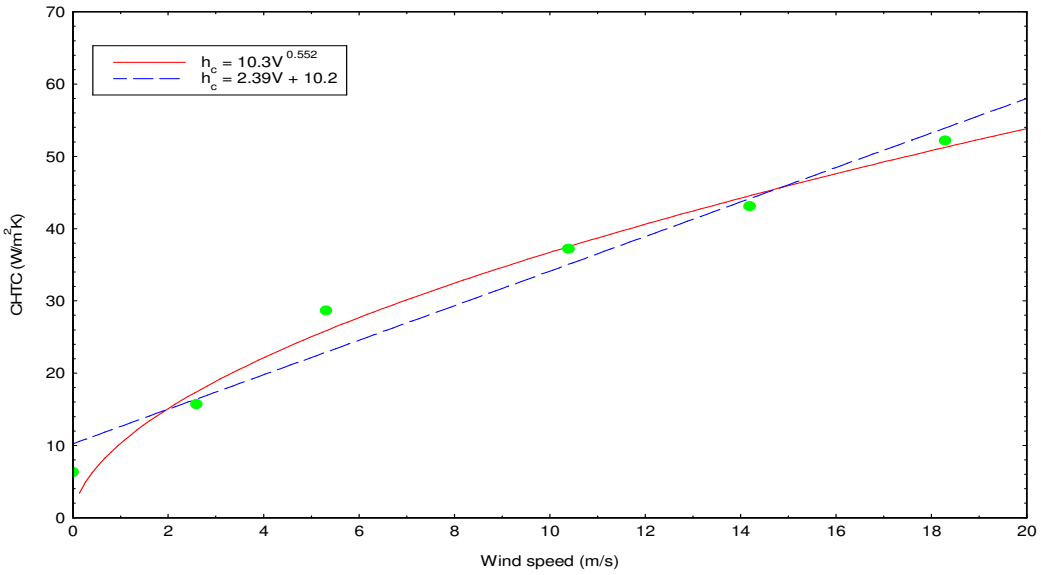

Figure 9.6: Average convection coefficient data across the windward surface

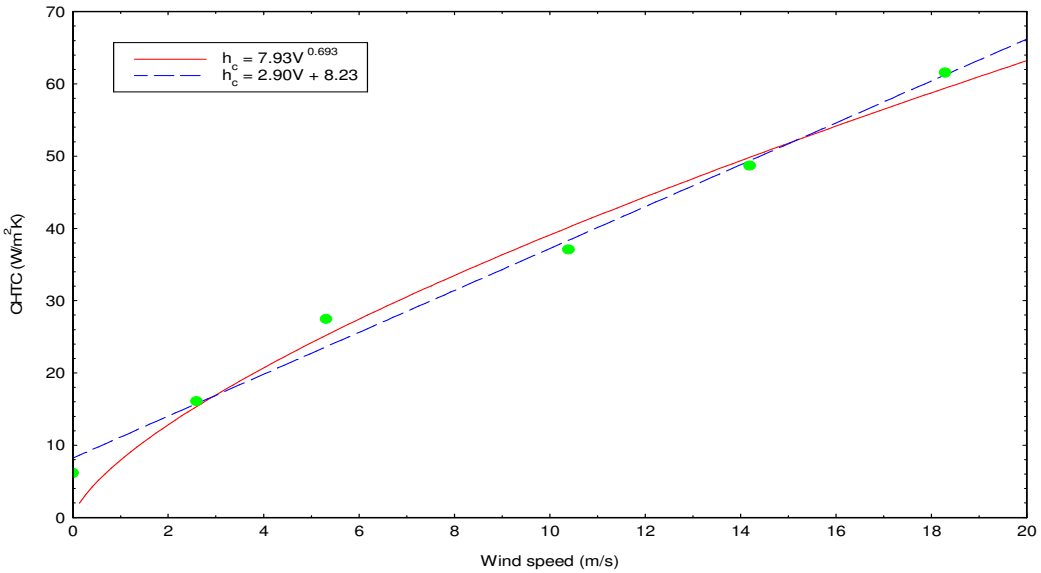

Figure 9.7: Average convection coefficient data across the roof surface

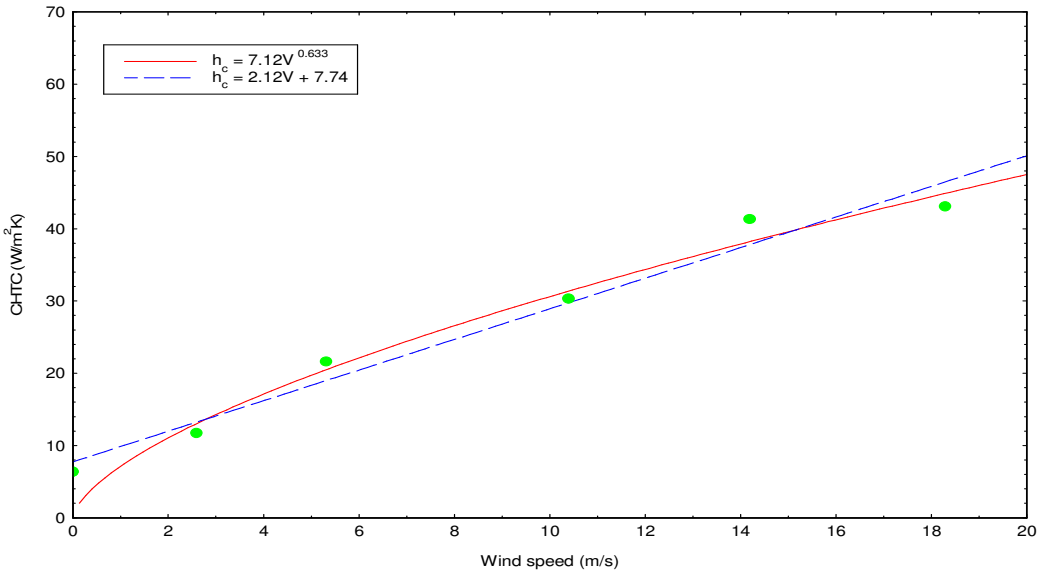

Figure 9.8: Average convection coefficient data across the leeward surface

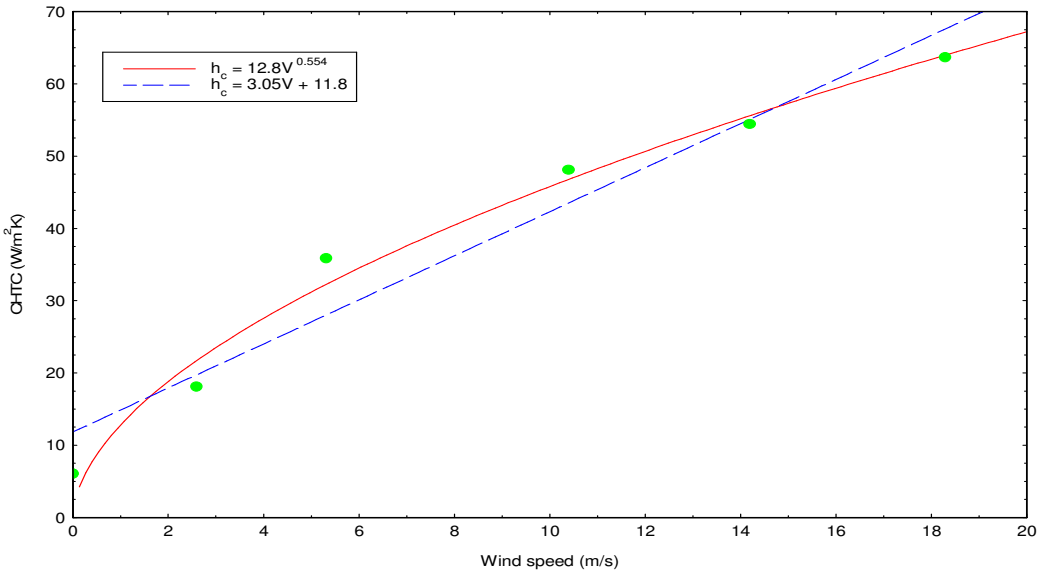

Figure 9.9: Average convection coefficient data at the exposed edge

The best-fit linear and power-law curves for each of these five data sets are summarised in Table 9.5 and Table 9.6 below. In order to help understand how well each of the proposed correlations 'fit' the experimental results, statistical information for each data set is also provided. The coefficient of determination (or R^2 value) provides a statistical measure of how well the proposed model fits the experimental data. It may be broadly interpreted as the proportion of variability in the measured property (in this case the convective heat transfer coefficient) that is attributed to the primary experimental variable (in this case wind speed). A value of $R^2 = 1.00$ indicates that all of the variation is explained by the proposed model (i.e. a perfect correlation), whereas a value of $R^2 = 0$ indicates that none of the variability is accounted for. An intermediate value such as $R^2 = 0.9$ suggests that 90% of the variability is attributable to the primary variable, with the remaining 10% being a result of unknown factors or inherent errors.

The maximum variation is a measure of the largest absolute error between the 'worst case' data point and the correlation curve. It therefore indicates the maximum error that would occur when employing the expression to determine the convective coefficient, but may be misleading since it depends only upon the worst case error for a single data point across the entire range. The averages of these two statistical measures for each of the two sets of correlations are provided in the tables in order that the overall quality of fit can be compared.

For both the linear and power-law correlations, the coefficients of determination are all very close to unity indicating that the variation in the rate of convective heat transfer between experiments is predominantly due to the variation of wind speed. The average R^2 value for the power-law curves (0.984) is slightly higher than that for the linear correlations (0.970) suggesting that this is a more appropriate form of relationship for the range of wind speeds considered.

Table 9.5: Summary of the derived linear correlations

Surface	**Linear correlation**	**R^2 value**	**Maximum deviation**
All	$h_c = 2.47V_f + 8.73$	0.983	3.98
Windward	$h_c = 2.39V_f + 10.20$	0.961	5.66
Roof	$h_c = 2.90V_f + 8.23$	0.990	3.75
Leeward	$h_c = 2.12V_f + 7.74$	0.970	3.47
Exposed edge	$h_c = 3.05V_f + 11.80$	0.945	7.75
Average	**-**	**0.970**	**4.92**

Table 9.6: Summary of the derived power-law correlations

Surface	**Power-law correlation**	**R^2 value**	**Maximum deviation**
All	$h_c = 8.41V_f^{0.626}$	0.993	6.22
Windward	$h_c = 10.30V_f^{0.552}$	0.985	6.24
Roof	$h_c = 7.93V_f^{0.693}$	0.985	6.10
Leeward	$h_c = 7.12V_f^{0.633}$	0.978	6.32
Exposed edge	$h_c = 12.8V_f^{0.554}$	0.980	6.01
Average	**-**	**0.984**	**6.18**

At lower velocities, the relationships between wind speed and convective transfer are not well represented by power-law relationships since these tend to zero in still conditions. The larger maximum deviations noted for the power-law expressions (compared to their linear counterparts) are generally as a result of the difference between this zero intercept and the actual free convection components that has been measured (approximately 6 W/m^2K).

However, the linear equations which have been determined from this curve fitting exercise have larger y-axis intercepts (i.e. free convection components) than was determined previously in Section 10.2. As Figure 9.10 illustrates, these are between 7 and 12 W/m^2K; up to almost double the previously obtained average value of 6.22 W/m^2K. One option would have been to fix the y-intercept at the desired value. This was rejected since it would tend to tilt the best-fit line, increasing it's gradient and thus reducing the quality of the fit.

Notwithstanding these issues, the linear-style expressions are able to reflect the smooth transition from free to forced convection in the low speed range more effectively than the equivalent power-law expression. Figure 9.10 illustrates the variation between the two types of equations for the current data at low speeds; the divergence at wind speeds less than approximately 1.5 m/s is clear.

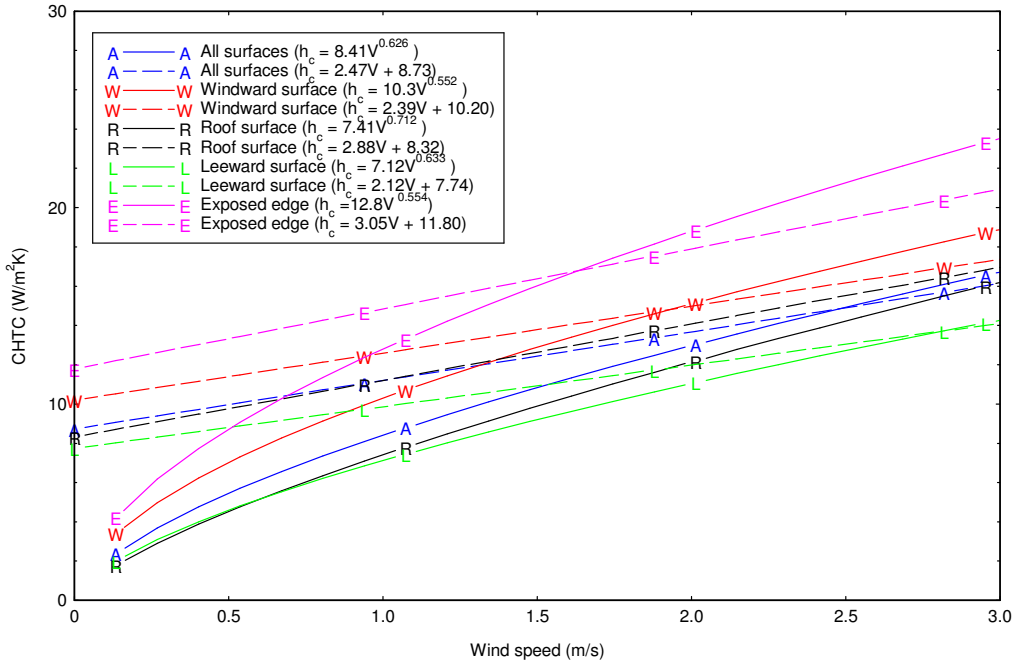

Figure 9.10: Comparison of equation types at low wind speeds

At higher wind speeds, the rate of increase of the convective heat transfer coefficients begins to diminish as the maximum rate is approached. In such scenarios, the power-law form of relationship becomes more representative since it is able to represent this levelling out of the data. In contrast, a linear relationship would predict infinitely increasing rates of convection as the wind speeds are increased. The correlations have been re-plotted in Figure 9.11 over a much larger wind speed range to illustrate the difference between the two expression types at these higher velocities. It can be seen that the two sets of curves begin to diverge at a wind speed of approximately 20 m/s[a]. Above this point, the linear correlations will tend to overestimate the convective coefficients to an ever increasing degree. These conflicting requirements make it difficult to determine which form of expression is most appropriate for the experimental data.

[a] The maximum wind speed at which the naphthalene sublimation experiments were conducted was 18.3 m/s. It should therefore be noted that the curves above this point on the graph are only extrapolations of this lower-speed data.

Mean wind speeds measured at building roof height (approximately 10 metres full-scale) may vary from still conditions up to around 30 m/s for typical locations in the UK. The upper extent of this range will be much higher still when considering wind speeds further above a building, as have been used to correlate the current set of data. Conditions in which higher rates of heat transfer occur are likely to be of greater importance in the majority of thermal modelling situations since convection is likely to be relatively insignificant at low speeds in comparison to other processes (e.g. radiation). From Figure 9.11 it would also appear that the power-law form of expression is likely to better model the convection coefficients over such an extended range of wind speeds. It is therefore suggested that power-law type expressions will provide the best fit to the experimental data over the majority of the wind speed range applicable to buildings.

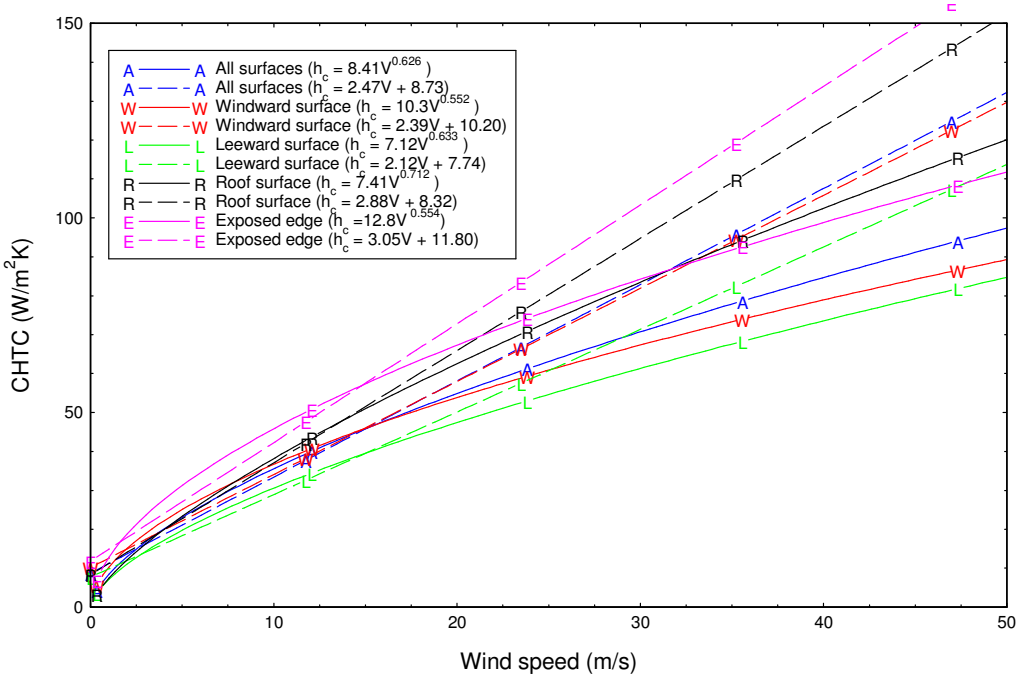

Figure 9.11: Comparison of equation types at high wind speeds

However, this still leaves the problem of the poor low wind speed accuracy of such expressions. One possibility that has already been mentioned would be to specify a lower wind speed limit for application of the expression and then provide a fixed value for the convection coefficient for use below this limit. This is perhaps not an ideal solution since it adds additional scope for error or misinterpretation. Another option would be to determine two separate equations for 'low' and 'high' wind speeds as per the work of Juerges (1924). However this approach often leads to discrepancies for values calculated in the transition zones between the two equations.

Therefore, the author suggests an alternative form of expression be employed which combines the desired high wind speed characteristics of a power-law equation with the ability of a linear equation to include the free convection component. The form of the proposed 'offset power-law' expression is as follows:

$$h_c = a + b.V^c \qquad \text{where a, b and c are constants.} \qquad \text{(Eq. 9.1)}$$

The value of constant 'a' is taken to be the appropriate value for the free convection component of heat transfer for the surface. The constants 'b' and 'c' may then be determined by the curve-fitting process. The expression thereby derived will tend to the value of the free convection coefficient (constant 'a') at low wind speeds, but also includes the high wind speed tailing-off characteristic of power-law expressions as a result of the inclusion of the constant 'c'.

Such offset power-law curves have been fitted to the naphthalene sublimation experimental data and presented in Figures 9.12 to 9.16. The previous linear and standard power-law curves remain shown in order to permit comparison between the proposed and traditional forms of expression. The experimental data points through which the curves have been fitted are shown in green. The value selected for the free convection offset (constant 'a' in Equation 10.1) is the average of the values shown in Table 9.1, i.e. 6.22 W/m^{2}K. This same value has been taken for all surfaces; whilst theory and the literature have each suggested that the values for horizontal and vertical surfaces will differ, this was not significantly borne out in the naphthalene sublimation results and hence the average value has been taken for simplicity.

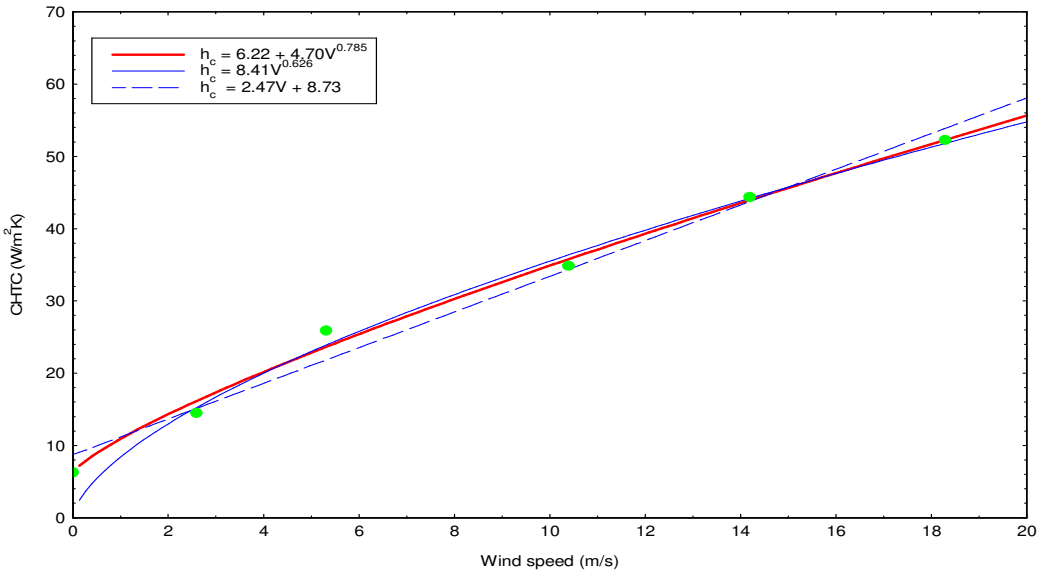

Figure 9.12: Offset power-law best-fit curve for all surfaces

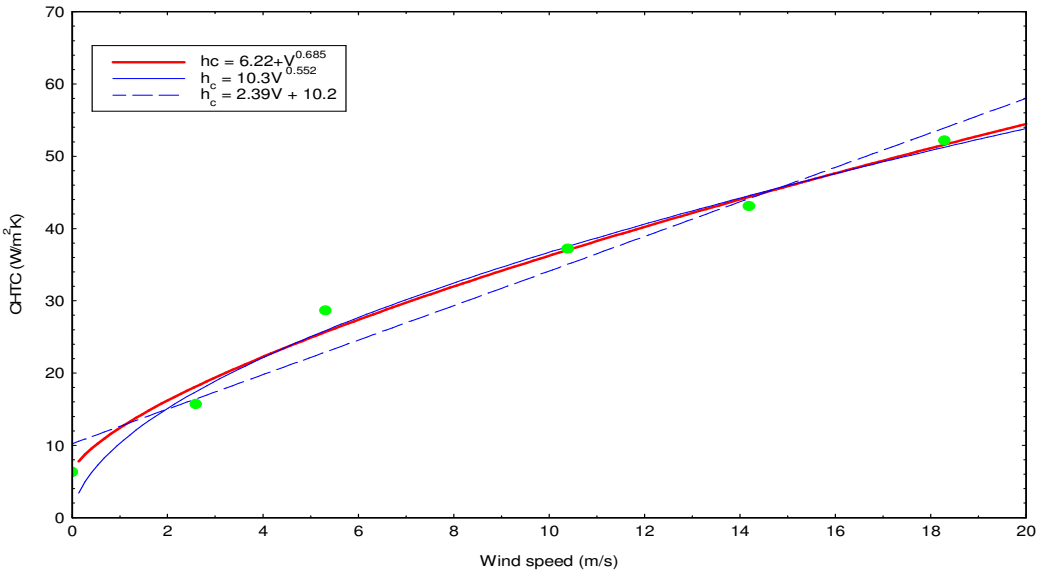

Figure 9.13: Offset power-law best-fit curve for the windward surface

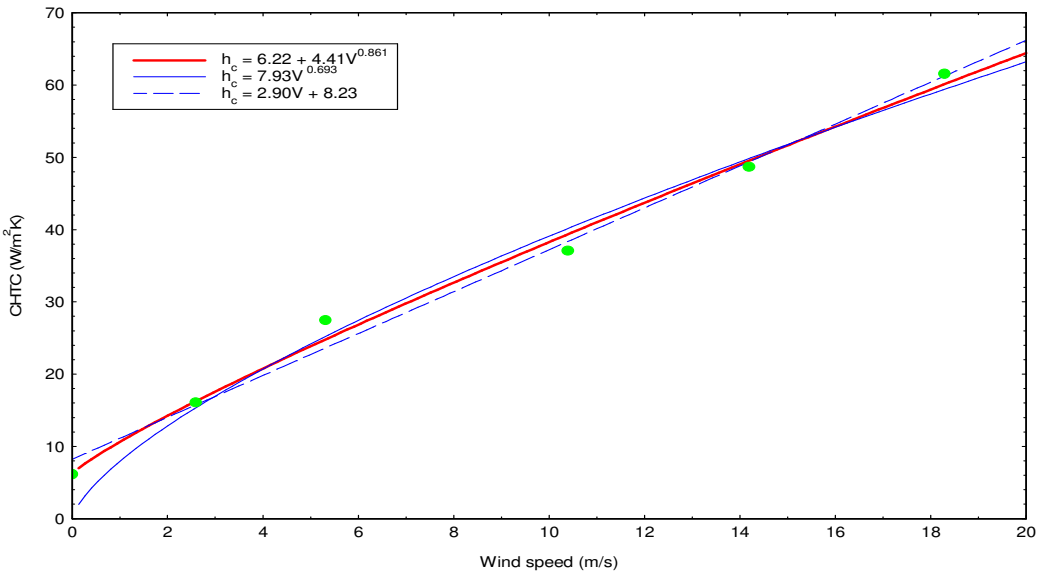

Figure 9.14: Offset power-law best-fit curve for the roof surface

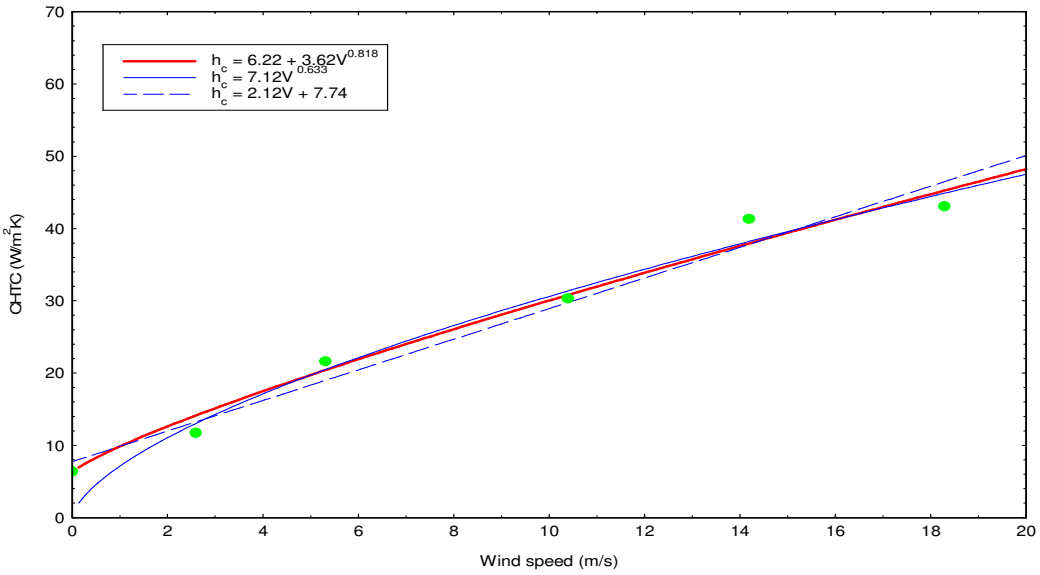

Figure 9.15: Offset power-law best-fit curve for the leeward surface

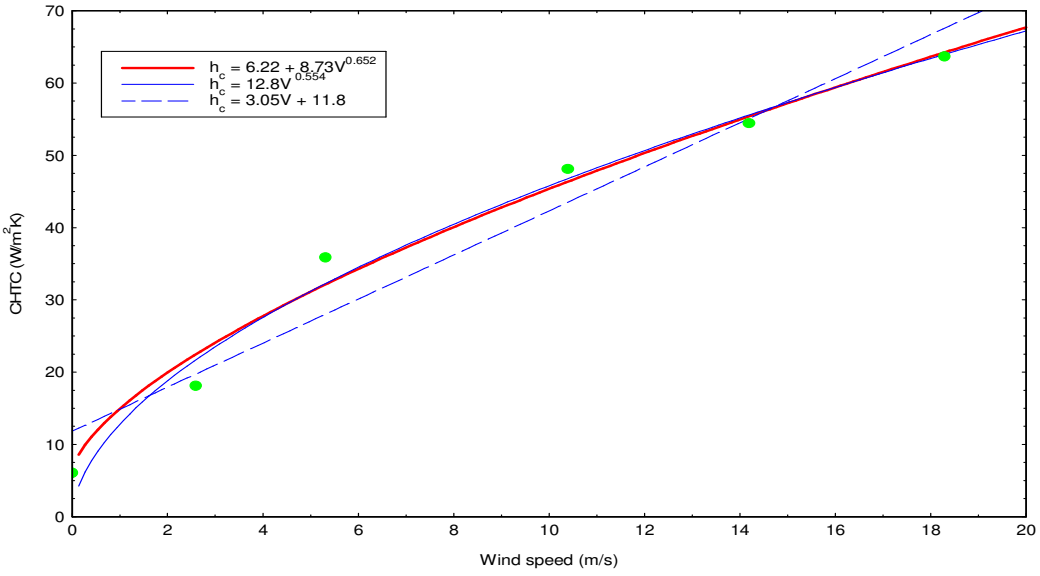

Figure 9.16: Offset power-law best-fit curve for the exposed edge

The offset power-law correlation curves derived from these plots are summarised in Table 9.7 below, alongside the corresponding statistical measures. The average maximum deviations have successfully been reduced from 6.18 for the standard power-law expressions to only 3.30. The new value is also an improvement over that of the linear type equations (4.92), signifying that the new curves fit the experimental data points more accurately over the full wind speed range considered.

Table 9.7: Offset power-law expressions

Surface	**Offset power-law correlation**	**R^2 value**	**Maximum deviation**
All	$h_c = 6.22 + 4.70V_f^{0.785}$	0.991	2.16
Windward	$h_c = 6.22 + 6.20V_f^{0.685}$	0.981	2.89
Roof	$h_c = 6.22 + 4.41V_f^{0.861}$	0.989	2.57
Leeward	$h_c = 6.22 + 3.62V_f^{0.818}$	0.970	3.32
Exposed edge	$h_c = 6.22 + 8.73V_f^{0.652}$	0.974	4.45
Average	**-**	**0.981**	**3.08**

The lowest coefficient of determination for the offset power-law correlations was for the leeward face for which the statistics indicate that 97% of the variation in the convection coefficients is attributable to the wind speed. This leaves only 3% of the variation as a result of other factors or errors. The coefficients of determination for the remaining expressions range up to 98.9%; such values are much greater than was anticipated.

A further advantage of this correlation of the data is that the free convection offset can be directly substituted with alternative values as required, for example to take into account the variation between horizontal and vertical surfaces not apparent for the naphthalene sublimation results.

The correlation curves tabulated in Table 9.7 above are also plotted in Figure 9.17 in order to permit easier comparison of the relative rates of convection from each surface. The higher rate of convective heat transfer predicted in the ‘exposed edge’ region is clear across the full range of wind speeds, as is the relatively sheltered nature of the leeward surface. The windward surface curve remains close to the overall average for all three surfaces, indicating that the rapid heat transfer occurring near to the top of this surface is largely offset by the lower rates of transfer taking place nearer to its base.

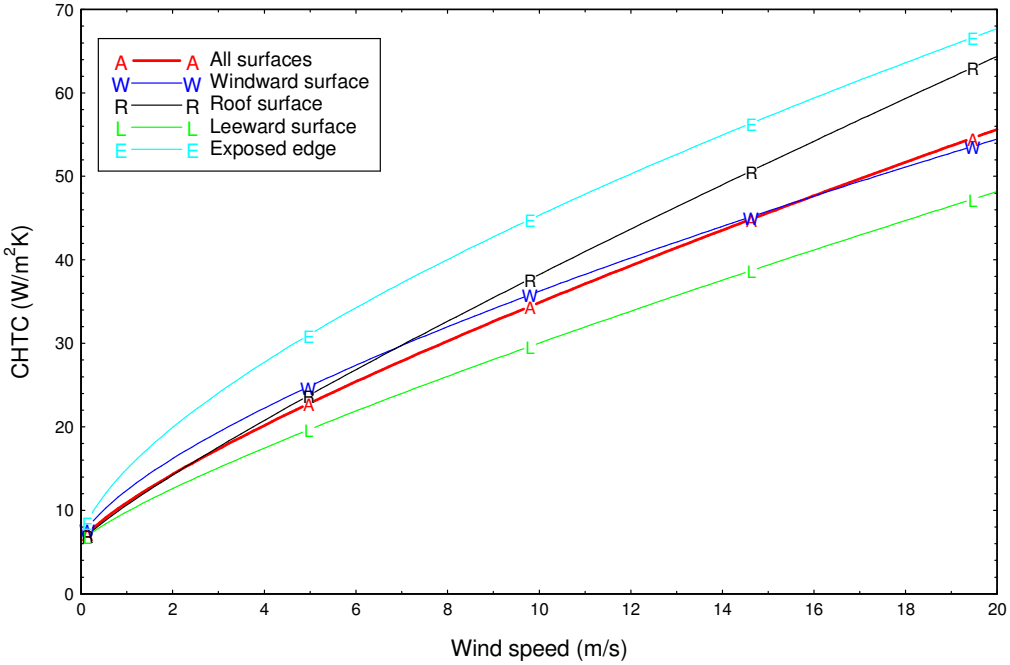

Figure 9.17: Summary plot of offset power-law correlation curves

9.5 The effect of reference wind speed height

The reference wind speed during each of the naphthalene sublimation experiments was measured relatively high in the wind tunnel boundary layer so as to be unaffected by the local flow fluctuations induced by the models near to ground level. It is this 'free-stream' wind speed (V_f) which has been used to correlate the experimental convection data in the previous section of this thesis. However, the majority of previous researchers have proposed correlations which relate the convective coefficients to the wind speed either directly above the building or adjacent to the surface in question. It is therefore desirable to investigate the effect that using alternative reference wind speed heights will have on the convection coefficient expressions.

The mean wind speeds at lower (or indeed higher) heights in the boundary layer may be calculated based upon knowledge of the shape of the velocity profile obtained in Section 6.2. The form of the mean velocity profile is known to be represented by Equation 10.2 shown below, where the roughness length (z_0) has been measured to be 11.4 mm for the 'inner-city' boundary layer simulation developed for this study.

$$V = 2.5u_* \ln\left(\frac{z}{z_0}\right) \qquad \text{(Eq. 9.2)}$$

This equation allows the mean wind speed measured at the reference height to be factored in order to give the respective mean wind speed at any alternative height within the boundary layer. In this way, wind speeds nearer to the height of the model can be calculated and results from experiments conducted using differing reference velocity heights can be directly compared. The wind speeds calculated at heights from 900 mm down to 50 mm are shown in Table 9.8 below for each of the five wind tunnel speed settings. The scaling factors used for this conversion are also shown; further factors to obtain the wind speeds at other heights are given by Figure 6.7. The heights shown relate to model-scale and should therefore be multiplied by one hundred to convert to full-scale.

Table 9.8: Mean wind speeds through the boundary layer

		Mean wind speed at given height (m/s)				
Height (mm)	**Scaling factor**	**Low speed (7.5%)**	**Slow speed (15%)**	**Medium speed (30%)**	**Fast speed (45%)**	**High Speed (60%)**
900	1.000	2.60	5.32	10.40	14.20	18.30
700	0.942	2.45	5.01	9.80	13.38	17.24
500	0.865	2.25	4.60	9.00	12.29	15.74
300	0.749	1.95	3.98	7.79	10.63	13.71
200	0.656	1.71	3.49	6.82	9.31	12.00
100	0.497	1.29	2.64	5.17	7.06	9.10
50	0.338	0.88	1.80	3.52	4.80	6.19

The average convective heat transfer coefficients across all surfaces of the model were presented previously in Figure 9.12 with respect to the reference wind speed measured at 900 mm in the boundary layer. These results have been re-plotted in Figure 9.18 below as offset power-law curves with respect to the calculated wind speeds at alternative heights in the wind tunnel. It is clear from this figure that the location at which the reference wind speed is measured has a significant effect upon the equations which are thereby derived. Whilst this is not an issue so long as the correct wind speed reference height is taken, it is likely to be a large source of error when other sources of wind speed data are employed.

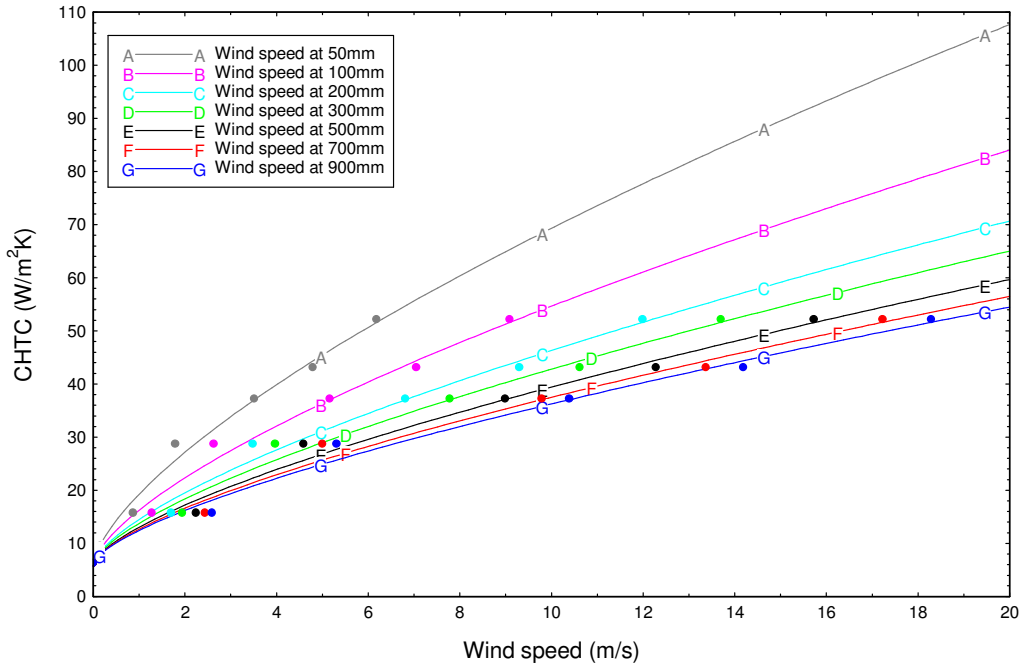

Figure 9.18: Offset power-law curves for wind speeds at alternative heights

The equations of each of the best-fit curves presented in Figure 9.18 are listed in Table 9.9 below. A free convection offset value of 6.22 W/m^{2}K has been assumed, as discussed in the previous Section of this Chapter. The variation in the expressions lies within the term by which the velocity is multiplied; the offset and power terms are constant.

Table 9.9: Correlations for various wind speed measurement heights

Wind speed measurement height (mm)	Offset power-law correlation
50	$h_c = 6.22 + 13.00V^{0.685}$
100	$h_c = 6.22 + 10.00V^{0.685}$
200	$h_c = 6.22 + 8.27V^{0.685}$
300	$h_c = 6.22 + 7.56V^{0.685}$
500	$h_c = 6.22 + 6.82V^{0.685}$
700	$h_c = 6.22 + 6.46V^{0.685}$
900	$h_c = 6.22 + 6.20V^{0.685}$

It has been shown in this Section that the height at which the reference wind speed measurement is recorded can have a significant effect upon the convection expressions which are thereby deduced. If the reference height is higher in the boundary layer, the measured wind speeds will inherently be faster. Using such values of velocity in the correlating equations will result in smaller values of the multiplying factor (constant 'b' in Equation 10.1), and hence to potentially very different expressions.

Two key requirements for the correlating equations are therefore apparent:

- When presenting expressions for determining convective heat transfer coefficients, it must be made clear exactly what form of wind speed measurement they are given with respect to.
- When applying a given convective heat transfer expression, it must be ensured that the correct form of wind speed measurement is employed.

These points might seem very obvious when highlighted in this way. However, it is believed that inconsistencies between the required and selected wind speed measurement locations are one of the most important sources of error in convection calculations. It is not always clear what type of wind data is required for a given equation, and even when it is, this may often be incorrectly substituted by an inexperienced end-user with another type which is more readily available. It is also not just the height above ground at which the wind speed is measured that is critical; other important factors which require consideration include the proximity to a given surface, local flow acceleration effects and levels of turbulence in the flow.

Wind speeds recorded during previous full-scale convection measurements on real structures have typically been taken either adjacent to the test surface or else above the roof of the building. The flow at either location will be affected by the geometry of the building itself, and also by the presence of surrounding structures, trees, etc. If these local flow effects are not accounted for, they are likely to result in measurements which are uniquely applicable to the exact building geometry and surroundings for which they were recorded. It is then difficult to make the convection expressions thus obtained more generally relevant to other buildings and situations since the flow patterns may vary widely.

Such wind modifying effects are however taken into account with wind data provided by the Meteorological Office since the speeds recorded at the respective weather stations are corrected for factors such as topography, altitude and surface roughness. These data can easily be made applicable to alternative sites with different topographies, altitudes, building heights or surroundings. The methodology required to undertake such calculations is provided in BS 6399-2 (BSI, 1997a) which allows the site wind speed at any given height to be determined, taking into account the full range of wind modifying factors. The same procedure may be undertaken automatically using the *'BREVe'* computer program developed by BRE. This software also includes a database of terrain types and ground heights for Great Britain so that the correct boundary layer profiles may be determined for each of the 12 incident wind directions.

For the current work, it is important to determine which of these wind measurement locations will be the most easily applied in practice. Wind speeds directly adjacent to the surface of interest are likely to yield the most accurate correlations since the rate of convection is directly proportional to the flow speed at a given point. However, such wind measurements are rarely available in practice for a given real building; the flow patterns will vary greatly depending upon the buildings geometry and its surroundings so such an approach would require knowledge of the mean wind speeds over every surface. Such expressions are therefore often of limited applicability for use in practical problems concerning real buildings.

Up to this point, the convection equations derived from the naphthalene sublimation experiments have been determined with respect to the free-stream mean wind speeds (V_f) high above the building. Winds at this height are unaffected by the geometry of the buildings below and such expressions are thereby more widely applicable. Variation in the rate of convection from different surfaces of the model has been modelled by determining different equations for each, rather than by using a single equation which is applied using differing wind speeds for each location. It is proposed that this approach is much simpler to apply since only a single wind speed is required. However, anemometers at weather stations are typically located much closer to the ground and it is standard practice to specify wind speeds at a height of 10 m above the ground in flat open terrain (i.e. without the effect of nearby obstructions). Such values may be factored up to give the wind speeds higher up in the boundary layer using the methods described above, but this introduces an additional step into the calculation.

9.6 Derivation of equations with respect to met. standard wind speeds

It is standard practice to quote meteorological wind speeds at a height of 10 metres above open, level countryside. This is known as the *'Meteorological Standard Windspeed'* (MSW) and is the wind speed that would occur at that site if there were no obstructions or significant topographical effects nearby. Clearly this is not the same as the actual wind speed that would be measured at a height of 10 m in an urban area since the buildings will modify the local wind profile. Even wind data recorded at weather stations in urban areas is corrected to give the effective met. standard wind speed for an open site to remove the local influences of its surroundings to make the data more generically applicable.

In the same way, the boundary layer profile simulated for this study in the wind tunnel was measured for the open site, without the presence of the models. The actual wind speeds with the models in place will be very different close to the ground as a result of the shelter effect of the buildings[a], but this differential will diminish with increasing height until the speeds are identical to those recorded with the open site. The free-stream wind speed will be the same in both cases and will remain so for all arrangements of the models; this is the reason that the convection expressions derived up until this point have been with respect to the free-stream wind speed recorded at a height of 900 mm (90 metres full-scale) in the wind tunnel boundary layer.

However, because both the current wind tunnel boundary layer profile and standard met. wind data are recorded for an open site, it is possible to take the derived convection equations one step further. These may also be derived with respect to the wind speed measured at a height of 100 mm in the clear wind tunnel (i.e. without the models) and such expressions are therefore applicable to full-scale situations using the met. standard wind speed for the site. These equations could then be applied directly for the site, without needing to factor the standard met wind data to determine the free-stream wind speed above the site.

The calculated open site wind tunnel velocities at a height of 100 mm for each of the running speeds are given in Table 9.10 below. Best fit offset power-law curves have been fitted to the naphthalene sublimation data for each of the surfaces as shown in Figure 9.19 to Figure 9.23. The standard linear and power law curve fits are also shown in these plots for comparison. The heights shown relate to model-scale and should therefore be multiplied by one hundred to convert to full-scale.

Table 9.10: Wind speeds at 10 m full-scale

		Wind tunnel speed setting				
Measurement	**Units**	**Low (7.5%)**	**Slow (15%)**	**Medium (30%)**	**Fast (45%)**	**High (60%)**
Measured reference velocity at 90m	(m/s)	2.60	5.32	10.40	14.20	18.30
Calculated wind speed at 10m	(m/s)	1.29	2.64	5.17	7.06	9.03

a A height of 10 metres at full-scale would equate to 100 mm at the current 1/100th model scale. This is approximately the same as the building height (H = 94 mm).

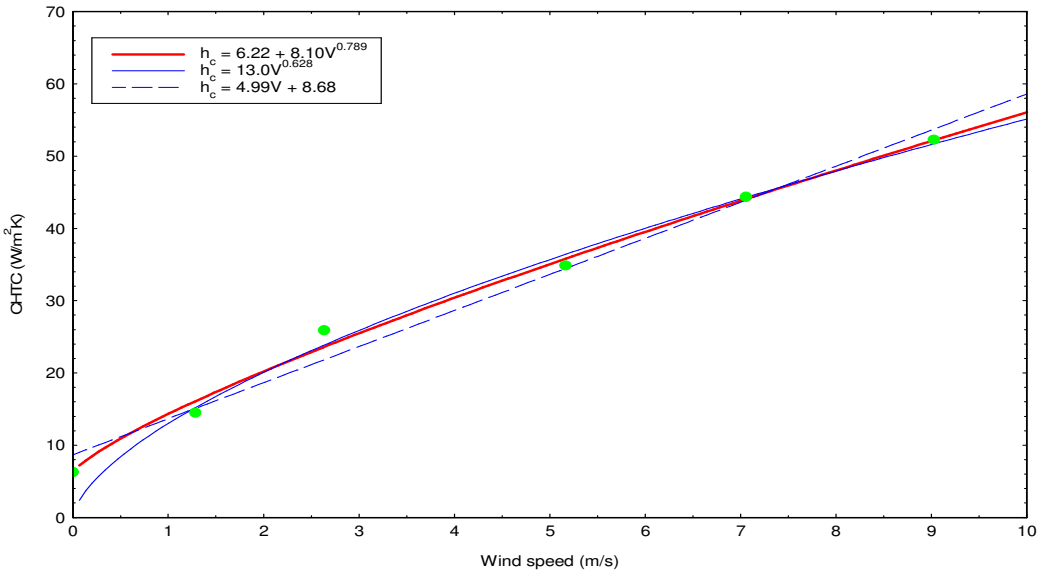

Figure 9.19: Average for all surfaces

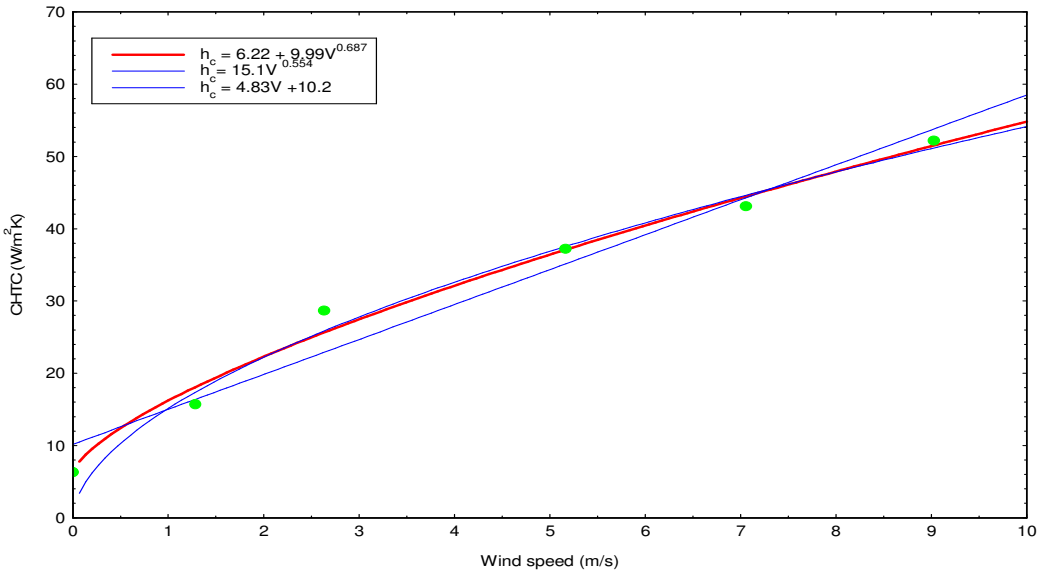

Figure 9.20: Average across the windward surface

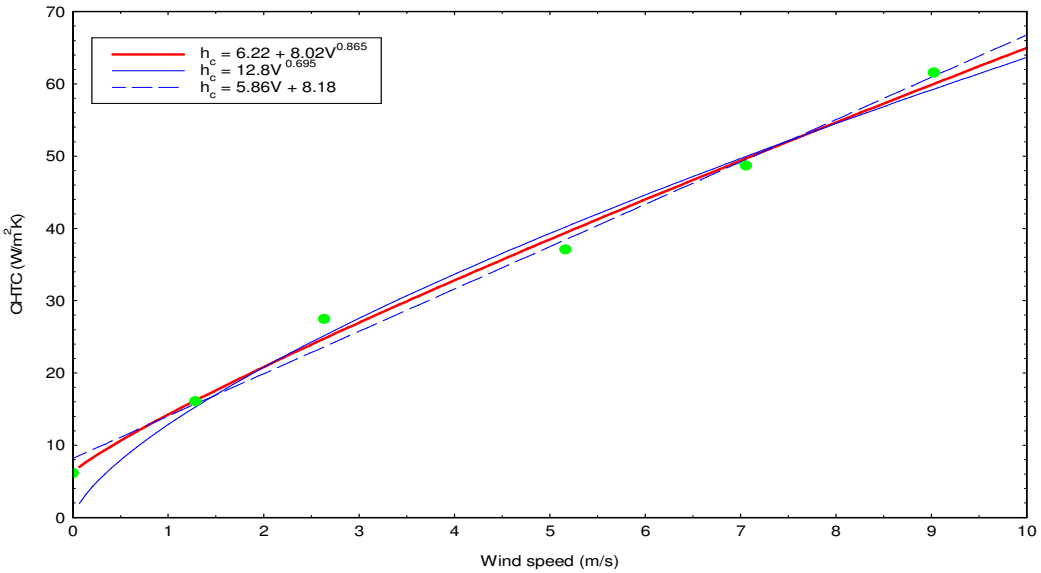

Figure 9.21: Average across the roof surface

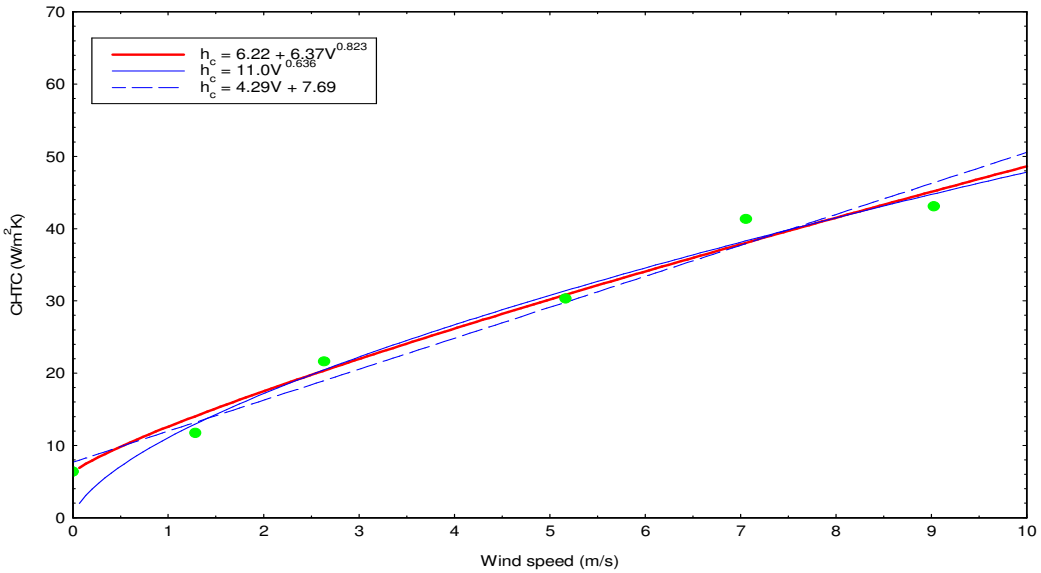

Figure 9.22: Average across leeward surface

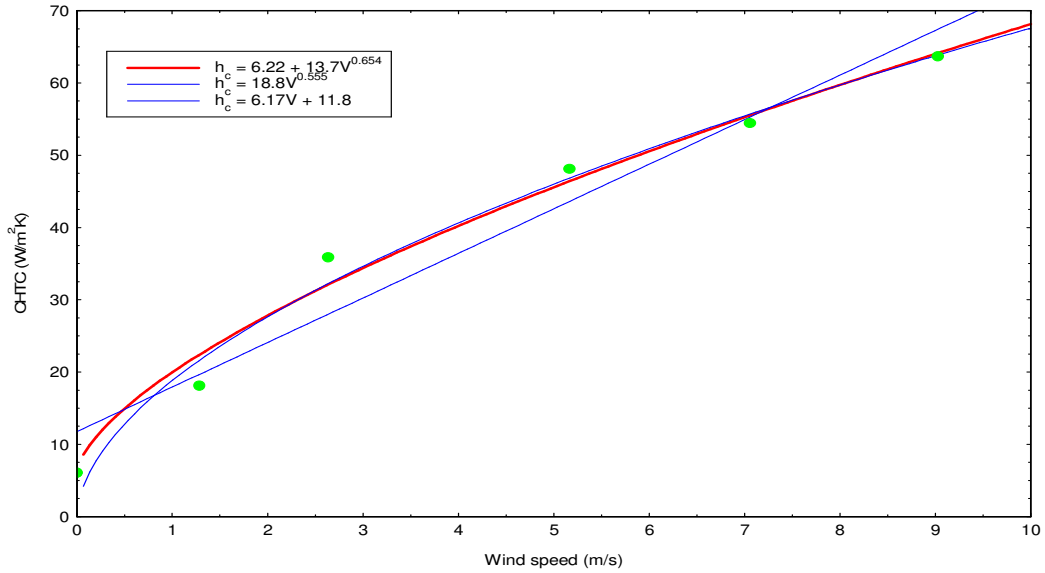

Figure 9.23: Average for exposed edge area

The best fit offset power-law expressions derived from these plots are summarised in Table 9.11 below, alongside the usual statistical information. It is noted that the R^2 and maximum deviations are identical to those for the expressions determined previously in Table 9.7, a reflection of the fact that it is the same naphthalene sublimation data which has been correlated. The correlating equations tabulated below are also plotted for comparison in the following Figure 9.24

Table 9.11: Offset power-law correlations with respect to the MSW (V_m)

Surface	**Offset power-law equations**	**R^2 value**	**Maximum deviation**
All	$h_c = 6.22+8.10V_m^{0.789}$	0.991	2.20
Windward	$h_c = 6.22+9.99V_m^{0.687}$	0.981	2.92
Roof	$h_c = 6.22+8.02V_m^{0.865}$	0.989	2.61
Leeward	$h_c = 6.22+6.37V_m^{0.823}$	0.971	3.21
Exposed edge	$h_c = 6.22+13.70V_m^{0.654}$	0.975	4.40
Average	**-**	**0.981**	**3.07**

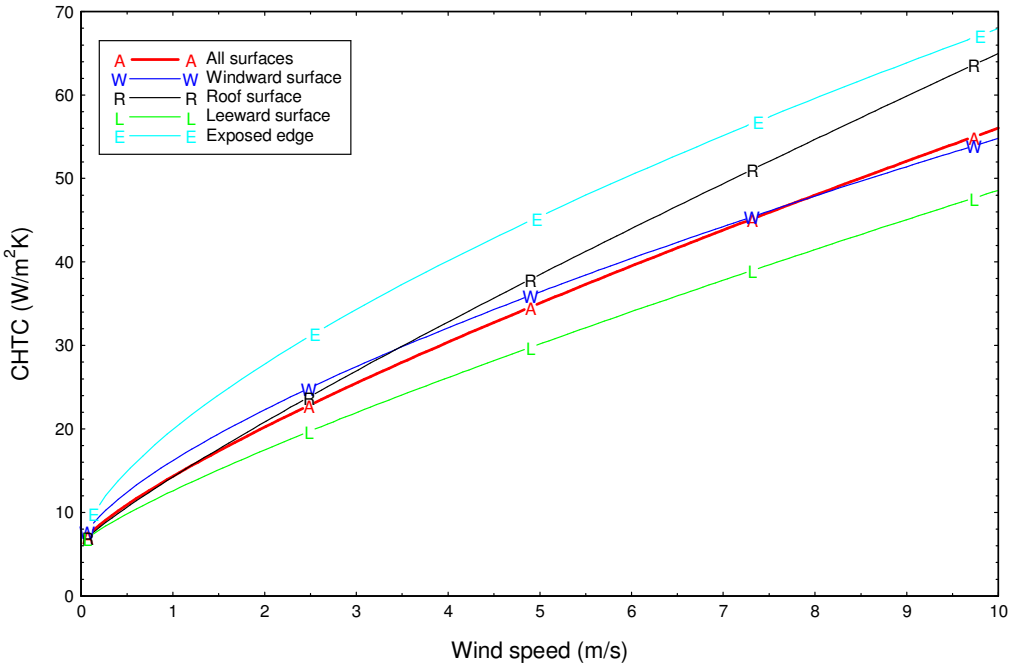

Figure 9.24: Summary plot of offset power-law correlation curves

9.7 Comparison with standard correlations

Earlier in this thesis, a review of current design guidance and British Standards revealed that the convective heat transfer equations presented are largely based upon work conducted using flat plates more than eighty years ago. It was proposed that these correlations are not representative of the convection which occurs from the more complicated three-dimensional geometries of buildings within an urban environment. In order to test this theory, the relationships derived from the naphthalene sublimation tests presented in the previous sections will be compared with values obtained using the primary equations presented in the current British design guidance.

The latest CIBSE Guide (CIBSE, 2006) provides values for convective heat transfer based upon the following equation taken from BS EN ISO 6946 (BSI, 1997b):

$$h_c = 4 + 4V \qquad \text{(Eq. 9.3)}$$

The wind speed referred to by the above formula is that adjacent to the surface, measured in metres per second. It was noted in the previous Section that such surface wind speed information is not typically available for real buildings.

Equation 10.3 is shown in Figure 9.25 below as the solid red line which has been plotted against the offset power-law expressions for the convection from all surfaces with respect to the wind speed at a range of heights. The dotted red line represents the Standard equation with an increased free convection component so as to match that of the naphthalene derived expressions (i.e. $h_c = 6.22 + 4v$). This second line has been added so as to permit easier comparison of the forced components of convection given by the respective equations.

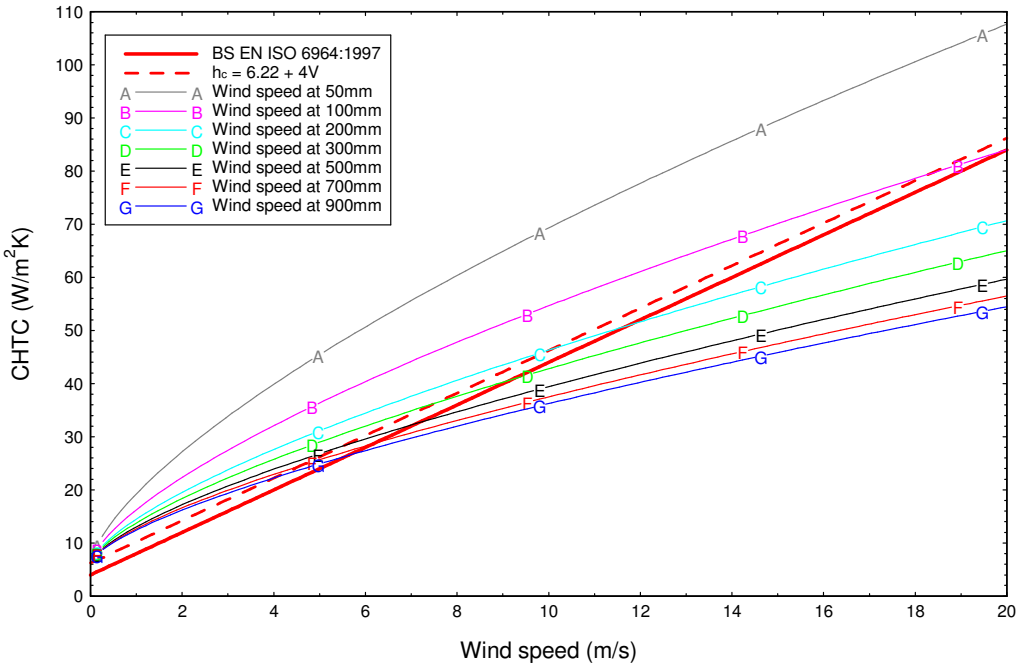

Figure 9.25: Comparison of results with the equation of BS EN 6946

On first inspections, it appears that the Standard equation shows reasonable agreement with the naphthalene derived expressions, giving a similar range of results across the wind speed range. However, for lower wind speeds up to around 6 m/s, the Standard equation produces values similar to the experimental results with respect to wind speeds measured at between 500 mm and 900 mm in the boundary layer. This is surprising since the Standard equation uses surface wind speeds and therefore it would seem more appropriate for it to resemble experimental results with respect to wind speeds at lower levels, closer to the model surfaces in question. At faster wind speeds, the Standard equation results do indeed approach those given by the 100 mm wind speed height experimental results, but this is only as a result of the tailing-off effect of the power-law curve versus the continuous increase of a linear expression.

The most likely cause of this disagreement is the geometry for which the two types of equation have been derived. The Standard equation is based upon results obtained for convective heat transfer for flat plates with air flowing parallel to the surface. The current experimental results on the other hand have been obtained using a much more realistic three-dimensional urban geometry with a more complicated flow around the test surfaces and higher levels of turbulence. Therefore, whilst it may initially appear that the current experimental results give values of convection within the range of those calculated from the Standard expressions, the results are in fact significantly different. This conclusion supports the argument described earlier in this thesis that the convective heat transfer equations detailed in the current design guidance are unlikely to be appropriate for the more complex processes surrounding real buildings in an urban environment.

This finding also highlights the importance of both clearly defining the required wind speed for a given equation and also ensuring that this correct wind speed data is used in subsequent calculations. Using the wrong wind speed data will almost certainly result in an incorrect value for convection, even if it appears to be within a sensible range.

9.8 Comparison with full-scale measurements

A number of researchers have previously conducted full-scale experiments in an attempt to determine the rate of convective heat transfer occurring from the surfaces of real buildings. A selection of the respective convection correlations found in the literature was presented earlier in this thesis as Figure 3.5. This graph emphasises the large variation in the convection coefficients which may be obtained using the various expressions derived by various workers in the four decades since Sturrock undertook the first full-scale measurements. It is therefore of interest to consider how the current data determined using the naphthalene sublimation technique compare with these full-scale results. As the current work has simulated the appropriate atmospheric boundary layer and turbulence for an urban area (unlike work conducted using flat-plates in a laminar wind tunnel, for example) it was anticipated that the wind tunnel results should show good agreement with the measurements on real buildings.

Such a direct comparison is by no means straight forward. In a number of cases, the location and height at which the correlating wind speed was recorded is unclear. The problem is further compounded by differences in the local wind environment (for example, surface roughnesses, building density and spacing) between each measurement scenario. This can make it particular difficult to compare alternative results and expressions, since each typically uses a slightly different wind speed input. The most accurate convection equations are usually defined with respect to surface wind speeds measured close to the test area. However this data is not generally available for buildings in practice and wasn't measured in the current experiments. Such surface flow conditions will be highly dependent upon the buildings size, geometry and surroundings and so the convection expressions obtained may only be applicable to the surface on which they were originally measured.

However, such comparisons remain useful in order to validate the results obtained using the naphthalene sublimation technique. Therefore the current results are compared to full-scale experimental expressions derived by Nicol, Schwarz, Loveday and Taki, Sharples, Sturrock and Shao *et al.* in the following sections. The latter of these is of particular interest since the results were obtained by applying a variation of the naphthalene sublimation technique at the surface of a real building. Either the free-stream wind speed or met. standard wind speed expressions have been selected for comparison depending upon how the wind speed was measured in the full-scale study.

Nicol (1977)

The expression presented by Nicol for convective heat transfer was derived from measurements made on a vertical glass window at the Canadian Arctic Research Station. The location at which the wind speed was recorded is not documented, neither are any details of the surrounding landscape or buildings. However, as the measurements were made at an Arctic research station it seems reasonable to assume that the building was low-rise and in a relatively open, exposed site and that the wind speed was measured relatively near to the ground. The expression proposed by Nicol is therefore plotted in Figure 9.26 alongside the current results with respect to the meteorological standard wind speed at a height of 10 metres.

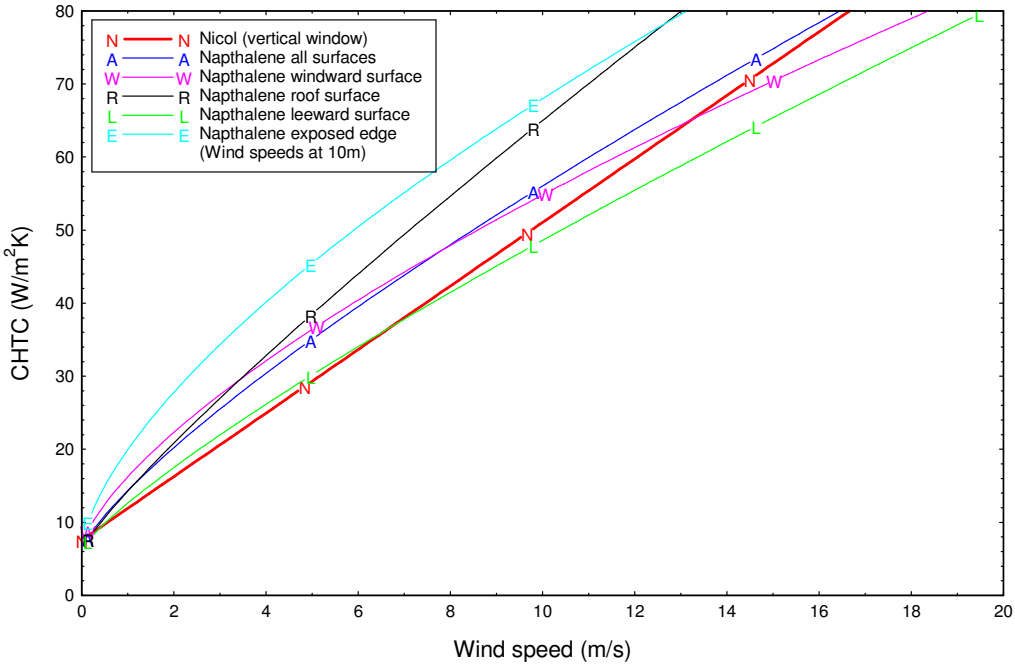

Figure 9.26: Comparison of results with Nicol's expression

The agreement between the expression proposed by Nicol and the current relationships is clear, especially for the leeward and windward equations. The exposed edge values are significantly higher than the values recorded by Nicol on the window, but this is unsurprising since the window is likely to be located at the centre of the wall away from the edge effects. The low rise geometry of the Arctic research station is perhaps the most similar to that modelled in the current wind tunnel study, with the other full-scale studies having considered higher-rise test buildings. This is likely to be a key factor in the close agreement between the two sets of results.

Schwarz (1972)

The relationships presented by Schwarz employed wind speeds measured at a height of 10 metres at a nearby weather station. The expressions he presented for convection from windward and leeward vertical surfaces are therefore plotted in Figure 9.27 alongside the current expressions derived with respect to the met. standard wind speeds at 10 metres.

It can be seen that although the Schwarz data gives values close to that of the current work for windward surfaces at low (< 3 m/s) wind speeds, there is otherwise very little agreement. One possible explanation for this is that the measurement site was in relatively open countryside as opposed to a dense urban environment. For such locations, the lower surface roughness results in the free-stream velocity occurring at a significantly lower height in the boundary layer. The wind speeds nearer the ground will therefore be greater than in the current inner-city simulation and consequently are perhaps more comparable with the current free-stream velocities. To determine whether this is indeed the case, Schwarz's expressions have been replotted in Figure 9.28 alongside the naphthalene expressions given with respect to the free-stream wind speeds.

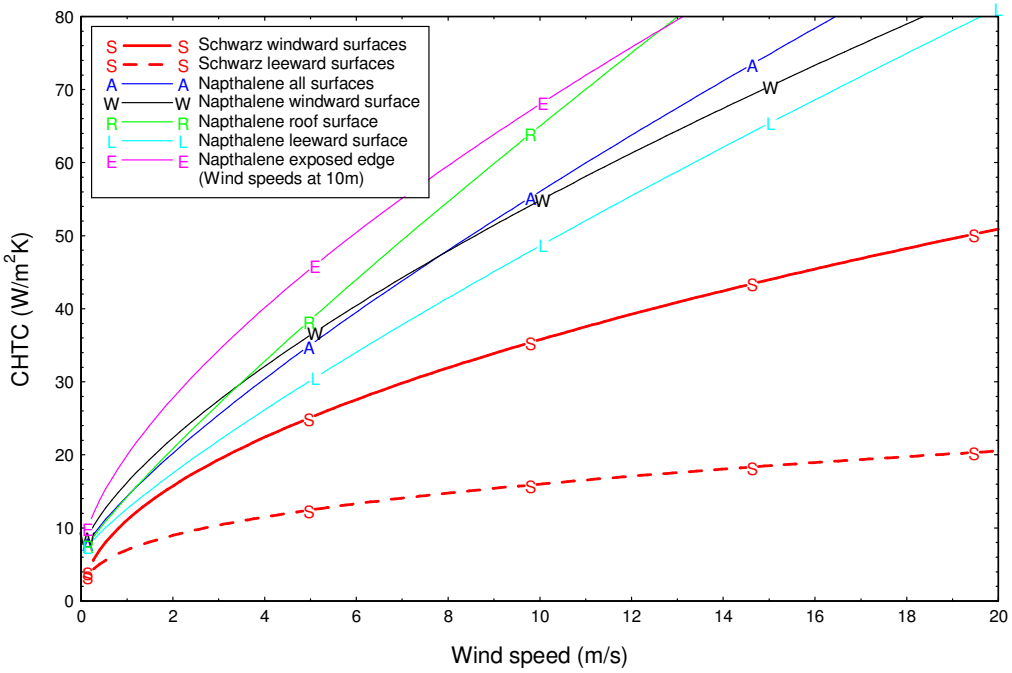

Figure 9.27: Comparison of results (10 m winds) with Schwarz's expressions

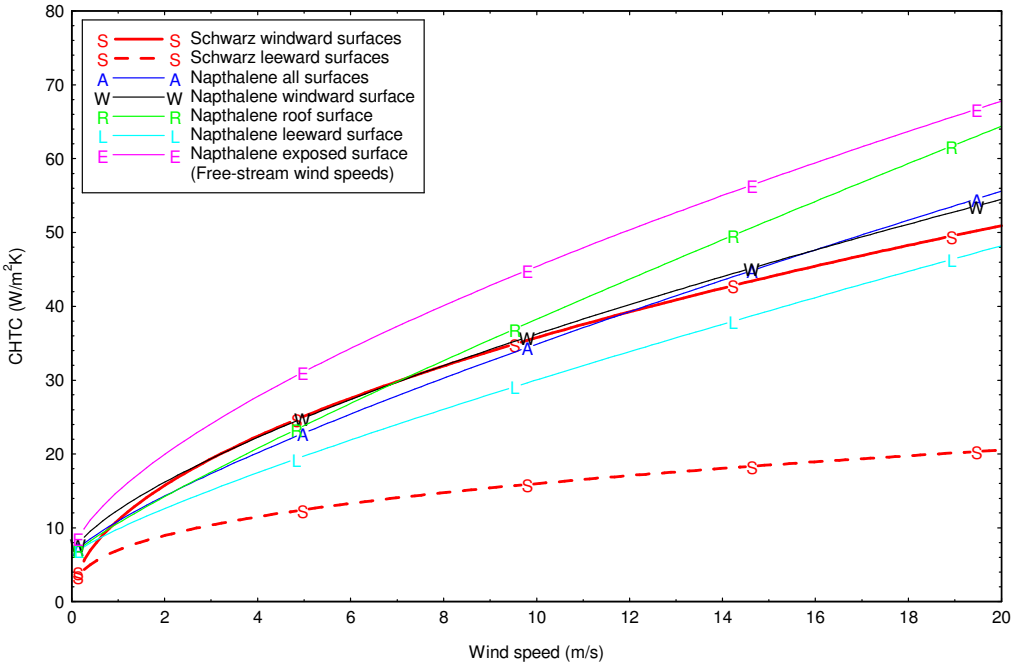

Figure 9.28: Comparison of free-stream results with Schwarz's expressions

When presented in this manner, there is much clearer correlation between the current results and those obtained by Schwarz at full-scale for windward surfaces. Indeed, the two curves for the windward surface data are virtually overlapping for wind speeds between 2 and 14 m/s, and diverge by less than 4 W/m^{2}K at either extreme.

Schwarz's data for leeward surfaces shows less agreement with the current naphthalene derived results. Whilst it is unclear why this might be the case, it is notable that the windward and leeward relationships deduced by Schwarz are significantly more varied than those of the current study. The wind speeds for the full-scale measurements were made at a nearby weather station. One possible cause for this variation may therefore be that the winds at the weather station may vary from those at the measurement site for the leeward wind directions. Nearby buildings, fences, trees, etc. may have provided the test building with additional shelter for particular wind directions resulting in the apparently low rates of convection. Alternatively it may be as a result of lower levels of turbulence at the rural site which would reduce the forced convection in the wake of the building, hence reducing forced convection from the leeward façade.

Loveday and Taki (1996)

Loveday and Taki measured their wind speeds at a height of 11 m above a Loughborough University residential block. This height was determined by consideration of the height required to reach undisturbed flow above the building. The expressions presented by Loveday and Taki for windward and leeward surfaces are thus presented in Figure 9.29 alongside the current results with respect to free-stream wind speeds.

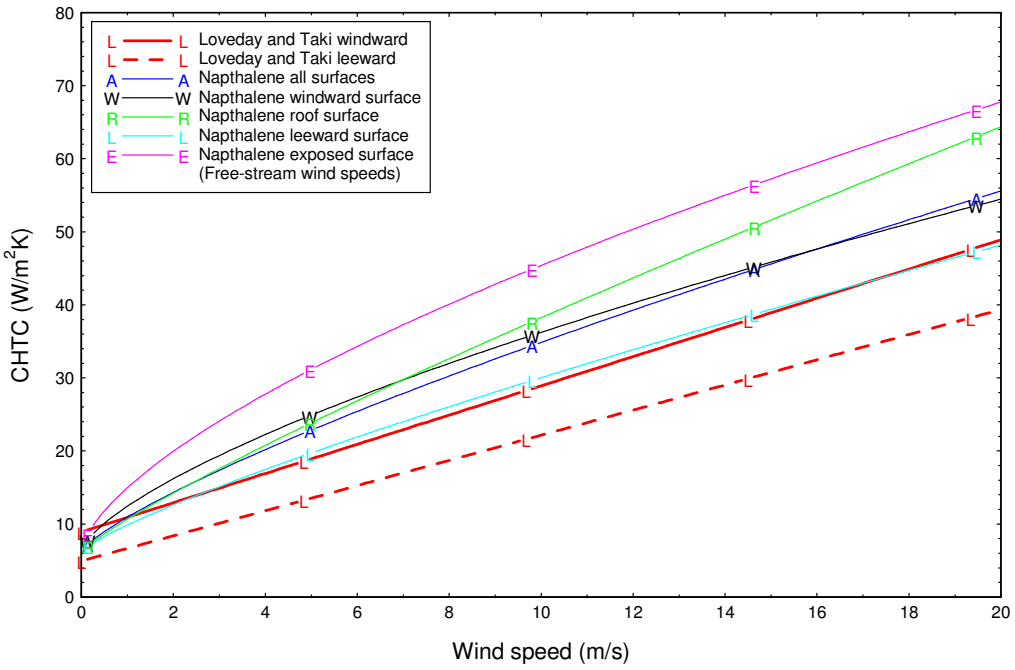

Figure 9.29: Comparison of results with Loveday and Taki's expressions

It can be seen that the results presented by Loveday and Taki are slightly lower than those which have been derived in the current study. Their higher windward surface expression is an almost perfect fit with the current leeward surface results. The significant difference between Loveday and Taki's results for the two surfaces is with the free convection component (4.93 versus 8.91 W/m^{2}K); the forced convection components (i.e. the gradients of the lines) are very similar. The current average value of forced convection (6.22 W/m^{2}K) is very close to the midpoint of the two values they proposed for the windward and leeward façades.

This slight difference in the values for free convection may partially account for their leeward surface values being slightly lower, but does certainly not account for all of the variation. The university campus at which these measurements were made is in a relatively open rural landscape with a few large university buildings nearby. The wind characteristics around the site were therefore different to the inner-city conditions in the BRE wind tunnel. Wind directions at the test site were not always perpendicular to the test panel; in fact both windward and leeward measurements each included a 180 degree range of wind directions. Hence both of Loveday and Taki's expressions are derived from data which includes some flow at lesser incident angles to the test surface whereas the wind tunnel tests were always conducted with perfectly perpendicular flow. It is probable that it is a combination of these factors along with variations in the test building geometry and measurement locations which account for the variation between the two sets of results. Notwithstanding these slight disagreements, the two sets of results remain within approximately 6 W/m^{2}K of each other for windward surfaces, and within approximately 8 W/m^{2}K for leeward surfaces.

Loveday and Taki also presented expressions with respect to wind speeds measured one metre above the test surface, however no appropriate data is available from the current study with which to compare these results as surface velocities were not measured.

Sharples (1984)

For his full-scale convection experiments at Sheffield University, Sharples measured wind speeds at a height of 6 metres above the roof of the University's 78 metre tall Arts Tower. However, Sharples found that it was difficult to relate the measured convective coefficients to these wind speeds. Instead he chose to present expressions with respect to wind speeds measured at a height of 10 metres at a nearby weather station. The expressions he derived from these tests are shown in Figure 9.30 below for windward surfaces and Figure 9.31 for leeward surfaces. The results of the current work are also plotted with respect to the meteorological standard wind speed at the same 10 metre height.

Sharples also recorded local wind speeds at a distance of 1 metre from the test surface and was able to correlate his convection measurement with these values. Although these results showed stronger correlation that those with respect to the wind speeds measured at the nearby weather station, no surface wind speed expressions are available for the current work with which to compare them.

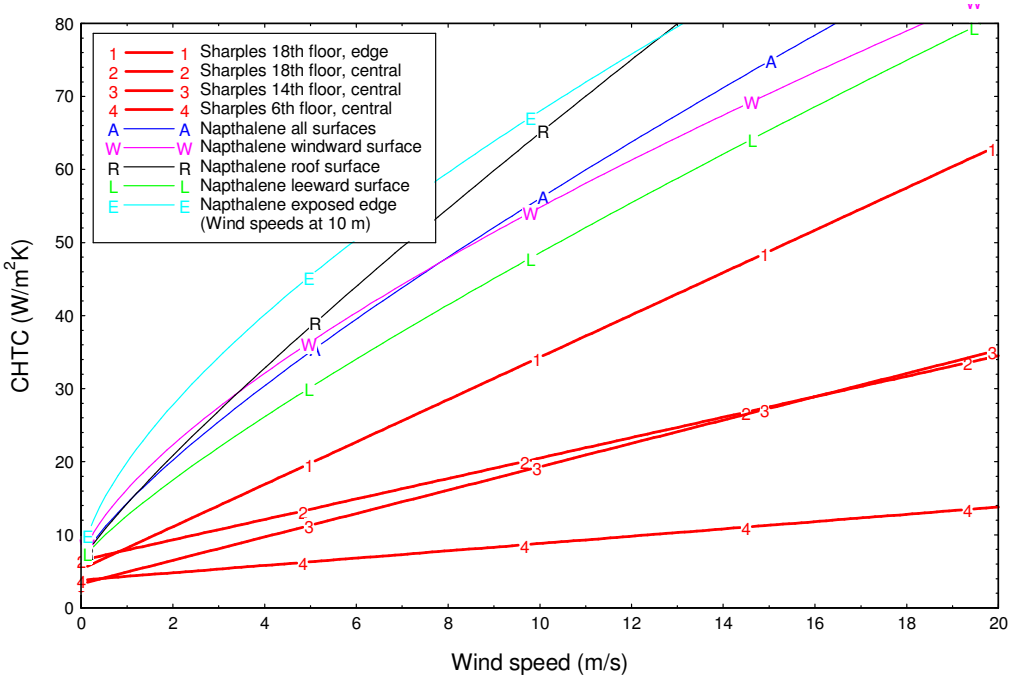

Figure 9.30: Comparison of results with Sharples' windward expressions

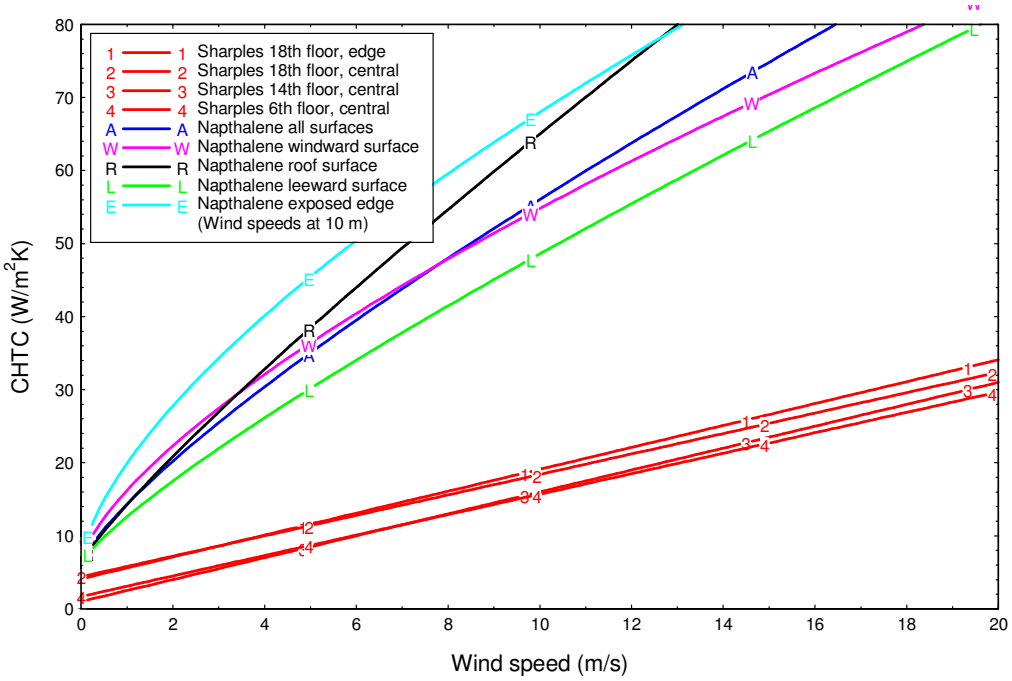

Figure 9.31: Comparison of results with Sharples' leeward expressions

The convection equations presented by Sharples yield amongst the lowest values of any of those determined by previous researchers (see Figure 3.5). As such, the results are significantly less than those of the current experiments, particular for leeward surfaces. The 78 metre tower block on which measurements were made is the tallest building in the city and will therefore have a significant effect upon the wind microclimate around its façades. These flow modifications will not be reflected at the weather station at which the correlating wind speeds were recorded and could therefore be one explanation for the apparently low rates of convection predicted by Sharples' equations. Indeed, a close similarity of results should not be expected between the convection occurring from an isolated tower block and that from a low-rise building at the centre of a uniform array.

Sturrock (1971)

The expressions presented by Sturrock following his full-scale convection measurements are shown in Figure 9.32 alongside the current results with respect to the free-stream wind speeds. Sturrock's data for exposed surfaces is generally regarded in the literature as yielding unrealistically high results. It was also shown in Figure 3.5 that his results were significantly higher than those determined in full-scale measurements by other researchers; the line representing Sturrock's data is the lies significantly above the range of the other data for all wind speeds above around 4 m/s.

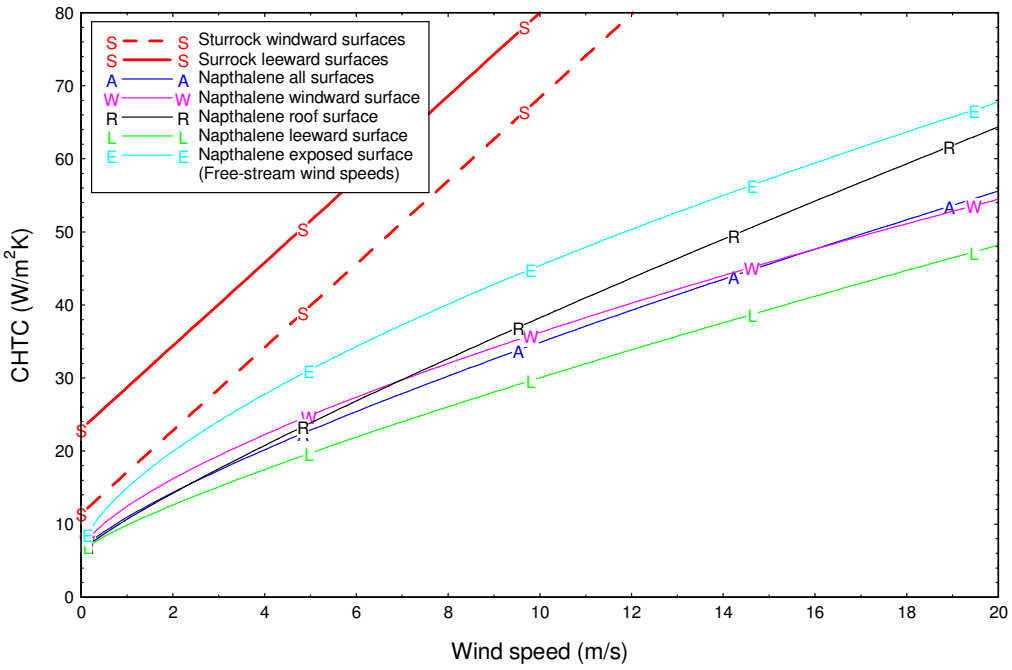

Figure 9.32: Comparison of results with Sturrock's expressions

It is therefore not surprising to find that the expressions presented by Sturrock are also significantly in excess of the current results determined using the naphthalene sublimation technique. The reason for this disagreement with the current work and that of previous workers is not know. Care should therefore be taken when applying Sturrock's expressions since it appears likely that the results thereby attained will overestimate the rate of convection that will occur from the respective building surfaces.

Shao, Liu, Zhao, Zhang, Sun and Fu (2009)

Lastly, it is interesting to compare the current results with the expression derived by Shao *et al.* as both sets of results were obtained using implementations of the naphthalene sublimation technique. This therefore provides a direct verification of testing at the two different scales since all variation must be due to actual flow conditions as opposed to differences between experimental techniques.

Wind speed was measured during the full-scale study using an anemometer mounted at a height of 1.6 m on top of the 46 m tall test building. Whilst this total height above ground is closer to the current free-stream reference height (90 m), the influence of the buildings mean that the flow patterns are very dissimilar. Instead the current 10 meter reference wind speed height is perhaps more appropriate for the purposes of this comparison since it is also measured just above the building's roof. The two data sets are presented for comparison in this way in Figure 9.33 over the full wind speed range considered in the current study. However the results presented by Shao *et al.* were for the wind speed range 0.72 to 4.93 m/s, therefore it is more appropriate to restrict comparison to this lower range. The data has been replotted in Figure 9.34 accordingly. The current roof results have been highlighted, however the curves for the other wall surfaces have also been shown to permit further comparison.

It can be seen that there is close agreement between the naphthalene sublimation results obtained at model and full-scale which provides confidence in the experimental methodology. Different values for the exponent 'n' were taken in the mass-heat transfer analogy (0.34 for the current work, 0.40 by Shao *et al.*), but it can be shown that this results in a variation of less than 8% in the CHTC values (see Section 8.1 for further details). The agreement is particularly close in the lower wind speed range ($V < 5$ m/s) for which the full-scale results were obtained. It can be seen in Figure 9.34 that the majority of the variation at lower wind speeds is as a result of the significantly difference free convection coefficients that have been employed (6.22 W/m^2K in the current study versus 3.9 W/m^2K by Shao *et al.*). The forced convection components of the two expressions are more similar and hence the curves converge at 5 m/s (although they do then diverge at higher wind speeds due to the linear form of the full-scale correlation).

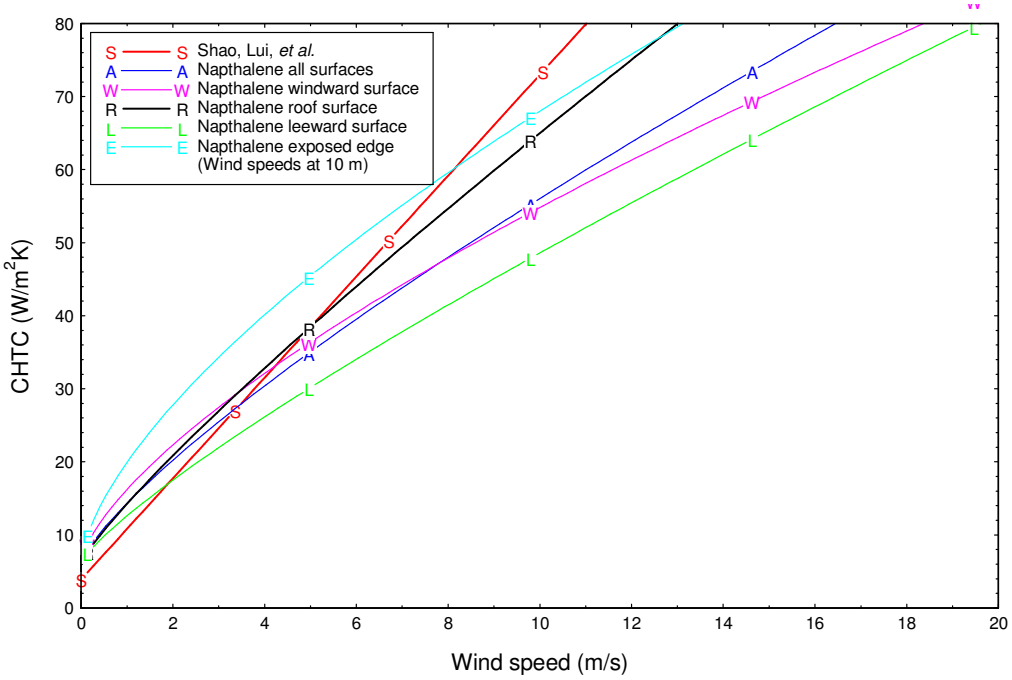

Figure 9.33: Comparison of results with the expression of Shao *et al.*

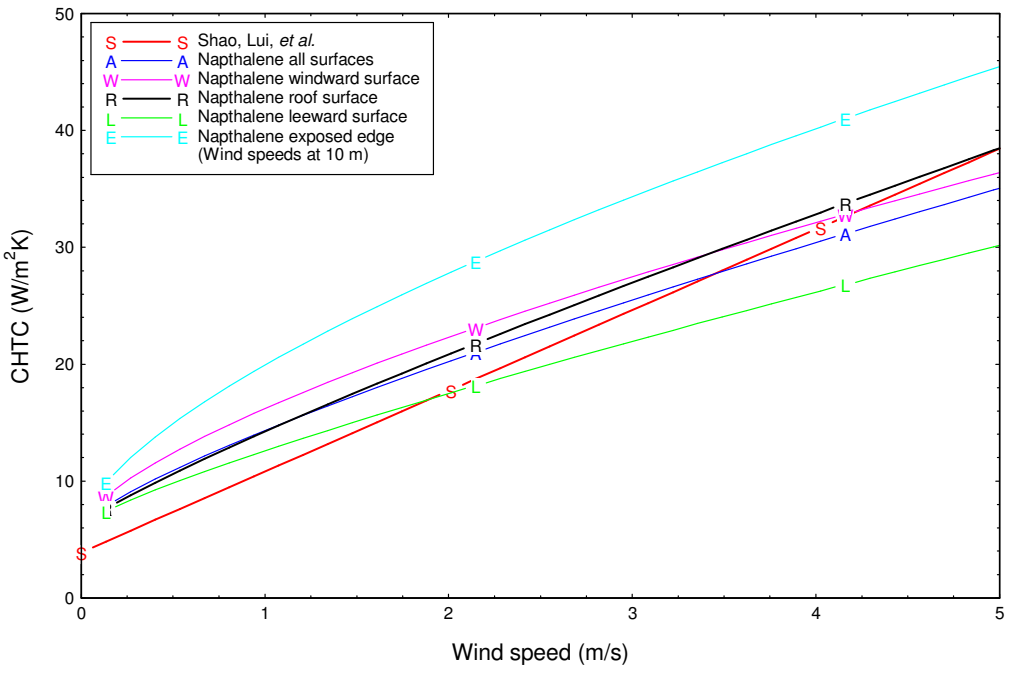

Figure 9.34: Comparison with the expression of Shao *et al.* for V < 5 m/s

9.9 Summary and conclusions

In this Chapter, the results of a series of naphthalene sublimation experiments have been presented which aimed to determine the relationship between wind speed and the rate of convective heat transfer from the surfaces of buildings. The geometry selected for these tests was that of long street canyons orientated perpendicular to the wind at a height-to-width ratio of 0.5. This arrangement was selected as being typical of the uniform rows of buildings found in numerous towns and cities around the world. The experiments have thereby allowed a set of convection coefficient expressions to be determined for a generic low-rise urban environment which are more widely applicable than those proposed in the existing literature.

A naphthalene sublimation experiment was initially conducted at zero wind speed in order to determine the rate of free convection occurring from the various model surfaces. It was found that there was little variation in the rate of convection between the horizontal and vertical surfaces; this was an unexpected result since both theory and the literature suggested otherwise. The lack of differentiation between the two surface orientations was attributed to a lack of spatial separation and to the small length scale of the wind tunnel models. The average rate of convection over all three of the model surfaces was calculated to be 6.22 W/m^2K. This is at least 50% greater than the values prescribed in the most recent British Standards and design guides, but is close to the centre of the range of values proposed by the selection of previous work which has been considered. It is also very close to the values determined by Juerges (1924) in his pioneering work from which many current convection equations are still derived.

A number of researchers have demonstrated the dependence of the rate of free convection upon the length of a vertical surface. The current results also appear to show a slight decrease in the levels of convection with height over the vertical faces of the cube model, although it is noted that this variation does lie within the range of experimental error and may therefore not necessarily be real. A length scale of 1:100 was chosen for the wind tunnel models and so the effects of differential convection on the vertical surfaces are similarly reduced. Thus it is possible that the measured levels of free convection are representative of that which will occur near to the base of a larger full-scale building surface and that lower rates will occur at higher locations. The surface averaged rate of convective heat transfer would thereby be less than that derived, perhaps closer to the value prescribed in the Standards. Further free convection measurements from full-scale surfaces would be required in order to confirm such a phenomenon, but this lies outside the scope of the current work. The effect is therefore highlighted solely for information purposes and for possible future consideration. The average value of 6.22 W/m^2K has been adopted as the free component of convection for the presentation of the current results.

The most apparent advantages of the naphthalene sublimation technique have been with regards to modelling the effects of forced convection within an inner-city context. By drawing upon knowledge of the urban boundary layer simulation developed in the wind tunnel it has been possible to determine convection expressions involving the meteorological standard wind speed, as well as the free-stream wind speed originally measured. Two sets of convective heat transfer correlations have therefore been presented from which may be selected the appropriate equation based upon the available wind data for a given scenario.

The effect of varying the height at which the reference wind speed is defined has also been investigated. It was shown that this can have a significant effect upon the form of the derived expressions and hence upon the convection values which are calculated if an inappropriate wind speed is later used. The free-steam and met. standard wind speed expressions which have been derived cover the two most likely types of wind speed data that will be available in practice. Whilst other researchers have shown that the best correlations may be obtained using more local wind speeds measured directly adjacent to the surface in question, such data is rarely available. This can lead to alternative wind speed data being incorrectly substituted thereby giving incorrect values for the rate of convection. In contrast, met. standard wind speeds are recorded at hundreds of weather stations across the United Kingdom as well as in many other countries. This data is readily available and may already have been obtained for use in other aspects of the design of a building (e.g. to enable calculation of wind loads on cladding or roofing elements). It is essential that the correct wind speed reference location is specified for any given equation and that designers are aware of the risks of not complying with this requirement.

The convective heat transfer coefficients obtained from the experiments were initially presented as the traditional linear and power-law forms of equation. Linear expressions were shown to better represent the smooth transition from free to forced convection, whereas power-law curves are able to model the tailing-off of the rise in the convection coefficients at higher wind speeds. Neither form of expression was therefore fully adequate and hence an alternative 'offset power-law' form of expression was proposed which encompasses the advantages of both standard types of equation.

The resulting offset power-law expressions relating the convective heat transfer coefficients for each building surface to the free-stream and met. standard wind speeds are summarised in Table 9.12 below. Separate equations have been derived for windward, roof and leeward façades, as well as an overall average of these three surfaces. In addition, the peak convective coefficients occurring at the leading edge of the building are given by the 'exposed edge' equations.

Table 9.12: Summary of derived offset power-law correlations

	Correlating wind speed measurement height	
Surface	**Free-stream (90 m)**	**MSW height (10 m)**
All	$h_c = 6.22 + 4.70V_f^{0.785}$	$h_c = 6.22+8.10V_m^{0.789}$
Windward	$h_c = 6.22 + 6.20V_f^{0.685}$	$h_c = 6.22+9.99V_m^{0.687}$
Roof	$h_c = 6.22 + 4.41V_f^{0.861}$	$h_c = 6.22+8.02V_m^{0.865}$
Leeward	$h_c = 6.22 + 3.62V_f^{0.818}$	$h_c = 6.22+6.37V_m^{0.823}$
Exposed edge	$h_c = 6.22 + 8.73V_f^{0.652}$	$h_c = 6.22+13.70V_m^{0.654}$

The convection results derived from the naphthalene sublimation experiments have been compared with the equation presented in BS EN 6946 (BSI, 2007). Whilst the values obtained from this equation are within the same range as the current experimental results, there are obvious discrepancies particularly at the highest and lowest wind speeds. The Standard equation was derived from work conducted in laminar-flow wind tunnels using flat plates. Atmospheric turbulence and surface roughness effects will tend to increase the rate of convective heat transfer and this is anticipated to be the prime cause of the discrepancy noted. This finding implies that the values given by the Standard and related design guides may significantly underestimate the rate of forced convection occurring from the surfaces of real buildings. It has therefore been proposed that the correlations determined in the current study are more appropriate for application to full-scale building surfaces in urban environments.

Comparisons have also been made to full-scale measurements conducted by several previous researchers; the full-scale naphthalene sublimation results of Shao *et al.* (2009) were of particular interest. The naphthalene sublimation results have been shown to compare well with full-scale convection measurements made on low-rise buildings, but differ significantly to those made on higher-rise buildings and tower blocks. This has highlighted the importance of convective relationships being applicable to the building geometry in question; it is proposed that the current results are widely applicable to low-rise urban areas as are common in towns and cities. Further work will be required in order to fully understand the process of convective heat transfer occurring from isolated high-rise structures.

In conclusion, the naphthalene sublimation technique has allowed a series of convective heat transfer expressions to be developed which significantly increase the scope and applicability of those found in the current literature. It is proposed that these equations will permit more accurate calculation of the levels of convection from buildings in urban areas which take account not only of the building geometry, but also the relevant characteristics of the wind in our towns and cities.

Chapter 10 The effect of canyon width upon convective transfer

10.1 Introduction

The geometry of urban street canyons varies widely from city to city, and from country to country. London is unusual for a Western capital in that it has relatively wide streets. North American cities, for example, typically have much narrower streets and also higher-rise buildings giving rise to much deeper canyons with larger height-to-width ratios. Similarly, some southern European cities are designed with deep, narrow street canyons so as to minimise solar penetration and hence maintain cool indoor temperatures during the hot summer periods.

It is known that wider street canyons promote greater turbulent air exchange from between the buildings. It is therefore anticipated that the convective heat transfer coefficients are also greater when the buildings are more widely spaced. To test this thesis, a series of nine naphthalene sublimation experiments have been conducted in order to determine the effect of street canyon width on the convective heat transfer rates from the surfaces of the buildings. By using the non-dimensional height-to-width ratio (H/W) as a measure of canyon spacing, the effect of building heights can be neglected (assuming that these are uniform) in favour of the overall form of the canyon.

The effect of canyon spacing is most notable when the wind is blowing perpendicular to the orientation of the streets (i.e. 0 degrees). Hence this orientation has been selected as the basis for the current series of tests, with the naphthalene coated model positioned in the middle of a long row of buildings. Three further rows of buildings were positioned on both the windward and leeward sides of the active model. Height-to-width ratios of 1.00, 0.50 and 0.25 were tested, which correspond with the skimming, wake-interference and isolated flow regimes respectively, as was discussed in Chapter 7. A height-to-width ratio of 1.00 signifies that the street width and building height are equal, a ratio of 0.50 indicates that the street width is twice the height of the building, and so on.

Each of these three geometries were tested at wind tunnel speeds settings of 15%, 30% and 45%; the optimum range for the naphthalene sublimation technique noted in the previous Chapter. The wind speeds presented are those measured at a reference height of 900 mm in the wind tunnel boundary layer as this corresponds to the free-stream wind speed above an urban area. All other parameters were kept the same as per these preceding tests.

10.2 Experimental results

The experimental data obtained during the series of nine naphthalene sublimation tests are summarised in Table 10.1 below. For each height-to-width ratio, results are given for slow (S), medium (M) and fast (F) wind tunnel speeds. These correspond to speed settings of 15%, 30% and 45% of maximum tunnel speed. The average result for each of the fifteen horizontal rows of measurement locations is presented, along with the average results for each of the three surfaces and the combined average over the whole model. Full results from these experiments are detailed in Annex F at the end of this report.

Table 10.1: Summary of convective coefficients obtained in tests

		CHTC's (W/m^2K)								
		H/W = 1.00			**H/W = 0.50**			**H/W = 0.25**		
	Row	**S**	**M**	**F**	**S**	**M**	**F**	**S**	**M**	**F**
Windward	1	16.65	23.84	27.01	25.44	33.32	37.32	21.77	40.07	49.29
	2	14.15	22.75	28.64	21.98	30.22	36.92	24.18	39.12	49.27
	3	23.10	23.56	27.11	27.32	34.59	42.04	26.82	41.64	53.21
	4	29.01	27.26	28.46	32.50	40.60	47.91	29.12	46.44	59.00
	5	33.98	35.24	28.09	35.76	47.02	51.96	32.79	48.19	67.11
	Av.	**23.38**	**26.53**	**27.86**	**28.60**	**37.15**	**43.23**	**26.94**	**43.09**	**55.57**
Roof	6	25.28	29.97	31.97	35.84	49.07	58.87	42.77	44.78	76.88
	7	22.50	24.37	34.27	29.45	35.92	47.32	32.58	35.85	63.84
	8	25.69	23.05	38.25	24.67	34.68	43.16	31.59	29.80	57.52
	9	18.63	23.27	36.73	22.62	32.62	47.51	29.72	35.00	54.31
	10	19.11	18.70	32.92	24.40	32.86	44.54	25.97	25.43	51.89
	Av.	**22.24**	**23.87**	**34.83**	**27.40**	**37.03**	**48.28**	**32.53**	**34.17**	**60.89**
Leeward	11	10.90	16.29	27.13	18.58	25.66	37.11	17.17	19.74	34.52
	12	11.33	14.48	28.60	19.20	28.79	40.25	19.06	22.38	36.86
	13	18.17	19.61	26.92	22.88	30.52	41.69	27.02	25.06	38.58
	14	23.61	27.35	27.25	24.54	32.96	42.98	20.10	25.06	39.88
	15	25.85	31.27	24.73	22.48	33.38	43.87	16.99	28.07	36.86
	Av.	**17.97**	**21.80**	**26.93**	**21.54**	**30.26**	**41.18**	**20.07**	**24.06**	**37.34**
Overall average		**21.20**	**24.07**	**29.87**	**25.84**	**34.81**	**44.23**	**26.51**	**33.78**	**51.27**

The same results are also displayed graphically in Figure 10.1 for a height-to-width ratio of 1.00, Figure 10.2 for a height-to-width ratio of 0.50 and Figure 10.3 for a height-to-width ratio of 0.25. In these graphs, the vertical axis shows the calculated convective heat transfer coefficient (measured in W/m^2K) averaged over each horizontal row of taps. The assumption that the flow is two-dimensional implies that the there should be negligible variation between the five measurement locations in each row. Therefore averaging the values across each horizontal row gives more confidence in the results and allows the data to be presented in a more convenient two-dimensional format.

The horizontal axis of the following graphs show the position on the model with horizontal rows numbered from 1 at the base of the windward face through to 15 at the base of the leeward side. The graphs have also been split into three sections by dotted lines in order to indicate the windward (left-hand side), roof (centre) and leeward (right-hand side) surfaces.

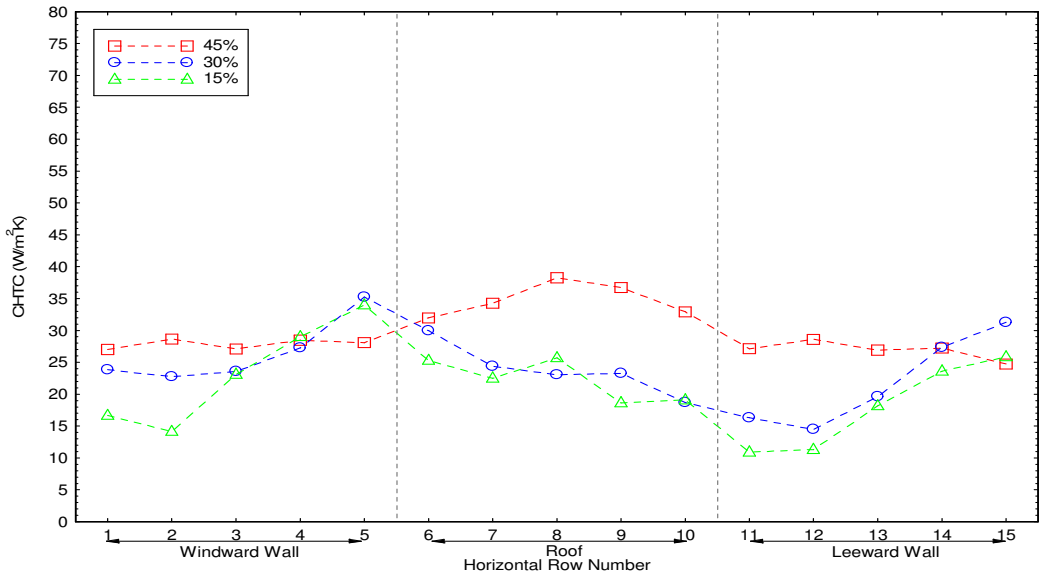

Figure 10.1: Measured CHTC's for a height-to-width ratio of 1.00

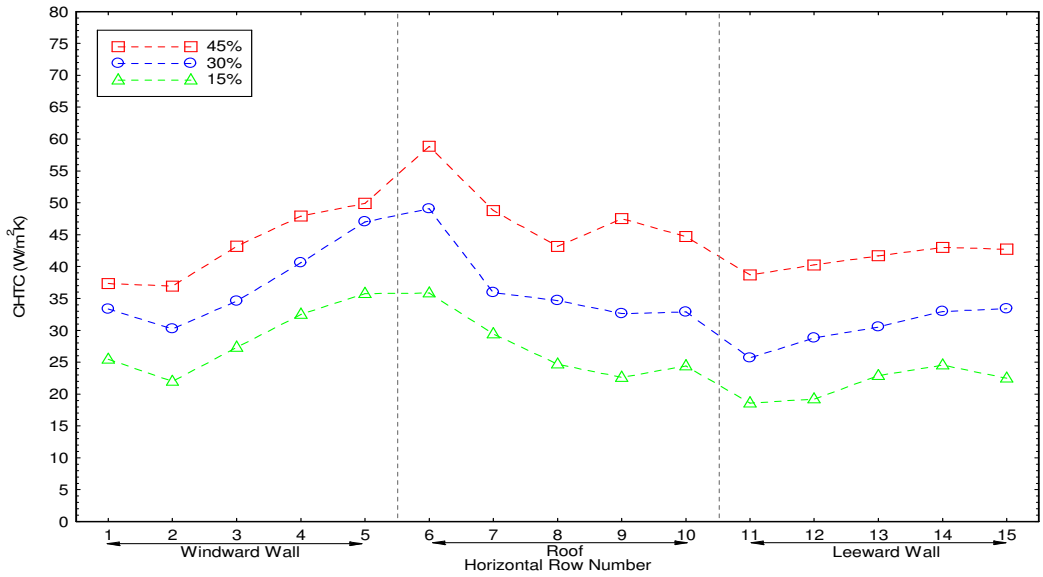

Figure 10.2: Measured CHTC's for a height-to-width ratio of 0.50

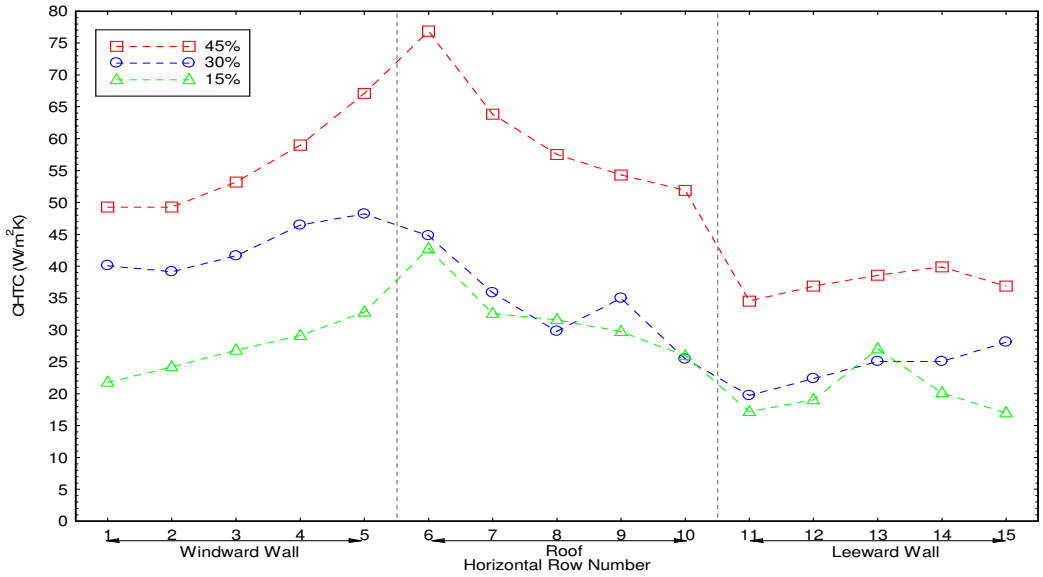

Figure 10.3: Measured CHTC's for a height-to-width ratio of 0.25

It is evident from these three figures that there are clear differences in the rates and patterns of convective heat transfer from buildings at alternative canyon spacings. The results obtained at a canyon height-to-width ratio of 1.00, shown in Figure 10.1, are relatively uniform across the three surfaces in comparison to the more spatially-varied results presented in previous Chapters. The results for the fast (45%) wind speed are the most uniform and shown significant variation from the two lower speed results across the roof and leeward surfaces. In contrast, Figure 10.2 shows the typical pattern of peaks and troughs in the convective coefficients for a height-to-width ratio of 0.50 with which we have become familiar in the proceeding Chapter.

The results obtained for a height-to-width ratio of 0.25, shown in Figure 10.3, are an exaggerated form of those for the height-to-width ratio of 0.50. The data for the medium (30%) wind speed appears to be missing the larger peak at the leading edge of the roof seen at other wind speeds and alternative canyon geometries. The data for this experiment has been reprocessed and checked, and no error or anomalies have been found which could lead to this variation. There is also no obvious theoretical reason why the flow should be any different at this particular speed, and so the reason for this variation currently remains unclear.

10.3 Comparison of results for varying height-to-width ratios

In order to aid comparison of the results for the three different height-to-width ratios, the data for each of the experiments conducted at the fast (45%) wind tunnel speed setting are plotted together in Figure 10.4 below.

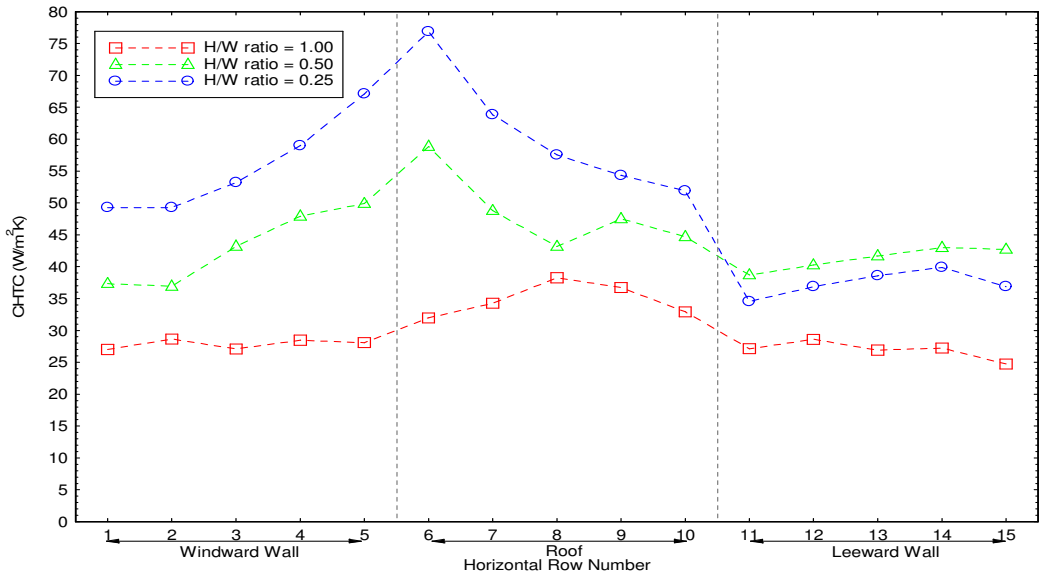

Figure 10.4: Variation of the height-to-width ratio at 45% tunnel speed

The greatest convective heat transfers can be seen to occur at the smaller height-to-width ratios. Such ratios correspond to greater spacings of the rows of buildings and hence to more exposed flow regimes, high local velocities and greater turbulent flushing of the 'polluted' air from within the streets.

At a height-to-width ratio of 1.00, a skimming flow regime exists whereby the majority of the wind passes over the top of the roofs with little interaction within the canyon itself. At a height-to width ratio of 0.50, air flow in the canyon is increased by the wake-interference flow regime giving greater exposure to the vertical building façades. Ultimately, at a height-to width ratio of 0.25 (or less), the gap between each row of buildings is such that they each behave as an isolated row. A ratio of 0.25 is therefore typical of rural areas, a ratio of 0.50 relates to typical urban areas, and a ratio of 1.00 corresponds to high-density inner-city areas. Whilst this guide is approximate, it gives a good feel for the significance of the data to different scenarios.

In Figure 10.4, the data relating to convection at a height-to-width ratio of 0.50 shows the typical features of a wake-interference regime that have been discussed in detail in the preceding Chapter. Convective transfer from the windward face increases with height up to a peak at the exposed leading edge of the model. The coefficient across the roof diminishes from this peak to a minimum at the top of the leeward surface, before rising slightly down the leeward façade.

The data obtained at a height-to-width ratio of 1.00, is both the lowest of those plotted and also the most uniform across the surfaces. The convection occurring from both the windward and leeward vertical surfaces is very similar and there is minimal variation with height over each surface. This indicates that air circulation within the canyons on both sides of the model is slow and relatively uniform. The peaks at the top of the windward edge identified in tests at wider canyon spacings are not present, and neither are the areas of lesser convective transfer at the top of the leeward surface. The convection coefficient pattern across the roof surface is also unusual in that it is almost symmetrical along the centreline, without the usual peak at the leading edge.

In contrast, the data obtained at a height-to-width ratio of 0.25 exhibits the greatest convection coefficients. The pattern across the windward and roof surfaces is similar to that for the wake-interference regime, except that the convection coefficients are on average approximately 12 W/m^{2}K higher. The coefficients at the windward roof edge are approximately 18 W/m^{2}K higher. However, the rate of convection occurring from the leeward surface is actually less than that occurring at a height-to-width ratio of 0.50. Whilst this may appear surprising at first sight, consideration of the flow patterns in the wake region provides the explanation. At narrower canyon widths, the wake region behind a building is constrained by the following row of buildings and therefore the flow is trapped. In contrast, at a height-to-width ratio of 0.25, the rows of buildings are sufficiently well spaced to allow each subsequent wake region to dissipate resulting in lower wind speeds adjacent to the leeward façades. Lower wind speeds result in less forced convection and hence whilst the coefficients elsewhere on the model increase, those on the leeward surface are seen to reduce.

The respective plot of results for the tests conducted at a 30% wind tunnel speed setting is shown in Figure 10.5.

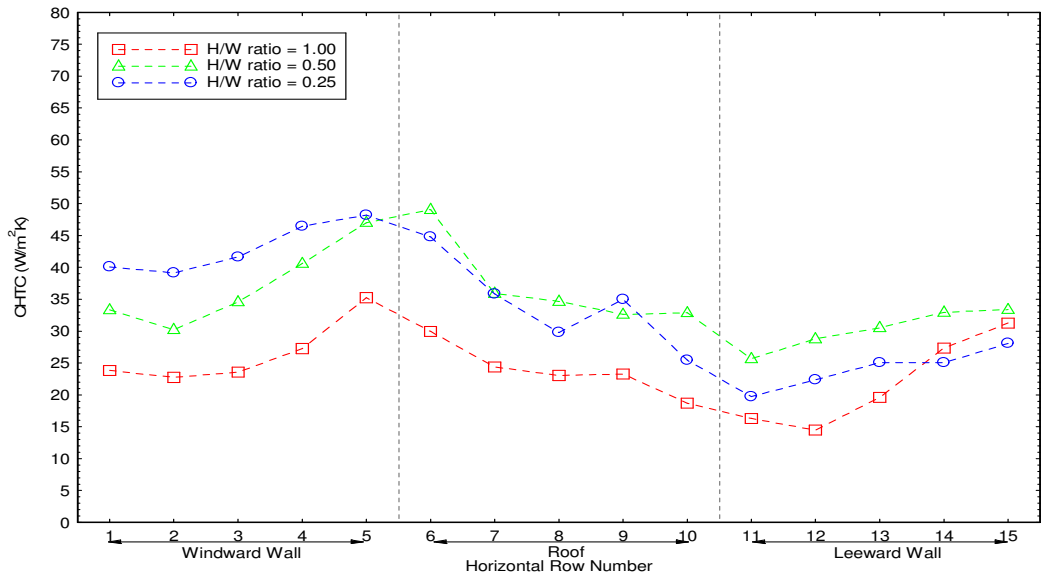

Figure 10.5: Variation of the height-to-width ratio at 30% tunnel speed

Although the characteristics described previously for the 45% speed settings results are less distinct, they are still discernable. In particular, the reduction in the rate of convection occurring from the leeward surface of the model is clear and this also extends over the roof surface.

It is however much less easy to make such comparisons between the results of the tests conducted at a wind tunnel speed setting of 15%, as shown below in Figure 10.6. The lower rates of sublimation in these tests mean that each set of data is less distinct and so the effect of varying the canyon spacing is less obvious.

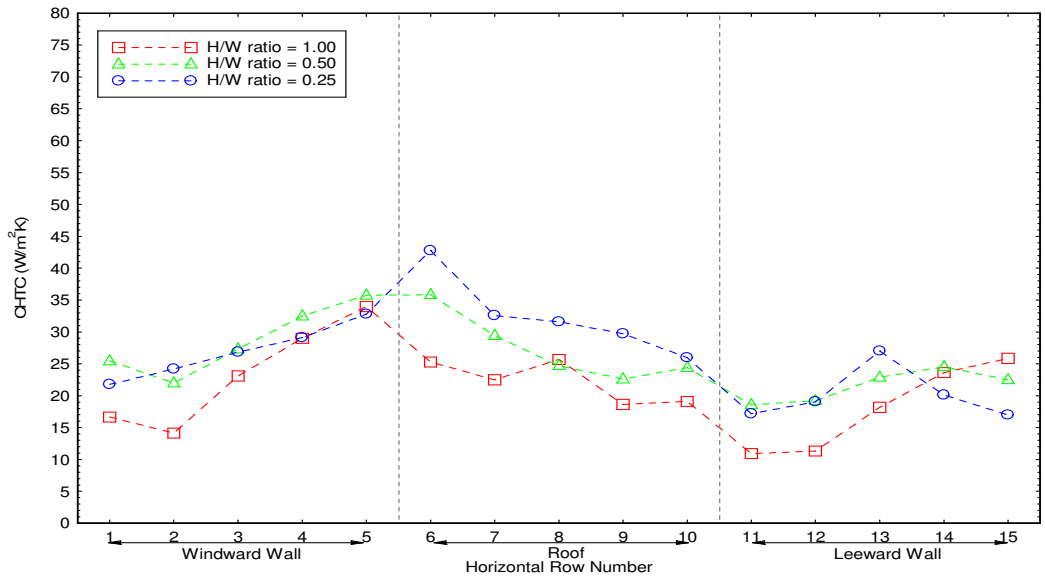

Figure 10.6: Variation of the height-to-width ratio at 15% tunnel speed

10.4 Quantifying the effects of changing canyon widths

In order to provide a quantifiable measure of the effect of canyon geometry upon the convective heat transfer from building surfaces, the variation in the values between alternative model arrangements will now be considered. The results from experiments conducted with the canyons spaced at a height-to-width ratio of 0.50 will be used as a baseline for this analysis, as the wake-interference flow regime is the most typical of the majority of urban areas. This particular geometry was also that used to determine the effects of wind speed upon convective transfer and a range of correlations has already been determined to express this relationship.

There is currently insufficient data available from which to determine reliable expressions linking canyon height-to-width ratio to the rate of convection from the individual surfaces. However, it is proposed that it may be possible to determine a general percentage increase or decrease from the baseline case. This factor could then be applied to results calculated using the previously determined equation so that appropriate convection coefficients for alternative flow regimes may be obtained.

The results of this analysis are shown Table 10.2 below for canyon height-to-width ratios of 1.00 and 0.25. A height-to-width ratio of 0.50 has been used as the baseline and is therefore not included in this table. The presented data gives the average percentage increase or decrease for each surface. These values are calculated with respect to the values obtained for the same surface and speed setting, at a height-to-width ratio of 0.50. Values are given for the slow (S), medium (M) and fast (F) wind tunnel speed settings as well as the average value for the three speeds.

Table 10.2: Percentage changes in convection coefficients at alternative canyon geometries

	H/W = 1.00				**H/W = 0.25**			
Location	**S**	**M**	**F**	**Aver.**	**S**	**M**	**F**	**Aver.**
Windward average	-18.3%	-28.6%	-35.6%	-27.5%	-5.8%	+16.0%	+28.5%	+12.9%
Roof average	-18.8%	-35.5%	-27.9%	-27.4%	+18.7%	-7.7%	+26.1%	+12.4%
Leeward average	-16.6%	-28.0%	-34.6%	-26.4%	-6.8%	-20.5%	-9.3%	-12.2%
Overall average	**-18.0%**	**-30.9%**	**-32.5%**	**-27.1%**	**+2.6%**	**-3.0%**	**+15.9%**	**+5.2%**

The tabulated values are colour-coded to aid interpretation; red signifies a decrease and green (also underlined) an increase in the respective convective heat transfer coefficients.

It is evident that the relationship between canyon width and convective transfer rates from the buildings surfaces is not straightforward as may have been originally assumed. Whilst the results for the narrower street canyons all show similar reductions compared to the baseline scenario, the results for wider canyon spacings depend upon the individual surface.

For a height-to-width ratio of 0.25, a mixture of percentage increases and decreases are shown in the table for the windward and roof surfaces. Only the leeward surface experiences the same direction of variation for all three wind speeds. This is a significant result and is attributable to the wake region no longer being constrained by a subsequent row of buildings as it would be at closer canyon spacings. The wake is therefore more able to dissipate and so wind speeds are lower. Air flow may be further reduced by the lack of a nearby windward vortex generated by the downwind buildings. Lower wind speeds in this region result in the lower rates of convection from the leeward façade which have been noted. The average reduction in the convection coefficients is approximately 12% which, although around half the magnitude of the increase resulting from narrower canyon spacings, is still very significant.

This also implies that there must be an optimum canyon spacing at which peak convective transfer from the leeward surface of the building is experienced, although it is not possible to determine the magnitude of this dimension from the current data. Wake flows will be minimal at close building spacings and so such geometries will experience the lowest rates of convection from their leeward surfaces. At intermediate spacings, wake flow is increased by the windward vortex effect of subsequent rows of buildings and so leeward surface convection will reach a peak. As the canyon width increases further, the dissipation of the wake region and removal of the windward vortex effects will see the leeward convection rates decrease once more. The non-linearity of this relationship may also account for some of the variation in the results seen in Table 10.2.

The average percentage increases for the more exposed windward and roof surfaces at this wider canyon spacing are between 12 and 13%. However, the datasets each also feature a percentage decrease in the results for the slow and medium speed tests respectively. The cause of this variation is not clear, although it may be as a result of the varying levels of local turbulence created by the different model layouts. The average value for the three speeds has therefore been taken (including the negative results) in order to give a conservative estimate of the likely increases in convection from the windward and roof surfaces for this geometry.

The results for the narrower street canyon (a height-to-width ratio 1.00) are more clear and consistent. Whilst there is again variation in the percentage decreases of the convection coefficients between the three wind speeds, there is very close to a 27% reduction in every case. It is therefore proposed that when buildings are closely spaced so that a skimming flow regime exists (see Figure 7.9), the convection coefficients calculated from the equations presented in the previous Chapter be multiplied by a factor of 0.73 (i.e. a 27% reduction). Similarly, for more widely spaced canyons in which the isolated flow regime will predominate (see Figure 7.8), it is proposed that the results be factored by 0.88 for the leeward surface (a 12% reduction), and by 1.12 for windward and roof surfaces (a 12% increase).

The canyon geometry factors (F_g) which have been derived in the above discussion are summarised in Table 10.3 correct to three decimal places. The equations for convection rates at various wind speeds derived in the previous Chapter were based upon data for experiments conducted at a height-to-width ratio of 0.50. Therefore the values calculated using the proposed equation for such canyon spacings do not require factoring (i.e. a factor of unity should be used).

Table 10.3: Canyon geometry factors

	Canyon geometry factor		
Surface	**H/W = 1.00**	**H/W = 0.50**	**H/W = 0.25**
Windward	0.725	1.000	1.129
Roof	0.726	1.000	1.124
Leeward	0.736	1.000	0.878
All surfaces	0.729	1.000	1.052

These results have been determined using convective coefficients defined with respect to free-stream wind speeds (V_f). However they are equally applicable to equations determined for other wind speed measurements (the met. standard wind speed (V_m), for example) since the ratios of the results will remain the same.

10.5 Conclusions

It has been shown in this Chapter that the spacing of rows of buildings in urban areas can have a significant effect upon the rate of convection which occurs from their surfaces. A series of nine naphthalene sublimation tests have been conducted at various wind speeds and canyon height-to-width ratios. Canyon spacings of one, two and four times the height of the model buildings were selected for test as these generate the required skimming, wake-interference and isolated flow regimes respectively. These geometries were each tested at wind tunnel settings of 15%, 30% and 45%; the optimum range of tunnel speeds identified during previous tests.

The differences between alternative canyon spacings have been shown to be most pronounced at higher wind speeds. Conversely, the results of tests conducted at the lowest wind speed showed the least variation between canyon geometries. The results obtained in the previous Chapter for canyons at a height-to-width ratio of 0.50 have been used as the baseline with which to compare the results for the alternative canyon spacings.

A height-to-width ratio of 1.00 designates the most sheltered urban geometry that has been tested. In such scenarios, the flow above the rows of buildings is largely detached from that within the street canyon. This was evident by the significantly lower rates of convective transfer measured from models arranged in such configurations. The average reductions in convection coefficient compared to the baseline geometry were relatively uniform across the three surfaces at approximately 27%.

As streets become narrower, so they become more sheltered and hence experience lower wind speeds. The air movement within the canyon will become increasingly detached from the winds above the canopy layer since there is little potential for the mixing of the two. At the closest building spacings it is likely that the convection coefficients from the windward and leeward surfaces will each tend towards those of free-convection as any air movements become damped out. In such circumstances, the convection from the array of closely spaced flat roofs is likely to become like that from a single horizontal surface as the distinction between individual rows is lost. Such geometries would however be rare in practice.

The effect of increasing the canyon spacing has been showed to be more complex. A minimal height-to-width ratio of 0.25 was tested; here the flow around each subsequent row of buildings behaves as if it were in isolation. The windward and roof surfaces of the model are fully exposed to the prevailing wind and therefore experience an approximate 12% rise in convection coefficients compared to the baseline. However, the leeward surfaces experience a reduction in the rate of convection of approximately 12%.

The leeward surfaces of buildings are the least affected by the spacing of the rows of buildings. This is a reflection of the smaller variation in the flow patterns adjacent to this sheltered surface. However, the variation is more complex than that of the other surfaces since the rate of convection reduces at both narrow and wide canyon spacings. There is an optimum spacing at a height-to-width ratio of around 0.50 at which the convective heat transfer from the leeward surface is maximised.

At larger height-to-width ratios, wind speeds in the canyon are lower as a result of increased shelter. At smaller height-to-width ratios, the wake is able to dissipate and the windward vortex generated by the subsequent buildings is removed. Both of these effects give rise to lower rates of convection from the respective leeward surfaces. Conversely, the greatest variation in convective coefficient was found to be at the top of windward façade and leading edge of the roof. This region has already been shown to be the most exposed on the model and this increased variation at alternative canyon widths is therefore not unexpected.

By comparison of the results obtained for height-to-width ratios of 1.00 and 0.25 with those previously obtained at a height-to-width ratio of 0.50, a set of canyon geometry factors have been derived. These factors can be applied to the results calculated from the equations presented in the preceding Chapter in order to give adjusted results for greater or lesser canyon spacings.

The significance of canyon spacing to CHTC magnitude further supports the argument that the relationships detailed in the most recent British Standards and design guides do not appropriately deal with convection from the surfaces of buildings in urban environments. As these existing relationships are based mainly upon work conducted in laminar wind tunnels using flat plates, the effects of building geometry have until now be largely neglected. The canyon geometry factors determined in this Chapter further extend the scope of the equations previously derived for application in real world situations.

Chapter 11 The effect of wind direction upon convective transfer

11.1 Introduction

The nature of the local flow regimes which exists around street canyons not only depend upon the canyon spacing, but also upon the direction of the approaching wind. Until this point only flow moving perpendicular to the canyons has been discussed. Whilst this arrangement has allowed the effects of wind speed and canyon geometry to be studied, such idealised conditions will occur infrequently in practice. Therefore the effect of alternative approaching wind directions was also considered. A further series of naphthalene sublimations experiments were conducted with the approaching wind both parallel to the streets and also at an intermediate 45 degree 'diagonal' angle. Previous researchers concluded that the flow regime which exists at a given intermediate wind direction is a combination of those which occur for the perpendicular and parallel cases (Oke, 1987). It was therefore not necessary to test the whole range of intermediate angles since these only vary between the two extremes.

Winds blowing parallel to a street canyon flow along its length and can reach ground level between the buildings more readily. The channelling effect of the rows of buildings can accelerate the flow leading to even higher wind speeds than those above the roofs. This may result in increased heat transfer from the vertical walls compared with the perpendicular flow scenario previously described. However, the decreased roughness seen by the wind will create less turbulent flow around the buildings and the separation region at the windward edge of the roof will be lost. This may result in reduced rates of convective heat transfer from such regions which were relatively exposed for perpendicular flow conditions.

When the wind approaches the rows of buildings at an intermediate angle, the effects of along-canyon flow (noted for parallel winds) and the windward vortices (observed with perpendicular winds) is combined. This gives rise to a 'corkscrew' motion whereby the wind spirals along the street canyon. The particular angle of the approaching wind determines the relative importance of each of the two flow effects and thereby the pitch of the spiralling winds. The closer the wind direction is to being parallel with the streets, the more elongated the corkscrew will be.

In order to investigate the impact of these varying flow regimes upon rate of convective heat transfer from building surfaces, a series of experiments were conducted on an array of seven rows of buildings. These were arranged at a height-to-width ratio of a half to represent a typical urban street layout. Using the rotating turntable of the BRE wind tunnel, this layout was tested at approaching wind angles of 0 degrees (perpendicular to the canyons), 45 degrees (diagonal to the canyons, see Figure 11.1) and 90 degrees (parallel to the canyons, see Figure 11.2).

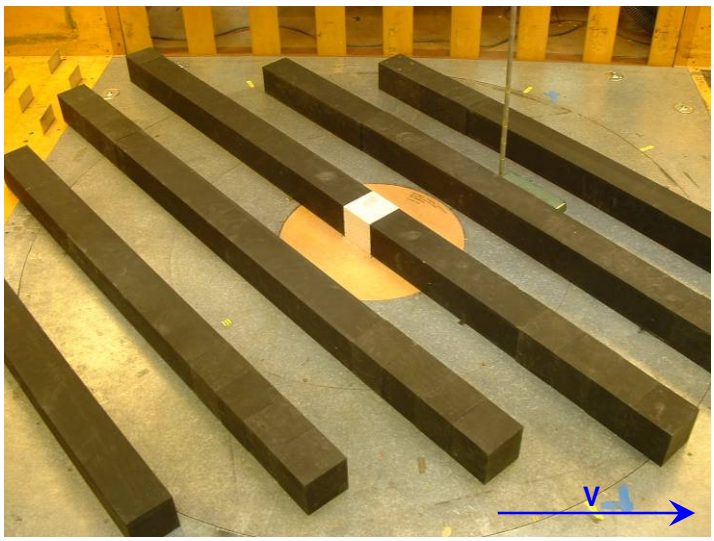

Figure 11.1: The model street canyons arranged diagonal to the flow

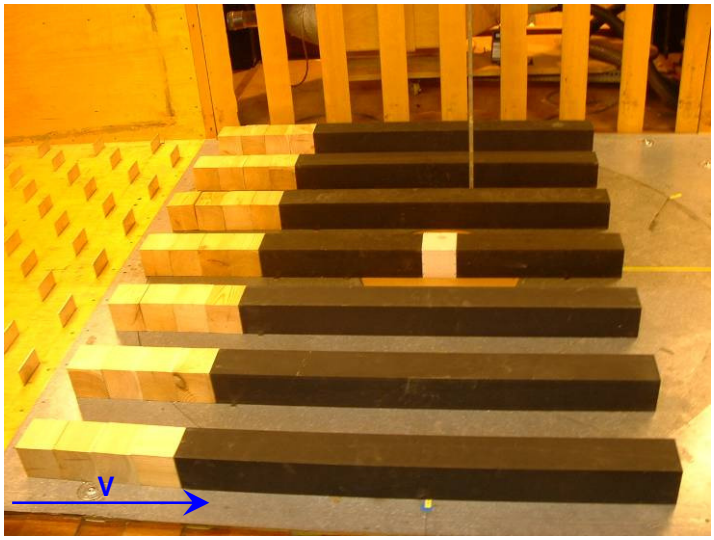

Figure 11.2: The model street canyons arranged parallel to the flow

Extra wooden blocks were positioned at the upwind end of the rows of buildings for the 45 and 90 degree wind directions in order to extend the array of models up to the end of the wind tunnel roughness plates. This was necessary in order to ensure that the generated velocity profile was maintained across the turntable and to remove any possible end effects from the measurements. The extra blocks (some bare pinewood and some painted black) can be seen in the above two photographs. These additions were not required for the perpendicular flow experiments described in previous Chapters since the number of upstream canyons already spanned the whole of the turntable area. The active naphthalene coated model on which measurements were made is the light coloured block at the centre of the turntable in the above photographs.

11.2 Experimental results

Results for the perpendicular (0 degrees) flow configuration have been presented previously in Chapter 9 but are reproduced below in Figure 11.3 for ease of reference. In summary, it was shown that the highest levels of convective heat transfer occur at the leading edge of the roof where the separation region lies. The convective coefficients then decrease towards the leeward edge of the roof. A similar convective peak is seen towards the top of the windward wall and so it is concluded that the maximum peak lies along this vertex. In contrast, the rates of convective transfer over the leeward wall of the model remain almost constant across its height signifying more homogenous flow in the wake region.

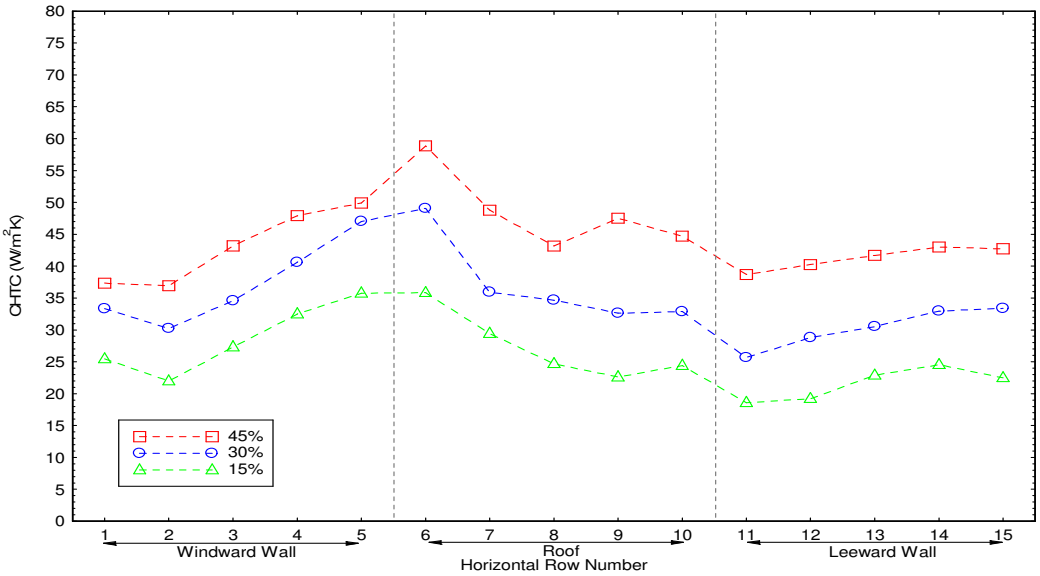

Figure 11.3: Experimental results for perpendicular (0 degrees) flow angle

Figure 11.4 shows the experimental results obtained with the canyons arranged at the 45 degree intermediate angle to the approaching flow. It can be seen that the peaks noted for perpendicular flow along the exposed front edge of the model are now less pronounced and that the pattern of convection coefficients is generally smoother. On the leeward surface, the dip in the rate of convection at the top of the façade is much more prominent and a definite peak appears nearer to the ground. This is evidence that there is greater variation in the flow next to this surface as a result of the corkscrewing motion described previously. In other regards the data retains the same basic trends and characteristics as identified for the perpendicular flow case.

The results of the experiments conducted with the street canyons orientated parallel (90 degrees) to the approaching flow are plotted in Figure 11.5. Two unique features of this data are immediately obvious which differentiate it from the other flow directions considered. Firstly, there is less variation in the rate of convection occurring across the three surfaces. The data is smoothest for the lower wind speed tests, which indicates that extra turbulence is generated at higher speeds, possibly by small gaps between adjacent models. Secondly, as would be expected, the data can be seen to be symmetrical along the centre line of the roof

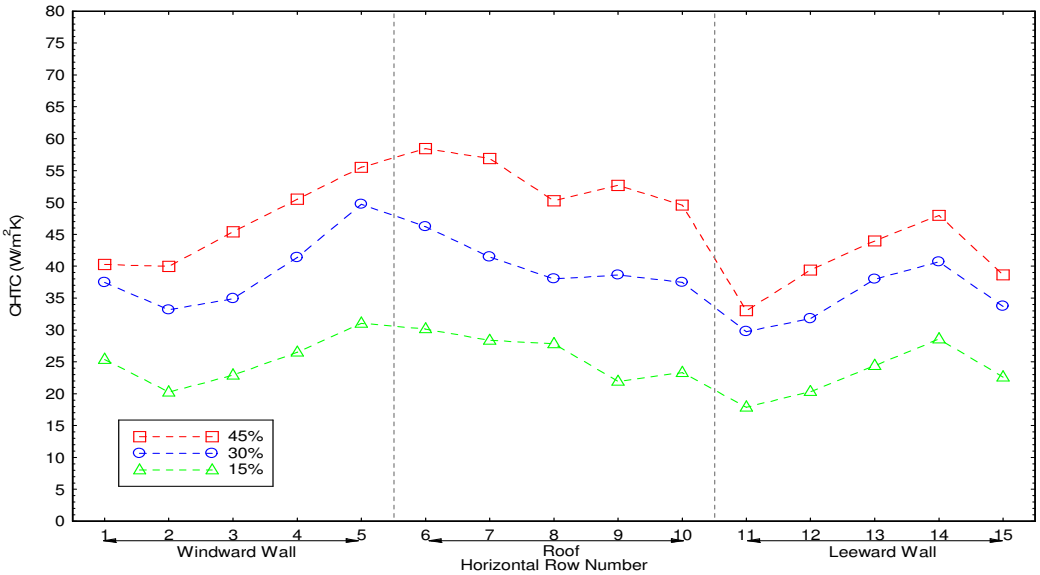

Figure 11.4: Experimental results for intermediate (45 degree) flow angle

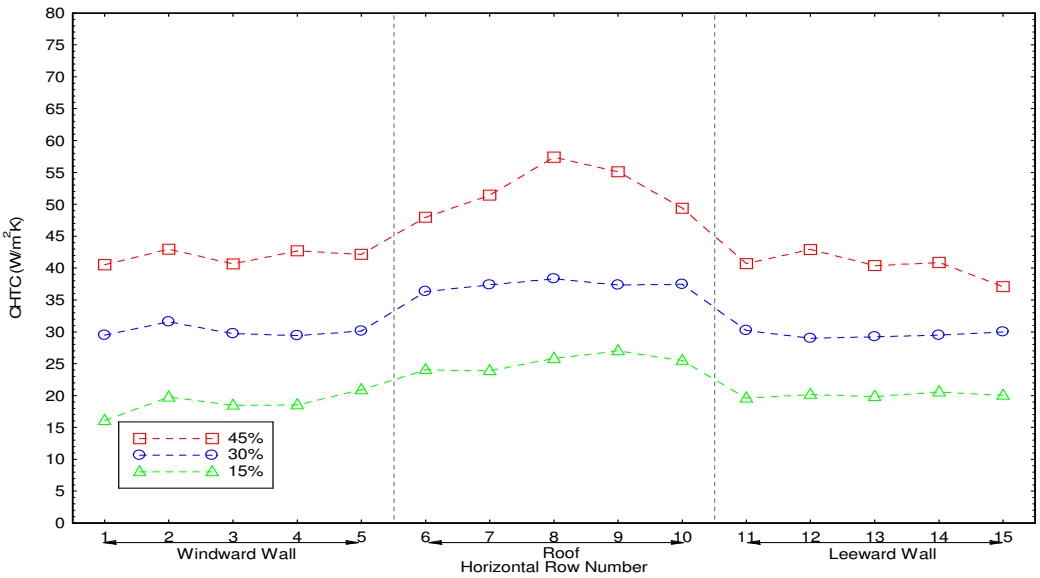

Figure 11.5: Experimental results for parallel (90 degree) flow angle

11.3 Comparison of results for varying wind angles

In order to permit easier comparison between the three sets of convective heat transfer data, the results of the fast speed (45%) tests for each wind angle have been re-plotted together in Figure 11.6 below. This format makes direct comparison and identification of the differences between the various scenarios much easier.

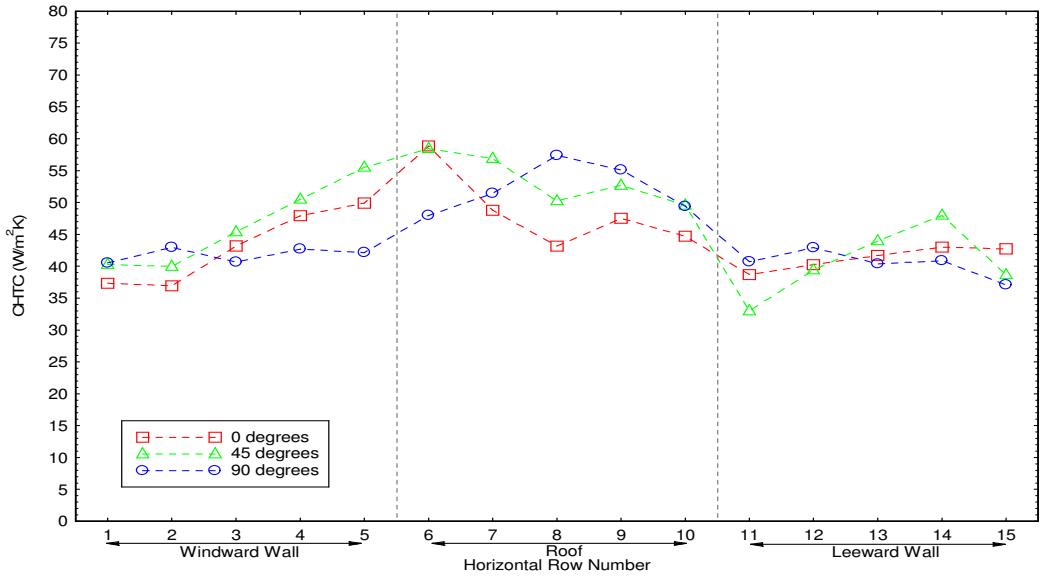

Figure 11.6: Comparison of CHTC for different wind directions

The first observation that can be noted from this graph is that the range of magnitudes of the convection coefficients is approximately the same for all three wind directions. The peaks on the roof of the model, although varying in location, are all approximately 58 W/m^{2}K. The lowest values measured on the vertical surfaces are also of a similar magnitude irrespective of the angle. From this observation it is evident that varying the orientation of the street canyon with respect to the approaching wind does not have a great effect on the range of local wind speeds, but does affect how these are distributed around the buildings.

Across the roof of the model, the results for the perpendicular and diagonal flow conditions (0 and 45 degrees) are similar. They both exhibit a peak value at the leading edge which diminishes towards the leeward surface, excepting a smaller secondary peak at measurement row 9 which is most likely due to flow reattachment.

The data for the roof in the parallel wind scenario is quite different, being almost symmetrical along the centreline of the roof. Similarly, the results for the two vertical façades are near mirror-images of each other. This finding is not unexpected since the flow pattern along the street canyons will be identical on either side of the models; there are no longer windward and leeward surfaces since they are now both aligned parallel with the flow path. It is expected that this symmetry will only exist for a very limited range of wind directions close to parallel flow. Outside this range, the convective coefficients will begin to resemble those of the 45 degree wind direction shown in the figure above.

On the windward building surface, the convective coefficients for a 45 degree wind direction are slightly greater than those for perpendicular flow. This is likely to be because this façade is more exposed, with a greater diagonal along-wind distance between the two adjacent rows of buildings. This allows the flow above the roofs of the buildings to enter the canyons to a larger extent and hence local wind speeds next to the windward surface will be increased. The additional along-canyon component of the flow resulting from the corkscrew motion of the air will also serve to increase the local wind speeds. The top of the windward surface is the most exposed leading to increasing rates of convection with height over the surface of this façade.

In contrast, the results for the vertical surfaces of the model in parallel flow are much more uniform. In such a scenario, the rows of buildings will channel the flow along the street giving relatively uniform wind speeds adjacent to the surfaces. A slight reduction in the convective coefficients is seen at the bottom of each vertical façade (also noted for the other wind directions) which is due to lower velocities at the bottom corners of the street canyons.

To provide a more quantifiable measure of how the average convective heat transfer coefficients for the various surfaces vary with wind direction, the data for the three tested scenarios are tabulated in Table 11.1 below. The average coefficients over the whole model are also included. For the diagonal (45 degree) and parallel (90 degree) flow results, the percentage changes in each value compared to the baseline perpendicular (0 degree) flow scenario are provided in parenthesis to give a numerical significance to the variation in the results. The results are colour coded for ease of reference; red signifies a reduction in the rate of convection and green (also underlined) an increase.

Table 11.1: Comparison of surface average convection coefficients

	Average convective heat transfer coefficient (W/m^2K)		
Surface	**Perpendicular flow (0°)**	**Diagonal flow (45°)**	**Parallel flow (90°)**
Windward	43.23	46.33 (+7.2%)	41.80 (-3.3%)
Roof	48.28	53.58 (+11.0%)	52.25 (+8.2%)
Leeward	41.18	40.60 (-1.3%)	40.40 (-1.9%)
Average	**44.23**	**46.83 (+5.9%)**	**44.81 (+1.3%)**

When presented in this way, it is clear that there is little variation in the average rates of convection across the building surfaces for different wind directions. The greatest effect is seen on the roof surface of the building where increases of 11% and 8% are seen for the 45 and 90 degree flow conditions respectively. In contrast, there is only a 1% to 2% variation on the leeward surface of the building which is negligible. The windward surface experiences the largest reduction in the convection coefficients for parallel flow, but this is still limited to around 3%.

On average, the three surfaces of the model experience an overall increase in the rate of convective heat transfer for both the parallel and diagonal flow patterns compared to the perpendicular flow baseline. The average percentage increases is 1.3% for parallel flow and 5.9% for diagonal flow. These variations are much smaller than might be expected considering the significant differences in the respective flow patterns for the three wind directions. Ultimately, this result suggests that in terms of overall building average convective heat transfer, wind direction may actually be relatively insignificant.

This is a very significant finding. It implies that the results obtained previously in this thesis for perpendicular flow may be applied universally to urban areas without the requirement for consideration of the flow direction. This simplifies calculations of the rate of convection needed for building thermal simulations since neither the orientation of the building or highly variable wind direction need to be taken into account.

In circumstances where it is desirable to take account of the effect of wind direction, the wind direction factors (F_d) given in Table 11.2 may be applied to the expressions presented previously for perpendicular flow. Note that an average reduction of 2.6% has been taken for the 'windward' and 'leeward' walls in the parallel flow case since, in reality, both of the surfaces are aligned identically to the flow.

Table 11.2: Wind direction factors

	Wind direction with respect to street canyon		
Surface	**Perpendicular**	**Intermediate**	**Parallel**
Windward	1.000	1.072	0.974
Roof	1.000	1.110	1.082
Leeward	1.000	0.987	0.974
Average	**1.000**	**1.059**	**1.013**

These results have been determined using convective coefficients defined with respect to free-stream wind speeds. However they are equally applicable to equations determined for other wind speed measurements (the met standard wind speed, for example) since the ratios of the results will remain the same.

11.4 Conclusions

The naphthalene sublimation experiments conducted previously have now been extended in order to determine the effect that wind direction has on the rate of convection from the surfaces of buildings within urban street canyons. Results have been obtained for flow perpendicular to the streets, parallel to the streets and for an intermediate diagonal angle.

The results at the intermediate angle were found to follow the same general trends as those for the perpendicular flow discussed in the preceding Chapters. However the peaks and troughs in the convective coefficients were seen to be more smoothed out. Also, the convection coefficients on the windward surface were found to be approximately 7% higher than for the perpendicular case. This is as a result of the greater along-wind spacing of the rows at intermediate angles, and of the extra along-canyon component of air movement. These two factors increase the wind speeds within the street canyon and hence give rise to the raised convection coefficients which have been identified.

The results for winds parallel to the rows of buildings are quite different. The pattern of convection coefficients is much smoother and more uniform, with a slight increase across the roof compared to the wall surfaces. The results are also symmetrical across the centreline of the roof as a result of the identical flows passing along the canyons on either side of the building.

It has been surprising to discover that the range of convective heat transfer coefficients for each wind angle were remarkably similar, given the significant differences between the respective flow patterns. The convective peaks and troughs for each case were of similar magnitude, only varying in their location across the building surfaces. Tabulation of the average convection coefficients across each of the individual surfaces confirmed how similar the results for the three wind angles actually were. The largest variation from the baseline perpendicular flow results was an 11% increase over the roof surface for diagonal flow. Such a value is probably well within the error bounds of determining the rate of convection, taking into account uncertainties such as the wind speed and the nature of the surroundings. The least variation was shown to occur on the leeward surface with percentage decreases of only 1.3% and 1.9% respectively for the diagonal and parallel flow conditions. The average variations across all surfaces were shown to be a 5.9% increase for the intermediate wind direction, and a 1.3% increase for the parallel wind direction.

This finding is highly significant since it means that the building orientation and wind direction are of relatively low significance for typical street canyon geometries. Therefore, the expressions presented in the previous Chapters for perpendicular flow are equally applicable to all other wind directions. This has many important benefits since the calculations required for building thermal simulations are greatly simplified if consideration of the wind direction can be omitted. The high variability of wind direction with time would make any expressions using this variable difficult to implement in practice, and so a ‘one size fits all’ relationship is very convenient.

Chapter 12 Identifying regions of peak convective transfer

12.1 Introduction

Whilst monitoring the various naphthalene sublimation experiments conducted for this study, it was noted that the coating eventually became visibly thinner at certain locations on the model. The duration of the tests was selected so as to maximise the sublimation depth and thus to minimise the effects of experimental error. It was essential to avoid the complete erosion of naphthalene from any area of the model as this would significantly alter the boundary conditions; an uncoated area of the model is inactive and so is no longer analogous to the required isothermal surface. However, after completion of the measurements for the primary tests, it was decided that the model would be returned to the wind tunnel for a further period. By doing so, the first areas to be cleared of naphthalene could be identified and hence the regions at which peak convection occurs could be pinpointed.

A variation upon the naphthalene sublimation technique involves measuring the time taken for a known surface coating to be completely eroded. This alternative implementation of the naphthalene sublimation technique has been employed by several previous researchers who used it to study the effects of a jet of air impinging upon a flat surface. The need for precise measurement of the naphthalene thickness is eliminated, in favour of a much simpler measurement of elapsed time. Whilst this method of measuring the rate of sublimation may be easier, there are several important disadvantages which meant that this technique was unsuitable for use in the current study. Firstly, it requires that the initial coating is of uniform thickness in order that the erosion times across the model are directly comparable. Whilst this may be straight forward for a flat plate test specimen, it is difficult to achieve over a three-dimensional model. Secondly (and more importantly) is the fact that once the naphthalene has eroded from a particular area, the boundary conditions are changed since there is no longer a uniform mass flux. The rate of sublimation of the adjacent naphthalene coating will be accelerated and therefore subsequent measurements may not be directly comparable. Reliable data are therefore only obtained for the regions of highest sublimation (i.e. the regions of peak convection) and not for more sheltered regions of the model.

The current technique of measuring the thickness of the naphthalene coating at a number of discrete locations has been shown to have many significant benefits over the methods used in previous studies. However, one minor drawback has been that it was not possible to make measurements very close to the vertices of the model. The minimum distance from the measurement location to the edge of the model is limited by the requirement for a minimum surrounding area of substrate in which the eddy currents are induced (see Section 5.1.1). The results presented already in this thesis have indicated that there are likely to be regions of peak convective heat transfer at the building vertices. The naphthalene erosion technique can therefore be used to provide additional, qualitative information which may prove useful in the interpretation of the results .

12.2 Results and discussion

Several of the naphthalene coated models were returned to the wind tunnel after completion of the primary thickness measurement experiments which have already been discussed. The coating thickness was already substantially reduced during the preceding experimental run so that the additional time required before complete erosion occurred was in the order of 30 to 60 minutes. The overall run time was therefore between 3.5 to 4.5 hours. The erosion of the naphthalene coating over the model was monitored visually at regular intervals. Photographs were taken of the model once areas of complete erosion became visible in order to record the convection 'hot spots'.

A series of these photographs which show the typical erosion patterns on the cube model are shown in Figure 12.1 below. These results correspond to a canyon height-to-width ratio of 0.50 with the rows of buildings orientated perpendicular to the flow (i.e. at 0 degrees). The vertical surfaces shown are the windward faces of the cube and the black dummy models which formed the street canyon can be seen on either side. The areas on the windward façade over which the naphthalene coating has been eroded are highlighted with a red outline as the reflectivity of the aluminium substrate reduces clarity in the photographs.

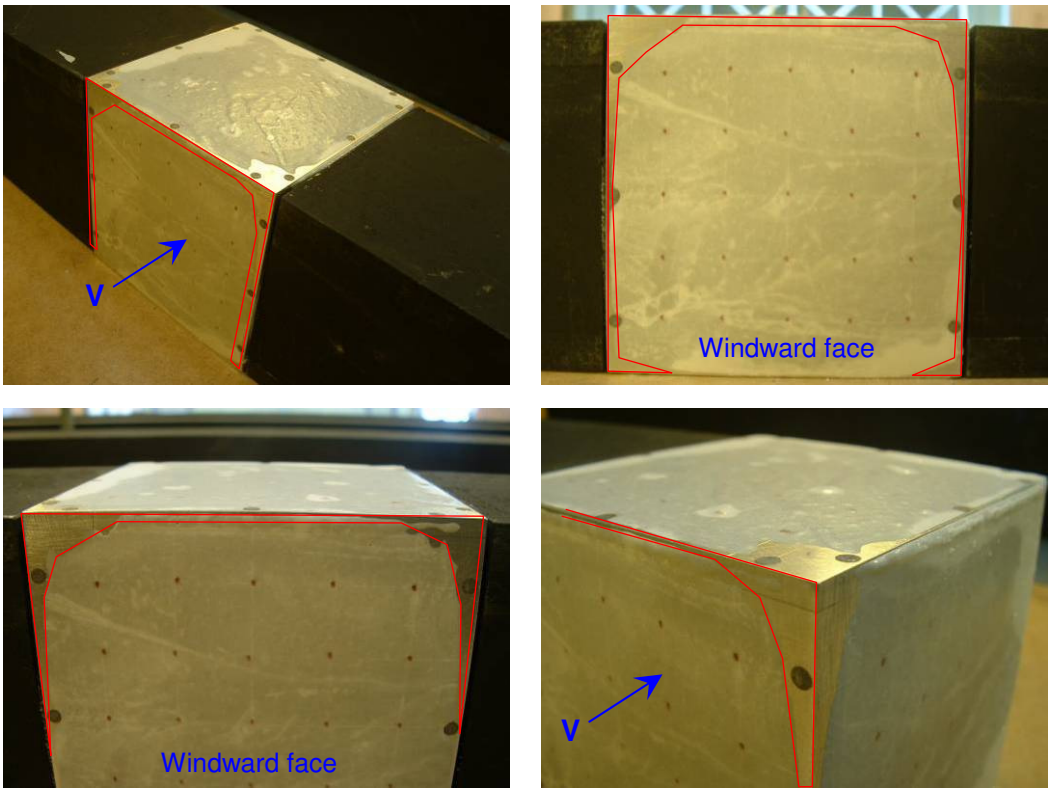

Figure 12.1: Photographs showing the typical patterns of naphthalene erosion

It can be seen that the first areas of naphthalene coating to be completely eroded are located along the edges of the windward and roof surfaces. The areas adjacent to the top, front two corners of the model were particularly scoured, however no erosion was noted on the leeward façade of the cube.

Photographs of the erosion of naphthalene from the model with the canyons orientated parallel to the flow are shown in Figure 12.2 below. The direction of airflow is from left to right, as indicated by the arrows. It can be seen that the coating has only been completely removed from narrow strips along the three vertices at the windward side of the cube. Such effects were not present along the leeward edges of the model.

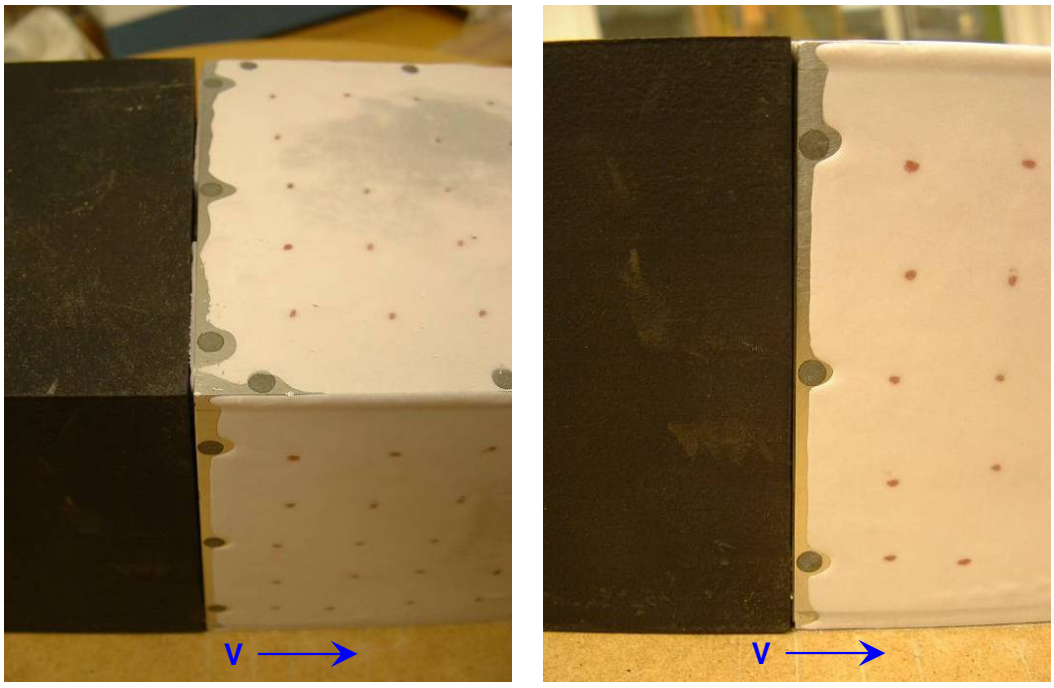

Figure 12.2: Erosion of naphthalene with parallel flow

These results support the findings of the primary naphthalene sublimation tests which have been discussed in previous chapters. A region of peak convective heat transfer between measurement row 5 (at the top of the windward surface) and row 6 (at the windward edge of the roof) was predicted based upon sublimation depth results (see for example Figure 10.2). This effect is clearly visible in the photographs shown in Figure 12.1 where the naphthalene coating has completely sublimated from areas on both sides of the vertex.

Similarly, the leeward surface has been shown to be subject to the lowest rates of convective transfer over the cube. No parts of the surface became cleared of the naphthalene coating during these extended tests indicating that there are no convective ‘hot-spots’ in this region.

12.3 Conclusions

After noting that certain areas of the naphthalene coating were substantially thinner than others after the main sublimation experiments, it was decided to return some of the models to the wind tunnel. The extended tests were continued until the first areas of the model were seen to have become completely bare of the naphthalene coating. These 'hotspots' therefore indicate the regions at which the highest rates of convective transfer will occur.

Photographs of the results have been presented for both perpendicular and parallel flow scenarios, for street canyons arranged at a height-to-width ratio of 0.50. These highlight the same regions of peak convective transfer at the vertices as were predicted based upon the results of sublimation measurements. The main area of high convection to note is that which occurs along the top of the windward surface and leading edge of the roof; the so-called *exposed-edge*.

This extension of the naphthalene sublimation technique has been able to provide some useful additional information and confirm predictions made based upon consideration of the sublimation measurements. However it is unlikely that it would be able to provide significantly useful data on its own. The removal of the coating at the models corners and vertices is indicative of the higher levels of convection which may be expected in these areas, but it is also influenced by local turbulence effects. For example, along the vertical edges of the windward wall of the cube, the rate of convective transfer are assumed to be the same as across the rest of the face and indeed along the majority of the length of the canyon. The long rows of buildings were chosen to give two-dimensional flow for exactly this reason. In spite of this, the naphthalene was seen to become eroded in a narrow strip along these vertices indicating increased mass (and thus heat) transfer.

This increased sublimation along these edges of the cube is due to local irregularities of the surface between the active model and the adjoining dummy cubes. Whilst the models were all notionally of the same dimension, the naphthalene coating increased the size of the active model and small irregularities in the surface finish restricted how tightly the adjacent models were abutted. This effect was most evident with flow parallel to the street canyons. Accelerated sublimation of the coating occurred at the leading edges of the model (see Figure 12.2) where theoretically there should be no cause for such a localised increase. Hence the results of these additional tests must be considered in combination with those from the primary sublimation tests and with knowledge of flow conditions around the buildings.

This finding also raises another point which until know has not been considered. The buildings which have been modelled in this study have been considered to have smooth, regular façades. The effect of features such as doors and windows have not been considered, and yet these will create exactly the same localised 'hot spots' as have been identified at the edges of the cube. Whilst the current results do not permit any quantitative analysis of these effects, it is important to note that any features on a building surface which increase the surface roughness are also likely to create localised regions of raise convective heat transfer. A study of the effect of such features would therefore be a useful extension of the current work.

Chapter 13 The effect of surface roughness

13.1 Introduction

Rowley, Algren and Blackshaw (1930) extended the pioneering work of Juerges (1924) to show that surface roughness can have a significant effect upon the rate of convective transfer from buildings. The relationships they proposed for a range of six typical building roughnesses were presented earlier in this document as Equation 3.53 and Table 3.7. Surface roughnesses appropriate to typical building materials ranging from stucco (rough) to glass (smooth) were studied by Rowley's team. The results of this research are still used in many applications today (e.g. the DOE-2 building simulation code) as there remains little other information available regarding the effect of the surface roughness or variation between alternative construction materials.

Unfortunately, it is not possible to investigate the effect of surface roughness using the naphthalene sublimation technique. The surface roughness of the model is dependent upon the quality of the coating process, with the aim being to achieve the smoothest finish possible. This is necessary to permit accurate measurement of the sublimation depth using the Elcometer coating thickness gauge. It was also found during the course of preliminary trials that any imperfections (e.g. drips, runs or unsmooth areas) sublimate at a higher rate than the surrounding area. The net effect of this is that the model surfaces soon becomes smooth during storage and the initial period of testing, even if the original finish was less than perfect. Therefore only a single (smooth) surface roughness was tested during the series of naphthalene sublimation experiments conducted for this thesis.

However, it is desirable to compare the current experimental data with the expressions obtained by Rowley *et al.* for the various building material roughnesses. Other workers have suggested that results obtained for flat surfaces are valid only for smooth surfaces with a friction coefficient of unity, but that values may be obtained for rougher materials by multiplication of the results by the relevant friction coefficient. It is therefore of interest to compare the current results with those presented by Rowley *et al.* for the six typical roughnesses in order to determine which materials the current equations may be applicable to. If, as suggested, the results acquired using smooth models are applicable to smooth building materials, it may be possible to deduce respective convection correlations for other materials.

13.2 Results and discussion

In order to allow comparison of the current naphthalene derived correlations with those proposed by Rowley *et al.* for the various surface roughnesses, these two sets of data have been plotted on the same axis in Figure 13.1 below. The current naphthalene sublimation results (with respect to the free-stream wind speed) are indicated by dashed lines and the Rowley data by solid lines. As the equations presented by Rowley were of a linear form, the original straight-line correlations derived for the naphthalene sublimation results have been used rather than the offset power-law equations.

Rowley's data for the various building materials showed that rougher surfaces will experience higher rates of convective heat transfer. This is partly because rougher materials will have a greater total surface area per unit area of building surface, so there is a greater active area over which convection can occur. Also, surface roughness increases the level of near-wall turbulence which in turn raises the level of mixing within the fluid. This trend applies to both the free and forced components of convection in the same way, so that the correlation for stucco has both a larger intercept (free convection) and steeper gradient (forced convection) than that of smoother materials.

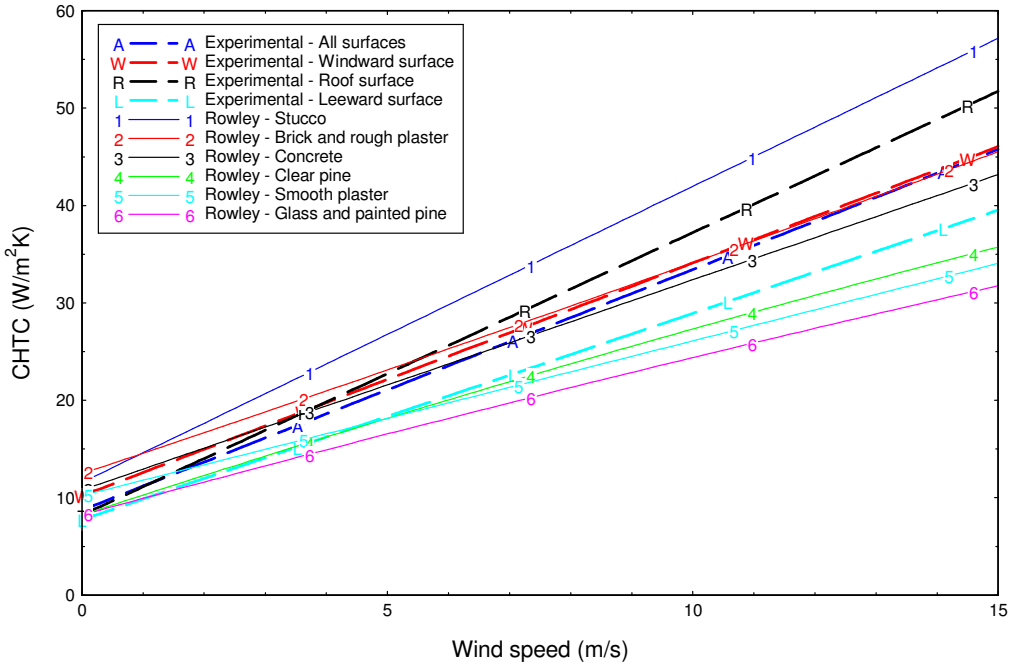

Figure 13.1: Comparison with surface roughness relationships

It is evident from Figure 13.1 that the results obtained using the naphthalene technique show good agreement with the range of correlations presented by Rowley *et al*. The current all surface average result lies at the centre of Rowley's data and shows particularly good agreement with the equations for concrete and brick. The variation in the y-axis intercepts of these data makes it a little difficult to compare the forced convection relationships. Therefore both sets of data have been redrawn in Figure 13.2 with their free convection components subtracted. In this way, all of the lines have an intercept of zero and the forced convection components (i.e. the gradients of the lines) can be more easily evaluated.

In this modified presentation the agreement between the current experimental data and that presented by Rowley's becomes even more apparent. Rowley's equations for concrete and brick/rough plaster are almost identical and lie at the centre of the range of gradients plotted. Similarly, the correlations for smooth plaster and glass/painted pine are very similar and together form the lower limit of the range of data.

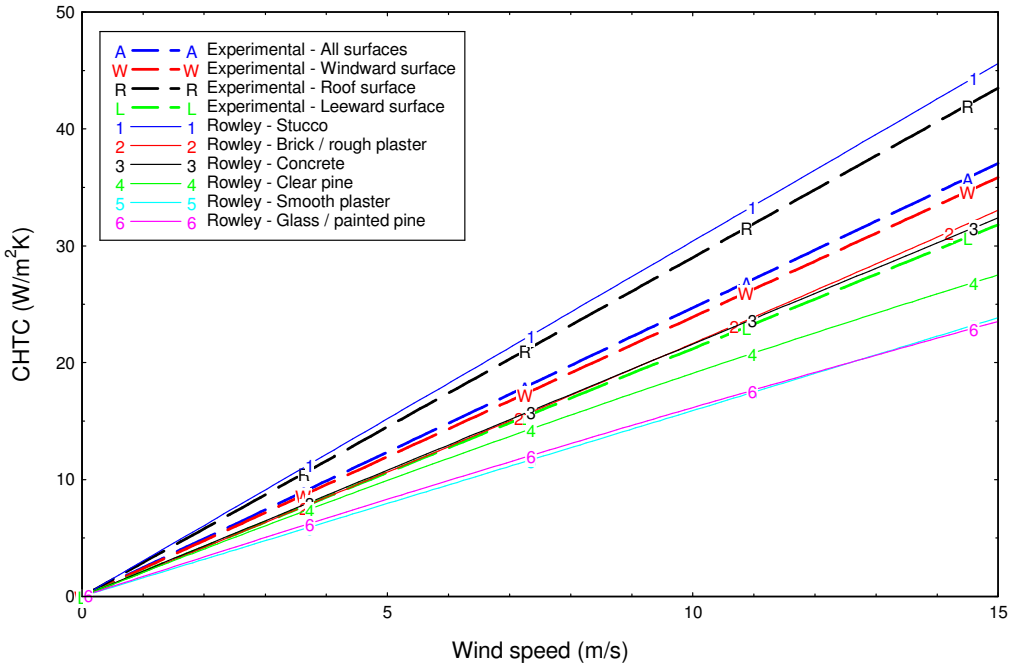

Figure 13.2: Comparison of the forced component of convection

When shown in this way, it is apparent how similar the current experimental data (especially for leeward surfaces) is to the data presented by Rowley *et al.* for brick and concrete surfaces. The higher rates of convection measured on the roof surface of the wind tunnel model make this data more comparable to Rowley's data for the rougher stucco material. However, it is clear that the results obtained using the naphthalene sublimation technique are most comparable to those for brick and concrete building surfaces.

The naphthalene data generally lies at the centre of the data presented for the various surface roughness, and it happens that the correlations for brick and concrete also lie towards the centre of the this range. Therefore it can be expected that the naphthalene results are indicative of full-scale convective heat transfer results for an average roughness. Fortunately, concrete and brick are the predominant building materials in the UK and so the current results are likely to be directly applicable to the majority of typical urban structures.

The results for the roof surface of the model appear to correlate better with data for rougher surfaces such as stucco. This similarity should not be misinterpreted as indicating that the naphthalene technique represents a rougher material on the top of the model. Rather, it is because the roof surface experiences the highest levels of convective transfer across the model, in the same way that the roughest materials also give rise to greater levels of convection.

13.3 Conclusions

The results presented by Rowley, Algren and Blackshaw are unique in that they indicate the relative magnitudes of convective heat transfer which are likely to occur for a range of typical building surfaces. Whilst other researchers have offered correlations for two or more different roughnesses, the connection with the types of building materials they represent is generally unclear.

For this reason, the results obtained in the current naphthalene sublimation study have been compared with the correlations of Rowley *et al.* in order to provide some indication as to the types of surfaces to which the current data may be applicable. This of course assumes that Rowley's data is accurate, and it was noted in Section 3.2 that these results are in fact combined radiative and convective coefficients. However, by forcing each curve through a zero-intercept, the effects of both radiation and free-convection are both removed so that only the forced component of convection remains. Even given some uncertainty over the precise accuracy of these results, it is likely that the relative magnitudes for the different surface roughnesses are correct and this is currently the focus of interest.

The comparison was made using the current correlations derived for the convective heat transfer coefficients with respect to free-stream wind speeds. The current data compares most favourably with that presented by Rowley *et al.* for concrete and brick building surfaces. Since these materials make up a large proportion of building surfaces in the UK, this results suggests that the current correlations are directly applicable to typical building surfaces. It will therefore not generally be necessary to further consider the effects of surface roughness when calculating surface averaged convection coefficients, which means that the simplicity of the proposed relationships may be maintained.

Chapter 14 Conclusions

14.1 The naphthalene sublimation technique

The success of the current research has been a result of significant advances in the implementation of the naphthalene sublimation experimental technique to modelling convective heat transfer from building surfaces. Whilst variations of this technique have been employed by several previous researchers, the work documented herein has greatly extended the scope of application in several key areas.

Undoubtedly the most significant development of the naphthalene sublimation technique has been with regards to the means by which the change in coating thickness has been measured. Previous workers have used either expensive LVDT-type instruments to map surface profiles, or else have relied upon simple weighing processes to determine only the average rate of sublimation occurring over a model surface. Neither of these techniques were appropriate for the current study. Instead, an innovative approach has been developed which employs a handheld coating thickness gauge (primarily designed for use in production line quality control applications) to measure the thickness of the naphthalene coating upon a metallic wind tunnel model. The application of this technology to the naphthalene sublimation technique is unique to the current research.

The benefits of measuring the thickness of the naphthalene coating using such a device are clear. An array of individual measurements can be taken over each surface of interest allowing spatial variations to be determined in addition to surface averages. The ease with these measurements can be performed using the Elcometer 456 handheld gauge means that it is not necessary to remove the active model from the wind tunnel arrangement. Measurement times (and hence experimental errors due to extraneous sublimation) are therefore minimised and it becomes convenient to make intermediate measurements to monitor sublimation with the model in-situ. The accuracy of the measurements is high, with errors typically less than ±2.5 μm when the probe is calibrated prior to use at the appropriate thickness range.

The use of this thickness measurement device required a rethink of the design and construction of the model. Whilst standard wind tunnel models are typically made from a combination of timber, plastic and high-density modelling foam, the current models required a metallic substrate in order for the Elcometer gauge to function. Related to this was consideration of the method by which the naphthalene coating would be applied to the model; several alternative combinations were trialled before success was achieved. The final model design was constructed from 5 mm aluminium plate to form a hollow cube. This gave sufficient substrate depth in order for the thickness gauge to function, whilst at the same minimising the thermal capacity of the model and hence permitting a smooth coating to be applied by dipping into a bath of molten naphthalene.

An additional benefit of the hollow model design was that it allowed warmed water from a digitally controlled water bath to be pumped through the cavity, thus maintaining the surface temperature of the model (and hence the naphthalene coating) to with ±0.1 °C. Since the rate of sublimation of naphthalene is highly dependent on temperature, being able to stabilise the model temperature in this way is a key advantage of the methodology which has been developed. A further innovation was the inclusion of a series of internal fins to direct the water flow back and forth through the cube. This ensured that no stagnation points occurred at any of the internal vertices, thereby maintaining a uniform temperature throughout the model.

Another crucial factor to the success of this research has been the combining of the naphthalene sublimation technique with knowledge of simulating appropriate atmospheric boundary layers within the BRE wind tunnel facility. Simulation of the correct urban atmospheric flow conditions is considered vital to determining convective heat transfer results that are applicable to real buildings in typical urban environments. By modelling the appropriate mean wind velocity profile and turbulence characteristics of an inner-city boundary layer, the flow patterns around the rows of models simulate those around full-scale streets and buildings. The convection results obtained during this research are therefore similarly applicable to full-scale, low-rise buildings situated in the majority of urban areas around the world.

The large number of individual measurements recorded for each experiment (300 for a typical test) required an automated approach to processing and calculation of the convective heat transfer coefficients. A spreadsheet application has been developed which takes into account all of the relevant experimental variables and environmental conditions. In addition to automating the processing of the data and thereby reducing the likelihood of errors, this approach also made it possible to calculate the appropriate chemical properties (for example, the density of air and saturation vapour pressure of naphthalene) for each set of experimental conditions.

The net result of these innovations and advances in the naphthalene sublimation technique has been a level of experimental error calculated at less than 6% for the determination of a typical convective heat transfer coefficient. Air temperature, atmospheric pressure and humidity were all shown to have negligible impact upon the results obtained.

One of the key advantages of the developed experimental procedures is that they are relatively uncomplicated and the equipment required is comparatively low-cost. Further experimentation using the methodology documented herein could therefore be easily conducted by other researchers. The most technical component is the Elcometer 456 coating thickness measurement device, yet this is a readily available off-the-shelf piece of equipment. Implementing an existing technology in this innovative way means that the device itself has already been tried and tested. The metal coating industry for which the device was originally developed may be a significantly different application in terms of its objectives; however the requirements for precision, ease of operation and the magnitude of the coating thickness to be measured are identical.

After the measurement of the naphthalene coating thickness, the next most difficult procedure when using the naphthalene sublimation technique has previously been the application of the coating to the model. However, in the current work, the most simple of the coating techniques has been used. Dipping is not only fast and efficient for even complicated three-dimensional geometries, it also provides the required high quality smooth finish without the need for expensive or time consuming preparation of the model. The key to this success of the dipping procedure employed for this research has been the use of a hollow aluminium cube to reduce the thermal capacity of the model. This type of model construction not only complies with the requirement of the Elcometer coating thickness gauge for a metallic substrate, but it also allows warmed water to be circulated through the model during testing to maintain the boundary conditions. The synergy of these three factors has not been achieved by any previous workers, yet they greatly increase the ease and accuracy with which future workers may take advantage of the technique.

14.2 Convective heat transfer from building surfaces

An array of cube models were arranged in the wind tunnel so as to form long street canyons at a range of spacings corresponding with known 'isolated', 'wake interference' and 'skimming' flow regimes. With the active model located at the centre of the row of buildings, convective heat transfer measurements were made on the front (windward), rear (leeward) and flat-roof surfaces of the model. The sides of the active cube abutted the neighbouring cubes and so were not exposed to the flow.

An initial naphthalene sublimation test conducted with the wind tunnel turned off was used to determine the rate of free convection from the model surfaces in the absence of wind. The average rate occurring from the windward, leeward and roof surfaces was found to be 6.22 W/m^2K. The maximum variation between the horizontal and vertical surfaces was approximately 0.2 W/m^2K with the lack of clear definition between the two orientations being attributable to the small length scales involved. This value is significantly greater than that prescribed by current European Standards (4.0 W/m^2K), but lies at the centre of the range of values determined from experimental measurements made by previous workers in the field. It is therefore not clear which of these values is most appropriate although it has been suggested that the higher values measured in the current study are actually more representative of the peak rate of free convection which occurs near to the base of a larger (full-scale) surface. The lower values prescribed in the Standards may therefore be more representative of the average rate of free convection over a larger surface. However, for consistency, the average value determined during the current naphthalene sublimation experimental work has been used in derivation of the convection expressions presented.

When correlating the forced convection data obtained using the naphthalene sublimation technique, the traditional linear and power-law forms of expression used by the majority of previous researchers were not found to be satisfactory. Such expressions are unable to represent both the smooth transition from free to forced convection at low wind speeds, as well as the tailing-off effect of the rate of convection at the highest wind speeds. Therefore, an alternative *offset power-law* form of expression has been proposed which combines the advantages of both of the traditional linear and power-law equations.

It has been noted that in many instances the reference wind speed location for existing forced convection expressions is often poorly defined in the literature. In addition, even where the required type of wind data is well specified, this may be of a type which is not readily available for a given scenario. This raises the risk of an alternative wind dataset being incorrectly substituted instead. It has therefore been a primary concern to both explicitly state the appropriate type and location of wind speed data which should be used in the derived expressions, and also to ensure that this is of a type which is readily available in the majority of circumstances. The convective heat transfer coefficient relationships presented are thereby given with respect to the two most commonly available wind data types; the free-stream wind speed at high level above an urban environment, and the meteorological standard wind speed at a height equivalent to 10 metres above open, level countryside (the Meteorological Standard Windspeed or MSW). Offset power-law equations have been derived from the naphthalene sublimation results for windward, leeward and flat-roof building surfaces. All were found to show a strong correlation with wind speed, with coefficients of determination (R^2 values) in excess of 0.970.

The greatest rates of convective heat transfer have been shown to occur at the top of the windward wall and leading edge of the roof, otherwise dubbed the ‘exposed edge’. The roof value was shown to be similar to the overall average at low wind speeds, but rises to near exposed edge values at higher wind speeds indicating a down-wind spread of the peak transfer region in such conditions. The lowest rates of convective heat transfer have been shown to occur from the leeward wall of a building as a result of the adjacent flow in the wake region being slower and less turbulent. The average coefficient value across the windward surface tends to be similar to the combined average across all three building surfaces for the majority of wind speeds.

Expressions for the convective heat transfer coefficients (h_c) over the windward, leeward and roof surfaces of the models have been derived from the naphthalene sublimation data. Additional expressions have also been derived for the average coefficient across all three building surfaces, as well as for the localised peak at the exposed edge. Whilst it is suggested that the new offset power-law equations should be employed for calculation purposes, the tradition linear and power-law forms of equation are also presented for reference and comparison with experimental results derived by previous workers.

Rows of buildings spaced at a canyon height-to-width ratio of 0.50 are common of many streets, both in the UK and worldwide. For wind directions approximately perpendicular to the streets, the wake-interference flow regime will dominate. This scenario has therefore been taken as the baseline model arrangement at which the majority of experiments in the current study have been conducted.

For narrower street canyons, a skimming flow regime exists whereby the flow between the buildings becomes detached from that above the roofs. The convection coefficients are thereby reduced and may be significantly different to those that are determined by the wake-interference flow expressions. In wider street canyons, the convective coefficients on the exposed windward and roof surfaces of buildings have been shown to be increased. In contrast, the values on the leeward wall surface are lessened due to the distancing of the windward vortex effects from the downstream row of buildings. In order to account for these variations between alternative street geometries, the results of naphthalene sublimation tests conducted at both greater and smaller canyon height-to-width ratios have been compared with the baseline scenario. A series of canyon geometry factors (F_g) has thereby been deduced which may be applied to the wake-interference flow (baseline) expressions in order to determine results for skimming and isolated flow scenarios. Separate factors are given for the individual surfaces, as well as for the overall average and local exposed edge region.

Further naphthalene sublimation experiments have been conducted to study the effect of wind direction upon the rate of convective heat transfer from building surfaces. This was achieved by rotating the arrangement of models on the wind tunnel turntable to model flow parallel to the street canyons and at an intermediate (45 degree) diagonal wind direction. By comparison of these results with those obtained previously for flow perpendicular to the street canyons, it has been shown that the effect of wind direction is relatively small. The maximum variation from the baseline (perpendicular flow) case was an approximate 11% increase over the roof surface for the intermediate wind angle. The variation was shown to be significantly less for the other surfaces and wind directions with average percentage increases of 5.9% for intermediate wind angles and 1.3% for parallel winds.

This finding is highly significant since it suggests that the correlations obtained for the perpendicular wind direction can be applied generically to urban areas without requiring further consideration of the wind direction. The levels of variation resulting from wind direction are likely to be well within the error inherent in other aspects of determining the rate of convective heat transfer and so may be neglected in the majority of situations. However, a full breakdown of the variations across each surface has of course been provided for instances where these effects are of greater significance.

A region of peak convective transfer was identified from the naphthalene sublimation measurements at the top of the windward surface and leading edge of the roof. The rate of convection occurring from this exposed edge was shown to be significantly greater than elsewhere on the cube model. Such regions of high convective transfer were further investigated by returning the naphthalene coated model to the wind tunnel after conclusion of the main experiments. The naphthalene coating was visually monitored and the test sustained until complete sublimation of the coating was noted at a given location. This highlighted the areas from which the greatest convective heat transfer occurs. Whilst such observations are not quantitative, they are useful in providing additional information with which to interpret the experimental results.

For parallel flow conditions, it was found that the small irregularities between adjoining cubes gave rise to increased sublimation from the edges of the models. This suggests that features in the surfaces of buildings (such as doors and windows) are also likely to result in localised increases in the rate of convective heat transfer.

The current experimental results have been compared with those from full-scale experiments conducted by a range of previous researchers. The naphthalene sublimation results have been shown to compare well with full-scale convection measurements made on low-rise buildings, but differ significantly to those made on more exposed high-rise buildings and tower blocks. This highlights the importance of applying only convective heat transfer relationships appropriate to the building geometry in question.

It is proposed that the current results are widely applicable to low-rise buildings in approximately uniform urban areas, as are common in the majority of worldwide towns and cities.

14.3 Application of results

The implications and application of the results described in this thesis are both significant and wide-ranging. On a practical level, predicted global warning is likely to increase both surface and air temperatures in the majority of worldwide urban areas. The convective cooling effects of the wind will thereby become of ever-greater relevance and importance. It has been shown that there exists an optimum canyon spacing at which the rate of overall convective heat transfer from the building surfaces is maximised. This occurs at a canyon height-to-width ratio of approximately 0.50 at which the wake-inference flow regime occurs. Town planners, architects and developers are able to employ such simple ‘rules of thumb’ in order to design building layouts which best promote the convective removal of heat from the building surfaces. Whilst it is acknowledged that maximisation of convective exchange will not always be the prime consideration for the layout of a new development, such factors will be of increasing value as urban temperatures continue to rise.

On a more fundamental level, accurate convective heat transfer data appropriate to real urban areas is key to the functioning of computation thermal models, both of individual buildings are also of wider urban environments. Such models rely upon the governing relationships for the various heat transfer processes as the basis of their computational routines. However, there has been a lack of convection data appropriate to the external surfaces of buildings which also take into account the flow patterns around the envelope. It is hoped that the data derived in the current work will at least partly fill this void and it has been presented in a dimensional form in order to facilitate this incorporation within existing calculation routines.

Several new applications for this type of external convection coefficient data have also been identified. In particular, solar panel manufacturers require knowledge of the rate of convection which is likely to occur from the surface of their devices when mounted upon a building, in order to determine the surface temperatures. Cooler solar panels perform more efficiently and therefore data allowing such factors to be considered both during design and installation will be of benefit.

14.4 Example calculation

The following calculation provides an example of how the convective heat transfer data presented in this thesis may be used to determine the convection coefficient for a typical building surface.

Let us assume that we wish to calculate the rate of convective heat transfer that occurs from the flat roof of a low-rise building in a particular city. The building is at the centre of a wide street canyon (common for example in London) which is orientated in an east-west direction. The average met. standard wind speed for the site has been determined from Meteorological Office wind records to be 5 m/s.

The convective heat transfer expression for the roof of such a building is given in Table 9.11 as:

$$h_c = 6.22 + 8.02V_m^{0.865}$$

Substituting in the average wind speed gives:

$$h_c = 6.22 + (8.02 \times 5^{0.865})$$

$$h_c = 38.49$$

Hence the basic convective heat transfer coefficient is 38.5 W/m^{2}K. For wide streets, the canyon geometry factor (F_g) is given in Table 10.3 as 1.124. Since the prevailing wind direction in the majority of the UK is south-westerly, winds will on average approach the east-west street canyon at an intermediate (diagonal) angle. The corresponding wind direction factor (F_d) is given for roofs in Table 11.2 as 1.110.

The corrected convective heat transfer coefficient (h_{cc}) can therefore be obtained by multiplying the basic coefficient by the canyon geometry and wind direction factors, thus:

$$h_{cc} = h_c \times F_g \times F_d$$

$$h_{cc} = 38.49 \times 1.124 \times 1.110$$

$$h_{cc} = 48.02$$

The corrected convective heat transfer coefficient for the roof is therefore calculated to be **48.0 W/m^{2}K**.

14.5 Suggestions for further work

A comprehensive set of experimental procedures has been developed during the course of this research which means that the naphthalene sublimation technique can now be readily applied to a wide range of convective heat transfer applications and scenarios in the built environment and beyond. The following areas of research are proposed as being the most useful extensions to the current area of study:

A: The effect of alternative building arrangements
The experiments conducted for this thesis have employed long street canyons of varying height-to-width ratios. An unexpected result of these tests was that the orientation of the street canyon with respect to the approaching flow had relatively little influence on the overall rate of convection occurring from the buildings. It is therefore suggested that a series of additional experiments could be conducted to investigate the effect of alternative building geometries. These could include streets consisting of multiple shorter rows of buildings (semi-detached houses) or isolated buildings (detached houses). If the convection for these street geometries are also shown to be largely independent of wind direction, this would imply that building orientation may be neglected from future consideration of convective heat transfer from urban areas.

B: Determination of the optimum canyon spacing to maximise convective transfer
It has been shown in the current investigation that the average rate of convective heat transfer from the surfaces of buildings decrease at both larger and smaller canyon spacings. Maximum convective heat transfer during perpendicular flow was shown to occur for wake-interface flow regimes resulting from a canyon height-to-width ratio of approximately 0.50. Determining the building spacing at which the maximum rate of convection occurs would provide town planners and architects with valuable information with which to optimise convective cooling.

C: Investigation of the impact of pitched roofs
The scope of the current work has been limited to flat-roofed buildings in order to simplify the building geometries and flow patterns for development and verification of the naphthalene sublimation technique. However, the majority of roofs on domestic dwellings in the United Kingdom are duo-pitched designs of varying inclinations. It would therefore be useful to conduct measurements using the naphthalene sublimation technique on various pitched roofed models in order to determine the effect of roof pitch upon the rate of convection.

D: Investigation of the rate of convection occurring from solar panels
Photovoltaic panels are being increasing installed on to roofs and façades to provide a source of renewable electricity. The efficiency of such units depends upon their temperature with output falling as they get hotter. Convective cooling of solar panels is therefore advantageous to maximise efficiency. It is also necessary for manufacturers and installers to be able to determine the likely surface temperatures of the panels in order to calculate the resultant output and hence correctly ‘size’ a system for a given application. The naphthalene sublimation technique could readily be extended to provide such data, possibly in combination with an investigation of pitched roofs since these will be the base onto which the majority of such systems would typically be installed.

E: Investigation of the effect of discontinuities such as windows and doors
Additional wind tunnel testing conducted after the primary naphthalene sublimation measurements had been taken on the models revealed that small discontinuities between adjoining cubes gave rise to increased levels of local convection. It is therefore likely that any irregularities in a building surface (for example, the recesses of doors and windows) will give rise to similar localised increases in the rate of convective heat transfer. It would be useful to investigate the effect of such features as these will influence the distribution of convection coefficients, as well as the average rate of convection over building surfaces. Such an investigation is likely to require further development of the naphthalene coating process in order to resolve such features in the model surface.

F: Application of the naphthalene technique to more complicated geometries
The primary objective of the current research has been to develop an experimental technique which permits appropriate convective heat transfer data to be obtained for representative building geometries. Taking this progression one stage further, the naphthalene sublimation technique could be employed to determine the actual convective coefficients over a specific building surrounded by the actual neighbouring buildings and local topography. Such tests could be employed in the same way that wind tunnel testing is already used to determine the likely pedestrian wind environments and external wind loads around proposed developments. Such results could be used, for example, to highlight areas at which high convection rates are likely to occur on the building and thereby allow the thermal design to be optimised. Such specific application of the naphthalene technique would mark the ultimate extreme in contrast to the generic flat-plate derived results detailed at the start of this thesis in the review of the current literature.

Chapter 15 References

AKBARI, H., MENON, S. & ROSENFELD, A., 2009. Global cooling: increasing world-wide urban albedos to offset CO2. *Climatic Change,* 94(3), pp.275-286.

ALAMDARI, F. & HAMMOND, G.P. 1982. *Time-dependent convective heat transfer in warm-air heated rooms. Proceedings of the International Symposium on Energy Conservation in the Built Environment. Dublin*.

ALAMDARI, F. & HAMMOND, G.P., 1983. Improved data correlations for buoyancy-driven convection in rooms. *Building Services Engineering Research and Technology,* 4(3), pp.106-112.

AMBROSE, D., LAWRENSON, I.J. & SPRAKE, C.H.S., 1975. The vapour pressure of naphthalene. *The Journal of Chemical Thermodynamics,* 7(12), pp.1173-1176.

AMERICAN ROOFTILE COATINGS, 2006. *Manufacturers web site* [online]. Available from: http://www.americanrooftilecoatings.com/ [Accessed 11th November 2006].

AMERICAN SOCIETY OF CIVIL ENGINEERS, 1999. *Wind Tunnel Studies of Buildings and Structures, ASCE Manuals and Reports on Engineering Practice No. 67.* Virginia: ASCE.

AMERICAN SOCIETY OF HEATING REFRIGERATING AND AIR-CONDITIONING ENGINEERS, 1977. *Handbook of Fundamentals.* New York: ASHRAE.

AMERICAN SOCIETY OF HEATING REFRIGERATING AND AIR-CONDITIONING ENGINEERS, 1981. *Handbook of Fundamentals.* New York: ASHRAE.

BARLOW, J.F. & BELCHER, S.E., 2002. A Wind Tunnel Model for Quantifying Fluxes in the Urban Boundary Layer. *Boundary-Layer Meteorology,* 104(1), pp.131-150.

BARLOW, J.F., HARMAN, I.N. & BELCHER, S.E., 2004. Scalar fluxes from urban street canyons. Part I: Laboratory simulation. *Boundary-Layer Meteorology,* 113(3), pp.369-385.

BASS, B., 2002. *Mitigating the urban heat island with green roof infrastructure*. Proceedings of The North American Urban Heat Island Summit, 2-3 May 2002, Toronto.

BASS, B. & BASKARAN, B., 2003. *Evaluating Rooftop and Vertical Gardens as an Adaptation Strategy for Urban Areas.* Toronto: National Research Council Canada. (NRCC-46737).

BEAUSOLEIL-MORRISON, I., 2001. An algorithm for calculating convection coefficients for internal building surfaces for the case of mixed flow in rooms. *Energy and Buildings,* 33(4), pp.351-361.

BLACKMORE, P.A. & TSOKRI, E., 2006. Wind loads on curved roofs. *Journal of Wind Engineering and Industrial Aerodynamics,* 94(11), pp.833-844.

BOBVILA.COM, 2001. *Roof Terms and Terminology web page* [online]. Available from: http://www.bobvila.com/HowTo_Library/Roof_Terms_and_Terminology-Miscellaneous_Roofing_Topics-A1936.html [Accessed 10th November 2006].

BONACQUISTI, V., CASALE, G.R., PALMIERI, S. & SIANI, A.M., 2006. A canopy layer model and its application to Rome. *Science of The Total Environment,* 364(1-3), pp.1-13.

BRE, 1972. Library Translation number 1729: Schwarz, B., 1972. "*Heat and mass transfer on external wall surfaces. Report from the Building Research No. 79".* Thesis. Stuttgart University, Germany. (Translated from the German).

BRE/SERC, 1988. *An investigation into analytical and empirical validation techniques for dynamic thermal models of buildings, Part 7 - External convection.* Watford: BRE.

BS 6399-2:1997. *Loading for buildings - Part 2 - Code of practice for wind loads*. London, BSI.

BS EN ISO 6946:1997. *Building components and building elements - Thermal resistance and thermal transmittance - Calculation method*. London, BSI.

BS EN ISO 12241:1998. *Thermal insulation for building equipment and industrial installations - Calculation Rules.* London, BSI.

BS EN ISO 13791:2004. *Thermal performance of buildings - Calculation of internal temperatures of a room in summer without mechanical cooling - General criteria and validation procedures*. London, BSI.

BS EN 1991-1-4:2005. *Eurocode 1 - Actions on structures - General actions - Wind actions*. London, BSI.

BS EN ISO 13792:2005. *Thermal performance of buildings - Calculation of internal temperatures of a room in summer without mechanical cooling - Simplified method*. London, BSI.

BS EN ISO 6946:2007. *Building components and building elements - Thermal resistance and thermal transmittance - Calculation method*. London, BSI.

BUREAU INTERNATIONAL DES POIDS ET MESURES, 2008. *GUM: Guide to the Expression of Uncertainty in Measurement* [online]. BIPM. Available from: http://www.bipm.org/en/publications/guides/gum.html [Accessed 23rd April 2009].

CALIFORNIA ENERGY COMMISSION, 2005. *Title 24: Building Energy Efficiency Standards for Residential and Non-residential Buildings.* 2005 ed. California: California Energy Commission.

CALIFORNIA ENERGY COMMISSION, 2008. *Title 24: Building Energy Efficiency Standards for Residential and Non-residential Buildings.* 2008 ed. California: California Energy Commission.

CHANDLER, T.J., 1965. *The Climate of London.* London: Hutchinson.

CHEN, J., HENDERSON, G., GRIMM, C.C., LLOYD, S.W. & LAINE, R.A., 1998. Termites fumigate their nests with naphthalene. *Nature,* 392(6676), pp.558-559.

CHO, H.H., JABBARI, M.Y. & GOLDSTEIN, R.J., 1997. Experimental mass (heat) transfer in and near a circular hole in a flat plate. *International Journal of Heat and Mass Transfer,* 40(10), pp.2431-2443.

CHO, K., 1989. *Measurement of the diffusion coefficient of naphthalene into air.* Thesis (Ph.D.). State University of New York, New York.

COLE, R.J. & STURROCK, N.S., 1977. The convective heat exchange at the external surface of buildings. *Building and Environment,* 12(4), pp.207-214.

COOK, N.J., 1973. On simulating the lower third of the urban adiabatic boundary layer in a wind tunnel. *Atmospheric Environment (1967),* 7(7), pp.691-705.

COOK, N.J., 1978. Determination of the model scale factor in wind-tunnel simulations of the adiabatic atmospheric boundary layer. *Journal of Wind Engineering and Industrial Aerodynamics,* 2(4), pp.311-321.

COOK, N.J., 1985. *The designer's guide to wind loading of building structures, Part 1: Background, damage survey, wind data and structural classification.* London: Butterworths.

COOL ROOF RATING COUNCIL, 2008. *Why Cool Roofs Are Way Cool.* California: CRRC.

COOL ROOF RATING COUNCIL, 2009. *CRRC Cool Roof Codes and Programs* [online]. CRRC. Available from: http://www.coolroofs.org/codes_and_programs.html [Accessed 4th July 2009].

COOPER, K.W. & TREE, D.R. 1972. *A re-evaluation of the average convection coefficient for flow past a wall. Proceedings of the ASHRAE Semi-annual meeting. Chicago*, *ASHRAE*.

DANTEC DYNAMICS LIMITED, 2006. *Company home page* [online]. Available from: http://www.dantecdynamics.com/ [Accessed 11th November 2006].

DAWSON, D., 2002. *National Geographic News article: Plant-Covered Roofs Ease Urban Heat* [online]. Available from: http://news.nationalgeographic.com/news/2002/11/1115_021115_GreenRoofs.html [Accessed 10th July 2009].

DEPARTMENT FOR ENVIRONMENT FOOD AND RURAL AFFAIRS, 2003. *The Impacts of Climate Change.* London: DEFRA.

DEPARTMENT OF TRADE AND INDUSTRY, 2002. *Energy consumption in the United Kingdom.* London: DTI.

DEPARTMENT OF TRADE AND INDUSTRY, 2007. *Quarterly Energy Prices: March 2007.* London: DTI.

DUTRA, A.S., MENDES, P.R.S. & PARISE, J.A.R., 1991. Transport coefficients for laminar and turbulent flow through a four-cusp channel. *International Journal of Heat and Fluid Flow,* 12(2), pp.99-105.

ELCOMETER LIMITED, 2009. *Company home page* [online]. Available from: http://www.elcometer.com/index.htm [Accessed 30th June 2009].

EMMEL, M.G., ABADIE, M.O. & MENDES, N., 2007. New external convective heat transfer coefficient correlations for isolated low-rise buildings. *Energy and Buildings,* 39(3), pp.335-342.

ENVIRONMENTAL DESIGN SOLUTIONS LIMITED, 2008. *A-TAS (v8.5) Theory Manual.* Milton Keynes: EDSL Limited.

ESDU INTERNATIONAL, 1974. *Engineering data sheet 74031: Characteristics of atmospheric turbulence near the ground - Part II - single point data for strong winds (neutral atmosphere).* London: ESDU International.

ESDU INTERNATIONAL, 1985. *Engineering data sheet 85020: Characteristics of atmospheric turbulence near the ground - Part II - single point data for strong winds (neutral atmosphere), (1990 edition with amendments A to E).* London: ESDU International.

ESDU INTERNATIONAL, 2002. *Engineering data sheet 82026: Strong winds in the atmospheric boundary layer - Part1 - hourly-mean wind speeds.* London: ESDU International.

FEDERAL ENERGY MANAGEMENT PROGRAM, 2004. *Federal Technology Alert: Green Roofs.* Washington: U.S. Department of Energy. (DOE/EE-0298).

FINNIGAN, J.J. & LONGSTAFF, R.A., 1982. A wind-tunnel model study of forced convective heat transfer from cylindrical grain storage bins. *Journal of Wind Engineering and Industrial Aerodynamics,* 10(2), pp.191-211.

FISHER, D.E., 1995. *An experimental investigation of mixed convection heat transfer in a rectangular enclosure.* Thesis (Ph.D.). University of Illinois, Urbana.

GANDRILLE, T., HAMMOND, G.P. & MELO, C., 1988. An intermediate-level model of external convection for building energy simulation. *Energy and Buildings,* 12(1), pp.53-66.

GATES, D.M., 1962. *Energy exchange in the biosphere.* New York: Harper and Row.

GEER, I.W., 1996. *Glossary of weather and climate.* Boston: American Meteorological Society.

GIRIDHARAN, R., LAU, S.S.Y. & GANESAN, S., 2005. Nocturnal heat island effect in urban residential developments of Hong Kong. *Energy and Buildings,* 37(9), pp.964-971.

GOLDSTEIN, R.J. & CHO, H.H., 1995. A review of mass transfer measurements using naphthalene sublimation. *Experimental Thermal and Fluid Science,* 10(4), pp.416-434.

GRAVES, H., WATKINS, R., WESTBURY, P. & LITTLEFAIR, P., 2001. *Cooling Buildings in London: Overcoming the Heat Island.* Watford: BRE. (BRE Publication Draft Number 76263).

GRIMMOND, S., 2007. Urbanization and global environmental change: local effects of urban warming. *Geographical Journal,* 173(1), pp.83-88.

HAGISHIMA, A. & TANIMOTO, J., 2003. Field measurements for estimating the convective heat transfer coefficient at building surfaces. *Building and Environment,* 38(7), pp.873-881.

HASSID, S., SANTAMOURIS, M., PAPANIKOLAOU, N., LINARDI, A., KLITSIKAS, N., GEORGAKIS, C. & ASSIMAKOPOULOS, D.N., 2000. The effect of the Athens heat island on air conditioning load. *Energy and Buildings,* 32(2), pp.131-141.

HIRSH, J., 2006. *DOE-2: Building Energy Use and Cost Analysis Tool* [online]. Available from: http://doe2.com/DOE2/index.html [Accessed 3rd December 2006].

HOWARD, L., 1833. *The Climate of London Deduced From Meteorological Observations Made In The City And At Various Places Around It. (Volume 1).* Second ed. London: Harvey and Darton.

HUGHES, K., 2006. The impact of urban areas on climate in the UK: a spatial and temporal analysis, with an emphasis on temperature and precipitation effects. *Earth & E-nvironment,* (2), pp.54-83.

HUNT, J.C.R., POULTON, E.C. & MUMFORD, J.C., 1976. The effects of wind on people; New criteria based on wind tunnel experiments. *Building and Environment,* 11(1), pp.15-28.

HYDRO-STOP INCORPORATED, 2006. *Hydro-Stop Incorporated company home page* [online]. Available from: http://www.hydro-stop.com/Frameset-1.html [Accessed 11th November 2006].

ISO/IEC Guide 98-3:2008. *Uncertainty of measurement - Part 3: Guide to the expression of uncertainty in measurement*. Geneva, ISO.

ITO, N., KIMURA, K. & OKA, J., 1972. A field experiment study on the convective heat transfer coefficient on exterior surface of a building. *ASHRAE Transactions,* 78(1), pp.184-191.

JAYAMAHA, S.E.G., WIJEYSUNDERA, N.E. & CHOU, S.K., 1996. Measurement of the heat transfer coefficient for walls. *Building and Environment,* 31(5), pp.399-407.

JOINT COMMITTEE FOR GUIDES IN METROLOGY, 2008a. *JCGM 100: GUM 1995 with minor corrections. Evaluation of measurement data - Guide to the expression of uncertainty in measurement*. 1st ed. JCGM.

JOINT COMMITTEE FOR GUIDES IN METROLOGY, 2008b. *JCGM 101: Evaluation of measurement data - Supplement 1 to the "Guide to the expression of uncertainty in measurement" - Propagation of distributions using a Monte Carlo method.* 1st ed. JCGM.

JUERGES, W., 1924. Der waermeuebergang an einer ebenen Wand. *Gesundheits Ingenieur ("Health Engineer"),* 19, pp.5-52.

KELNHOFER, W.J. & THOMAS, C.J., 1976. *External convection heat transfer coefficients on a building model*. Proceedings of *ASME Winter Annual Meeting*, *New York*.

KIM, Y.H. & BAIK, J.J., 2004. Daily maximum urban heat island intensity in large cities of Korea. *Theoretical and Applied Climatology,* 79(3), pp.151-164.

KIND, R.J., GLADSTONE, D.H. & MOISER, A.D., 1983. Convective heat losses from flat-plate solar collectors in turbulent winds. *Transactions of the ASME, Journal of Solar Energy Engineering,* 105, pp.80-85.

KLYSIK, K. & FORTUNIAK, K., 1999. Temporal and spatial characteristics of the urban heat island of Lódz, Poland. *Atmospheric Environment,* 33(24-25), pp.3885-3895.

LAWRENCE BERKELEY LABORATORY, 1982. *DOE-2 Engineers Manual (v2.1A).* Berkeley: Lawrence Berkelely Laboratory.

LAWRENCE BERKELEY NATIONAL LABORATORY, 2009. *The Cool Colours Project home page* [online]. Available from: http://coolcolors.lbl.gov/

LAWSON, T., 2001. *Building Aerodynamics.* London: Imperial College Press.

LEE, Y.N., 1986. Heat transfer and pressure drop characteristics of an array of plates aligned at angles to the flow in a rectangular duct. *International Journal of Heat and Mass Transfer,* 29(10), pp.1553-1563.

LEVINSON, R., 2004. *Characterizing the Radiative Properties of Pigments for Cool Roofs*. Proceedings of Environmental Energy Technologies Division Noon Seminar, 22nd April 2004, LBNL, California.

LEVINSON, R. & AKBARI, H., 2009. Potential benefits of cool roofs on commercial buildings: conserving energy, saving money, and reducing emission of greenhouse gases and air pollutants. *Energy Efficiency*.

LEVINSON, R., BERDAHL, P., AKBARI, H., MILLER, W., JOEDICKE, I., REILLY, J., SUZUKI, Y. & VONDRAN, M., 2007. Methods of creating solar-reflective nonwhite surfaces and their application to residential roofing materials. *Solar Energy Materials and Solar Cells,* 91(4), pp.304-314.

LIU, K. & BASS, B., 2005. *Performance of green roof systems.* Ottawa: National Research Council Canada. (NRCC-47705).

LIU, Y. & HARRIS, D.J., 2007. Full-scale measurements of convective coefficient on external surface of a low-rise building in sheltered conditions. *Building and Environment,* 42(7), pp.2718-2736.

LOVEDAY, D.L. & TAKI, A.H., 1996. Convective heat transfer coefficients at a plane surface on a full-scale building facade. *International Journal of Heat and Mass Transfer,* 39(8), pp.1729-1742.

MCADAMS, W.H., 1954. *Heat transmission.* 3rd ed. London: McGraw-Hill.

MEINDERS, E.R. & HANJALIC, K., 2002. Experimental study of the convective heat transfer from in-line and staggered configurations of two wall-mounted cubes. *International Journal of Heat and Mass Transfer,* 45(3), pp.465-482.

MERONEY, R.N., PAVAGEAU, M., RAFAILIDIS, S. & SCHATZMANN, M., 1996. Study of line source characteristics for 2-D physical modelling of pollutant dispersion in street canyons. *Journal of Wind Engineering and Industrial Aerodynamics,* 62, pp.37-56.

MILLS, A.F., 1962. Experimental investigation of turbulent heat transfer in the entrance region of a circular conduit. *ARCHIVE: Journal of Mechanical Engineering Science 1959-1982 (vols 1-23),* 4(1), pp.63-77.

MORRIS, C.J.G. & SIMMONDS, I., 2000. Associations between varying magnitudes of the urban heat island and the synoptic climatology in Melbourne, Australia. *International Journal of Climatology,* 20(15), pp.1931-1954.

MURAKAMI, S. & DEGUCHI, K., 1981. New criteria for wind effects on pedestrians. *Journal of Wind Engineering and Industrial Aerodynamics,* 7(3), pp.289-309.

NASA VISIBLE EARTH, 2000. *Earth's City Lights.* Electronic image. From: http://visibleearth.nasa.gov/view_rec.php?id=1438.

NEAL, S.B.H.C., NORTHOVER, E.W. & HITCHCOCK, J.A., 1970. The development of a technique for applying naphthalene to surfaces for mass transfer analogue investigations. *Journal of Physics E: Scientific Instruments,* 3(8), pp.636-638.

NICOL, K., 1977. The energy balance of an exterior window surface, Inuvik, N.W.T., Canada. *Building and Environment,* 12(4), pp.215-219.

NUSSELT, W. & JUERGES, W., 1928. Das Temperaturfeld ueber einer lotrecht stehenden geheizten Platte. *Zeitschrift des Vereines Deutscher Ingenieure ("Magazine of the Association of German Engineers"),* 72(18), pp.597-603.

OCKENDON, N., DAVIS, S.E., MIYAR, T. & TOMS, M.P., 2009. Urbanization and time of arrival of common birds at garden feeding stations. *Bird Study,* 56(3), pp.405-410.

OKE, T., 1987. *Boundary layer climates.* 2nd ed. London: Methuen.

OKE, T., 2002. *Urban heat islands: an overview of the research and its implications*. Proceedings of The North American Urban Heat Island Summit, 2-3 May 2002, Toronto.

OKE, T.R., 1988. Street design and urban canopy layer climate. *Energy and Buildings,* 11(1-3), pp.103-113.

OKE, T.R. & MAXWELL, G.B., 1974. Urban heat island dynamics in Montreal and Vancouver. *Atmospheric Environment,* 9, pp.191-200.

PARKINSON, G.V. & COOK, N.J., 1992. Blockage tolerance of a boundary-layer wind tunnel. *Journal of Wind Engineering and Industrial Aerodynamics,* 42(1-3), pp.873-884.

PARMELEE, G.V. & HUEBSCHER, G., 1947. Forced convection heat transfer from flat surfaces. *Transactions of ASHRAE,* 58, pp.85-106.

PASCHEKE, F., BARLOW, J. & ROBINS, A., 2008. Wind-tunnel Modelling of Dispersion from a Scalar Area Source in Urban-Like Roughness. *Boundary-Layer Meteorology,* 126(1), pp.103-124.

PAVAGEAU, M. & SCHATZMANN, M., 1999. Wind tunnel measurements of concentration fluctuations in an urban street canyon. *Atmospheric Environment,* 33, pp.3961-3971.

PECK, S.W., CALLAGHAN, C., KUHN, M.E. & BASS, B., 1999. *Greenbacks From Green Roofs: Forging A New Industry In Canada, prepared for Canada Mortgage and Housing Corporation.* Toronto: Peck and Associates.

PENWARDEN, A.D., 1973. Acceptable wind speeds in towns. *Building Science,* 8(3), pp.259-267.

PHILLIPS, R., BLACKMORE, P., J ANDERSON, M.C., AGUILO-RULLAN, A. & PESTER, S., 2007. *Micro-wind turbines in urban environments - an assessment.* Watford: BRE Press.

PINHO, O.S. & ORGAZ, M.D.M., 2000. The urban heat island in a small city in coastal Portugal. *International Journal of Biometeorology,* 44(4), pp.198-203.

PRIYADARSINI, R., HIEN, W.N. & WAI DAVID, C.K., 2008. Microclimatic modeling of the urban thermal environment of Singapore to mitigate urban heat island. *Solar Energy,* 82(8), pp.727-745.

RICH, B.R., 1953. An investigation of heat transfer from an inclined flat plate in free convection. *Transactions of the ASME,* 75, pp.489-497.

RICHARDSON, L.F. 1920. *The Supply of Energy from and to Atmospheric Eddies*. *Proceedings of the Royal Society of London - Series A - Containing Papers of a Mathematical and Physical Character.*

RIZWAN, A.M., DENNIS, L.Y.C. & LIU, C., 2008. A review on the generation, determination and mitigation of Urban Heat Island. *Journal of Environmental Sciences,* 20(1), pp.120-128.

ROBERTSON, A.P., HOXEY, R.P., SHORT, J.L., FERGUSON, W.A. & BLACKMORE, P.A., 1998. Prediction of structural loads from fluctuating wind pressures: Validation from full-scale force and pressure measurements. *Journal of Wind Engineering and Industrial Aerodynamics,* 74-76, pp.631-640.

ROGERS, G.F.C. & MAYHEW, Y.R., 1995. *Thermodynamic and transport properties of fluids, SI units.* 5th ed. Oxford: Blackwell.

ROWLEY, F.B., ALGREN, A.B. & BLACKSHAW, J.L., 1930. Surface conductances as affected by air velocity, temperature and character of surface. *Transactions of ASHVE,,* 36, pp.429-446.

ROWLEY, F.B. & ECKLEY, W.A., 1932. Surface coefficients as affected by wind direction. *Transactions of ASHRAE,* 38.

RYERSON UNIVERSITY, 2005. *Report on the Environmental Benefits and Costs of Green Roof Technology for the City of Toronto.* Toronto: Ryerson University.

S. W. CHURCHILL & R. USAGI, 1972. A general expression for the correlation of rates of transfer and other phenomena. *AIChE Journal,* 18(6), pp.1121-1128.

SAARONI, H., BEN-DOR, E., BITAN, A. & POTCHTER, O., 2000. Spatial distribution and microscale characteristics of the urban heat island in Tel-Aviv, Israel. *Landscape and Urban Planning,* 48(1-2), pp.1-18.

SAILOR, D.J., 2002. *Urban Heat Islands: Opportunities and Challenges for Mitigation and Adaptation*. Proceedings of The North American Urban Heat Island Summit, 2-3 May 2002, Toronto.

SAITOH, T.S., SHIMADA, T. & HOSHI, H., 1996. Modeling and simulation of the Tokyo urban heat island. *Atmospheric Environment,* 30(20), pp.3431-3442.

SCANIVALVE CORPORATION, 2006. *Scanivalve Miniature Pressure Scanners home page* [online]. Available from: http://www.scanivalve.com/doc/product_pressure_miniature.htm [Accessed 12th Novemeber 2006].

SCHWARZ, B., 1972. *Die Warme und Stoffubertragung an Aussenwandoberflachen*. *Berichte aus der Bauforschung,* 79.

SHAO, J., LIU, J., ZHAO, J., ZHANG, W., SUN, D. & FU, Z., 2009. A novel method for full-scale measurement of the external convective heat transfer coefficient for building horizontal roof. *Energy and Buildings,* 41(8), pp.840-847.

SHARPLES, S., 1984. Full-scale measurements of convective energy losses from exterior building surfaces. *Building and Environment,* 19(1), pp.31-39.

SHASHUA-BAR, L. & HOFFMAN, M.E., 2000. Vegetation as a climatic component in the design of an urban street: An empirical model for predicting the cooling effect of urban green areas with trees. *Energy and Buildings,* 31(3), pp.221-235.

SHERIDAN, S., 2002. *The development of the new Toronto Heat-Health Alert System*. Proceedings of The North American Urban Heat Island Summit, 2-3 May 2002, Toronto.

SILL, B.L., COOK, N.J. & BLACKMORE, P.A., 1989. IAWE Aylesbury Comparative Experiment -- Preliminary results of wind tunnel comparisons. *Journal of Wind Engineering and Industrial Aerodynamics,* 32(3), pp.285-302.

SILVA L.F., MARCZAK L.D.F. & MOLLER S.V., 2001. Determination of the local heat transfer coefficient in pipes with helical turbulence promoters through the naphthalene sublimation technique. *Latin American Applied Research,* 31(5), pp.495-500.

SMITH, C. & LINDLEY, S., 2008. *Sustainable Cities: Options for Responding to Climate cHange Impacts and Outcomes. WP3 Workshop Report.* Manchester: University of Manchester.

SMITH, J.O., 2004. *The development of the naphthalene sublimation technique to model convective heat transfer from external building surfaces*. Proceedings of *Proceedings of the Wind Engineering Society Conference*, 16th September 2004, Cranfield University.

SNYDER, W.H., 1972. Similarity criteria for the application of fluid models to the study of air pollution meteorology. *Boundary-Layer Meteorology,* 3(1), pp.113-134.

SOUZA MENDES, P.R., 1991. The naphthalene sublimation technique. *Experimental Thermal and Fluid Science,* 4(5), pp.510-523.

SPARROW, E.M., NELSON, J.W. & LAU, S.C., 1981. Wind related heat transfer coefficients for leeward-facing solar collectors. *Transactions of the ASHRAE,* 76(2), pp.227-239.

STATE OF CALIFORNIA ENERGY COMMISSION, 2005. *At home with cool roofs.* California: State of California Energy Commission.

STEDMAN, J.R., 2004. The predicted number of air pollution related deaths in the UK during the August 2003 heatwave. *Atmospheric Environment,* 38(8), pp.1087-1090.

STEINECKE, K., 1999. Urban climatological studies in the Reykjavík subarctic environment, Iceland. *Atmospheric Environment,* 33(24-25), pp.4157-4162.

STERN, N.H., 2006. *The Stern Review: The Economics of Climate Change.* London: HM Treasury.

STURROCK, N.S., 1971. *Localised boundary layer heat transfer from external building surfaces.* Thesis (Ph.D.). University of Liverpool, Liverpool.

TAKI, A.H. & LOVEDAY, D.L., 1996. External convection coefficients for framed rectangular elements on building facades. *Energy and Buildings,* 24(2), pp.147-154.

THE CHARTERED INSTITUTE OF BUILDING SERVICES ENGINEERS, 1986. *CIBSE Guide - Volume A - Design Data.* London: CIBSE.

THE CHARTERED INSTITUTE OF BUILDING SERVICES ENGINEERS, 2006. *CIBSE Guide - Volume A - Design Data.* London: CIBSE.

THE CHARTERED INSTITUTION OF BUILDING SERVICES ENGINEERS, 1999. *Environmental design - CIBSE Guide A.* London: CIBSE.

THE EARTH INSTITUTE, 2005. *Press release 3rd August 2005: The Growing Urbanization of the World* [online]. Columbia University. Available from: http://www.earth.columbia.edu/news/2005/story03-07-05.html [Accessed 13th April 2007].

THE INSTITUTE OF HEATING AND VENTILATING ENGINEERS, 1970. *IHVE Guide - Book A.* London: IHVE.

UEHARA, K., WAKAMATSU, S. & OOKA, R., 2003. Studies on critical Reynolds number indices for wind-tunnel experiments on flow within urban areas. *Boundary-Layer Meteorology,* 107(2), pp.353-370.

UNGER, J., 1996. Heat island intensity with different meteorological conditions in a medium-sized town: Szeged, Hungary. *Theoretical and Applied Climatology,* 54(3), pp.147-151.

UNITED KINGDOM ACCREDITATION SERVICE, 2007. *M3003: The Expression of Uncertainty and Confidence in Measurement.* 2nd ed. Middlesex: UKAS.

UNITED NATIONS DEPARTMENT OF ECONOMIC AND SOCIAL AFFAIRS (POPULATION DIVISION), 2006a. *Urban Agglomerations 2005.* New York: UN DESA.

UNITED NATIONS DEPARTMENT OF ECONOMIC AND SOCIAL AFFAIRS (POPULATION DIVISION), 2006b. *World Urbanization Prospects: The 2005 Revision.* New York: UN DESA.

UNIVERSITY COLLEGE LONDON, 2007. *LUCID project web site* [online]. Available from: http://www.lucid-project.org.uk/ [Accessed 27th July 2009].

VELAZQUEZ-LOZADA, A., GONZALEZ, J.E. & WINTER, A., 2006. Urban heat island effect analysis for San Juan, Puerto Rico. *Atmospheric Environment,* 40(9), pp.1731-1741.

VOOGT, J., 2006. *Urban Climatology and Urban Thermal Climates. Research homepage, Department of Geography, University of Western Ontario* [online]. Available from: http://publish.uwo.ca/~javoogt/urban%20climate%20.htm [Accessed 11th April 2007].

WATKINS, R., 2002. *The impact of the urban environment on the energy used for cooling buildings.* Thesis (Ph.D.). Brunel University, London.

WATKINS, R., PALMER, J., KOLOKOTRONI, M. & LITTLEFAIR, P., 2002. The balance of the annual heating and cooling demand within the London urban heat island. *Building Service Engineering,* 23(4), pp.207-213.

WATMUFF, J.R., CHARTERS, W.W.S. & PROCTOR, D., 1977. *Solar and wind induced external coefficients: Solar collectors.*

WIKIPEDIA, 2002. *Naphthalene. In: Wikipedia - the free encyclopedia* [online]. Available from: http://en.wikipedia.org/wiki/Napthalene [Accessed 30th June 2009].

WIKIPEDIA, 2003a. *Green roofs. In: Wikipedia - the free encyclopedia* [online]. Available from: http://en.wikipedia.org/wiki/Green_roof [Accessed 12th November 2006].

WIKIPEDIA, 2003b. *Primrose Hill. In: Wikipedia - the free encyclopedia* [online]. Available from: http://en.wikipedia.org/wiki/Primrose_Hill [Accessed 26th July 2009].

WIKIPEDIA, 2003c. *Thermography. In: Wikipedia - the free encyclopedia* [online]. Available from: http://en.wikipedia.org/wiki/Thermography [Accessed 20th September 2006].

WONG, N.H. & YU, C., 2005. Study of green areas and urban heat island in a tropical city. *Habitat International,* 29(3), pp.547-558.

YU, C. & HIEN, W.N., 2006. Thermal benefits of city parks. *Energy and Buildings,* 38(2), pp.105-120.

ANNEXES

Annex A - Naphthalene sublimation methodology

Annex B - Power spectral density plots for the BRE wind tunnel

Annex C - Calculations

Annex D - Assessment of experimental uncertainty

Annex E - Convective heat transfer coefficient spreadsheet

Annex F - Naphthalene sublimation result sheets

Annex G - Naphthalene sublimation results

Annex H - Apparatus

Annex I - Publications and conference papers by the author

Annex A Naphthalene sublimation methodology

Coating of the model

1. All preparation of the model took place in a fume cupboard to minimise inhalation. All handling of the naphthalene and the model was done wearing appropriate personal protective equipment (i.e. gloves and safety glasses).
2. The naphthalene powder was first transferred to a cylindrical metal storage tin which is large enough for the model to be comfortably placed inside (approximate 160 mm diameter). The lid was loosely fitted to the tin to minimise loss of chemical by evaporation.
3. The tin was then placed on the smaller of the two electric hotplates (1200 Watts heating power) and the thermostat set to approximately 50% in order to gently melt the naphthalene powder. This process took between 20 to 30 minutes during which time the chemical was occasionally gently stirred and any build-up on the sides and lid of the container removed. The heated water bath is also switched on and the temperature set at 80 °C.
4. Whilst the naphthalene was being heated, the metal cube was cleaned using ethanol to remove any residual naphthalene and dirt or grease which might have affected the quality of the coating or its adhesion to the model surface.
5. The measurement locations (25 per face as shown in Figure 5.3) were then highlighted with small dots using a fine permanent (i.e. waterproof) marker. It was found that red showed up most clearly on the aluminium base through the naphthalene coating. The model had a lightly scored grid on each face which permitted fast and accurate marking of the measurement points.
6. The two hose-tail fittings (later used to connect the warmed water supply) were loosely screwed into the base of the model. These were used to aid handling of the model during the coating procedure. A thin layer of PTFE plumbing tape was wrapped around the exposed thread of the hose-tail fittings in order to ease removal once the model was coated.
7. The model was lowered into the heated water bath and held submerged for approximately 20 seconds. Shorter times resulted in rapid re-crystallisation of the naphthalene when the cube was dipped, and longer times resulted in rapid sublimation and loss of the applied naphthalene coating. The model was then quickly but thoroughly dried.
8. With the model cube held by the two hose-tail fittings, it was slowly lowered into the molten naphthalene. This was done with the model tilted to one corner as far as possible within the constraints of the container so that any bubbles or contamination floating on the surface of the chemical are washed off the lower surface, rather than giving rise to a poor finish on the ‘roof’ of the model.

9. The model was gently rotated and moved up and down in the molten naphthalene to ensure a smooth and even coating on all surfaces. This was continued for approximately 10 seconds. As the model was removed, the rotation was continued so that any drips and runs were minimised.

10. It was important to quickly cool the model to prevent large amounts of sublimation taking place resulting in a very thin coating. This was achieved by filling the model with cold tap water via one of the hose-tail fittings and allowing the water to run through the model and out of the other hose-tail. This was continued for 20 to 30 seconds until the model was fully cooled.

11. The hose-tail fittings were then carefully removed taking care not to damage the surface coating, and the model gently dried.

12. Finally, the coated model was placed inside a sealable plastic food bag which was folded tightly around the cube in order to expel the maximum amount of air. The bag was then carefully sealed.

Storage and handling

13. Sublimation from the model prior to testing was minimised by keeping the model in the sealed bag right up to the point of testing. It was further reduced by storing the model in a freezer. The model was typically prepared two to three days prior to testing and allowed to condition in order that imperfections diminished and a smoother surface finish was achieved.

14. Care needed to be taken not to impact the model, for example when setting down on a surface, as the naphthalene coating was brittle and thus easily damaged. Therefore a soft piece of fabric was used to place under the model as a cushion.

15. The chilled model was removed from the storage freezer approximately one hour before testing and allowed to gently warm to room temperature, still sealed in its bag, before being installed in the tunnel.

Installation in wind tunnel

16. The heated water bath is switched on several hours prior to commencement of testing to allow the temperature (set to 40.0 °C) time to stabilise. The submersible water pump is also switched on (with the water just being circulated in a loop) to ensure that the water is well mixed and therefore of uniform temperature. The water level must also be checked to avoid the need for topping up during a test which would impact the water (and hence model) temperature.

17. During warmer periods, it was found that the heat input of the submersible pump would occasionally cause the temperature of the water bath to rise above the set-point temperature. It was therefore necessary to install a desk fan blowing cool air over the water so as to remove excess heat (see Figure 5.13 above). The digital control system of the water bath was then better able to regulate the water temperature and maintain it at the required 40.0 °C with an accuracy of within ±0.1 °C.

18. The surrounding building models were arranged into the desired simulation on the wind tunnel turntable. Care was taken to ensure that the street canyons were aligned accurately to the required angle in relation to the approaching wind. A series of gridlines drawn onto the turntable allowed accurate positioning of the models without the need for continuous measurement. Small but powerful magnets were positioned at the downwind bases of the models (in particular the upwind canyons which were most exposed to the approaching flow) to resist movement during the test.

19. At the last possible moment, the coated model was removed from its storage bag and placed upside down on a soft cloth on the work surface. The circular baseboard was rested on top if the model and the holes for the hose fittings were aligned.

20. Several layers of PTFE plumbing tape were wrapped around the threads of the two hose-tail fittings to prevent leakage of water when installed. These fittings were then screwed into the model through the baseboard. Large washers placed onto the hose-tails before installation allowed the fittings to be gently tightened without digging into the wooden baseboard.

21. The model and baseboard assembly was then placed into the wind tunnel, but left resting at an angle in the hole at the turntable centre. This assisted with flushing of the model when the water supply was connected to ensure all trapped air was removed.

22. With the pump turned off, the hoses were fitted onto the underside of the model and secured in place using jubilee clips. The taps were closed and the pump turned on. The tap on the supply hose was then opened to gradually begin to fill the model in order to ensure that it was slowly brought up to test temperature (i.e. 40 °C). The return hose tap was then also slowly opened to allow the water to begin to flow through the model, flushing out the air in the process.

23. Once both taps were fully opened and water was flowing through the model, the model was tilted and rotated to flush out any remaining air which may have been trapped in the upper corners.

24. The model was then seated into the wind tunnel turntable and aligned with angle markings on the baseboards. It was essential to ensure that the model was precisely aligned square-on to the approaching air flow.

Taking coating thickness measurements

25. The Elcometer 456 measurement gauge was calibrated prior to testing in order to maximise accuracy. An initial measurement was first taken on one of the surfaces of the model to indicate the approximate coating thickness. The calibration was then performed at zero thickness (for which a piece of uncoated aluminium plate was used) and at an upper limit (selected based upon the result of the initial reading) using a calibration foil of known thickness.

26. A new batch of readings was opened on the Elcometer measurement device and the batch number recorded. Measurements were then taken at the 75 marked locations (25 on each of the windward, top and leeward surfaces. The first measurement on each surface was taken at the top left-hand corner (nearest to the windward edge on the top surface). Subsequent measurements were then made working to the right across the rows, and down to the bottom right-hand corner (nearest to the leeward side on the top surface).

27. This measurement procedure was immediately repeated in order to provide two sets of data for later cross-checking and averaging, if required.

Running the wind tunnel

28. As soon as the measurement procedure was completed, the wind tunnel was started and its speed increased to the running speed for the experiment. A timer was then started.

29. Full details of the particular test arrangement were noted, including the arrangement of models and wind tunnel speed. Environment conditions (i.e. air temperature, water bath temperature, ambient pressure and humidity) were also recorded. These readings were monitored during the test to ensure minimal variation. They were also recorded at regular intervals during the experiment (approximately after each elapsed hour) as well as at the end of the test.

30. After the designated time (typically 2 to 3 hours depending upon running speed), the wind tunnel was stopped.

31. The measurement procedure conducted at the start of the test (outlined in steps 26 to 27) was repeated to determine the coating thicknesses at the end of the test.

32. With the water pump turned off, the hoses were disconnected one by one with the water being drained back down into the water bath.

33. The model was then removed from the wind tunnel, separated from its baseboard by removal of the hose-tail fittings and placed back in its storage bag.

34. The remaining naphthalene coating was separated from the model by providing a sharp blow onto each face using a blunt object (such as the end of a screwdriver), whilst taking care not to damage the model. The majority of the chemical was removed from the model quite cleanly in this way and was then bagged ready for reuse.

Processing of the data

35. The Elcometer thickness measurement device was supplied with a cable to allow the batches of readings to be downloaded to a PC. Two separate copies of the results were kept for backup purposes.

36. Average values of the temperatures (both air and model), humidity and atmospheric pressure readings that had been recorded at intervals throughout the experiment were calculated to provide a single value for each variable for use in the analysis.

37. The results were then processed using custom Microsoft Excel spreadsheet programs (see Annex E) which were developed specifically for this work by the author. The coating thickness results were imported and variables relating to the experimental conditions (including air and model temperatures, wind tunnel speed and run times) were entered. The spreadsheet converted the measured mass transfer rates to convective heat transfer rates via the heat-mass transfer analogy discussed previously in Section 4.4. Results were determined in this way for each individual location, the average along each horizontal row of taps, and also the average across each surface

Annex B Power spectral density plots for the BRE wind tunnel

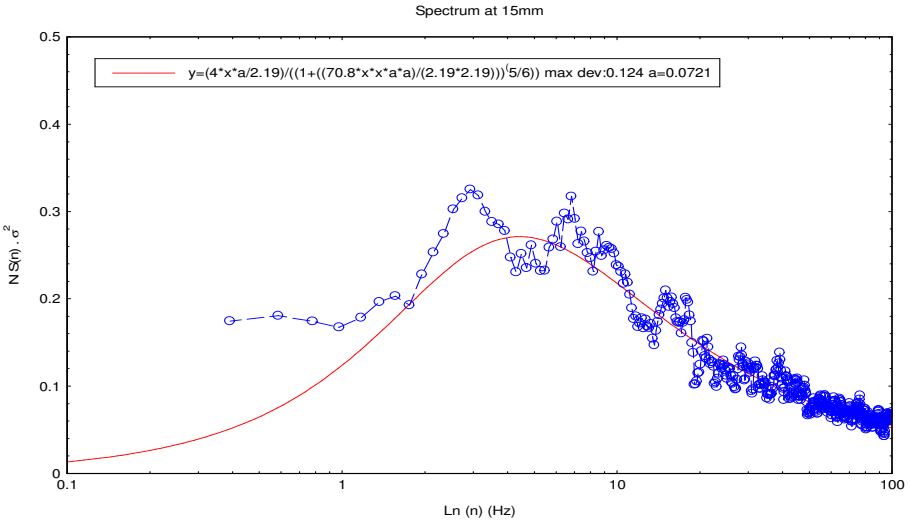

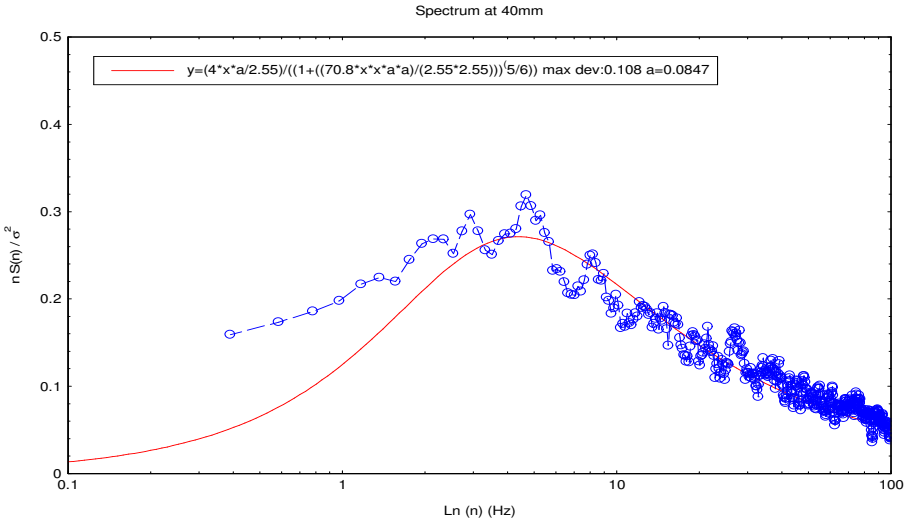

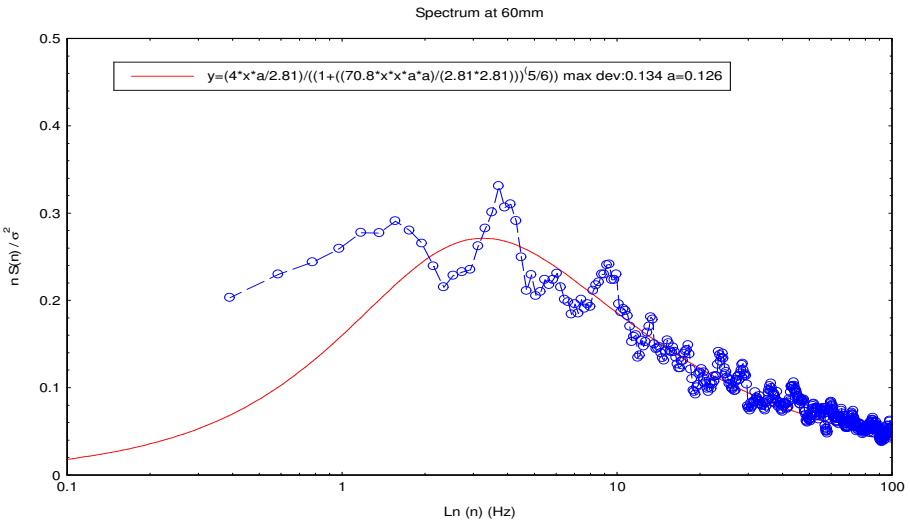

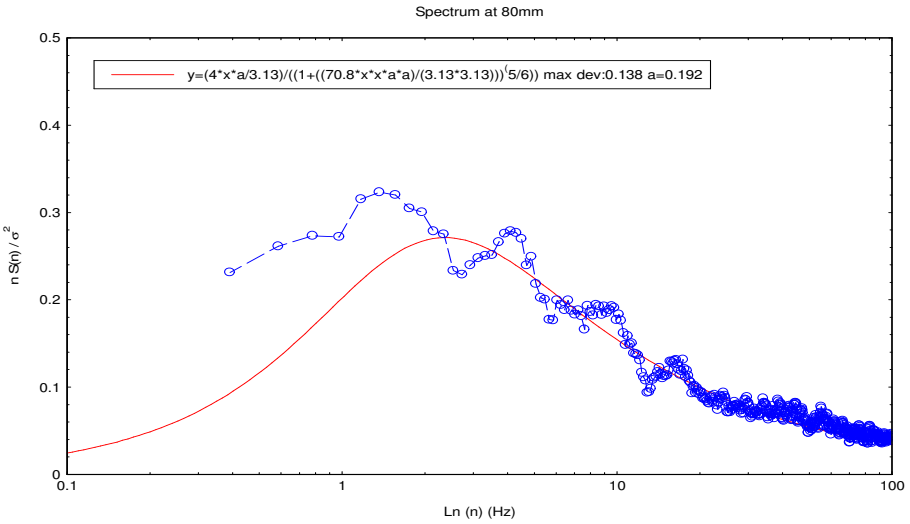
Spectrum at 80mm
y=(4*x*a/3.13)/((1+((70.8*x*x*a*a)/(3.13*3.13)))^(5/6)) max dev:0.138 a=0.192
n S(n) / σ²
Ln (n) (Hz)
0.5
0.4
0.3
0.2
0.1
0
0.1
1
10
100

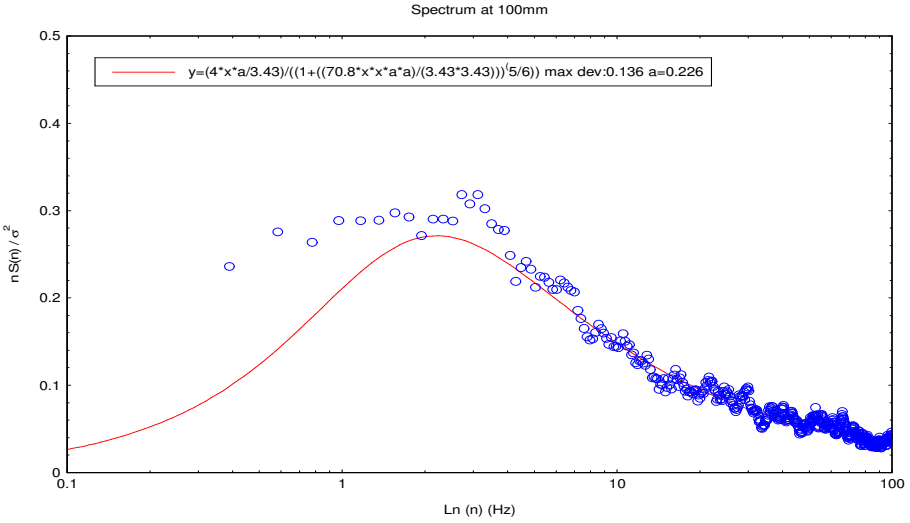
Spectrum at 100mm
y=(4*x*a/3.43)/((1+((70.8*x*x*a*a)/(3.43*3.43)))^(5/6)) max dev:0.136 a=0.226
n S(n) / σ²
Ln (n) (Hz)
0.5
0.4
0.3
0.2
0.1
0
0.1
1
10
100

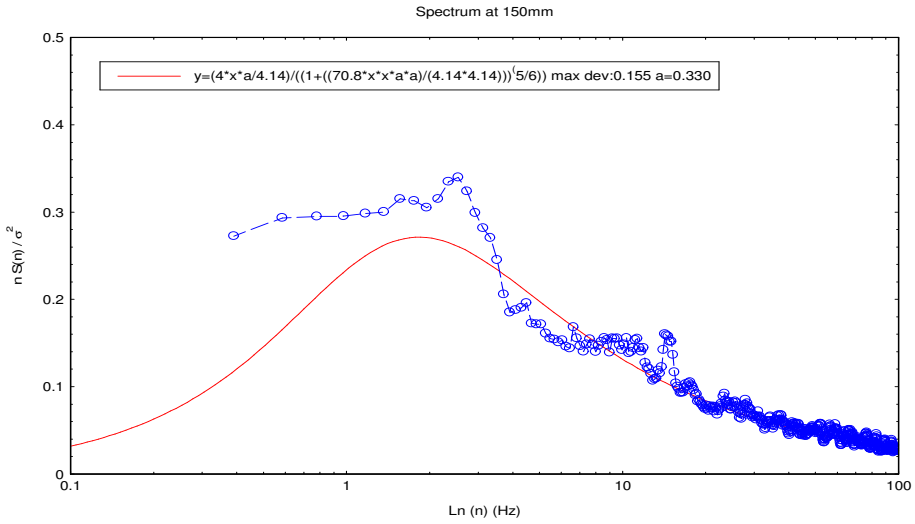
Spectrum at 150mm
y=(4*x*a/4.14)/((1+((70.8*x*x*a*a)/(4.14*4.14)))^(5/6)) max dev:0.155 a=0.330
n S(n) / σ²
Ln (n) (Hz)
0.5
0.4
0.3
0.2
0.1
0
0.1
1
10
100

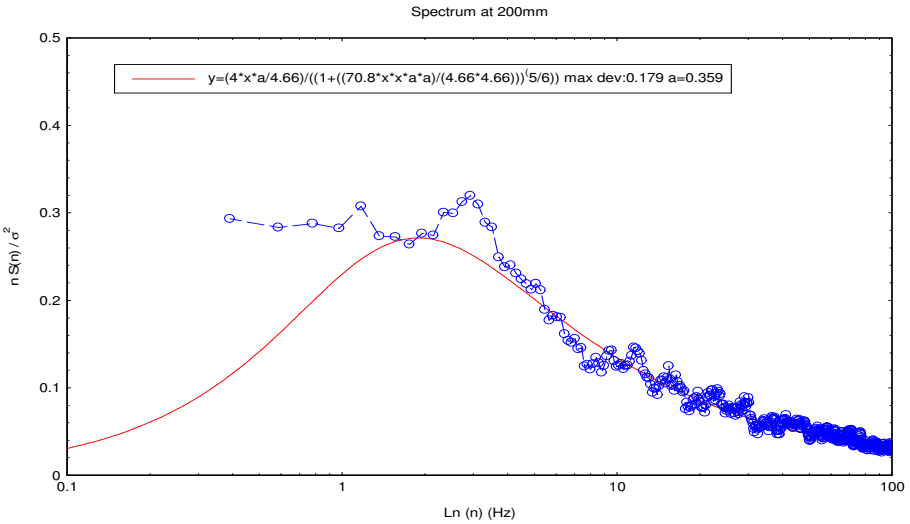
Spectrum at 200mm
y=(4*x*a/4.66)/((1+((70.8*x*x*a*a)/(4.66*4.66))^(5/6)) max dev:0.179 a=0.359
n S(n) / σ²
Ln (n) (Hz)
0.5
0.4
0.3
0.2
0.1
0
0.1
1
10
100

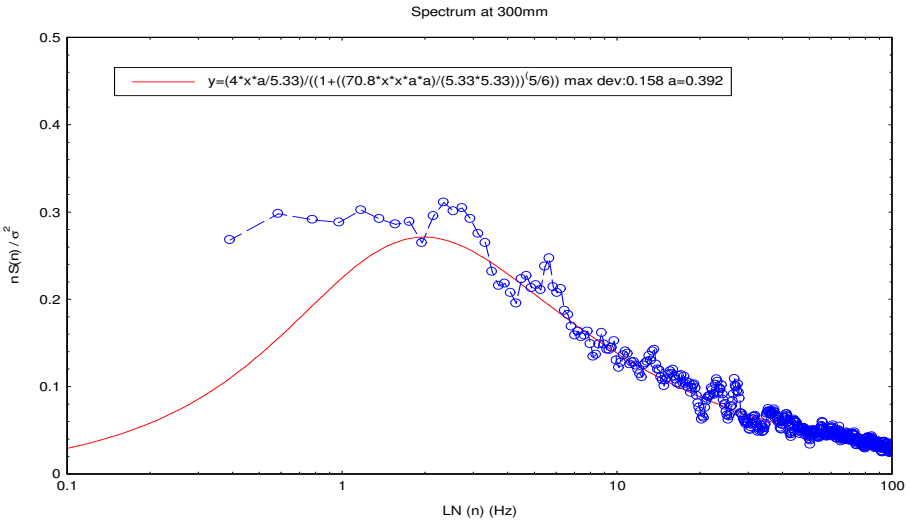
Spectrum at 300mm
y=(4*x*a/5.33)/((1+((70.8*x*x*a*a)/(5.33*5.33))^(5/6)) max dev:0.158 a=0.392
n S(n) / σ²
LN (n) (Hz)
0.5
0.4
0.3
0.2
0.1
0
0.1
1
10
100

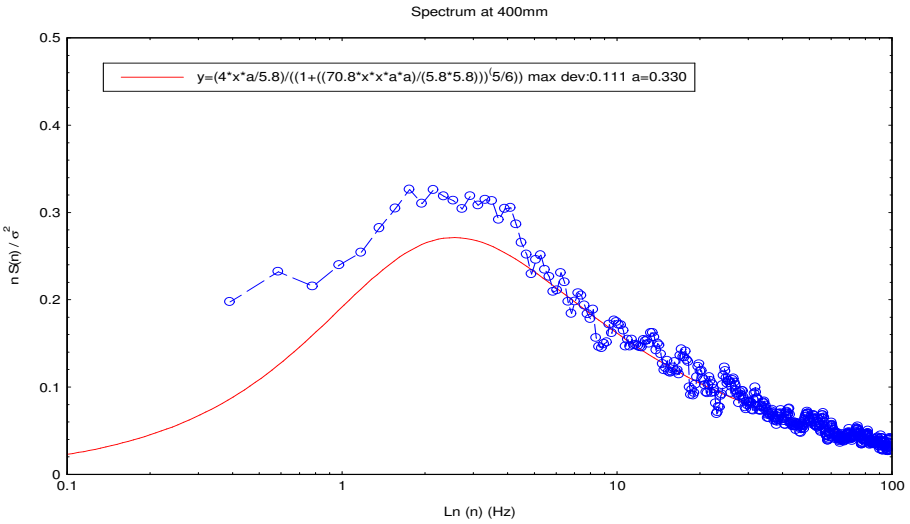
Spectrum at 400mm
y=(4*x*a/5.8)/((1+((70.8*x*x*a*a)/(5.8*5.8)))^(5/6)) max dev:0.111 a=0.330
n S(n) / σ²
Ln (n) (Hz)
0.5
0.4
0.3
0.2
0.1
0
0.1
1
10
100

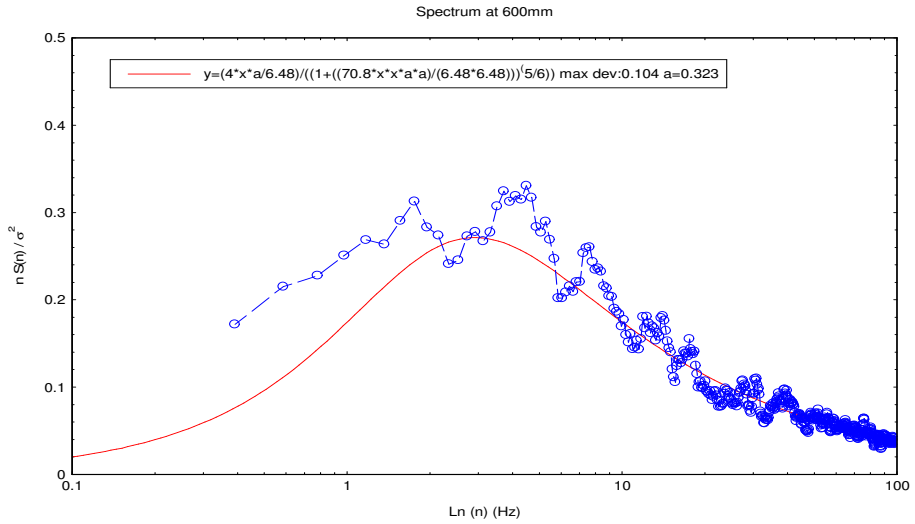
Spectrum at 600mm
y=(4*x*a/6.48)/((1+((70.8*x*x*a*a)/(6.48*6.48)))^5/6)) max dev:0.104 a=0.323
n S(n) / σ²
Ln (n) (Hz)
0.5
0.4
0.3
0.2
0.1
0
0.1
1
10
100

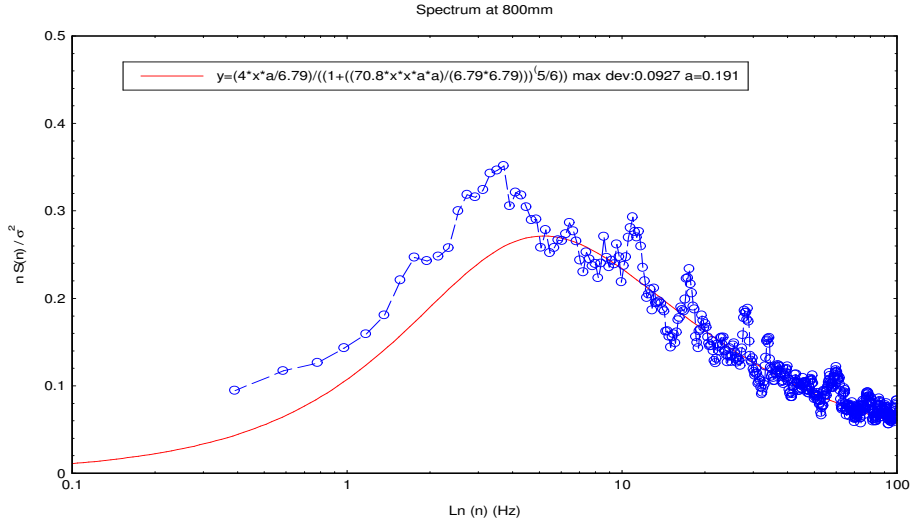
Spectrum at 800mm
y=(4*x*a/6.79)/((1+((70.8*x*x*a*a)/(6.79*6.79)))^5/6)) max dev:0.0927 a=0.191
n S(n) / σ²
Ln (n) (Hz)
0.5
0.4
0.3
0.2
0.1
0
0.1
1
10
100

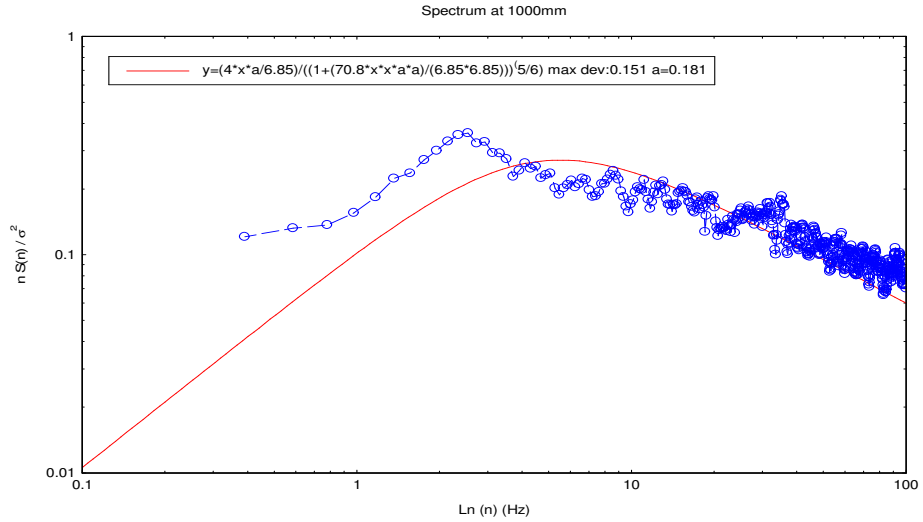
Spectrum at 1000mm
y=(4*x*a/6.85)/((1+(70.8*x*x*a*a)/(6.85*6.85)))^5/6) max dev:0.151 a=0.181
n S(n) / σ²
Ln (n) (Hz)
1
0.1
0.01
0.1
1
10
100

Annex C Calculations

Annex C1 - Calculation of the turbulence scale factor (S)

Measurement of velocities at a height of 100 mm in the BRE wind tunnel yielded a value of 4.15 mm for the zero plane displacement (d) and a value of 11.4 mm for the roughness length (z_0). The along-wind length scale of the turbulence in the wind tunnel is given by Equation 6.8:

$$L_{x_u} = 25(z-d)^{0.35} z_0^{-0.063}$$

The full-scale value for the turbulent length scale may be determined by multiplication of the relevant terms by the scale factor (S), hence:

$$SL_{x_u} = 25 \times [S\,(z-d)]^{0.35} \times [S\,z_0]^{-0.063}$$

A solution for the scale factor (S) may therefore be obtained by rearrangement of the above equation as follows:

$$\frac{SL_{x_u}}{S^{0.35} \times S^{-0.063}} = 25 \times (z-d)^{0.35} \times z_0^{-0.063}$$

$$S^{0.713} = \frac{25 \times (z-d)^{0.35}}{L_{x_u} \times z_0^{0.063}}$$

$$S = \frac{25^{1.403} \times (z-d)^{0.491}}{L_{x_u}^{1.403} \times z_0^{0.088}}$$

$$S = \frac{91.3 \times (z-d)^{0.491}}{L_{x_u}^{1.403} \times z_0^{0.088}}$$

By substitution of known values derived from the wind tunnel measurements, a value for the turbulence scale factor at a height of 100 mm may be obtained :

$$S = \frac{91.3 \times (0.1-0.00415)^{0.491}}{0.226^{1.403} \times 0.0114^{0.088}}$$

$$S = \frac{91.3 \times 0.09585^{0.491}}{0.226^{1.403} \times 0.0114^{0.088}}$$

$$S = 344.8$$

The wind tunnel scale factor with respect to the simulated turbulence is therefore 1:345. In practice, a spreadsheet allows exact values (rather than the above rounded figures) to be used, although this actually makes only a minor difference to the calculated values.

Annex C2 - Calculation of convective heat transfer coefficient (CHTC)

The full calculation of the convective heat transfer coefficient for a typical set of experimental results is presented below. The data is taken from Experiment 2 (see Annex F for full details) which was for a canyon height-to-width ratio of 0.5 with the flow perpendicular to the rows of buildings.

The average change in thickness of the naphthalene coating on the windward surface of the model was 283 µm (0.000283 m) over a 3.0 hour period. The average air temperature during the run was 18.8 °C (292.0 K) and the model was maintained at 40.0 °C (313.2 K). The atmospheric air pressure was 1012.5 mb (101250 Pa). The values of other air and naphthalene properties are noted as required next to the relevant equations below.

The convective heat transfer coefficient may be calculated as follows:

Kinematic viscosity: $$v_a = \frac{0.1556}{10000} \times \left(\frac{\theta_a}{298.16} \right)^{1.7774} \left(\frac{101300}{P_{atm}} \right)$$

$$v_a = \frac{0.1556}{10000} \times \left(\frac{292.0}{298.16} \right)^{1.7774} \left(\frac{101300}{101250} \right) = \underline{1.500 \times 10^{-5} \text{ m}^2\text{s}^{-1}}$$

Thermal diffusivity: $$k_a = \frac{K_a}{C_a \times \rho_a}$$ where: $K_a = 0.02526$ W.m^{-1}K^{-1}, $C_a = 1004.4$ J.kg^{-1}K^{-1}, $\rho_a = 1.205$ kg.m^3

$$k_a = \frac{0.02526}{1004.4 \times 1.205} = \underline{2.087 \times 10^{-5} \text{ m}^2\text{s}^{-1}}$$

Prandtl number: $$Pr = \frac{v_a}{k_a} = \frac{1.500 \times 10^{-5}}{2.087 \times 10^{-5}} = \underline{0.719}$$

Schmidt number: $$Sc = 2.28 \times \left(\frac{\theta_a}{298.16} \right)^{-0.1526}$$

$$Sc = 2.28 \times \left(\frac{292.0}{298.16} \right)^{-0.1526} = \underline{2.287}$$

Vapour pressure: $$\log P = \left(\frac{a_0}{2} + \sum a_x E_x \right) \div \theta_n$$

where: $a_0 = 301.6247$ $\quad x = (2\theta_n - 574)/114 = 0.4596$

$a_1 = 791.4937$ $\quad E_1 = x = 0.4596$

$a_2 = -8.2536$ $\quad E_2 = 2x^2 - 1 = -0.5775$

$a_3 = 0.4043$ $\quad E_3 = 4x^3 - 3x = -0.9905$

$$\log P = \left(\frac{301.6247}{2} + 363.8094 + 4.7660 - 0.4005 \right) \div 313.2$$

$$\log P = \frac{518.9516}{313.2} = 1.6570$$

$$\log P = 10^{1.6569} = \underline{45.399 \text{ Pa}}$$

Vapour density: $\rho_n = \frac{P}{R_n \times \theta_n}$ where: $R_n = 64.890 \text{ J.kg}^{-1}\text{K}^{-1}$

$$\rho_n = \frac{45.399}{64.890 \times 313.2} = \underline{0.0022338 \text{ kg.m}^{-3}}$$

Mass transfer coeff: $h_m = \frac{\partial T \times \rho_n}{t \times (\rho_v - \rho_{v.a})}$ where: $\rho_n = 1175.0 \text{ kg.m}^{-3}$

$\rho_{v,a} = 0.0 \text{ kg.m}^{-3}$

$$h_m = \frac{0.000283 \times 1175.0}{3 \times (0.0022338 - 0)} = \underline{49.620 \text{ m.s}^{-1}}$$

Sherwood number: $Sh = \frac{h_m \times L}{D}$ where: $L = 0.094$ m

$D = 0.02324 \text{ m}^2\text{hr}^{-1}$

$$Sh = \frac{49.620 \times 0.094}{0.02324} = \underline{200.701}$$

Nusselt number: $Nu = \left(\frac{Pr}{Sc} \right)^n \times Sh$ where: $n = 0.34$

$$Nu = \left(\frac{0.719}{2.287} \right)^{0.34} \times 200.701$$

$$Nu = \underline{135.421}$$

CHTC: $h_c = \frac{Nu \times K_a}{L}$

$$h_c = \frac{135.421 \times 0.02526}{0.094}$$

$$h_c = \underline{36.391 \text{ W.m}^{-2}\text{K}^{-1}}$$

In practice, a spreadsheet was designed to carry out these calculations and select the appropriate air and naphthalene properties based upon actual environmental conditions measured during the experiments.

Annex C3 - Calculation of the density of humid air

All quantities and values given in this section are taken from 'Thermodynamic and Transport Properties of Fluids' (Rogers and Mayhew, 1995).

The *ideal gas law* is may be expressed according to the following equation:

$$PV = mR\theta$$

where: P = pressure (Pa)
V = volume (m^3)
m = mass (kg)
R = gas constant (kJ/kg.K)
θ = temperature (K)

The density of a gas is a measure of its mass per unit volume:

$$\rho = \frac{m}{V}$$

Therefore an expression for the density of a gas can be determined in terms of its pressure, temperature and the specific gas constant:

$$\rho = \frac{P}{R\theta}$$

The addition of water vapour to dry air will have the effect of reducing the overall density. This may seem contrary to logic as water is denser than air and so it may (wrongly) be assumed that humid air will also be denser than dry air. The reason for this is that the molar mass of water (18.015 kg/mol) is significantly less than that of air (28.960 kg/mol). By introducing water vapour into the dry air, the 'average' molar mass reduces as the total number of molecules in a volume (assuming constant temperature and pressure) must remain constant. Therefore, when working with humid air, it is important to consider the combined densities of both the dry air and the water vapour:

$$\rho_{hum} = \frac{P_a}{R_a\theta} + \frac{P_w}{R_w\theta}$$

where: P_a = partial pressure of dry air
P_v = partial pressure of water vapour

For dry air, the specific gas constant (R_a) is equal to the ratio of the molar gas constant ($\tilde{R}$) and the molar mass ($\tilde{m}_a$) as follows:

$$R_a = \frac{\tilde{R}}{\tilde{m}_a} = \frac{8.3145 \text{ kJ/mol.K}}{28.960 \text{ kg/mol}} = 287.1 \text{ J/kg.K}$$

For water vapour, the specific gas constant (R_v) is equal to the ratio of the molar gas constant ($\tilde{R}$) and the molar mass ($\tilde{m}_v$) as follows:

$$R_v = \frac{\tilde{R}}{\tilde{m}_v} = \frac{8.3145 \text{ kJ/mol.K}}{18.015 \text{ kg/mol}} = 461.5 \text{ J/kg.K}$$

The vapour pressure of the water may be determined with knowledge of the relative humidity (ϕ) and saturated vapour pressure:

$$P_v = \phi \times P_{sat}$$

From *Dalton's law of partial pressures*, the partial pressure of the dry air may be calculated by subtracting the partial pressure of the water vapour from the measured atmospheric pressure, thus:

$$P_a = P_{atm} - P$$

A range of vapour pressures for typical experimental temperatures are shown in Table C1 below.

Table C1: The saturation pressure of water vapour at various temperatures (source: Rogers and Mayhew, 1995)

Temperature (°C)	**P_s (Pa)**
10	1227
15	1704
20	2337
25	3166
30	4242

Example calculation

As an example, for air at a temperature of 20 °C (293.15 K), relative humidity of 20% and atmospheric pressure of 1016 mb (101600 Pa), then:

The partial pressure of the water vapour will be:

$$P_v = 0.20 \times 2337 = 467.4 \text{ Pa}$$

The dry air partial pressure will be:

$$P_a = 101600 - 467.4 = 101132.6 \text{ Pa}$$

And therefore the density of the humid air may be calculated, thus:

$$\rho_{hum} = \frac{101132.6}{287.1 \times 293.15} + \frac{467.4}{461.5 \times 293.15}$$

$$\rho_{hum} = 1.202 + 0.003$$

$$\rho_{hum} = 1.205 \text{ kg/m}^3$$

The density of the humid air is therefore 1.205 kg/m^3. It can be seen the addition of humidity to the air has a reasonably small effect upon the density (the density of dry air for the above conditions would have been 1.207 kg/m^3).

Annex C4 - Calculation of the Reynolds number

The Reynolds numbers based upon building height may be calculated using the following equation:

$$Re_H = \frac{\rho V l}{\mu}$$

where: $\rho = 1.200\ kg/m^3$ (density of humid air at 293 K and 30% RH)

$l = 0.094\ m$ (height of the wind tunnel model)

$\mu = 1.786 \times 10^{-5}\ kg/ms$ (dynamic viscosity of air at 293 K)

and V is wind tunnel velocity measured at the building roof height (100 mm).

The Reynolds numbers for each of the five wind tunnel speed settings used in the current naphthalene sublimation experiments have been calculated and are shown in Table C2 below.

The Reynolds number range for the naphthalene sublimation tests was therefore 8,174 to 57,474 (or 8.2×10^3 to 5.7×10^4)

Table C2: The Reynolds number for the naphthalene sublimation experiments based upon velocity at 100 mm height.

Wind tunnel setting	Wind tunnel velocity at 100 mm (m/s)	Reynolds number (Re_H)
7.5%	1.29	8,174
15%	2.64	16,674
30%	5.17	32,653
45%	7.06	44,589
60%	9.10	57,474

Annex D Assessment of experimental uncertainty

Annex D1 – Background to the 'GUM' approach

The expression of uncertainty in measurement has long since been the subject of debate with significant variation in methodology, terminology and notation from laboratory to laboratory, and country to country. In 1977, the Comité International des Poids et Mesures* (CIPM) - the worlds highest authority in metrology - requested the Bureau International des Poids et Mesures† (BIPM) to address this problem and put forward proposals for its resolution. After surveying the various national metrology laboratories, the need for an internationally accepted procedure for determining measurement uncertainty was confirmed, but no clear consensus was arrived at regarding the methodology that should be employed. A meeting of world experts in the field was therefore convened with the objective of *"arriving at a uniform and generally acceptable procedure for the specification of uncertainty".*

The task of developing these early recommendations into a detailed guide was referred to the Technical Advisory Group on Metrology (TAG4) of the International Standards Organisation (ISO). The resulting 'Guide to the Expression of Uncertainty in Measurement' document (ISO, 2008) was first published in 1993, but has recently been revised and updated. For brevity, this document is now more usually referred to by its 'GUM' acronym.

Responsibility for the maintenance and promotion of this document now lies with the Joint Committee for Guides in Metrology (JCGM) which is a committee of the BIPM. The text of the latest ISO GUM document has been republished by a number of the member organisations, some of which are available for download free of charge. Most notable of these is the JCGM 100 (2008a) document and accompanying JCGM 101 (2008b) supplement which may be downloaded from the BIPM web site (2008).

A more practical guide to determining experimental uncertainty for laboratory workers is provided by the United Kingdom Accreditation Service (UKAS). The document 'M3003: The Expression of Uncertainty and Confidence in Measurement' (2007) is aimed at both beginners and those with more experience in the field and provides a relatively straightforward approach to the subject. In terms of its methodology and terminology, the method described is based upon and fully consistent with the original ISO document. It does however provide additional guidance and examples to assist the user with implementation, and for these reasons the uncertainty analysis for the current work has been conducted mainly with reference to the UKAS document.

A summary of the uncertainty calculation methodology is provided in the following section with reference to the naphthalene sublimation technique; the guidance documents noted previously should be consulted where a more complete description of the procedure is required.

* In English: The International Committee for Weights and Measures.
† In English: The International Bureau of Weights and Measures.

The GUM approach to determining measurement uncertainty has a number of significant advantages over other methodologies. Most importantly, it provides a single internationally recognised and accepted approach which allows workers and laboratories around the world to 'speak the same language' with regards to uncertainty analysis. This consistency ensures that results obtained by different individuals and organisations are compatible and hence may be directly compared.

The GUM methodology is therefore essential for calibration and industrial laboratories, and is rapidly becoming accepted in various other scientific fields. It is however still not well known within some parts of the academic community, perhaps mainly as a result of the limited material currently available for teaching of the topic. Some of the terms and definitions used in the methodology may be unfamiliar to those well practised in other methodologies which may also contribute to a reluctant uptake.

However, the approach described is becoming ever more widely accepted and practised in academic fields and thus it has been selected as the basis for the uncertainty analysis for the current naphthalene sublimation measurements. It represents the current state-of-the-art and as an internationally accepted methodology, its use will ensure that the results are best most easily interpreted by other researchers.

Annex D2 - Overview of methodology

The terms "error" and "uncertainty" are frequently used when discussing experimental measurements. They are not however interchangeable and so it is vital to both understand and correctly employ the terms as described in the GUM.

Measurement **error** is defined as the measured value minus the 'true' value, but as the 'true' value may never actually be known, the error must also remain unknown. It is therefore much more useful to talk in terms of the **uncertainty** in a measurement which can be determined and is defined by the GUM as:

> *"A parameter, associated with the result of a measurement, that characterises the dispersion of the values that could reasonably be attributed to the measurand".*

The **measurand** is the quantity of a phenomena, substance or body that is to be measured. The purpose of the measurement is therefore to assign a magnitude to the measurand. Since all measurements will typically include some degree of error, the assigned value is considered to be the 'best estimation' of the magnitude. The value assigned to the measurand is therefore only complete when accompanied by a statement of the **uncertainty** in that value.

In many experiments, the measurand is not measured directly but rather it is determined based upon the values of other associated quantities. In the current work for example, it was not possible to measure the convective heat transfer coefficient directly and so instead its value was calculated based upon the values of the naphthalene sublimation depth, model temperature, environmental conditions, chemical properties, etc. The measurand is assigned the symbol Y and is a function of the various 'input' variables X_1, X_2, X_3, etc.

Therefore:

$$Y = f(X_1, X_2, \ldots X_n)$$

For the current work:

$$h_c = f(\partial T, t, \theta_m, v, k, \rho_v, \ldots. \text{etc})$$

Each of these input variables has a value x_i which may itself be subject to an uncertainty $u(x_i)$; these are the **standard uncertainties**. Each input may also be considered to be a measurand in its own right (and therefore subject to the uncertainties in its own input variables) and hence the uncertainties in every applicable quantity may be propagated through to the primary measurand. For the current analysis, a multi-stage approach is therefore required in order to determine the standard uncertainty of each sub-calculation in turn, before determining the overall standard uncertainty in the value of the convective heat transfer coefficient.

In a GUM analysis, each of the input components is regarded as a random variable which may be characterised by a given probability distribution. The assigned distribution encodes available knowledge about the quantity and the uncertainty in its magnitude. These uncertainties may arise in a number of forms and maybe either random or systematic.

Some of these uncertainties may, for example, be due to simple rounding errors such as when reading from a digital display of limited resolution. In these cases, it is not known where within the given limits (±0.5 of the least significant digit, denoted 'a') the 'true' value actually lies. It must therefore be assumed that the 'true' value is equally likely to lie at any point within this range, and hence a rectangular probability distribution (as illustrated in Figure D1) is assigned.

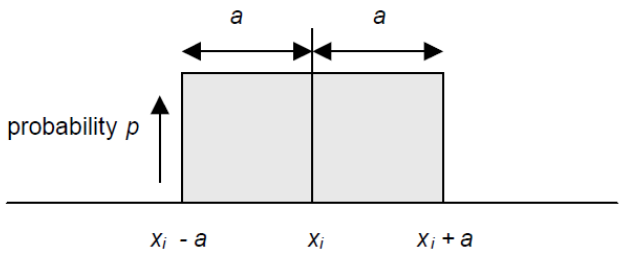

Figure D1: A rectangular probability distribution
(source: UKAS, 2007)

The form of the probability distribution that is selected for a given value depends on how much is known about the respective quantity. A rectangular probability distribution such as that shown above is used where little or no such information is available. However if more is known about the quantity, it may be possible to assign an alternative, less onerous probability distribution.

Measurements are often taken as the difference between two separate readings on a single digital scale (such as the in the current experiments where the initial naphthalene coating thickness reading is subtracted from the final reading to determine the thickness change). If the measurement scale is linear, then both of these readings will have an associated rectangular probability distribution of identical size. When two identical rectangular distributions are combined, the resulting probability distribution will be triangular in form as illustrated in Figure D2. In such circumstances, the semi-range of the distribution is doubled (±2a), but it is more likely that the 'true' reading will lie at the centre of this range (at the peak of the triangle)

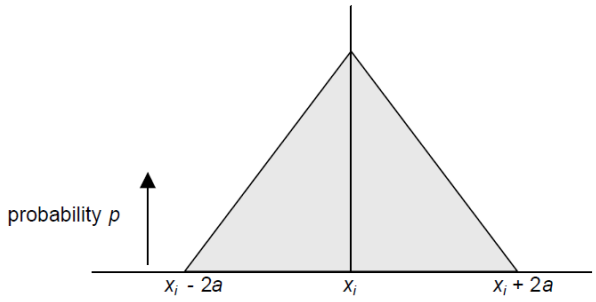

Figure D2: A triangular probability distribution
(source: UKAS, 2007)

Uncertainties which are based upon statistical methods or taken from instrument calibration datasheets will often be of a normal (Gaussian) form, as shown in Figure D3 below. Such probability distributions also occur when a number of distributions are combined, irrespective of their individual forms. The resulting probability distribution tends towards the normal form in accordance with the central limit theory, except where a single uncertainty input dominates. In such cases, the resulting probability distribution form departs little from the dominating input distribution and hence this original form is largely maintained.

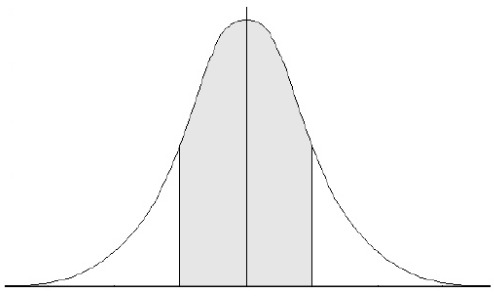

Figure D3: A normal probability distribution
(source: UKAS, 2007)

Various other probability distributions are also possible, but these will not be considered further as they are not relevant to the current uncertainty calculations. For each distribution type, the GUM provides expressions for determining the respective **standard uncertainty** ($u(x_i)$) from the input uncertainty (a_i). For the three probability distributions of relevance to the current work, these expressions are as follows:

Rectangular: $$u(x_i) = \frac{a_i}{\sqrt{3}}$$

Triangular: $$u(x_i) = \frac{a_i}{\sqrt{6}}$$

Normal: $$u(x_i) = \frac{a_i}{\sqrt{1}} = a_i$$

The quantities Y and X_i may not have a direct one-to-one relationship, in fact they may be entirely unrelated units altogether (for example length and time). It is therefore necessary to determine how sensitive the output quantity (Y) is to the various individual input quantities (X_i). The **sensitivity coefficient** (c_i) describes how the measurand quantity (or more precisely the best estimate of the measurand quantity) varies with a small change in the respective input quantity. This may be determined by partial differentiation of the various relationships, however this can be lengthy for complicated experiments involving a range of variables.

A more straightforward approach in such situations is to determine the change in the function (Δf) that results from a small change (Δx_i) in the value of each input quantity (x_i). It is essential to select the values of x_i and Δx_i carefully to ensure both mathematical accuracy and an acceptable approximation of the partial derivative. An appropriate value of x_i is typically one within the range of expected values for the given application, and Δx_i may be selected as the expected uncertainty in x_i. The **sensitivity coefficient** is therefore:

$$c_i = \frac{\Delta f}{\Delta x_i}$$

Once the standard uncertainties (x_i) and the sensitivity coefficients (c_i) have been determined, these may then be combined in order to provide a single value of the uncertainty in the value (y) of the measurand (Y). This is known as the **combined standard uncertainty** ($u_c(y)$) and it may be calculated by summing the squares of the individual standard uncertainties and then taking the square root of the result, thus:

$$u_c(y) = \sqrt{\sum_{i=1}^{n} c_i^2 u^2(x_i)}$$

or: $$u_c(y) = \sqrt{c_1^2 u^2(x_1) + c_2^2 u^2(x_2) + c_3^2 u^2(x_3) + ... c_n^2 u^2(x_n)}$$

To simplify both the uncertainty calculations and their subsequent presentation, it is convenient to set out the process in tabular form as shown in Table D1. The various sources of uncertainties (the inputs) are listed in the first column and their respective uncertainty values, probability distributions and sensitivity coefficients are noted in the following columns. For each row, the standard uncertainty is determined and noted in the final column. In the final row, the combined standard uncertainty is calculated using the expressions shown above and the form of its probability distribution determined based upon those of its input terms.

In accordance with the central limit theorem, a combined standard uncertainty based upon a number of varying probability distributions tends to the form of a normal distribution. As the various input uncertainties were expressed in terms of a standard uncertainty, the resulting normal distribution is expressed as one standard deviation. A range of ±1 standard deviation encompasses around 68% of the area under the curve, which means that there is about 68% confidence that the measured value lies within these limits (i.e. a 68% **coverage probability**).

Table D1: Example combined standard uncertainty calculation table

Source of uncertainty	**Value ±**	**Probability distribution (divisor)**	**Sensitivity coefficient c_i**	**Standard uncertainty $u_i(y)$**
X_1	a_1	Rectangular ($\sqrt{3}$)	c_1	$u_1(y)^2 = a_1/\sqrt{3} \times c_1$
X_2	a_2	Rectangular ($\sqrt{3}$)	c_2	$u_2(y)^2 = a_2/\sqrt{3} \times c_2$
$u_c(y)$	-	Rectangular	-	$u_c(y) = \sqrt{(u_1(y)^2 + u_2(y)^2)}$

Where a higher degree of confidence associated with an uncertainty is required, the **expanded uncertainty** (U) may be calculated. This is done by multiplying the combined standard uncertainty by a **coverage factor** (k), thus:

$$U = k \cdot u_c(y)$$

Accepted practice is to use a coverage factor of two to calculate the expanded uncertainty for normal distributions in order to give a confidence of approximately 95% that the measured values lies within these limits. (It is noted that k = 2.00 actually gives a coverage probability of 95.45%; for 95% exactly, k = 1.96 should be used but the difference is generally not significant in practice). A range of coverage factors with their respective coverage probabilities are given in Table D2 below.

Table D2: Alternative coverage factors and the resulting coverage probabilities (source: UKAS, 2007)

Coverage factor (k)	Coverage probability
1.00	68.27%
1.64	90%
1.96	95%
2.00	95.45%
2.58	99%
3.00	99.73%

Once the expanded uncertainty has been calculated for a given experimental measurement, the magnitude of the measurand (y) and expanded uncertainty (U) should be reported in the form of y ± U. The UKAS document recommends that this result is accompanied by the following statement (for example, when the typical 95% coverage probability has been employed):

> *"The reported expanded uncertainty is based on a standard uncertainty multiplied by a coverage factor k = 2, providing a coverage probability of approximately 95%. The uncertainty evaluation has been carried out in accordance with UKAS requirements".*

The calculated expanded uncertainties will vary between measurements if any of the relationships between the input quantities are non-linear (the sensitivity coefficients will vary depending upon where on the scales the measurements are made). However, for more complicated experiments such as the current naphthalene sublimation work, it may not be feasible to calculate specific expanded uncertainties for every case because of the number of calculations this would entail. In such cases, it may be sufficient to determine the expanded uncertainty for a typical measurement in order to obtain an approximate ‘feel’ for the uncertainties in the more general results.

Annex D3 – Calculation of uncertainty in the CHTC values

An analysis of the measurement uncertainty for the value of the convective heat transfer coefficient determined using the naphthalene sublimation technique has been conducted using the previously described GUM methodology. Experiment number 2 (see Annex F and Annex G for further details) was selected as providing a typical set of measurements with which to perform the analysis. This experimental setup modelled a long street canyon of height-to-width ratio of a half which was aligned perpendicular to the approaching flow at a relatively low wind speed. The significant measurements taken during this experiment are reproduced for ease of reference in Table D3 below.

Table D3: Measurements taken during Experiment 2

Measurement	Value
Change in thickness	283 µm
Run time	3 hrs
Water temperature	40.0 °C (292.0 K)
Air temperature	18.8 °C (313.2 K)
Atmos. pressure	101250 Pa
Model length	0.094 m

The value used for the change in thickness of the naphthalene coating during the experimental run time is the average over the front (windward) surface of the model. Other derived measurements (for example, the naphthalene vapour density and dynamic viscosity of air) were determined using the calculation spreadsheet shown in Annex E based upon the above environmental factors.

The 'best estimate' value of the convective heat transfer coefficient calculated for this experiment is 36.4 $W.m^{-2}K^{-1}$.

Kinematic viscosity of air

The kinematic viscosity of air (v_a) may be calculated from the following equation:

$$v_a = \frac{0.1556}{10000} \times \left(\frac{\theta_a}{298.16} \right)^{1.7774} \left(\frac{101300}{P_{atm}} \right) \quad m^2 s^{-1}$$

thus: $v_a = f(\theta_a, P_{atm})$

Air temperature:

The manufacturers stated accuracy of the *Rotronic Hygrolog-D* digital thermometer used to measure air temperature (θ_a) is ±0.3 °C. A rectangular probability distribution is assumed as no data is available regarding where within these limits a reading is likely to lie.

If the uncertainty in the air temperature is ±0.3°C, the resulting value for the kinematic viscosity could be between:

$$v_a = \frac{0.1556}{10000} \times \left(\frac{292.0 + 0.3}{298.16} \right)^{1.7774} \left(\frac{101300}{101250} \right) = 1.503 \times 10^{-5} \text{ m}^2\text{s}^{-1}$$

and: $$v_a = \frac{0.1556}{10000} \times \left(\frac{292.0 - 0.3}{298.16} \right)^{1.7774} \left(\frac{101300}{101250} \right) = 1.497 \times 10^{-5} \text{ m}^2\text{s}^{-1}$$

A change of ±0.3 °C in the air temperature thereby results in a change of 0.006×10^{-5} m^2s^{-1} in the value of the kinematic viscosity. The sensitivity coefficient is calculated from the change in the kinematic viscosity (0.006×10^{-5} m^2s^{-1}) divided by the total change in the air temperature (0.6 °C) which equals 1.0×10^{-7} m^2s^{-1} per °C.

Atmospheric pressure:

The manufacturers stated accuracy of the *Prosser Weathertrend* digital barometer used to measure atmospheric air pressure (P_{atm}) is ±100 Pa (±1 mb). A rectangular probability distribution is assumed as no data is available regarding where within these limits a reading is likely to lie.

If the uncertainty in the atmospheric pressure is ±100 Pa, the resulting value for the kinematic viscosity could be between:

$$v_a = \frac{0.1556}{10000} \times \left(\frac{292.0}{298.16} \right)^{1.7774} \left(\frac{101300}{101250 + 100} \right) = 1.499 \times 10^{-5} \text{ m}^2\text{s}^{-1}$$

and: $$v_a = \frac{0.1556}{10000} \times \left(\frac{292.0}{298.16} \right)^{1.7774} \left(\frac{101300}{101250 - 100} \right) = 1.502 \times 10^{-5} \text{ m}^2\text{s}^{-1}$$

A change of ±100 Pa in the atmospheric pressure thereby results in a change of 0.003×10^{-5} m^2s^{-1} in the value of the kinematic viscosity. The sensitivity coefficient is calculated from the change in the kinematic viscosity (0.003×10^{-5} m^2s^{-1}) divided by the total change in the atmospheric pressure (200 Pa) which equals 1.5×10^{-10} m^2s^{-1} per Pa.

Calculation of combined standard uncertainty:

The combined standard uncertainty for the kinematic viscosity of air is calculated in Table D4 below.

Table D4: The combined standard uncertainty for the kinematic viscosity of air

Source of uncertainty	**Value ±**	**Probability distribution (divisor)**	**Sensitivity coefficient c_i**	**Standard uncertainty $u_i(y)$**
Air temperature	0.3 °C	Rectangular ($\sqrt{3}$)	$1.0\text{x}10^{-7}$ m^2s^{-1} per °C	$0.3/\sqrt{3} \times 1.0\text{x}10^{-7} = 1.732\text{x}10^{-8}$ m^2s^{-1}
Atmospheric pressure	100 Pa	Rectangular ($\sqrt{3}$)	$1.5\text{x}10^{-10}$ m^2s^{-1} per Pa	$100/\sqrt{3} \times 1.5\text{x}10^{-10} = 8.660\text{x}10^{-9}$ m^2s^{-1}
Combined standard uncertainty	-	Rectangular	-	$\sqrt{((1.732\text{x}10^{-8})^2 + (8.660\text{x}10^{-9})^2)} = 1.936\text{x}10^{-8}$ m^2s^{-1}

The combined standard uncertainty in the value of the kinematic viscosity of air is therefore **$\pm 1.936\text{x}10^{-8}$ m^2s^{-1}**. This uncertainty is of the order of 10^3 smaller than the typical value of the kinematic viscosity ($1.500\text{x}10^{-5}$ m^2s^{-1}). A rectangular probability distribution is assumed as the uncertainty calculation was based upon two sources of uncertainty which themselves have rectangular probability distributions.

Prandtl number

The non-dimensional Prandtl number (Pr) may be calculated from the following equation:

$$\text{Pr} = \frac{v}{k}$$

thus: $\text{Pr} = f(v,k)$

Kinematic viscosity of air:

The combined standard uncertainty in the value of the kinematic viscosity of air (v_a) was calculated previously to be $\pm 1.936\text{x}10^{-8}$ m^2s^{-1} and a rectangular probability distribution is assumed as the uncertainty calculation was based upon the combination of two rectangular probability distributions (i.e. those of air temperature and atmospheric air pressure).

If the uncertainty in the kinematic viscosity of air is $\pm 1.936\text{x}10^{-8}$ m^2s^{-1}, the resulting value for the Prandtl number could be between:

$$\text{Pr} = \frac{\left(1.500\times10^{-5} + 1.936\times10^{-8}\right)}{2.087\times10^{-5}} = 7.197\times10^{-1}$$

and: $\mathrm{Pr} = \frac{\left(1.500\times10^{-5} - 1.936\times10^{-8}\right)}{2.087\times10^{-5}} = 7.178\times10^{-1}$

A change of ±1.936x10^{-8} m^{2}s^{-1} in the kinematic viscosity of air thereby results in a change of 0.019x10^{-1} in the value of the Prandtl number. The sensitivity coefficient is calculated from the change in the Prandtl number (0.019x10^{-1}) divided by the total change in the kinematic viscosity of air (3.872x10^{-8} m^{2}s^{-1}) which equals 49070.248 per m^{2}s^{-1}.

Thermal diffusivity of air:

The value of the thermal diffusivity of air (k_a) is calculated based upon properties of air which do not vary during the measurements (thermal conductivity, specific heat capacity and density). It is therefore not subject to any experimental error and hence not included in the calculation of the combined standard uncertainty of the Prandtl number.

Calculation of combined standard uncertainty:

The combined standard uncertainty for the Prandtl number is calculated in Table D5 below.

Table D5: The combined standard uncertainty for the Prandtl number

Source of uncertainty	**Value ±**	**Probability distribution (divisor)**	**Sensitivity coefficient c_i**	**Standard uncertainty $u_i(y)$**
Kinematic viscosity	1.936 x10^{-8} m^{2}s^{-1}	Rectangular (√ 3)	49070.248 per m^{2}s^{-1}	1.936x10^{-8}/√ 3 x 49070.248 **= 5.485x10^{-4}**
Combined standard uncertainty	-	Rectangular	-	√ ((5.485x10^{-4})^2) = **5.485x10^{-4}**

The combined standard uncertainty in the value of the Prandtl number is therefore **±5.485x10^{-4}**. This uncertainty is of the order of 10^3 smaller than the typical value of the Prandtl number (0.719). A rectangular probability distribution is assumed as the uncertainty calculation was based upon only the thermal diffusivity of air which itself has been shown to have a rectangular probability distribution.

Schmidt number

The Schmidt number (Sc) may be calculated from the following equation:

$$\mathrm{Sc} = 2.28\times\left(\frac{\theta_a}{298.16}\right)^{-0.1526}$$

thus: $\mathrm{Sc} = f(\theta_a)$

Air temperature:

The manufacturers stated accuracy of the *Rotronic Hygrolog-D* digital thermometer used to measure air temperature (θ_a) is ±0.3 °C. A rectangular probability distribution is assumed as no data is available regarding where within these limits the reading is likely to lie.

If the uncertainty in the air temperature is ±0.3 °C, the resulting value for the thermal diffusivity could be between:

$$Sc = 2.28 \times \left(\frac{292.0 + 0.3}{298.16} \right)^{-0.1526} = 2.287$$

and: $$Sc = 2.28 \times \left(\frac{292.0 - 0.3}{298.16} \right)^{-0.1526} = 2.288$$

A change of ±0.3 °C in the air temperature thereby results in a change of 0.001 in the value of the Schmidt number. The sensitivity coefficient is calculated from the change in the Schmidt number (0.001) divided by the total change in the air temperature (0.6 °C) which equals 1.667×10^{-3} per °C.

Calculation of combined standard uncertainty:

The combined standard uncertainty for the Schmidt number is calculated in Table D6 below.

Table D6: The combined standard uncertainty for the Schmidt number

Source of uncertainty	**Value ±**	**Probability distribution (divisor)**	**Sensitivity coefficient c_i**	**Standard uncertainty $u_i(y)$**
Air temperature	0.3 °C	Rectangular ($\sqrt{3}$)	1.667×10^{-3} per °C	$0.3/\sqrt{3} \times 1.667 \times 10^{-3} = 2.887 \times 10^{-4}$
Combined standard uncertainty	-	Rectangular	-	$\sqrt{((2.887 \times 10^{-4})^2)} =$ **2.887×10^{-4}**

The combined standard uncertainty in the value of the Schmidt number is therefore **$\pm 2.887 \times 10^{-4}$**. This uncertainty is of the order of 10^4 smaller than the typical value of the Schmidt number (2.287). A rectangular probability distribution is assumed as the uncertainty calculation was based upon only the air temperature which itself has a rectangular probability distribution.

Saturated vapour pressure of naphthalene

The saturated vapour pressure of naphthalene in air (P) may be calculated using the following equation:

$$\theta_n \log P = \left({}^{a_0}\!/_{2} + \sum a_x E_x \right)$$

where: $E_1 = x$ and: $a_0 = 301.6247$

$E_2 = 2x^2 - 1$ $a_1 = 791.4937$

$E_3 = 4x^2 - 3x$ $a_2 = -8.2536$

$x = \frac{(2\theta - 574)}{114}$ $a_3 = 0.4043$

thus: $P = f(\theta_n)$

In the current experiments, the temperature of the naphthalene coating on the model (θ_n) is dependent upon the temperature of the heated water (θ_w) which is pumped through the hollow model. It is assumed that the two temperatures are equivalent (i.e. that $\theta_n = \theta_w$).

Model (water) temperature:

The manufacturers stated accuracy of the digital temperature control system in the 'Memmert WB14' water bath used to supply heated water to the hollow model is ±0.5 °C. A rectangular probability distribution is assumed as no data is available regarding where within these limits a reading is likely to lie.

If the uncertainty in the model (water) temperature is ±0.5 °C, the resulting value for the saturated vapour pressure of naphthalene could be between:

$$P = f(\theta_w + 0.5) = 47.436 \text{ Pa}$$

and: $P = f(\theta_w - 0.5) = 43.443$ Pa

Note that the individual calculations have not been shown above as these are lengthy; an example calculation is shown in full in Annex C if required.

A change of ±0.5 °C in the model temperature thereby results in a change of 3.993 Pa in the saturated vapour pressure of the naphthalene coating. The sensitivity coefficient is calculated from the change in the vapour pressure (3.993 Pa) divided by the total change in the air temperature (1.0 °C) which equals 3.993 Pa per °C.

Calculation of combined standard uncertainty:

The combined standard uncertainty for the saturated vapour pressure of naphthalene is calculated in Table D7.

Table D7: The combined standard uncertainty for the saturated vapour pressure

Source of uncertainty	**Value ±**	**Probability distribution (divisor)**	**Sensitivity coefficient c_i**	**Standard uncertainty $u_i(y)$**
Model (water) temperature	0.5 °C	Rectangular ($\sqrt{3}$)	3.993 Pa per °C	0.5/$\sqrt{3}$ x 3.993 = 1.153 Pa
Combined standard uncertainty	-	Rectangular	-	$\sqrt{(1.153^2)}$ = 1.153 Pa

The combined standard uncertainty in the value of the saturated vapour pressure of naphthalene is therefore **±1.153 Pa**. This uncertainty is of the order of 2.5% of the typical value for the saturated vapour pressure (45.399 Pa) and is therefore the most significant source of uncertainty examined so far. However, it is still to be seen how this uncertainty will propagate through the calculation of the mass transfer coefficient and Sherwood number to the ultimate value of the convective heat transfer coefficient.

A rectangular probability distribution is assumed as the uncertainty calculation was based upon only the model (water) temperature which itself has a rectangular probability distribution.

Naphthalene vapour density

The naphthalene vapour density (ρ_v) may be calculated from the following equation:

$$\rho_v = \frac{P}{R_n \times \theta_n}$$

thus: $\rho_v = f(P, R_n, \theta_n)$

In the current experiments, the temperature of the naphthalene coating on the model (θ_n) is dependent upon the temperature of the heated water (θ_w) which is pumped through the hollow model. It is assumed that the two temperatures are equivalent (i.e. that $\theta_n = \theta_w$).

Naphthalene saturated vapour pressure:

The combined standard uncertainty in the value of the saturated vapour pressure of naphthalene (P) was calculated previously to be ±1.153 Pa. A rectangular probability distribution was assumed as the uncertainty calculation was based upon only the model (water) temperature which itself has a rectangular probability distribution.

If the uncertainty in the saturated vapour pressure is ±1.153 Pa, the resulting value for the naphthalene vapour density could be between:

$$\rho_v = \frac{(45.399 + 1.153)}{64.89 \times 313.2} = 2.291 \times 10^{-3} \text{ kg.m}^{-3}$$

and: $$\rho_v = \frac{(45.399 - 1.153)}{64.89 \times 313.2} = 2.177 \times 10^{-3} \text{ kg.m}^{-3}$$

A change of ±1.153 Pa in the naphthalene saturated vapour pressure thereby results in a change of 1.140×10^{-4} kg.m^{-3} in the vapour density. The sensitivity coefficient is calculated from the change in the vapour density (1.140×10^{-4} kg.m^{-3}) divided by the total change in the saturated vapour pressure (2.306 Pa) which equals 4.944×10^{-5} kg.m^{-3} per Pa.

Naphthalene gas constant:

The value of the gas constant for naphthalene (R_n) is assumed to be fixed at 64.89 Jkg^{-1}K^{-1}. It is therefore not subject to any experimental error and hence not included in the calculation of the combined standard uncertainty of the mass transfer coefficient.

Model (water) temperature:

The manufacturers stated accuracy of the digital temperature control system in the *Memmert WB14* heated water bath used to measure air temperature is ±0.5 °C. A rectangular probability distribution is assumed as no data is available regarding where within these limits the reading is likely to lie.

If the uncertainty in the model (water) temperature is ±0.5 °C, the resulting value for the naphthalene vapour density could be between:

$$\rho_v = \frac{45.399}{64.89 \times (313.2 + 0.5)} = 2.230 \times 10^{-3} \text{ kgm}^{-3}$$

and: $$\rho_v = \frac{45.399}{64.89 \times (313.2 - 0.5)} = 2.237 \times 10^{-3} \text{ kgm}^{-3}$$

A change of ±0.5 °C in the model (water) temperature thereby results in a change of 0.007×10^{-3} kg.m^{-3} in the vapour density of the naphthalene coating. The sensitivity coefficient is calculated from the change in the vapour density (0.007×10^{-3} kg.m^{-3}) divided by the total change in the model temperature (1.0 °C) which equals 7.0×10^{-6} kg.m^{-3} per °C.

Calculation of combined standard uncertainty:

The combined standard uncertainty for the Schmidt number is calculated in Table D8 below.

Table D8: The combined standard uncertainty for the naphthalene vapour density

Source of uncertainty	**Value ±**	**Probability distribution (divisor)**	**Sensitivity coefficient c_i**	**Standard uncertainty $u_i(y)$**
Saturated vapour pressure	1.153 Pa	Rectangular ($\sqrt{3}$)	4.944×10^{-5} $kg.m^{-3}$ per Pa	$1.153/\sqrt{3} \times 4.944 \times 10^{-5} = 3.291 \times 10^{-5}$
Model (water) temperature	0.5 °C	Rectangular ($\sqrt{3}$)	7.0×10^{-6} $kg.m^{-3}$ per °C	$0.5/\sqrt{3} \times 7.0 \times 10^{-6} = 2.021 \times 10^{-6}$
Combined standard uncertainty	-	Rectangular	-	$\sqrt{((3.291 \times 10^{-5})^2 + (2.021 \times 10^{-6})^2)} = 3.297 \times 10^{-5}$

The combined standard uncertainty in the value of the naphthalene vapour density is therefore **$\pm 3.297 \times 10^{-5}$ $kg.m^{-3}$**. A rectangular probability distribution is assumed as the uncertainty calculation was based upon measurements which themselves each have rectangular probability distributions.

Mass transfer coefficient

The local mass transfer coefficient (h_m) may be calculated from the following equation:

$$h_m = \frac{\partial T \times \rho_n}{t \times \rho_v}$$

thus: $h_m = f(\partial T, \rho_n, t, \rho_v)$

Change in naphthalene coating thickness:

The manufacturers stated accuracy of the *Elcometer 456 coating thickness gauge* is ±2.5 µm. A rectangular probability distribution is assumed as no data is available regarding where within these limits the reading is likely to lie. However, the change in the naphthalene coating thickness (δT) is calculated based upon the difference between two sets of measurements. Both of these measurements will have an associated rectangular probability distribution of equal size. So when their difference is taken, the resulting probability distribution will be triangular with a semi-range of twice that of the original rectangular distributions. Therefore a triangular probability distribution is assumed for the change in naphthalene coating thickness of semi-range 2 x ±2.5 µm = ±5.0 µm.

If the uncertainty in the change of thickness measurement is ±5.0 µm, the resulting value for the mass transfer coefficient could be between:

$$h_m = \frac{(0.000283 + 0.000005) \times 1175.0)}{3 \times 0.0022338} = 50.497 \text{ m.hr}^{-1}$$

and: $h_m = \frac{(0.000283 - 0.000005) \times 1175.0)}{3 \times 0.0022338} = 48.744 \text{ m.hr}^{-1}$

A change of ±5.0 µm in the change in coating thickness thereby results in a change of 1.753 $m.hr^{-1}$ in the value of the mass transfer coefficient. The sensitivity coefficient is calculated from the change in the mass transfer coefficient (1.753 $m.hr^{-1}$) divided by the total change in the naphthalene coating thickness (10 µm) which equals 1.753×10^{-1} $m.hr^{-1}$ per µm.

Naphthalene density at the surface:

The value of the naphthalene density at the surface (ρ_n) is assumed to be fixed at 1175.0 kg/m^3. It is therefore not subject to any experimental error and hence not included in the calculation of the combined standard uncertainty of the mass transfer coefficient.

Experimental run time:

Control of the experimental run time depends upon many factors including the time taken for the wind tunnel to stop and the time to remove the model and make the measurements, etc. It has been estimated at ±5 min (±0.0833 hrs) and a rectangular probability distribution is assumed as it is equally likely that the actual run time could fall anyway within these limits.

If the uncertainty in the run time is ±0.0833 hours, the resulting value for the mass transfer coefficient could be between:

$$h_m = \frac{0.000283 \times 1175.0}{(3 + 0.0833) \times 0.0022338} = 48.280 \text{ mhr}^{-1}$$

and: $$h_m = \frac{0.000283 \times 1175.0}{(3 - 0.0833) \times 0.0022338} = 51.037 \text{ mhr}^{-1}$$

A change of ±0.0833 hours in the experimental run time thereby results in a change of 2.757 $m.hr^{-1}$ in the value of the mass transfer coefficient. The sensitivity coefficient is calculated from the change in the mass transfer coefficient (2.757 $m.hr^{-1}$) divided by the total change in the experimental run time (0.1666 hours) which equals 16.549 $m.hr^{-1}$ per hour.

Naphthalene vapour density:

The combined standard uncertainty in the value of the naphthalene vapour density (ρ_v) was previously calculated to be $\pm 3.297 \times 10^{-5}$ $kg.m^{-3}$. A rectangular probability distribution was assumed as the uncertainty calculation was based upon measurements which both had rectangular probability distributions.

If the uncertainty in the naphthalene vapour density is $\pm 3.297 \times 10^{-5}$ $kg.m^{-3}$, the resulting value for the mass transfer coefficient could be between:

$$h_m = \frac{0.000283 \times 1175.0}{3 \times (0.0022338 + 3.297 \times 10^{-5})} = 48.899 \text{ mhr}^{-1}$$

and: $$h_m = \frac{0.000283 \times 1175.0}{3 \times (0.0022338 - 3.297 \times 10^{-5})} = 50.364 \text{ mhr}^{-1}$$

A change of ±3.297x10^{-5} kg.m^{-3} in the naphthalene vapour density thereby results in a change of 1.465 m.hr^{-1} in the value of the mass transfer coefficient. The sensitivity coefficient is calculated from the change in the mass transfer coefficient (1.465 m.hr^{-1}) divided by the total change in the naphthalene vapour density (6.594x10^{-5} kg.m^{-3}) which equals 22217.167 m.hr^{-1} per kg.m^{-3}.

Calculation of combined standard uncertainty:

The combined standard uncertainty for the mass transfer is calculated in Table D9 below.

Table D9: The combined standard uncertainty for the mass transfer coefficient

Source of uncertainty	**Value ±**	**Probability distribution (divisor)**	**Sensitivity coefficient c_i**	**Standard uncertainty $u_i(y)$**
Change in thickness	5.0 µm	Triangular (√ 6)	1.753x10^{-1} m.hr^{-1} per µm	(5.0/√ 6) x 1.753x10^{-1} = 0.358 m.hr^{-1}
Experiment run time	0.0833 hr	Rectangular (√ 3)	16.549 m.hr^{-1} per hr	(0.0833/√ 3) x 16.549 = 0.796 m.hr^{-1}
Vapour density	3.297 x10^{-5} kg.m^{-3}	Rectangular (√ 3)	22217.167 m.hr^{-1} per kg.m^{-3}	(3.297x10^{-5}/√ 3) x 22217.167 = 0.423 m.hr^{-1}
Combined standard uncertainty	-	Normal	-	√ (0.358^2 + 0.796^2 + 0.423^2) = 0.970 m.hr^{-1}

The combined standard uncertainty in the value of mass transfer coefficient is therefore **±0.970 m.hr^{-1}**. The combination of the triangular and rectangular probability distributions of approximately equal dominance results in an assumed normal probability distribution for the combined standard uncertainty in the mass transfer coefficient in accordance with central limit theory.

Sherwood number

The non-dimensional Sherwood number (Sh) may be calculated from the following formula:

$$Sh = \frac{h_m \times L}{D}$$

thus: $Sh = f(h_m, L, D)$

Mass transfer coefficient:

The combined standard uncertainty in the value of the mass transfer coefficient (h_m) was calculated above to be ±0.970 m.hr^{-1} and a normal probability distribution is assumed.

If the uncertainty in the change of thickness measurement is ±0.970 m.hr^{-1}, the resulting value for mass transfer coefficient could be between:

$$\text{Sh} = \frac{(49.620 + 0.970) \times 0.094}{0.02324} = 204.624$$

and: $$\text{Sh} = \frac{(49.620 - 0.970) \times 0.094}{0.02324} = 196.777$$

A change of ±0.970 m.hr^{-1} in the mass transfer coefficient thereby results in a change of 7.847 in the value of the Sherwood number. The sensitivity coefficient is calculated from the change in the Sherwood number (7.847) divided by the total change in the mass transfer coefficient (1.940 m.hr^{-1}) which equals 4.045 per m.hr^{-1}.

Length of model:

The length of the wind tunnel model was measured to ±0.5 mm. A rectangular probability distribution is assumed as no data is available regarding where within these limits a reading is likely to lie.

If the uncertainty in the length is ±0.5 mm, the resulting value for the Sherwood number could be between:

$$\text{Sh} = \frac{49.620 \times (0.094 + 0.0005)}{0.02324} = 201.768$$

and: $$\text{Sh} = \frac{49.620 \times (0.094 - 0.0005)}{0.02324} = 199.633$$

A change of ±0.5 mm in the length of the wind tunnel model thereby results in a change of 2.135 in the value of the Sherwood number. The sensitivity coefficient is calculated from the change in the Sherwood number (2.135) divided by the total change in the atmospheric air pressure (1.0 mm) which equals 2.135 per mm.

Naphthalene mass diffusivity coefficient:

The value for the mass diffusivity constant for naphthalene (D) is taken from tables which provide values correct to ±0.0008 m^{2}hr^{-1}. A rectangular probability distribution is assumed as no data is available regarding where within these limits a value is likely to lie.

If the uncertainty in the mass diffusivity is ±0.0008 m^{2}hr^{-1}, the resulting value for the Sherwood number could be between:

$$\text{Sh} = \frac{49.620 \times 0.094}{(0.02324 + 0.0008)} = 194.022$$

and: $$\text{Sh} = \frac{49.620 \times 0.094}{(0.02324 - 0.0008)} = 207.856$$

A change of ±0.0008 m^2hr^{-1} in the mass diffusivity coefficient thereby results in a change of 13.834 in the value of the Sherwood number. The sensitivity coefficient is calculated from the change in the Sherwood number (13.834) divided by the total change in the atmospheric air pressure (0.0016 m^2hr^{-1}) which equals 8646.250 per m^2hr^{-1}.

Calculation of combined standard uncertainty:

The combined standard uncertainty for the Sherwood number is calculated in Table D10 below.

Table D10: The combined standard uncertainty for the Sherwood number

Source of uncertainty	**Value ±**	**Probability distribution (divisor)**	**Sensitivity coefficient c_i**	**Standard uncertainty $u_i(y)$**
Mass transfer coefficient	0.970 $m.hr^{-1}$	Normal (√ 1)	4.045 per $m.hr^{-1}$	0.970/√ 1 x 4.045 = 3.924
Length of model	0.5 mm	Rectangular (√ 3)	2.135 per mm	0.5/√ 3 x 2.135 = 0.616
Mass diffusivity constant	0.0008 m^2hr^{-1}	Rectangular (√ 3)	8646.250 per m^2hr^{-1}	0.0008/√ 3) x 8646.250 = 3.994
Combined standard uncertainty	-	Normal	-	√ (3.924^2 + 0.616^2 + 3.994^2) = 5.633

The combined standard uncertainty in the value of the Sherwood number is therefore **±5.633**. The combination of the normal and rectangular probability distributions results in an approximate normal probability distribution for the combined standard uncertainty in the value of the Sherwood number in accordance with the central limit theorem.

Nusselt number

The non-dimensional Nusselt number (Nu) may be calculated from the following formula:

$$\mathrm{Nu} = \left(\frac{\mathrm{Pr}}{\mathrm{Sc}}\right)^n \times \mathrm{Sh}$$

thus: $\mathrm{Nu} = f(\mathrm{Pr},\mathrm{Sc},\mathrm{Sh})$

Prandtl number:

The combined standard uncertainty in the value of the Prandtl number was previously calculated to be ±5.485x10^{-4} and a rectangular probability distribution was assumed.

If the uncertainty in the Prandtl number is ±5.485x10^{-4}, the resulting value for the Nusselt number could be between:

$$\mathrm{Nu} = \left(\frac{0.719 + 5.485 \times 10^{-4}}{2.287} \right)^{0.34} \times 200.701 = 135.456$$

and: $$\mathrm{Nu} = \left(\frac{0.719 - 5.485 \times 10^{-4}}{2.287} \right)^{0.34} \times 200.701 = 135.386$$

A change of ±5.485x10^{-4} in the Prandtl number thereby results in a change of 0.070 in the value of the Nusselt number. The sensitivity coefficient is calculated from the change in the Nusselt number (0.070) divided by the total change in the Prandtl number (1.097x10^{-3}) which equals 63.810.

Schmidt number:

The combined standard uncertainty in the value of the Schmidt number was previously calculated to be ±2.887x10^{-4} and a rectangular probability distribution was assumed.

If the uncertainty in the Schmidt number is ±2.887x10^{-4}, the resulting value for the Nusselt number could be between:

$$\mathrm{Nu} = \left(\frac{0.719}{2.287 + 2.887 \times 10^{-4}} \right)^{0.34} \times 200.701 = 135.415$$

and: $$\mathrm{Nu} = \left(\frac{0.719}{2.287 - 2.887 \times 10^{-4}} \right)^{0.34} \times 200.701 = 135.427$$

A change of ±2.887x10^{-4} in the Schmidt number thereby results in a change of 0.012 in the value of the Nusselt number. The sensitivity coefficient is calculated from the change in the Nusselt number (0.012) divided by the total change in the Schmidt number (5.774x10^{-4}) which equals 20.783.

Sherwood number:

The combined standard uncertainty in the value of the Sherwood number was previously calculated to be ±5.633 and a normal probability distribution is assumed.

If the uncertainty in the run time is ±5.633, the resulting value for the Nusselt could be between:

$$\mathrm{Nu} = \left(\frac{0.719}{2.287} \right)^{0.34} \times (200.701 + 5.633) = 139.222$$

and: $\mathrm{Nu} = \left(\frac{0.719}{2.287}\right)^{0.34} \times (200.701 - 5.633) = 131.620$

A change of ±5.633 in the Sherwood number thereby results in a change of 7.602 in the value of the Nusselt number. The sensitivity coefficient is calculated from the change in the Nusselt number (7.602) divided by the total change in the Sherwood number (11.266) which equals 0.675.

Calculation of combined standard uncertainty:

The combined standard uncertainty for the Nusselt number is calculated in Table D11 below.

Table D11: The combined standard uncertainty for the Nusselt number

Source of uncertainty	**Value ±**	**Probability distribution (divisor)**	**Sensitivity coefficient c_i**	**Standard uncertainty $u_i(y)$**
Prandtl number	5.485 x10^{-4}	Rectangular (√ 3)	63.810	5.485x10^{-4}/√ 3 x 63.810 = 0.020
Schmidt number	2.887 x10^{-4}	Rectangular (√ 3)	20.783	2.887x10^{-4}/√ 3 x 20.783 = 0.003
Sherwood number	5.633	Normal (√ 1)	0.675	5.633/√ 1 x 0.675 = 3.802
Combined standard uncertainty	-	Normal	-	√ (0.020^2 + 0.003^2 + 3.802^2) = 3.802

The combined standard uncertainty in the value of the Nusselt number is therefore **±3.802**. The combination of the normal (most significant) and rectangular probability distributions result in an approximate normal probability distribution for the combined standard uncertainty in accordance with the central limit theorem.

Convective heat transfer coefficient

The convective heat transfer coefficient (h_c) may be calculated from the following formula:

$$h_c = \frac{\mathrm{Nu} \times K_a}{L}$$

thus: $h_c = f(\mathrm{Nu}, K_a, L)$

Nusselt number:

The combined standard uncertainty in the value of the Nusselt number (Nu) was previously calculated to be ±3.802 and a normal probability distribution was assumed.

If the uncertainty in the change of thickness measurement is ±3.802, the resulting value for the convective heat transfer coefficient could be between:

$$h_c = \frac{(135.421 + 3.802) \times 0.02526}{0.094} = 37.412 \ \ Wm^{-2}K^{-1}$$

and: $$h_c = \frac{(135.421 - 3.802) \times 0.02526}{0.094} = 35.369 \ Wm^{-2}K^{-1}$$

A change of ±3.802 in the Nusselt number thereby results in a change of 2.043 in the value of the CHTC. The sensitivity coefficient is calculated from the change in the convective heat transfer coefficient (2.043) divided by the total change in the Nusselt number (7.604) which equals 0.269 $Wm^{-2}K^{-1}$ per Nu.

Thermal conductivity of air:

The value of the thermal conductivity of air (K_a) is taken for various temperatures from the reference text 'The thermodynamic and transport properties of fluids' (Rogers and Mayhew, 1995). It is therefore not subject to any experimental error and hence not included in the calculation of the combined standard uncertainty of the mass transfer coefficient.

Model length:

The length of the wind tunnel model (L) was measured correct to ±0.5 mm and a rectangular probability distribution is assumed.

If the uncertainty in the length is ±0.5 mm, the resulting value for the convective heat transfer coefficient could be between:

$$h_c = \frac{135.421 \times 0.02526}{0.094 + 0.0005} = 36.198 \ \ Wm^{-2}K^{-1}$$

and: $$h_c = \frac{135.421 \times 0.02526}{0.094 - 0.0005} = 36.585 \ \ Wm^{-2}K^{-1}$$

A change of ±0.5 mm in the model length thereby results in a change of 0.387 in the value of the CHTC. The sensitivity coefficient is calculated from the change in the convective heat transfer coefficient (0.387) divided by the total change in the model length (1.0 mm) which equals 0.387 per mm.

Annex D4 - Calculation of combined standard and expanded uncertainties

The combined standard and expanded uncertainties for the CHTC are calculated in Table D12 below.

Table D12: The combined standard and expanded uncertainties for the CHTC

Source of uncertainty	**Value ±**	**Probability distribution (divisor)**	**Sensitivity coefficient c_i**	**Standard uncertainty $u_i(y)$**
Nusselt number	3.802	Normal (√ 1)	0.269	3.802/√ 1 x 0.269 = 1.023 $W.m^{-2}K^{-1}$
Length	0.5 mm	Rectangular (√ 3)	0.387 per mm	0.5/√ 3 x 0.387 = 0.112 $W.m^{-2}K^{-1}$
Combined standard uncertainty	-	Normal	-	√ ($1.023^2 + 0.112^2$) = 1.029 $W.m^{-2}K^{-1}$
Expanded uncertainty	-	Normal (k=2)	-	1.029 x 2 = 2.058 $W.m^{-2}K^{-1}$

The combined standard uncertainty in the value of the convective heat transfer coefficient is therefore ±1.029 $W.m^{-2}K^{-1}$. The combination of the normal (most dominant) and rectangular probability distributions results in a normal probability distribution for the combined standard uncertainty.

The expanded uncertainly (taking k = 2 for 95% confidence level) is ±2.058 $W.m^{-2}K^{-1}$, but this should only be quoted to two significant figures.

The calculated value for the convective heat transfer coefficient is therefore 36.4 ± 2.1 $W.m^{-2}K^{-1}$, which equates to an error of ±5.8%.

Annex E Convective heat transfer coefficient spreadsheet

To simplify and speed the process of calculating the various non-dimensional parameters (and ultimately the convective heat transfer coefficient) from the experimentally obtained data, a multi-sheet spreadsheet was designed using Microsoft Excel. The following images are screenshots of the various worksheets.

Inputs to the calculations are entered in the white boxes. Sub-calculations for each of the parameters are fed back to the main worksheet from each of the following sheets.

Main worksheet

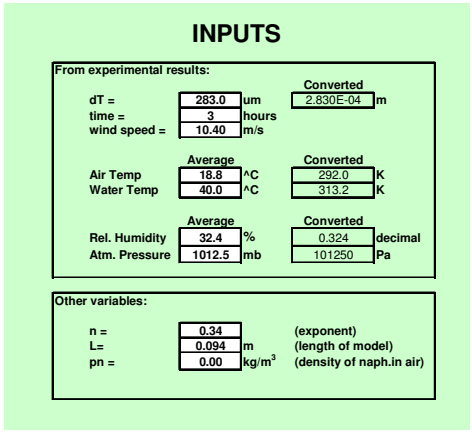

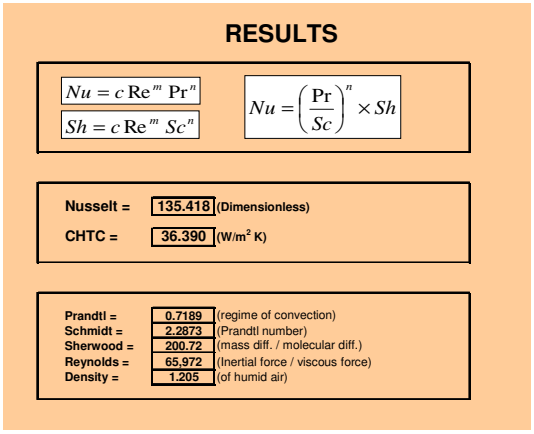

Calculation of Prandtl number worksheet

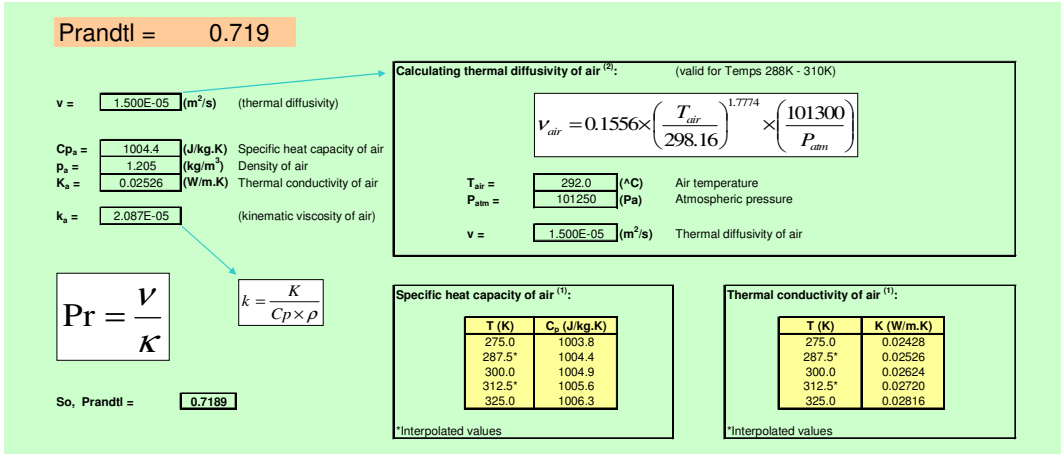

Calculation of Schmidt number worksheet

Schmidt = 2.2873

Calculation of Schmidt number [2]:

T =	292.0	K	Temp.
Schmidt =	2.287		

$$Sc = 2.28 \times \left(\frac{T}{298.16} \right)^{-0.1526}$$

Calculation of Sherwood number worksheet

Sherwood = 200.72

T =	292.0	(K)	Air temp.
ρn =	1175.0	(kg/m^3)	Density of naph.[2]
time =	3	(hours)	Run time
ρv =	0.002234	(kg/m^3)	Naph. vapour density
ρa =	0.00	(kg/m^3)	Density of naph. in the air in WT.
dT =	0.000283	(m)	Change in thickness

$$M = \frac{dT \times \rho_n}{t \times (\rho_v - \rho_a)}$$

M =	49.620	(m/hour)
L =	0.094	(m)
D =	0.02324	(m^2/hour)

$$Sh = \frac{ML}{D}$$

So, Sherwood = 200.72

Calculating naphthalene vapour density:

P =	45.399	(Pa)	Saturated vapour pressure
R =	64.890	(J/kg.K)	Gas constant for naphthalene [2]
T =	313.200	(K)	Temperature of naph.
ρv =	0.0022338		

$$\rho_s = \frac{P}{RT}$$

Values of mass diffusivity coefficient for naphthaene vapour in air [2]:

Temp (K)	D (m^2/hr)
290	0.02324
295	0.02402
300	0.02481
305	0.02561

Calculation of naphthalene vapour pressure worksheet

Pv = 45.399

Saturated vapour pressure of napthalene [2]:

T =	313.2	K
x =	0.459649	
a0 =	301.6247	
a1 =	791.4937	
a2 =	-8.2536	
a3 =	0.4043	
a_1E_1 =	363.8094	
a_2E_2 =	4.766003	
a_3E_3 =	-0.400457	
logP =	1.657048	
P =	45.39913	Pa

$$x = \frac{(2T - 574)}{114}$$

$$E_1(x) = x$$

$$E_2(x) = 2x^2 - 1$$

$$E_3(x) = 4x^3 - 3x$$

$$T \log P = \left(a_0/2 + \sum a_x E_x \right)$$

Calculation of Reynolds number worksheet

Re = 6.597E+04

Note: Reynolds number is NOT used in calculation of Nusselt or CHTC, but is for interest only.

Reynolds number:

t =	292.0	K	air temp.
p =	1.205	(kg/m^3)	density of air
u =	10.40	m/s	wind speed
l =	0.094	m	characteristic length
mu =	1.786E-05	kg/ms	viscosity of air

Dynamic viscosity of air [1]:

T (K)	mu (kg/ms)
275.0	1.725E-05
287.5*	1.786E-05
300.0	1.846E-05
312.5*	1.904E-05
325.0	1.962E-05

*Interpolated values

$$\mathrm{Re} = \frac{\rho u l}{\mu}$$

Calculation of humid air density worksheet

Density = 1.205

t =	292.0	K (Air temperature)
RH =	0.324	(Relative humidity - decimal)
Patm =	101250	Pa (Atmospheric pressure)
Ps =	1704	Pa
Pv =	552.1	Pa
Pa=	100697.9	Pa
Rv =	461.5	Gas constant for vapour (J/kgK) [1]
Ra =	287.1	Gas constant for dry air (J/kgK) [1]

Saturation pressure of water vapour [1]:

T (^C)	Ps (Pa)
273	611
278	872
283	1227
288	1704
293	2337
298	3166
303	4242

density (air) =	1.201	
density (vapour) =	0.004	
So, density (humid air) =	1.205	

$$\rho_{hum} = \frac{P_a}{R_a T} + \frac{P_w}{R_w T}$$

References worksheet

References

Ref 1: Thermodynamic and transport properties of fluids. Rogers and Mayhew.

Ref 2: A review of mass transfer measurements using naphthalene sublimation. Goldstein and Cho.

Annex F Naphthalene sublimation result sheets

To speed the rate of data processing, a spreadsheet was designed using Microsoft Excel which takes the raw output from the Elcometer gauge, processes this data and formats it into a more understandable matter. The experimental details (e.g. temperatures, run-times and model arrangements) were also recorded onto these record sheets.

The Nusselt number and CHTC are directly proportional to the sublimation depth (∂T). Therefore, for each experiment, the Nusselt number and CHTC were calculated using the spreadsheet shown in Annex E for a notional 1 mm sublimation depth. These values could then easily be factored to each of the actual sublimation depths at measurement locations over the model.

The results for each naphthalene sublimation experiment are shown in the worksheet screenshots shown on the following pages. The main experimental details are summarised below in Table D1 and the full (i.e. point by point) data sets are provided in Annex G.

Table F1: Summary of experiments

Experiment number	H/W ratio	Wind speed setting	Wind direction	Run time
1	0.50	45%	0°	3 hrs
2	0.50	30%	0°	3 hrs
3	0.50	15%	0°	3 hrs
4	0.50	45%	0°	2 hrs
5	0.25	45%	0°	2 hrs
6	0.25	15%	0°	3 hrs
7	0.50	45%	0°	3 hrs
8	0.50	45%	90°	2 hrs
9	0.50	45%	45°	2 hrs
10	0.50	15%	45°	3 hrs
11	0.50	30%	45°	3 hrs
12	0.50	15%	90°	3 hrs
13	0.50	30%	90°	3 hrs
14	0.50	0%	n/a	4 hrs
15	0.50	7.5%	90°	3 hrs
16	0.50	60%	90°	1 hrs
17	1.00	45%	90°	3 hrs
18	1.00	15%	90°	3 hrs
19	0.50	30%	90°	2 hrs

Experiment 1

Test Details						
Date:	28/04/2006 PM					
BL Info:	50mm roughness plates, 300mm step, filters and gauzes.					
Pot Setting:	45%					
Speed @ 900mm:	14.761	13.409	13.438	13.525	**Average:**	13.78
Run Time:	3	hrs				
Layout:						
	H/W ratio = 1/2					
	Canyon 11 cubes wide					
	3 upsteam and 3 downstream rows of cubes					
Conditions						
	0	**1**	**2**	**3**	**Average**	
Water:	0	0	0	0	**0.0**	deg C
Air:	23.5	25	25.1	24.8	**24.8**	deg C
Air pressure:	1016	1016	1016	1016	**1016.0**	mbar
R/H:	28.6	26.8	26.6	26.4	**27.0**	%

Location	Average dT	Nusselt	CHTC
	1	1.77859275	0.491951185
Front	131.0	233.03	64.46
1	152.2	270.70	74.87
2	112.9	200.80	55.54
3	136.1	242.07	66.95
4	111.8	198.85	55.00
5	142.1	252.74	69.91
Top	103.9	184.80	51.11
6	135.1	240.29	66.46
7	96.0	170.74	47.23
8	101.5	180.53	49.93
9	81.2	144.42	39.95
10	105.7	188.00	52.00
Back	86.8	154.31	42.68
11	88.4	157.23	43.49
12	81.4	144.78	40.04
13	101.2	179.99	49.79
14	75.2	133.75	36.99
15	87.6	155.80	43.09
All	107.2	190.71	52.75

Experiment 2

Test Details						
Date:	29/04/2006 PM					
BL Info:	50mm roughness plates, 300mm step, filters and gauzes.					
Pot Setting:	30%					
Speed @ 900mm:	10.525	10.417	10.247		**Average:**	10.40
Run Time:	3	hrs				
Layout:						
	H/W ratio = 1/2					
	Canyon 11 cubes wide					
	3 upsteam and 3 downstream rows of cubes					
Conditions						
	0	**1**	**2**	**3**	**Average**	
Water:	40	40	40	40	**40.0**	deg C
Air:	17.9	18.5	19.1	19.6	**18.8**	deg C
Air pressure:	1013	1013	1012	1012	**1012.5**	mbar
R/H:	34.4	32.6	31.8	31.1	**32.4**	%

Location	Average dT	Nusselt	CHTC
	1	0.47458679	0.131268688
Front	283.0	134.31	37.15
1	253.8	120.45	33.32
2	230.2	109.25	30.22
3	263.5	125.05	34.59
4	309.3	146.79	40.60
5	358.2	170.00	47.02
Top	282.1	133.87	37.03
6	373.8	177.40	49.07
7	273.6	129.85	35.92
8	264.2	125.39	34.68
9	248.5	117.93	32.62
10	250.3	118.79	32.86
Back	230.5	109.41	30.26
11	195.5	92.78	25.66
12	219.3	104.08	28.79
13	232.5	110.34	30.52
14	251.1	119.17	32.96
15	254.3	120.69	33.38
All	265.2	125.86	34.81

Experiment 3

Test Details						
Date:	29/04/2006 PM					
BL Info:	50mm roughness plates, 300mm step, filters and gauzes.					
Pot Setting:	15%					
Speed @ 900mm:	5.378	5.277	5.297	5.335	**Average:**	5.32
Run Time:	3	hrs				
Layout:						
	H/W ratio = 1/2					
	Canyon 11 cubes wide					
	3 upsteam and 3 downstream rows of cubes					
Conditions						
	0	**1**	**2**	**3**	**Average**	
Water:	40	40	40	40	**40.0**	deg C
Air:	19.7	20.3	20.5	20.3	**20.3**	deg C
Air pressure:	1012	1011	1010	1010	**1010.7**	mbar
R/H:	31.0	29.4	28.4	27.1	**29.0**	%

Location	Average dT	Nusselt	CHTC
	1	0.464113	0.12837168
Front	222.8	103.40	28.60
1	198.2	91.99	25.44
2	171.2	79.46	21.98
3	212.8	98.76	27.32
4	253.2	117.51	32.50
5	278.6	129.30	35.76
Top	213.4	99.05	27.40
6	279.2	129.58	35.84
7	229.4	106.47	29.45
8	192.2	89.20	24.67
9	176.2	81.78	22.62
10	190.1	88.23	24.40
Back	167.8	77.86	21.54
11	144.7	67.16	18.58
12	149.6	69.43	19.20
13	178.2	82.70	22.88
14	191.2	88.74	24.54
15	175.1	81.27	22.48
All	201.3	93.44	25.84

Experiment 4

Test Details						
Date:	29/04/2006 PM					
BL Info:	50mm roughness plates, 300mm step, filters and gauzes.					
Pot Setting:	45%					
Speed @ 900mm:	14.314	14.091			**Average:**	14.20
Run Time:	2	hrs				
Layout:						
	H/W ratio = 1/2					
	Canyon 11 cubes wide					
	3 upsteam and 3 downstream rows of cubes					
Conditions						
	0	**1**	**2**		**Average**	
Water:	40	40	40		**40.0**	deg C
Air:	20	21.2	21.3		**20.9**	deg C
Air pressure:	1010	1009	1009		**1009.3**	mbar
R/H:	27.7	26.6	26.9		**27.0**	%

Location	Average dT	Nusselt	CHTC
	1	0.69624331	0.192577938
Front	224.5	156.29	43.23
1	193.8	134.93	37.32
2	191.7	133.47	36.92
3	218.3	151.99	42.04
4	248.8	173.23	47.91
5	269.8	187.85	51.96
Top	250.7	174.55	48.28
6	305.7	212.84	58.87
7	245.7	171.07	47.32
8	224.1	156.03	43.16
9	246.7	171.76	47.51
10	231.3	161.04	44.54
Back	213.8	148.88	41.18
11	192.7	134.17	37.11
12	209.0	145.51	40.25
13	216.5	150.74	41.69
14	223.2	155.40	42.98
15	227.8	158.60	43.87
All	229.7	159.91	44.23

Experiment 5

Test Details						
Date:	30/04/2006 AM					
BL Info:	50mm roughness plates, 300mm step, filters and gauzes.					
Pot Setting:	45%					
Speed @ 600mm:	13.423	13.087	12.986	**Average:**	13.17	
Run Time:	2	hrs				
Layout:						
	H/W ratio = 1/4					
	Canyon 11 cubes wide					
	2 upsteam and 2 downstream rows of cubes					
Conditions						
	0	**1**	**2**	**Average**		
Water:	40	40	40	**40.0**	deg C	
Air:	17.9	19.5	20.2	**19.3**	deg C	
Air pressure:	1002	1001	1001	**1001.3**	mbar	
R/H:	35.5	32.0	31.0	**32.6**	%	

Location	Average dT	Nusselt	CHTC
	1	0.71194343	0.196920523
Front	282.2	200.92	55.57
1	250.3	178.20	49.29
2	250.2	178.13	49.27
3	270.2	192.37	53.21
4	299.6	213.30	59.00
5	340.8	242.63	67.11
Top	309.2	220.13	60.89
6	390.4	277.94	76.88
7	324.2	230.81	63.84
8	292.1	207.96	57.52
9	275.8	196.35	54.31
10	263.5	187.60	51.89
Back	189.6	135.00	37.34
11	175.3	124.80	34.52
12	187.2	133.28	36.86
13	195.9	139.47	38.58
14	202.5	144.17	39.88
15	187.2	133.28	36.86
All	260.3	185.35	51.27

Experiment 6

Test Details							
Date:	29/04/2006 PM						
BL Info:	50mm roughness plates, 300mm step, filters and gauzes.						
Pot Setting:	15%						
Speed @ 900mm:	5.586	5.671	5.689	5.711	**Average:**	5.66	
Run Time:	3	hrs					
Layout:							
	H/W ratio = 1/4						
	Canyon 11 cubes wide						
	3 upsteam and 3 downstream rows of cubes						
Conditions							
	0	**1**	**2**	**3**	**Average**		
Water:	40	40	40	40	**40.0**	deg C	
Air:	19.4	19.4	19.2	18.9	**19.3**	deg C	
Air pressure:	1000	1000	1000	999	**999.8**	mbar	
R/H:	32.9	33.2	33.9	34.6	**33.6**	%	

Location	Average dT	Nusselt	CHTC
	1	0.47462895	0.131280348
Front	205.2	97.38	26.94
1	165.8	78.69	21.77
2	184.2	87.43	24.18
3	204.3	96.97	26.82
4	221.8	105.27	29.12
5	249.8	118.56	32.79
Top	247.8	117.59	32.53
6	325.8	154.63	42.77
7	248.2	117.80	32.58
8	240.6	114.20	31.59
9	226.4	107.46	29.72
10	197.8	93.88	25.97
Back	152.9	72.55	20.07
11	130.8	62.08	17.17
12	145.2	68.92	19.06
13	205.8	97.68	27.02
14	153.1	72.67	20.10
15	129.4	61.42	16.99
All	201.9	95.84	26.51

Experiment 7

Test Details							
Date:	30/04/2006 PM						
BL Info:	50mm roughness plates, 300mm step, filters and gauzes.						
Pot Setting:	45%						
Speed @ 900mm:	11.274	11.314	11.288	11.365	**Average:**	11.31	
Run Time:	3	hrs					
Layout:							
	H/W ratio = 1/2						
	Canyon 11 cubes wide						
	3 upsteam and 3 downstream rows of cubes						
Conditions							
	0	**1**	**2**	**3**	**Average**		
Water:	40	40	40	40	**40.0**	deg C	
Air:	18.6	18.4	18.3	18.2	**18.4**	deg C	
Air pressure:	999	998	998	997	**998.0**	mbar	
R/H:	36.0	36.9	37.8	38.7	**37.4**	%	

Location	Average dT	Nusselt	CHTC
	1	0.47455302	0.131259345
Front	212.3	100.73	27.86
1	205.8	97.66	27.01
2	218.2	103.55	28.64
3	206.5	98.00	27.11
4	216.8	102.88	28.46
5	214.0	101.55	28.09
Top	265.3	125.92	34.83
6	243.6	115.60	31.97
7	261.1	123.91	34.27
8	291.4	138.28	38.25
9	279.8	132.78	36.73
10	250.8	119.02	32.92
Back	205.1	97.35	26.93
11	206.7	98.09	27.13
12	217.9	103.41	28.60
13	205.1	97.33	26.92
14	207.6	98.52	27.25
15	188.4	89.41	24.73
All	227.6	108.00	29.87

Experiment 8

Test Details						
Date:	30/04/2006 PM					
BL Info:	50mm roughness plates, 300mm step, filters and gauzes.					
Pot Setting:	45%					
Speed @ 600mm:	16.258	15.888		**Average:**	16.07	
Run Time:	2	hrs				
Layout:						
	90 degrees					
	H/W ratio = 1/2					
	Canyon 11 cubes wide					
	3 upsteam and 3 downstream rows of cubes					
Conditions						
	0	**1**	**2**	**Average**		
Water:	40	40	40	**40.0**	deg C	
Air:	17.7	19.4	20.2	**19.2**	deg C	
Air pressure:	996	996	994	**995.5**	mbar	
R/H:	40.8	38.7	38.7	**39.2**	%	

Location	Average dT	Nusselt	CHTC
	1	0.71193079	0.196917027
Front	212.3	151.11	41.80
1	205.8	146.52	40.53
2	218.2	155.34	42.97
3	206.5	147.01	40.66
4	216.8	154.35	42.69
5	214.0	152.35	42.14
Top	265.3	188.90	52.25
6	243.6	173.43	47.97
7	261.1	185.89	51.42
8	291.4	207.46	57.38
9	279.8	199.20	55.10
10	250.8	178.55	49.39
Back	205.1	146.05	40.40
11	206.7	147.16	40.70
12	217.9	155.13	42.91
13	205.1	146.02	40.39
14	207.6	147.80	40.88
15	188.4	134.13	37.10
All	227.6	162.02	44.81

Experiment 9

Test Details						
Date:	01/05/2006 PM					
BL Info:	50mm roughness plates, 300mm step, filters and gauzes.					
Pot Setting:	45%					
Speed @ 900mm:	15.322	15.021	14.834	**Average:**	15.06	
Run Time:	2	hrs				
Layout:						
	45 degrees					
	H/W ratio = 1/2					
	Canyon 11 cubes wide					
	3 upsteam and 3 downstream rows of cubes					
Conditions						
	0	**1**	**2**	**Average**		
Water:	40	40	40	**40.0**	deg C	
Air:	20.2	22	22.7	**21.7**	deg C	
Air pressure:	990	991	991	**990.8**	mbar	
R/H:	41.4	36.0	33.6	**36.8**	%	

Location	Average dT	Nusselt	CHTC
	1	0.69634152	0.192605101
Front	240.5	167.50	46.33
1	209.1	145.61	40.27
2	207.5	144.49	39.97
3	235.7	164.13	45.40
4	262.2	182.58	50.50
5	288.2	200.69	55.51
Top	278.2	193.69	53.58
6	303.5	211.34	58.46
7	295.5	205.77	56.91
8	260.9	181.68	50.25
9	273.5	190.45	52.68
10	257.4	179.24	49.58
Back	210.8	146.77	40.60
11	171.4	119.35	33.01
12	204.5	142.40	39.39
13	228.3	158.97	43.97
14	249.1	173.46	47.98
15	200.6	139.69	38.64
All	243.2	169.32	46.83

Experiment 10

Test Details							
Date:	01/05/2006 pm						
BL Info:	50mm roughness plates, 300mm step, filters and gauzes.						
Pot Setting:	15%						
Speed @ 900mm:	5.336	5.281	5.273	5.293	**Average:**	5.30	
Run Time:	3	hrs					
Layout:							
	45 degrees						
	H/W ratio = 1/2						
Conditions							
	0	**1**	**2**	**3**	**Average**		
Water:	40	40	40	40	**40.0**	deg C	
Air:	22.2	22.5	22.7	22.7	**22.6**	deg C	
Air pressure:	992	992	993	993	**992.5**	mbar	
R/H:	34.2	33.0	32.4	32.3	**32.9**	%	

Location	Average dT	Nusselt	CHTC
	1	0.46430113	0.128423717
Front	196.3	91.15	25.21
1	197.5	91.70	25.36
2	157.6	73.17	20.24
3	178.4	82.83	22.91
4	206.3	95.79	26.49
5	241.8	112.27	31.05
Top	204.9	95.15	26.32
6	234.8	109.02	30.15
7	220.8	102.52	28.36
8	216.8	100.66	27.84
9	170.7	79.26	21.92
10	181.6	84.32	23.32
Back	177.2	82.27	22.76
11	139.2	64.63	17.88
12	158.2	73.45	20.32
13	190.1	88.26	24.41
14	222.4	103.26	28.56
15	176.1	81.76	22.62
All	192.8	89.53	24.76

Experiment 11

Test Details							
Date:	02/05/2006 am						
BL Info:	50mm roughness plates, 300mm step, filters and gauzes.						
Pot Setting:	30%						
Speed @ 900mm:	10.764	10.441	10.325	10.246	**Average:**	10.44	
Run Time:	3	hrs					
Layout:							
	45 degrees						
	H/W ratio = 1/2						
Conditions							
	0	**1**	**2**	**3**	**Average**		
Water:	40	40	40	40	**40.0**	deg C	
Air:	19.6	22.1	22.8	23.6	**22.2**	deg C	
Air pressure:	998	998	998	997	**997.8**	mbar	
R/H:	37.3	33.9	33.3	33.2	**34.2**	%	

Location	Average dT	Nusselt	CHTC
	1	0.46426851	0.128414695
Front	306.1	142.13	39.31
1	291.6	135.38	37.45
2	258.1	119.83	33.14
3	271.8	126.19	34.90
4	322.1	149.54	41.36
5	387.1	179.72	49.71
Top	314.2	145.85	40.34
6	359.8	167.04	46.20
7	322.6	149.77	41.43
8	296.0	137.42	38.01
9	300.7	139.61	38.61
10	291.7	135.43	37.46
Back	270.8	125.73	34.78
11	231.7	107.57	29.75
12	247.5	114.91	31.78
13	295.6	137.24	37.96
14	316.7	147.03	40.67
15	262.6	121.92	33.72
All	297.0	137.91	38.14

Experiment 12

Test Details						
Date:	02/05/2006 PM					
BL Info:	50mm roughness plates, 300mm step, filters and gauzes.					
Pot Setting:	15%					
Speed @ 900mm:	5.239	5.269	5.297	**Average:**	5.27	
Run Time:	3	hrs				
Layout:						
	90 degrees					
	H/W ratio = 1/2					
	3 rows either side of test row					
	4 cubes on upwind end of standard canyons to join plates					
Conditions						
	0	**1**	**2**	**4**	**Average**	
Water:	40	40	40	40	**40.0**	deg C
Air:	23.1	23.5	23.4	23.4	**23.4**	deg C
Air pressure:	997	998	998	998	**997.8**	mbar
R/H:	34.8	34.3	35.0	35.2	**34.8**	%

Location	Average dT	Nusselt	CHTC
	1	0.46436624	0.128441726
Front	146.0	67.78	18.75
1	125.1	58.09	16.07
2	153.8	71.42	19.75
3	143.9	66.82	18.48
4	144.2	66.96	18.52
5	162.8	75.60	20.91
Top	196.5	91.27	25.24
6	187.1	86.88	24.03
7	185.9	86.33	23.88
8	201.0	93.34	25.82
9	210.2	97.61	27.00
10	198.5	92.18	25.50
Back	156.0	72.44	20.04
11	152.5	70.82	19.59
12	157.0	72.91	20.17
13	154.5	71.74	19.84
14	160.0	74.30	20.55
15	156.0	72.44	20.04
All	166.2	77.16	21.34

Experiment 13

Test Details						
Date:	03/05/2006 PM					
BL Info:	50mm roughness plates, 300mm step, filters and gauzes.					
Pot Setting:	30%					
Speed @ 900mm:	0				**Average:**	0
Run Time:	3	hrs				
Layout:						
	90 degrees					
	H/W ratio = 1/2					
	Canyon 11 cubes wide					
	3 upsteam and 3 downstream rows of cubes					
Conditions						
	0	**1**	**2**	**4**	**Average**	
Water:	40	40	40	40	**40.0**	deg C
Air:	20.4	23	24.2	24.3	**23.2**	deg C
Air pressure:	1004	1004	1005	1005	**1004.5**	mbar
R/H:	45.6	40.6	38.8	38.7	**40.5**	%

Location	Average dT	Nusselt	CHTC
	1	0.46568102	0.128805388
Front	233.3	108.65	30.05
1	228.7	106.50	29.46
2	245.1	114.14	31.57
3	230.7	107.43	29.72
4	228.3	106.31	29.41
5	233.8	108.88	30.11
Top	290.0	135.05	37.35
6	282.0	131.32	36.32
7	290.0	135.05	37.35
8	297.5	138.54	38.32
9	289.8	134.95	37.33
10	290.7	135.37	37.44
Back	229.6	106.94	29.58
11	234.5	109.20	30.20
12	225.1	104.82	28.99
13	226.9	105.66	29.23
14	228.8	106.55	29.47
15	232.9	108.46	30.00
All	251.0	116.88	32.33

Experiment 14

Test Details						
Date:	14/04/2007 PM					
BL Info:	Not applicable.					
Pot Setting:	0%					
Speed @ 900mm:	0				**Average:**	0
Run Time:	4	hrs				
Layout:						
	No wind.					
	Active cube with one model each side.					
Conditions						
	0	**2**	**4**		**Average**	
Water:	40	40	40		**40.0**	deg C
Air:	17.8	19	20.2		**19.0**	deg C
Air pressure:	1014	1014	1013		**1013.7**	mbar
R/H:	52.7	52.0	50.8		**51.8**	%

Location	Average dT	Nusselt	CHTC
	1	0.35880761	0.096420002
Front	64.7	23.21	6.24
1	72.7	26.09	7.01
2	65.8	23.61	6.34
3	59.4	21.31	5.73
4	69.3	24.87	6.68
5	56.3	20.20	5.43
Top	63.3	22.71	6.10
6	68.3	24.51	6.59
7	78.1	28.02	7.53
8	51.6	18.51	4.98
9	67.4	24.18	6.50
10	51.1	18.34	4.93
Back	65.6	23.53	6.32
11	46.8	16.79	4.51
12	66.4	23.82	6.40
13	61.6	22.10	5.94
14	74.3	26.66	7.16
15	78.8	28.27	7.60
All	64.5	23.15	6.22

Experiment 15

Test Details						
Date:	14/04/2007 PM					
BL Info:	50mm roughness plates, 300mm step, filters and gauzes.					
Pot Setting:	7.5%					
Speed @ 900mm:	2.6				**Average:**	2.6
Run Time:	3	hrs				
Layout:						
	H/W ratio = 1/2					
	Canyon 11 cubes wide					
	3 upsteam and 3 downstream rows of cubes					
Conditions						
	0	**1**	**2**	**3**	**Average**	
Water:	40	40	40	40	**40.0**	deg C
Air:	20.6	21.2	21.3	21.2	**21.1**	deg C
Air pressure:	1013	1014	1014	1014	**1013.8**	mbar
R/H:	50.6	49.1	49.8	50.3	**50.0**	%

Location	Average dT	Nusselt	CHTC
	1	0.47937188	0.128818444
Front	121.5	58.24	15.65
1	96.3	46.16	12.41
2	85.1	40.79	10.96
3	114.9	55.08	14.80
4	138.2	66.25	17.80
5	173.0	82.93	22.29
Top	124.4	59.63	16.03
6	107.1	51.34	13.80
7	113.4	54.36	14.61
8	114.6	54.94	14.76
9	142.8	68.45	18.40
10	144.1	69.08	18.56
Back	90.5	43.38	11.66
11	77.3	37.06	9.96
12	93.4	44.77	12.03
13	96.8	46.40	12.47
14	96.3	46.16	12.41
15	88.7	42.52	11.43
All	112.1	53.75	14.44

Experiment 16

Test Details					
Date:	14/04/2007 PM				
BL Info:	50mm roughness plates, 300mm step, filters and gauzes.				
Pot Setting:	60%				
Speed @ 900mm:	0			**Average:**	0
Run Time:	1	hrs			
Layout:					
	H/W ratio = 1/2				
	Canyon 11 cubes wide				
	3 upsteam and 3 downstream rows of cubes				
Conditions					
	0	**1**		**Average**	
Water:	40	40		**40.0**	deg C
Air:	21.3	23.2		**22.3**	deg C
Air pressure:	1014	1014		**1014.0**	mbar
R/H:	50.3	45.2		**47.8**	%

Location	Average dT	Nusselt	CHTC
	1	1.39328448	0.374408149
Front	139.2	193.92	52.11
1	104.3	145.32	39.05
2	109.2	152.15	40.89
3	118.2	164.69	44.26
4	173.0	241.04	64.77
5	191.2	266.40	71.59
Top	164.3	228.89	61.51
6	148.6	207.04	55.64
7	156.3	217.77	58.52
8	143.1	199.38	53.58
9	157.4	219.30	58.93
10	216.0	300.95	80.87
Back	114.9	160.12	43.03
11	130.1	181.27	48.71
12	108.5	151.17	40.62
13	111.6	155.49	41.78
14	112.7	157.02	42.20
15	111.7	155.63	41.82
All	139.5	194.31	52.21

Experiment 17

Test Details				
Date:	30/07/2004 PM			
BL Info:	50mm roughness plates, 300mm step, filters and gauzes.			
Pot Setting:	40%			
Speed @ 900mm:	0		**Average:**	0
Run Time:	3	hrs		
Layout:				
	H/W ratio = 1			
	Canyon 11 cubes wide			
	3 upsteam and 3 downstream rows of cubes			
Conditions				
	Start	**End**	**Average**	
Water:	40	40	**40.0**	deg C
Air:	29.1	28.8	**29.0**	deg C
Air pressure:	1009	1009	**1009.0**	mbar
R/H:	33.4	37.5	**35.5**	%

Location	Average dT	Nusselt	CHTC
	1	0.45457161	0.125732572
Front	211.0	95.91	26.53
1	189.6	86.19	23.84
2	180.9	82.23	22.75
3	187.4	85.19	23.56
4	216.8	98.55	27.26
5	280.3	127.42	35.24
Top	189.9	86.30	23.87
6	238.4	108.37	29.97
7	193.8	88.10	24.37
8	183.3	83.32	23.05
9	185.1	84.14	23.27
10	148.7	67.59	18.70
Back	173.4	78.82	21.80
11	129.6	58.91	16.29
12	115.2	52.37	14.48
13	156.0	70.91	19.61
14	217.5	98.87	27.35
15	248.7	113.05	31.27
All	**191.42**	**87.01**	**24.07**

Experiment 18

Test Details				
Date:	26/08/2004 PM			
BL Info:	50mm roughness plates, 300mm step, filters and gauzes.			
Pot Setting:	18%			
Speed @ 900mm:	0		**Average:**	0
Run Time:	3	hrs		
Layout:				
	H/W ratio = 1			
	Canyon 11 cubes wide			
	3 upsteam and 3 downstream rows of cubes			
Conditions				
	Start	**End**	**Average**	
Water:	40	40	**40.0**	deg C
Air:	20.9	22.4	**21.7**	deg C
Air pressure:	1008	1008	**1008.0**	mbar
R/H:	58.5	54.6	**56.6**	%

Location	Average dT	Nusselt	CHTC
	1	0.46422768	0.1284034
Front	182.1	84.52	23.38
1	129.7	60.21	16.65
2	110.2	51.16	14.15
3	179.9	83.51	23.10
4	225.9	104.87	29.01
5	264.6	122.83	33.98
Top	173.2	80.41	22.24
6	196.9	91.41	25.28
7	175.2	81.33	22.50
8	200.1	92.89	25.69
9	145.1	67.36	18.63
10	148.8	69.08	19.11
Back	140.0	64.97	17.97
11	84.9	39.41	10.90
12	88.2	40.94	11.33
13	141.5	65.69	18.17
14	183.9	85.37	23.61
15	201.3	93.45	25.85
All	**165.08**	**76.63**	**21.20**

Experiment 19

Test Details				
Date:	26/08/2004 PM			
BL Info:	50mm roughness plates, 300mm step, filters and gauzes.			
Pot Setting:	30%			
Speed @ 900mm:	0		**Average:**	0
Run Time:	2	hrs		
Layout:				
	H/W ratio = 1/2			
	Canyon 11 cubes wide			
	3 upsteam and 3 downstream rows of cubes			
Conditions				
	Start	**End**	**Average**	
Water:	40	40	**40.0**	deg C
Air:	22.9	21.4	**22.2**	deg C
Air pressure:	1008	1006	**1007.0**	mbar
R/H:	54.6	51.9	**53.3**	%

Location	Average dT	Nusselt	CHTC
	1	0.69640277	0.192622042
Front	223.7	155.80	43.09
1	208.0	144.85	40.07
2	203.1	141.44	39.12
3	216.2	150.56	41.64
4	241.1	167.90	46.44
5	250.2	174.24	48.19
Top	177.4	123.54	34.17
6	232.5	161.91	44.78
7	186.1	129.60	35.85
8	154.7	107.73	29.80
9	181.7	126.54	35.00
10	132.0	91.93	25.43
Back	124.9	86.99	24.06
11	102.5	71.38	19.74
12	116.2	80.92	22.38
13	130.1	90.60	25.06
14	130.1	90.60	25.06
15	145.7	101.47	28.07
All	**175.35**	**122.11**	**33.78**

Annex G Naphthalene sublimation results

The full results for the various naphthalene sublimation tests that have been conducted as part of the current research are provided in various formats on the enclosed CD-ROM disc.

Included data file formats:

- 'AxxexG.doc' – Result tables in a Microsoft Word document.
- 'AnnexG.pdf' – Result tables in Adobe 'PDF' format.
- 'Experiment1.xls' to 'Experiment19.xls' – Results spreadsheets in Microsoft Excel format (see Annex F for the details of experiment numbering).

Other files included:

- 'CHTC Calculation Sheet.xls' – The spreadsheet used to convert experimental naphthalene thickness change data to convective heat transfer coefficients, in Microsoft Excel format.

Annex H Apparatus

The following equipment was used during the course of the experimental work. Those items marked with an asterisk (*) are held as part of BRE calibrated equipment and subject to yearly calibration.

Constant temperature anemometry (CTA) apparatus:

- Dantec Streamline CTA control system
- Dantec 55P11 CTA probes and 55H20 probe support
- Kemo VBF/8 dual variable filter (0.01 Hz – 100 kHz high/low pass)
- Cambridge Electronics Division CED1401 analogue to digital converter

Pressure measurement apparatus:

- Scanivalve ZOC33 64-way pressure transducer
- Scanivalve ZOC22 32-way pressure transducer
- Scanivalve DSM 3200 data acquisition computer
- Dell Optiplex GX260 personal computer with BRE sampling and analysis software

Naphthalene sublimation apparatus:

- Cookworks Hotplate (1500/1200Watts)
- Memmert WB14 water bath (1800Watts, max 100 °C)
- Clarke CSE1 submersible water pump (280 Watts, 135 litre/min, 7 metre maximum head)
- Elcometer 456 coating thickness gauge

Photographic / flow visualisation equipment:

- Nikon Coolpix 885 3.0 mega-pixel digital camera
- Fuji FinePix 2800 Zoom 2.0 mega-pixel digital camera
- Aerotech SGS-90 smoke generator (uses crushed walnut oil)
- Lampo TE71/N projection lamp (500 Watts)

General laboratory equipment:

- Rotronic Hygrolog-D temperature and humidity gauge *
- Prosser Weathertrend digital barometer *
- TIM digital stopwatch *

Software:

- Surfer v8.04 surface mapping program by Golden Software Inc.
- EasyPlot v4.0.4 graphing program by Spiral Software
- Microsoft Excel 2002 spreadsheet program
- BRE WetCMA pressure measurement analysis software

Annex I Publications and conference papers by the author

i. Smith, J.O., 2004. The Development of the Naphthalene Sublimation Technique to Model Convective Heat Transfer from External Building Surfaces. *Proceedings of the Wind Engineering Society Conference, Cranfield University*, 16th September 2004.

ii. Smith, J.O., 2008. The Development of the Naphthalene Sublimation Technique to Model Convective Heat Transfer from External Building Surfaces. *Proceedings of the Wind Engineering Society Conference, University of Surrey*, 15th July 2008.

The Development of the Naphthalene Sublimation Technique to Model Convective Heat Transfer from External Building Surfaces.

James Smith
Building Research Establishment, Watford.
& Dept. of Mechanical Engineering, University of Bath.

Introduction

The next generation of urban climate models are likely to need increasingly accurate heat transfer data on which to base their predictions. Whilst both the radiative and conductive components of urban heat transfer are well understood, calculations for convective heat transfer are commonly still based on empirical relationships for unrepresentative flat plates. There is therefore a need for more appropriate convective heat transfer data which is specifically applicable to urban geometries.

A range of correlations for convective heat transfer currently exist, derived from a variety of theoretical and experimental studies. A selection of such relationships are compared in Figure 1 and it can be seen that these exhibit considerable spread. This may largely be due to inconsistencies regarding how (or more importantly where) the wind speed is defined. Some correlations were determined with wind speeds measured above the test building [5], others with so-called surface velocities [6] [7]. This inconsistency has lead to confusion regarding which wind speeds should be employed in such convective heat transfer calculations

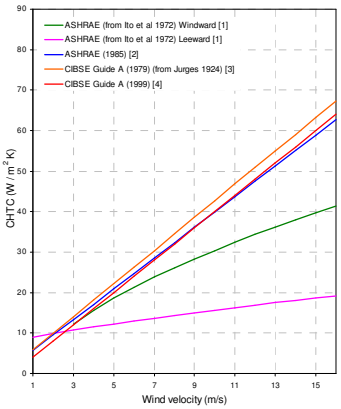

Figure 1: Design guidance for convective heat transfer coefficients

It is therefore suggested that a more consistent wind speed to use for such convection relationships is the Met. Standard Wind Speed (i.e. that at 10m above the open site at sea level). By correlating convective coefficients with respect to this velocity, it allows the convective heat flux to be obtained without specific knowledge of the local flow conditions around the building. As a means to generating such urban convective heat flux data, BRE is currently developing the Naphthalene Sublimation methodology to determine convective heat transfer coefficients for typical building surfaces.

The naphthalene sublimation technique is based upon the analogy between mass and heat transfer. This allows the convective heat flux to be determined from measurements of the erosion of a naphthalene[1] coating from a scale model. The model is coated with a thin layer of naphthalene and is then placed in a wind tunnel which simulates the urban boundary layer for a period of several hours. During this time, naphthalene sublimates from the model in a way directly analogous to surface heat removal by convection. By careful measurement of the naphthalene coating thickness both before and after the test, the thickness change and hence the mass transfer rate can be determined. An analogy between mass and heat transfer then allows this mass transfer rate to be converted into a convective heat transfer rate.

Development of the technique is focussed on the need to improve spatial resolution across the building surfaces. Previous researchers have used basic weighing techniques in order to obtain surface-averaged mass transfer values. In contrast, this current research uses a precision coating thickness gauge[2] working on the principal of eddy-current induction in order to determine the change in coating thickness rates at specific locations. Resolution has also been increased by using relatively large 1/100th scale models.

[1] Naphthalene ($C_{10}H_8$) is a white, aromatic hydrocarbon which sublimates at room temperature.

[2] Elcometer A456-FNFTS Coating Thickness Gauge with T456FNF1S probe. Range 0-1500µm, accuracy ±1-3% or ±2.5µm, resolution 1µm.

Current work is based on a 94mm cube (representative of a three storey full-scale building) which is arranged with dummy models to form a variety of typical street canyon geometries. However, it is believed that the methodology is suitable for application to more complex geometries associated with a particular building or development.

Theoretical basis of the method

In heat transfer studies, the rate of heat transfer between a solid and a fluid per unit area and unit temperature difference is expressed as the Convective Heat Transfer Coefficient (CHTC or *h*). It is common practice to non-dimensionalise this parameter into the Nusselt Number (*Nu*), which is in effect, the ratio of convective heat flux (Q_{conv}) to conductive heat flux (Q_{cond}):

$$Nu = \frac{Q_{conv}}{Q_{cond}} = \frac{h\ \Delta T}{k\ \Delta T/L} = \frac{h \times L}{k}$$

where: L = characteristic length
k = thermal conductivity of the fluid
ΔT = temperature change (1)

The Nusselt number therefore represents the enhancement of heat transfer by convection, relative to that resulting from conduction. Hence, the larger the number, the more effective the convective heat transfer is. The Nusselt number has been shown to be a function of the properties of both the air and naphthalene (expressed as the non-dimensional Prandtl and Schmidt numbers respectively), and the mass transfer rate (expressed as the non-dimensional Sherwood number). Thus:

$$Nusselt = \left(\frac{Prandtl}{Schmidt}\right)^{n} \times Sherwood \qquad (2)$$

The Prandtl number is known for air (0.688 at 295K), the Schmidt number can be determined for naphthalene (2.284 at 295K) and 'n' can be taken from literature (0.34) [8]. The Sherwood number is calculated from the mass transfer rate measured during the experiment, and hence the Nusselt number can be determined. The CHTC (h) can then be calculated using equation (1), taking 'L' as the model height (i.e. 94mm).

Advantages of methodology

The majority of techniques employed to measure convective heat transfer inevitably also include radiative and conductive components. The allowances made to compensate for this add uncertainty to the results. However, by using mass transfer as an analogy for heat transfer, both the radiative and conductive components are eliminated. Mass has no effects analogous to radiation and by constructing the model from non-porous material (in this case aluminium), absorption (i.e. conduction) can also be eliminated.

Convective heat transfer measurements using traditional, heated wind tunnel models typically require expensive and complicated thermocouples in order to measure heat fluxes. It is often also difficult to maintain uniform heating and provide sufficient insulation to minimise conduction from the model. In contrast, by employing the naphthalene sublimation technique, a surface is uniformly 'heated' merely by being coated in a layer of naphthalene. Therefore, the correct isothermal (coated) and adiabatic (uncoated) boundary conditions can be imposed with ease, and it is possible to change discontinuously from one condition to the other. Without the complications of temperature measurement devices and insulation, more complex geometries are possible and models are more economical.

Test geometry

A simplified urban geometry has been selected for these tests which represents a building in the middle of a long terrace of equal height buildings, with similar street canyons on either side. In order to make the flow conditions two-dimensional, the street canyon is 11H long (where 'H' represents the height of the test model). The height-to-width ratio of the canyon (H/W) is unity. This generates a skimming flow regime over the tops of the models which tends to drive a lee-vortex in the upstream and downstream canyons [9]. The canyons were aligned perpendicular to the wind direction, as is shown in Figure 2.

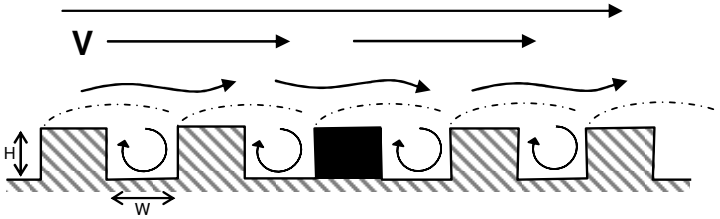

Figure 2: Skimming flow regime with H/W = 1 (taken from Oke [9])

Results and discussion

Initial results obtained using this simplified urban geometry have indicated mass transfer rates which lie within the range of previous correlations. The surface averaged CHTC data for the windward and leeward surfaces of the model are plotted in Figures 3 and 4, alongside a selection of full-scale data from previous researchers. Also plotted are local CHTC's taken on areas of the model representative of the exposed top floor at full-scale. This data may be more comparable to the full-scale data which has mostly been gathered on the side of isolated, high-rise buildings. The technique has also generated CHTC data for the roof surface of the cube (see Figure 3). Such surfaces are generally not covered by existing convective heat transfer correlations.

It can be seen in Figures 3 and 4 that the CHTC relationships determined using the naphthalene sublimation technique compare well with correlations presented by Sharples [7], Loveday and Taki [5] and Nicol [11]. The Sturrock [10] correlation is generally regarded as giving unrealistically high results due to errors with the measurement technique, and the naphthalene sublimation results would seem to support that conclusion. It should however be noted that these relationships are based on data obtained at only two wind speeds (approximately 5 and 10 ms^{-1}). Further tests could provide more data, but at present, these results are taken to be indicative of that trends that may be expected using the naphthalene technique.

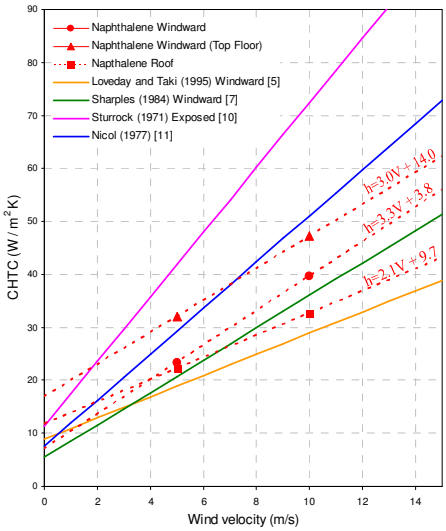

Figure 3: CHTC's versus wind velocity for windward building surfaces.

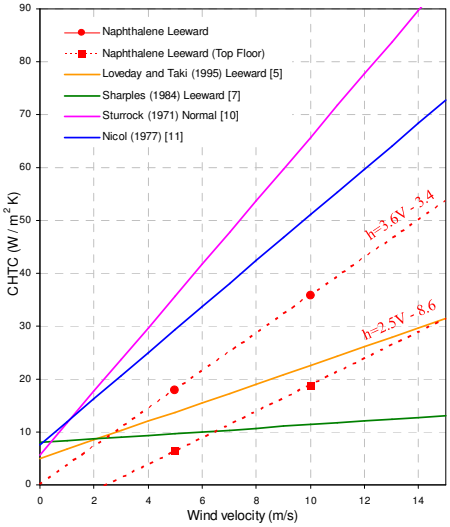

Figure 4: CHTC's versus wind velocity for leeward building surfaces.

The measurement of the naphthalene layer using the coating thickness gauge means that the results are not limited to surface averaged values. It is also possible to show the distribution of the CHTC's across the surfaces of the building. Naphthalene thickness measurements were made at 25 locations across each of the surfaces. Contour plots of the calculated CHTC's are shown in Figures 7 and 8. In each case, the contour plot represents an opened-out net of the windward, leeward and roof surfaces of the test cube, with the windward surface at the top (see Figure 6).

These plots represent two wind speeds over the same canyon geometry and as such, the patterns on the windward and leeward faces are very similar. A region of high convective heat transfer can be seen at the top of the windward face of the cube. The prevailing wind is likely to hit this exposed area of the building and be driven down to form a vortex within the canyon. Similarly, some of the flow hitting this exposed corner will be driven up and over the cube resulting in the higher CHTC's seen at the windward edge of the roof. As the flow separates over the roof, the convective heat transfer is also seen to diminish. The air flow within the canyon, and it's relation to the areas of high convective heat transfer, is illustrated by the areas of red shown in Figure 5.

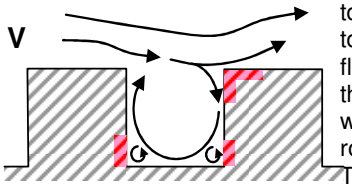

Figure 5: Wind low and CHTC 'hot-spots' around the cube

It is presently unclear why there are higher rates of convective heat transfer at the foot of the two vertical sides of the cube. It is speculated that this may be a result of scavenging vortices generated within the canyon (as depicted in Figure 5).

Such information regarding CHTC 'hot-spots' not only influences the average heat transfer rates across a building surface, but may also aid improved building design. For example, extra insulation could be applied at the areas identified as experiencing high convective heat transfer rates, and reduced insulation used at low CHTC locations to minimise cost.

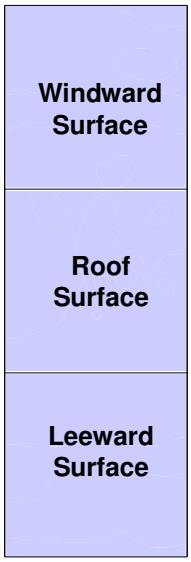

Figure 6: Contour plot key

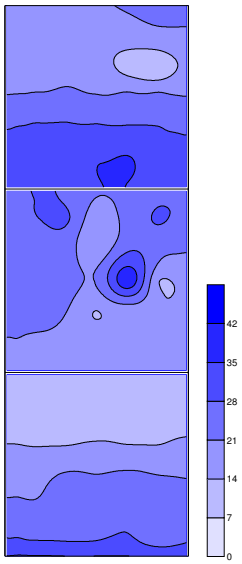

Figure 7: CHTC's for cube at 5ms^{-1}

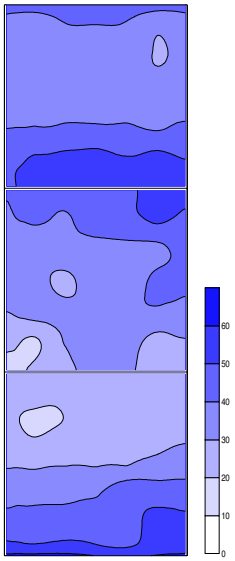

Figure 8: CHTC's for cube at 10ms^{-1}

Further work

Whilst the initial results presented are based on a simplified two-dimensional street canyon, comparison with existing theoretical and experimental data is allowing verification of the technique. Investigations will now focus on obtaining data for a range of wind speeds for this canyon geometry. Alternative geometries will then be investigated, both by off-setting the canyons at angles to the approaching flow and by changing the canyon height-to-width ratio.

If successful, the technique could then be employed with more complicated building configurations. This could involve models of specific buildings or developments, or investigating the sheltering effect caused by other street features such as trees and canopies. Such data would not only be of benefit in allowing heat losses from buildings to be minimised, but also in the light of expected climate change, would have applications in maximising heat transfer away from urban 'heat islands'.

References

1. American Society of Heating, Refrigeration and Air-conditioning Engineers (ASHRAE). (1972). ASHRAE Handbook of Fundamentals. ASHRAE, Atlanta, USA.
2. American Society of Heating, Refrigeration and Air-conditioning Engineers (ASHRAE). (1985). ASHRAE Handbook of Fundamentals. ASHRAE, Atlanta, USA.
3. Chartered Institute of Building Services (CIBS). (1979). Guide Book A, Section A3. CIBS, London.
4. Chartered Institute of Building Services Engineers (CIBSE). (1999). Guide A, Section A3. CIBSE, London.
5. Loveday, D.L. and Taki, A.H. (1996). Convective Heat Transfer Coefficients at a Plane Surface on a Full-Scale Building Façade. *International Journal of Heat and Mass Transfer*, **39** (8), pp. 1729-1742.
6. Ito, N., Kimura, K. and Oka, J. A Field Experiment Study on the Convective Heat Transfer Coefficient on Exterior Surface of a Building. *AHRAE Transactions*, **78** (1), pp.184-191.
7. Sharples, S. (1984). Full-scale Measurements of Convective Energy Losses from Exterior Building Surfaces. Building and Environment, **19** (1), pp.31-39.
8. Goldstein, R.J. and Cho, H.H. (1995). A Review if Mass Transfer Measurements Using Naphthalene Sublimation. *Experimental Thermal and Fluid Science*, **10**, pp.416-434.
9. Oke, T.R. (1987). Boundary Layer Climates. 2nd ed. Cambridge: Routledge.
10. Sturrock, N.S. (1971). Localised Boundary Layer Heat Transfer from External Building Surfaces. Ph.D. Thesis, University of Liverpool.
11. Nicol, K. (1977). The Energy Balance of an Exterior Window Surface, Inuvik, N.W.T., Canada. *Building and Environment*, **12**, pp.215-219.

The Development of the Naphthalene Sublimation Technique to Model Convective Heat Transfer from External Building Surfaces.

James Smith (smithj2@bre.co.uk)
Building Research Establishment, Watford.
& Dept. of Mechanical Engineering, University of Bath.

Introduction

In the summer of 2007 and for the first time in human history, the number of people living in the worlds urban areas exceeded that of those living in the countryside. The proportion of city-dwellers had been a mere thirteen percent only a century beforehand, a figure which had more than doubled by 1950. This rapid urbanisation has placed a whole range of stresses and strains upon our local urban environment. Of particular concern is the modification of the local microclimate which can result from increased building densities; a phenomena known as an 'urban heat island'. The geometries and fabrics of our built environment are not only more effective than natural surfaces at absorbing incoming solar radiation, they also retain more of this thermal energy for longer into the night. The resulting increased temperatures can be as much as 5° Celsius higher than the nearby countryside giving the characteristic appearance on a thermal map of a hot urban 'island' in a 'sea' of cooler countryside (Fig. 1). Predicted global warming is expected to further amplify these effects with numerous consequences for the urban population.

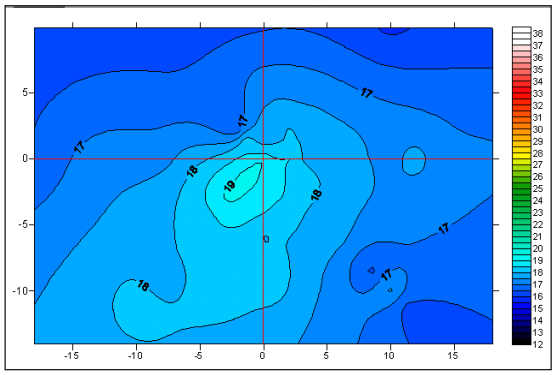

Fig. 1: London's nocturnal heat island

Therefore an understanding of the heat transfer processes which occur from the streets and buildings of our urban areas is becoming increasingly essential. Both radiation and conduction are relatively well understood phenomena. In contrast, convective heat transfer (especially that occurring from real building surfaces) is less well understood. Much of the convection data documented in current design guidance has evolved from pioneering work conducted in the early 1920's. This considered only flat plates in laminar flow; conditions unrepresentative of the complex three-dimensional air flow patterns and heat transfer processes which occur around real urban structures. The rates of convection calculated using such expressions are likely to be similarly unrepresentative, giving rise to inaccuracies in the building design calculations and thermal models which make use of these inputs.

The present research has therefore aimed to fill the void between the limited convection data which currently exists for buildings, and the requirements of increasingly complex simulation codes, thermal models and design calculations. A series of expressions has been determined for the convective heat transfer coefficients over various building surfaces in a range of representative street geometries. These expressions have been presented in a dimensional form which can be easily applied by designers, or else incorporated as subroutines into higher-level thermal codes and simulation models.

Methodology

The key to the measurement of this convective heat transfer coefficient (CHTC) data has been significant advances in the implementation of an experimental technique based on the sublimation of naphthalene (a crystalline aromatic hydrocarbon). Mass transfer and convective heat transfer are analogous processes. It follows that by measuring the rate at which naphthalene sublimates from a model, the respective rate at which convective heat transfer occurs may be determined. This heat-mass transfer analogy has several crucial advantages over more traditional experimental techniques: Boundary conditions may be more readily maintained and as neither conduction nor radiation has an analogous mass transfer equivalent, the technique provides a rare opportunity to study convective transfer in isolation.

The naphthalene sublimation technique has been enhanced and extended by the current research in several key areas. Perhaps the most significant of these is the novel approach which has been developed to measure the rate of sublimation of the naphthalene coating from the model. A handheld electronic gauge (Fig. 2) has been employed which utilises the principle of eddy-current induction to measure the distance of the probe tip from an underlying metallic substrate. The thickness of the naphthalene coating is obtained to an accuracy of ±2.5μm, and by taking readings at the start and end of an experimental run, the respective sublimation depth may thereby be calculated.

Fig. 2: Thickness measurement device.

The application of this technology to the naphthalene sublimation technique has a number of significant advantages over traditional measurement methods, resulting in increased accuracy and broadening of the scope of application. Taking measurements is as simple as touching the probe onto the model at the desired location. The process is therefore fast (minimising errors resulting from extraneous sublimation of the naphthalene layer) and also as equally applicable to complex three-dimensional models as it is to flat plates. By enabling measurements to be made at an array of discrete points over the model surfaces, spatial variation of the convection coefficient can be resolved. Such results permit a greater understanding of the convective processes to be gained than would be possible had only surface-average values been measured.

A further enhancement of the sublimation technique has been the development of a simple procedure for attaining a high quality surface coating by dipping the model into molten naphthalene. Whilst other coating methods have been developed by previous researchers, these have each had significant limitations or requirements which have made them unsuitable or impractical for the current study. The dipping methodology is, in contrast, fast, safe and low cost. The success of the methodology which has been developed is attributable to the use of a hollow aluminium model. A solid model has a high thermal capacity, resulting in either a roughly crystallised surface coating (if cold when dipped) or else to loss of areas of the coating through rapid sublimation (if heated). The thermal capacity of a hollow cube is much less, allowing it to be easily warmed to the optimum dipping temperature and then rapidly cooled following coating by flushing with cold water in order to minimise extraneous sublimation.

The vapour pressure (and thus rate of sublimation) of the naphthalene coating is highly dependant upon the surface temperature. The use of a hollow model has further benefits since it allows constant temperature water to be pumped through the internal cavity during a test. A series of fins within the model ensure that the internal flow is well mixed and that no

stagnation occurs at the vertices. In this way, it has been possible to maintain the model surface temperature to within 0.2° Celsius ensuring that the properties of the naphthalene coating remain constant throughout the experiment.

The rate of convection occurring from a given surface is primarily a function of the local wind speed. Therefore in order to be able to measure representative convective heat transfer coefficients for buildings, it is essential that the appropriate characteristics of the wind in the urban boundary layer are simulated by the flow surrounding the model. To this end, all tests have been conducted in the atmospheric boundary layer wind tunnel at BRE. This facility has a cross-sectional area of 2.0m (width) by 1.7m (height) and employs a series of flow-conditioning elements and roughness plates along its 14m upstream fetch to generate the required vertical mean velocity profile and turbulence characteristics.

An array of 100mm (nominal) cube models were arranged in the wind tunnel so as to form long rows of buildings (Fig. 3). These 'street canyons' were modelled at a range of building spacings corresponding with known isolated, wake interference and skimming flow regimes. Such arrangements are representative of typical geometries of buildings in the majority of towns and cities worldwide. The active (naphthalene coated) model on which measurements were made was located in the middle of the street canyon with a number of similar streets both up- and downstream. Convective heat transfer data were therefore recorded on the front, rear and flat-roof surfaces of the model (the sides of the cube abutted the neighbouring cubes).

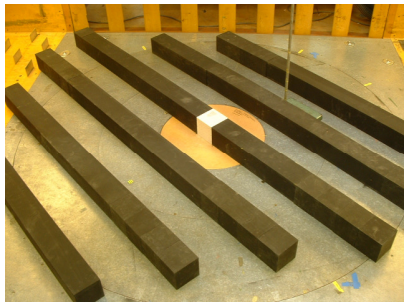

Fig. 3: Typical arrangement of models in the BRE boundary layer wind tunnel, with naphthalene coated model (white cube) at the centre.

The maximum error in the value of the convective heat transfer coefficient obtained in a typical naphthalene sublimation experiment has been calculated to be less than ±6%. Accurate measurement of the naphthalene sublimation depth was shown to be critical to obtaining high quality results, as was control of the experimental run time. The innovative coating thickness measurement procedure developed during this research has enabled both of these criteria to be satisfied. Air temperature, atmospheric pressure and humidity were all shown to have negligible impact upon the results obtained.

Results and discussion

For flow perpendicular to the street canyons, the average rate of free convection occurring from the windward, leeward and roof surfaces was found to be 6.22 W/m^2K. The maximum variation between the horizontal and vertical surfaces was approximately 0.2 W/m^2K with the lack of clear definition between the two orientations being attributable to the small length scales involved. This value is significantly greater than that prescribed by current European Standards (usually 4 W/m^2K), however it lies at the centre of the range of values determined by previous experimental measurements by other workers in the field.

The traditional linear and power-law forms of expression used by the majority of previous researchers to present forced convection data were not found to be satisfactory. Such expressions are unable to represent both the smooth transition from free to forced convection at low wind speeds, as well as the tailing-off effect of the rate of convection at the highest wind speeds. An alternative '*offset power-law*' form of expression has therefore been proposed which combines the advantages of both of the traditional linear and power-law equations.

For many of the convection equations documented in the existing literature, the reference wind speed location is often poorly defined, or the appropriate wind speed data may not be readily available. It has therefore been a primary concern of the current study to both explicitly state the appropriate type and location of wind speed data appropriate for the derived expressions, and also to ensure that this is of a type which is readily available in the majority of circumstances. The convective heat transfer coefficient relationships presented are thereby given with respect to the two most commonly available wind data types; the free stream wind speed at high level above an urban environment, and the meteorological standard wind speed at a height equivalent to 10m above open, level countryside. Expressions of this type have been determined using the naphthalene sublimation data for windward, leeward and flat-roof building surfaces. All were found to show a strong correlation with wind speed, with coefficients of determination (R^2 values) in excess of 0.970.

A typical set of experimental results are shown in Fig. 4 for a range of wind speeds. The

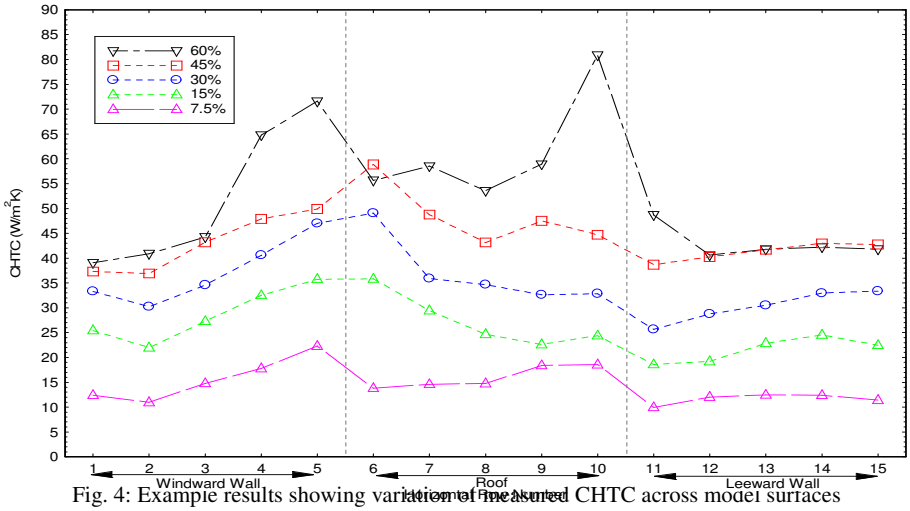

Fig. 4: Example results showing variation of measured CHTC across model surfaces

data points represent locations on the windward (left), roof (centre) and leeward (right) cube surfaces. The greatest rates of convective heat transfer have been shown to occur at the top of the windward wall and leading edge of the roof; the so-called 'exposed edge'. The average coefficient value across the windward surface tends to be similar to the combined average across all three building surfaces for the majority of wind speeds. The roof value was shown to be similar to the overall average at low wind speeds, but rises to near exposed edge values at higher wind speeds indicating a down-wind spread of the peak transfer region in such conditions. The lowest rates of convective heat transfer have been shown to occur from the leeward wall of a building.

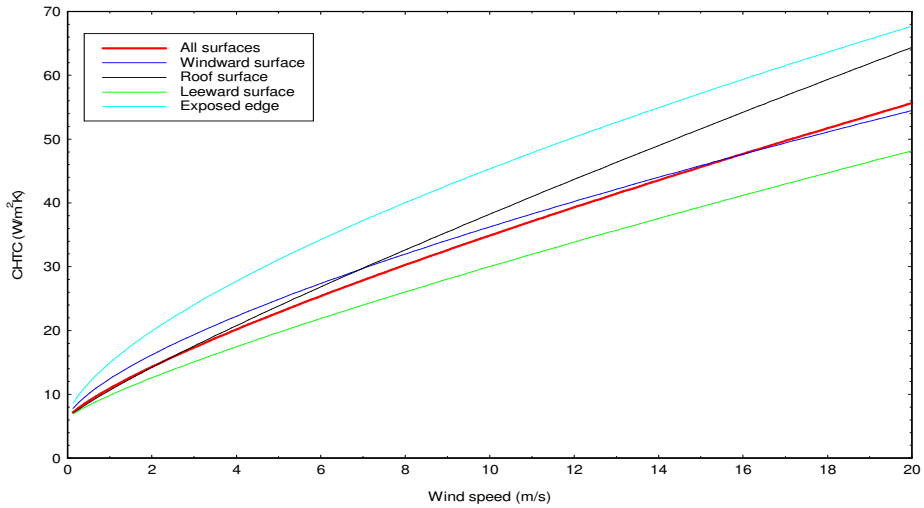

Fig. 5: Variation of CHTC with windspeed across the various model surfaces.

The variation of the convective heat transfer coefficient with windspeed is shown in Fig. 5 for the various model surfaces. The combined average convective transfer coefficients (h_c) over the windward, leeward and flat-roof surfaces of a low-rise building may be calculated with respect to the wind speed (V) using the following equations:

$h_c = 6.22 + 4.70V^{0.785}$ - with respect to the free-stream wind speed

$h_c = 6.22 + 8.10V^{0.789}$ - with respect to the met. standard wind speed

The above expressions have been derived from experiments conducted with the model buildings arranged at a street height-to-width ratio (H/W) of a half; a value typical of the majority of urban areas where the wake-interference flow regime will dominate. For narrow street canyons, a skimming flow regime exists whereby the flow between the buildings becomes detached from that above the roofs and hence convection coefficients are reduced. In wider street canyons, the convective coefficients on the exposed windward and roof surfaces of buildings have been shown to be higher. In contrast, the values on the leeward wall surface are lessened due to the distancing of the windward vortex effects from the downstream row of buildings.

Comparison of the wake-interference flow regime results with those of experiments conducted at alternative building spacings has indicated that factors can be applied to take into account the relevant exposure of the building. A series of canyon geometry factors (F_g) has thereby been deduced which may be applied to the wake-interference flow expressions above to provide results for skimming and isolated flow scenarios. The canyon geometry factors (F_g) determined for the average (all surface) convection expressions are as follows:

$F_g = 0.729$ - for skimming flow regimes (H/W > 0.65)

$F_g = 1.000$ - for wake interference flow regimes (0.30 > H/W > 0.65)

$F_g = 1.052$ - for isolated flow regimes (H/W < 0.30)

Further naphthalene sublimation experiments were conducted to study the effect of wind direction upon the rate of convective heat transfer from building surfaces. This was achieved by rotating the arrangement of models on the wind tunnel turntable to model flow parallel to the street canyons and at an intermediate 45° diagonal wind direction. By comparison of these results with those obtained previously for flow perpendicular to the street canyons, it has been shown that the effect of wind direction is relatively small.

The maximum variation from the baseline (perpendicular flow) case was an approximate 11% increase over the roof surface for the intermediate wind angle. The variation was shown to be significantly less for the other surfaces and wind directions with an average percentage increases of 5.9% for intermediate wind angles and 1.3% for parallel winds. This finding is highly significant since it suggests that the correlations obtained for the perpendicular wind direction can be applied generically to urban areas without requiring further consideration of the wind direction. Such levels of variation are likely to be well within the error inherent in other aspects of determining the rate of convective heat transfer and so may be neglected in the majority of situations.

A region of peak convective transfer was identified by naphthalene sublimation measurements during perpendicular flow experiments at the top of the windward surface and leading edge of the roof. The rate of convection occurring from this exposed edge was shown to be significantly greater than elsewhere on the cube model. Such regions of high convective transfer were further investigated by returning the naphthalene coated model to the wind tunnel after conclusion of the main experiment. This was then monitored until complete erosion of the coating was noted at a given location, hence highlighting the area from which the greatest convective heat transfer occurs. Whilst such observations are not quantitative, they are useful in providing additional information with which to interpret the experimental results. For parallel flow conditions, it was found that the small irregularities between adjoining cubes gave rise to increased sublimation from the edges of the models. This suggests that features in the surfaces of buildings such as doors and windows, are also likely to result in localised increases in the rate of convective heat transfer.

Comparison with full-scale data

The current experimental results have been compared with those from full-scale experiments conducted by a range of previous researchers. The naphthalene sublimation results have been shown to compare well with full-scale convection measurements made on low-rise buildings, but differ significantly to those made on more exposed high-rise buildings and tower blocks. This highlights the importance of applying only convective heat transfer relationships appropriate to the building geometry in question. It is suggested that the current results are widely applicable to low-rise buildings in approximately uniform urban areas, as are common in the majority of worldwide towns and cities.

Conclusions

For conciseness, only the convective heat transfer equations and factors relating to the overall average coefficients across the building have been presented in this paper. However, expressions have also been determined for each of the individual wall and roof surfaces, as well as for the peak convective region identified at the ‘exposed edge’.

These expressions have several distinct advantages over those which currently exist in the literature. Most significant is that they have been determined from wind tunnel experiments in which a representative urban atmospheric boundary layer has been simulated. Work conducted by previous researchers using flat plates in laminar wind tunnels has neglected the key importance of atmospheric turbulence and the three-dimensional flow effects around buildings. Whilst full-scale measurements inherently take account of such factors, the buildings which are employed tend not to have geometries and surroundings which are more widely applicable to generic urban areas. The current boundary layer wind tunnel experiments have allowed the effect of specific key variables (wind speed, building spacing and wind direction) to be determined for low-rise buildings, typical of the majority of towns and cities.

- End of Thesis -